GENERALIZED RAY MODELS OF STRONG GROUND MOTION

Thesis by

Thomas Harrison Heaton

In Partial Fulfillment of the Requirements

for the Degree of

Doctor of Philosophy

California Institute of Technology

Pasadena, California

1979

(Submitted 26 September 1978)

To

Norma Heaton

Acknowledgments

If a thesis could have a second author, then Don Helmberger's name would appear on the title page of this work. Without his help and guidance, this work would have been impossible. My sincere thanks goes to him for making our work into a pleasant and rewarding discovery process.

There are many people at the Seismological Laboratory who have enriched my stay. Professors Hiroo Kanamori and David Harkrider have been particularly helpful. Long discussions with Charles Langston were extremely enlightening. Larry Burdick, George Mellman and Tai-Lin Hong have also provided useful discussions. To the other students and members of the staff of the Laboratory, I give my sincere thanks.

Various parts of the text were critically reviewed by Hiroo Kanamori, Charles Langston, George Mellman, Paul Jennings, and James Brune. I would like to thank the California Institute of Technology, EERL, and G. Brady of the U.S. Geological Survey for their help with the strong ground motion recordings. Madeline Schnapp and Gary Fuis provided useful information concerning the Brawley earthquake. Shawn Biehler helped define the upper crustal structure in the Imperial Valley and he also allowed us to use several of his figures. I also thank Gladys Engen for helping with the San Fernando phase of this research. Useful discussions concerning San Fernando were provided by Hiroo Kanamori, Charles Langston and Tom Hanks.

Most of the figures were drafted by Laszlo Lenches and Joseph Galvan. The manuscript was typed by Donna Lathrop. Part of this research was funded

by the Advanced Research Agency of the Department of Defense and was monitored by the Air Force Office of Scientific Research under Contract No. F44620-72-C-0083. The remainder was funded by the National Science Foundation (ENV76-10506, ENV76-21652 and EAR76-06619).

Generalized Ray Models of Strong Ground Motion

Thomas H. Heaton

Abstract: A method for synthesizing local ground displacement from a model consisting of a finite fault located within a layered half-space is demonstrated. The response of a three-dimensional fault is evaluated by integrating the responses of point shear dislocations over the fault plane (Green's function technique). The response of each point shear dislocation is evaluated by using generalized ray theory in conjunction with the Cagniard-de Hoop technique. A basic review of these methods is given. In general, the complete solution to a three-dimensional fault in a layered half-space is complex and computationally unwieldy. Various simplifying approximations, whose validity depends upon the source to receiver geometry and seismic frequency, are discussed. The records from three Southern California earthquakes of different magnitudes and source to receiver geometries are modeled and appropriate approximations are demonstrated.

The smallest earthquake that is modeled is the largest earthquake (M 4.9) in the November, 1976 Brawley swarm. Long-period strong-motion instruments were located at distances of 33 km (IVC) and 36 km (ELC). The IVC record consists almost entirely of transversely polarized motion, whereas the ELC record contains an approximately equal proportion of transversely and radially polarized motion. A simplified shear wave velocity model was determined from the compressional wave refraction studies of

Biehler, Kovach and Allen (1964). The epicentral location and focal mechanism (right-lateral strike-slip) computed from P wave first arrival studies were used to locate and orient a double-couple point source within the layered half-space. Essentially, the far-field time function and source depth were the only parameters without good independent constraints. A far-field time function with a duration of 1.5 seconds along with a source depth of 7 km was sufficient to model the first 25 seconds of transverse ground motion. Although it seems clear that faulting had finite dimensions, the source to receiver geometries and small source dimension make it possible to model this earthquake with a single point dislocation having the appropriate far-field time function. It appears that the effects of velocity structure on the propagation of long period SH waves are predictable in the Imperial Valley. A study of the synthetic Fourier amplitude spectra indicates that wave propagation effects should be included in studies of source spectra and seismic wave attenuation.

Several synthetic models are constructed to fit the first 40 seconds of transversely polarized displacement, as recorded at El Centro (ELC), of the April 9, 1968 Borrego Mountain earthquake (M 6.5). Unfortunately, there are complications involving the non-planar seismic velocity structures which lie between source and receiver. A simplified structure of a layer over a half-space is used to roughly approximate the effect of the thick sequence of sediments in the Imperial Valley. The beginning 10 seconds of the observed record is used to model the spatial and temporal distribution of faulting, whereas the remaining portion is used to determine

the upper crustal structure based on surface-wave periodicity. A natural depth criterion is provided by comparing the amplitude of the direct arrival with the surface-wave excitations. Considerable non-uniqueness is present in the modeling process. If strong midcrustal seismic discontinuities are present, then it is possible to model the ground motion with a single point dislocation. Within the framework of a single layer over a half-space model, faulting of finite vertical extent is required, whereas the horizontal dimensions of faulting are not resolvable. A model which is also consistent with the teleseismic results of Burdick and Mellman (1976) indicates massive faulting near a depth of 9 km with a fast rise time producing a 10 cm displacement pulse of 1 second duration at El Centro. The faulting appears to slow down as it approaches the free surface. The moment is calculated to be approximately 7×10^{25} dyne-cm which is somewhat smaller than that found from teleseismic body waves by Burdick and Mellman (1976).

Because of the special source to receiver geometries present for the Brawley and Borrego Mountain earthquakes, it is necessary only to model SH waves. Furthermore, near-field source terms can be neglected and problems associated with fault finiteness are relatively easy to deal with. This is not true in the case of modeling the strong-motion recordings of the February 9, 1971 San Fernando earthquake (M 6.5). Three-dimensional models of a finite fault located in a half-space are constructed to study the ground motions observed at JPL, Palmdale, Lake Hughes and Pacoima Dam. Since the duration of faulting is comparable to the travel times for various wave types, very complex interference of

these arrivals makes a detailed interpretation of these waveforms difficult. By investigating the motion due to small sections of the fault, it is possible to understand how various wave types interfere to produce the motion due to the total fault. Rayleigh waves as well as S to P head waves are shown to be important effects of the free surface. Near-field source effects are also quite dramatic. Strong directivity is required to explain the difference in amplitudes seen between stations to the north and stations to the south. Faulting appears to have begun north of Pacoima at a depth of 13 km. The rupture velocity, which is near 2.8 km/sec in the hypocentral region, appears to slow to 1.8 km/sec at a depth of 5 km. Displacements on the deeper sections of the fault are about 2.5 meters. Fault offsets become very small at depths near 4 km and then grow again to 5 meters near the surface rupture. The large velocity pulse seen at Pacoima is a far-field shear wave which is enhanced by directivity. Peak accelerations at Pacoima are probably associated with the large shallow faulting. The total moment is 1.4×10^{26} ergs.

Table of Contents

Introduction

This thesis investigates the nature of ground motion in the near source region of earthquakes. Given a recording of strong ground motion, we would like to know what wave types are present and how they were formed. We would like to understand the relative effects of the characteristics of a particular earthquake source versus the effects of how waves from that source propagate to a receiver. A straightforward approach is taken to gain such insight. Records are synthesized for models consisting of a finite fault embedded in a layered half-space. These models are constructed to roughly approximate fault geometries and seismic velocity structures which occur in the earth. Anyone familiar with the complexities usually encountered in both the surface rupture of earthquakes and the fast variations in rock types between source and receiver, could easily despair at interpreting real data with such simplistic models. Because the real earth is not even included in our set of acceptable models, one should be very cautious about making detailed conclusions simply on the basis that the synthetics fit the data better. Yet there is virtue in these naive models. Even if, in some vision, the exact faulting process and geologic structure were revealed to us, it seems likely that we would not be able to fully appreciate the physics of how waves propagate through such structures. Although simple models do not allow us to make detailed conclusions about specific earthquakes, they do allow us to qualitatively evaluate the importance of such features as source orientation, source finiteness, the free surface, and sedimentary layering.

There are several techniques currently employed to compute the response of a layered medium to a point shear dislocation. Except for finite element and finite difference schemes, these methods involve solving the boundary value problem in a space where the time variable is transformed to frequency and the space variable is transformed to horizontal wavelengths. The major differences in techniques are the ways in which the solution is transformed back into the time and space domain. In most techniques the solution is obtained as a function of frequency and then transformed, via a finite Fourier transform, back into the time domain. Boundary conditions are normally matched by using a propagator matrix technique. These techniques have the advantage that well-dispersed wavetrains which have travelled through complex layering are relatively easy to synthesize. However, these techniques are not well-suited for synthesizing sharp pulse-like arrivals which have a very broad-band frequency content. The physical interpretation of synthetic arrivals is difficult using these techniques, since there is no explicit relationship between time and seismic arrivals.

In this study, we use generalized ray theory in conjunction with the Cagniard-de Hoop technique. The solution is decomposed into a series of terms which are roughly characterized by the travel path of different pulses. A change of variables allows the solution to be explicitly written as a function of time. This method has the advantage that pulse-like arrivals can be interpreted in terms of the mode of propagation for that arrival. In general, the modeling of well-dispersed wavetrains in a complexly layered stack requires so many generalized rays that the

method becomes impractical. Because we are trying to understand the physics of wave propagation for motions near a fault by using simple velocity structure models, we find generalized ray theory to be a desirable technique.

Chapter 1 has two parts. The first part is a brief review of the generalized ray technique for a point dislocation in a layered half-space. The solution for a whole-space is demonstrated first. This introduces fundamental concepts necessary to the solution of more complex problems. Generalized ray solutions which are valid for higher frequencies are then discussed for the layered medium problem. Particular attention is given to the problem of SH wave propagation in a layered medium. The exact near-field solution for a point dislocation in a half-space is then demonstrated. In Appendices A, B, C and D, some simple fluid problems are solved in detail. These problems help motivate generalized ray theory and demonstrate the Cagniard-de Hoop technique.

The second part of Chapter 1 describes a way to find the response of a layered medium to a finite fault. The technique merely consists of summing a large number of point sources which are evenly distributed over the fault plane. Approximations to the exact solution (which is amazingly complex) are discussed.

In Chapter 2 we model recordings of the 4 November 1976 Brawley earthquake (M 4.9). This earthquake occurred in a region of relatively flat-lying sediments whose velocity structure has been well studied. Furthermore, the epicentral solution and focal mechanism are also known. This provides an opportunity to test the validity of our modeling

techniques by predicting the observed SH motions. The results are very encouraging. The source appears to be simple and a single point dislocation, convolved with the appropriate time history, adequately reproduces the records. Because the faulting is of small dimensions, the source is trivially approximated by a point source. The separation of source and propagation effects seems easy for this earthquake since the duration of faulting appears short when compared to the overall length of record to be modeled. Some interesting frequency dependent wave propagation phenomena are also discussed in this chapter. Our modeling shows that caution is necessary when interpreting observed spectra in terms of source effects and anelastic wave propagation effects.

Synthetic records of the El Centro recording of the 1968 Borrego Mountain earthquake (M 6.5) are discussed in Chapter 3. Although this earthquake occurred in the same geologic province as the 4 November 1976 Brawley earthquake, it presents new complications to the modeling process. Source finiteness must now be considered since the dimensions of the faulting are larger. Structural effects are also more difficult to understand because there is considerable variation in the upper crustal structure between source and receiver. Our inability to effectively model this varying structure seriously undermines efforts to uniquely interpret the strong motions recorded at El Centro. Despite this problem, the Imperial Valley sediments are modeled with a simple layer over a half-space. The relative effects of source finiteness and wave propagation are studied within the framework of plane-layered velocity models. Only SH waves are modeled since El Centro lies on a P and SV radiation node.

Two approaches to source modeling are explored. Several models, consisting of merely one or two point sources, are shown to be adequate to explain the observed motion. These models are mathematically easy to deal with and are useful for exploring questions of uniqueness. One of these models is also shown to be consistent with teleseismic models proposed by Burdick and Mellman (1976). Three-dimensional finite fault models are also demonstrated which adequately reproduce the observed motion. Although these models are intuitively pleasing, they are also numerically cumbersome. Because of the special source to receiver geometry for this observation, many approximations and simplifications of the general exact three-dimensional solution are shown to be appropriate. Finally, the relationship between simple point source models and finite faults is discussed.

In Chapter 4, we study the ground motion associated with the 1971 San Fernando earthquake. Observations from four close stations are modeled. The dimension of faulting is comparable to the epicentral range of these stations and the effects of source finiteness are both complicated and important. Although the geologic structure is known to be complicated by mountain ranges and local basins, the earth is approximated by a simple half-space. This approximation may seem appalling, but is justifiable in the sense that synthetic motions are found to compare favorably with observations. Also, it is easy to recognize the free surface as the single most important seismic discontinuity. Even with such a simple velocity model, we will show the interaction between source and wave propagational effects to be quite complex. Understanding

the physics of the half-space models seems a prerequisite for understanding models containing more complex velocity structures. Because the stations were located so close to the earthquake, we find it necessary to include the near-field terms (e.g., static offsets). The Rayleigh wave and the S to P head wave are shown to be important phases in the records.

The effects of source finiteness are relatively dramatic for our models and these effects appear to be present in the data as well. At these ranges, source finiteness has two major effects. The first is caused by the relative timing of arrivals from different parts of the fault (e.g., directivity). Secondly, arrivals from different parts of the fault approach the receiver with different azimuths and take-off angles and thus have different radiation patterns and directions of polarization. Valid approximations to the exact solution are painfully few. Construction of numerical solutions for these models is tedious and patient study is required to fully grasp the physical significance of individual arrivals in the synthetic records.

San Fernando models are constructed in two stages. First we build a finite fault model based upon physical intuition and the results of other studies. The teleseismic models constructed by Langston (1978) are used as a starting place. After carefully studying our a priori models, we make detailed changes to our model which improve the comparison between synthetic and observed records. Once such a model is constructed, we must ask ourselves if our detailed source model is unique. Moreover, given the constraints of our simplistic assumptions about the earth, do our model details represent details present in the San Fernando

earthquake? Unfortunately, these questions are not adequately answered in this thesis. Although a sincere effort is made to understand specific earthquakes, the major goal of this thesis is to provide physical insight into phenomena which must be present in the earth.

Chapter 1

A Procedure for Modeling Strong Ground Motion with Generalized Rays

Introduction

This Chapter provides a basic review of the theory used to calculate the response of a layered elastic half-space to a three-dimensional fault. The response of a point dislocation is covered first and then a procedure for integrating this response over a finite fault is demonstrated. Finding the response of a layered half-space to a dislocation is a central problem in earthquake seismology and many workers have contributed to various aspects of the problem. In this thesis, we will not attempt to describe the historical development of the solutions we will present, but instead we will give a reasonably complete development of the techniques used in our later modeling studies. Most of what is covered in this Chapter are things which were taught to me by Don Helmberger and Dave Harkrider; either through class notes or publications.

For readers not familiar with generalized ray theory, perhaps the best place to begin this Chapter is in the Appendices. The Appendices are intended to be tutorial and several simple fluid problems are solved using the Cagniard-de Hoop technique. These problems help to motivate the methods used in this Chapter.

The first problem in this Chapter is that of a point dislocation in a homogeneous whole-space. We will demonstrate a simple solution in spherical coordinates and discuss the nature of this solution. This

solution is then transformed to cylindrical coordinates which is a coordinate system better suited to plane-layered problems. The Cagniard-de Hoop technique is used to derive the transient response. Various approximations to the exact solution are discussed. Generalized ray theory is employed to construct the solution to the layered problem. Particular attention is given to approximate solutions for SH waves in a layered medium. These solutions are important in our modeling of strong motions which are observed in the Imperial Valley sedimentary basin. The exact solution of a dislocation in a half-space is then demonstrated. The development of this solution is a necessary step in the construction of models for the San Fernando earthquake in which Rayleigh waves and near-field terms are important.

Finally, we show how these point source responses may be summed to approximate the response of a finite fault. To do this, we break the fault into a rectangular gridwork and approximate the response of small areas on the fault with point sources. The technique is extremely flexible in that it allows us to specify the dislocation history in practically any manner we like. Although the principle is simple, the actual numerical calculation of the exact solution is tedious. Approximations whose validity depends upon fault size and receiver distance are discussed.

Point Shear Dislocation in a Homogeneous Whole-Space

First, we will consider a shear dislocation in a whole-space expressed in spherical coordinates. Haskell (1964) introduced a model,

consisting of a discontinuity in displacement across a plane, which produced a double-couple radiation pattern. Following de Hoop's (1958) form of the elastodynamic representation, Harkrider (1976) has derived convenient expressions for displacements and displacement potentials for several different coordinate systems. His results for displacements produced by a point shear dislocation expressed in spherical coordinates are particularly simple and allow an easy interpretation in terms of relative near- and far-field effects. His time domain results for an arbitrarily oriented dislocation with the coordinate system of Figure 1.1 and a dislocation time history D(t) are

P-wave:

$$u_R^{(P)} = \frac{\mu}{4\pi\rho_\alpha}\frac{1}{3}\,\mathcal{R}_R(\delta,\lambda)\left\{\frac{\dot{D}(t-R/\alpha)}{R} + \frac{4\alpha}{R^2}D(t-R/\alpha) + \frac{9\alpha^2}{R^3}E(t-R/\alpha) + \frac{9\alpha^3 G(t-R/\alpha)}{R^4}\right\}$$

$$u_\theta^{(P)} = \frac{\mu}{2\pi\rho}\frac{1}{\alpha^2}\,\mathcal{R}_\theta(\delta,\lambda)\left\{\frac{D(t-R/\alpha)}{R^2} + \frac{3\alpha E(t-R/\alpha)}{R^3} + \frac{3\alpha^2 G(t-R/\alpha)}{R^4}\right\} \quad (1.1)$$

$$u_\phi^{(P)} = -\frac{\mu}{2\pi\rho}\frac{1}{\alpha^2}\,\mathcal{R}_\phi(\delta,\lambda)\left\{\frac{D(t-R/\alpha)}{R^2} + \frac{3\alpha E(t-R/\alpha)}{R^3} + \frac{3\alpha^2 G(t-R/\alpha)}{R^4}\right\}$$

S-wave:

$$u_R^{(S)} = -\frac{3\mu}{4\pi\rho}\frac{1}{\beta^2}\,\mathcal{R}_R(\delta,\lambda)\left\{\frac{D(t-R/\beta)}{R^2} + \frac{3\beta E(t-R/\beta)}{R^3} + \frac{3\beta^2 G(t-R/\beta)}{R^4}\right\}$$

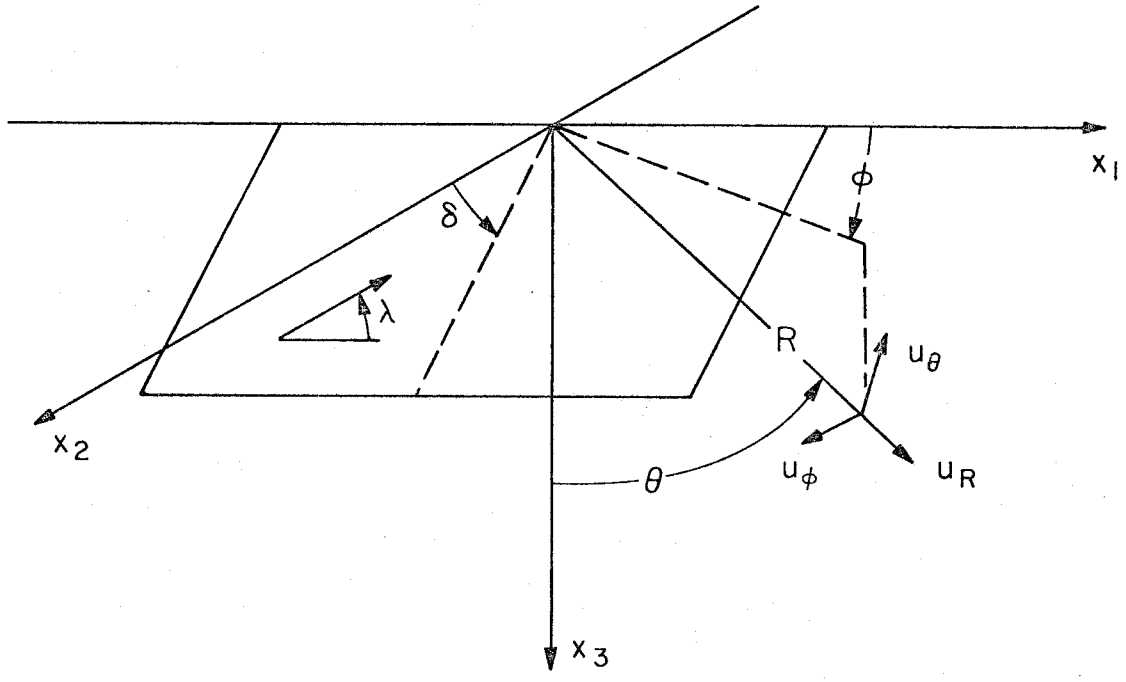

Figure 1.1. Spherical coordinate system showing orientation of point dislocation.

$$u_\theta^{(S)} = \frac{\mu}{8\pi\rho}\frac{1}{\beta^3} R_\theta(\delta,\lambda)\left\{\frac{\dot{D}(t-R/\beta)}{R} + \frac{3\beta}{R^2}D(t-R/\beta) + \frac{6\beta^2 E(t-R/\beta)}{R^3} + \frac{6\beta^3 G(t-R/\beta)}{R^4}\right\} \quad (1.2)$$

$$u_\phi^{(S)} = \frac{\mu}{4\pi\rho}\frac{1}{\beta^3} R_\phi(\delta,\lambda)\left\{\frac{\dot{D}(t-R/\beta)}{R} + \frac{3\beta}{R^2}D(t-R/\beta) + \frac{6\beta^2 E(t-R/\beta)}{R^3} + \frac{6\beta^3 G(t-R/\beta)}{R^4}\right\},$$

where

$$\dot{D}(t) = \frac{dD}{dt}, \quad E(t) = \int_0^t D(\tau)d\tau, \quad G(t) = \int_0^t E(\tau)d\tau$$

and

$\alpha \equiv$ compressional wave velocity

$\beta \equiv$ shear wave velocity

$\mu \equiv$ shear modulus

and

$$R_R(\delta,\lambda) = \cos\lambda\{\sin\delta\sin^2\theta\sin 2\phi - \cos\delta\sin 2\theta\cos\phi\} + \sin\lambda\{\sin 2\delta(\cos^2\theta - \sin^2\theta\sin^2\phi) + \cos 2\delta\sin 2\theta\sin\phi\}$$

$$R_\theta(\delta,\lambda) = \cos\lambda\{\sin\delta\frac{\sin 2\theta}{2}\sin 2\phi - \cos\delta\cos 2\theta\cos\phi\} - \sin\lambda\{\sin 2\delta\frac{\sin 2\theta}{2}(1+\sin^2\phi) - \cos 2\delta\cos 2\theta\sin\phi\}$$

$$R_\phi(\delta,\lambda) = \cos\lambda\,\{\sin\delta\,\sin\theta\,\cos 2\phi + \cos\delta\,\cos\theta\,\sin\phi\}$$

$$+ \sin\lambda\,\{\cos 2\delta\,\cos\theta\,\cos\phi - \frac{\sin 2\delta}{2}\,\sin\theta\,\sin 2\phi\}\ .$$

Notice in equations (1.1) and (1.2) that compressional waves produce both radial and transverse motions and shear waves also produce radial as well as transverse motions. Notice also that components which have terms containing $\dot{D}/R$ in them are only the radial for compressional waves and only the transverse for shear waves. Terms containing $\dot{D}/R$ are called far-field terms and are usually the dominant terms in body-wave seismology. These far-field terms behave as the time derivative of the dislocation history and $\dot{D}(t)$ is usually called the far-field time function. All other terms in equations (1.1) and (1.2) are defined to be near-field terms. These near-field terms all behave like the dislocation time history or integrals thereof and decay with distance as R^{-2}, R^{-3} or R^{-4}.

Equations (1.1) and (1.2) are not quite as simple as they first appear, however, and a closer inspection of them will help to illuminate difficulties which we will encounter later. First notice that all time behaviors are written through the variables $t-\alpha/R$ or $t-\beta/R$. Thus the solutions are really D'Alembert-type solutions and represent travelling waves. This representation is particularly useful for describing the far-field terms which are indeed travelling waves. However, at the other end of the spectrum, we know that static displacements persist in close to the dislocation. How does one represent these in terms of travelling waves? To answer this question, let us inspect the total displacements, u_i,

closely. Suppose that the dislocation occurs in one step, then

$$D(t) = H(t) \equiv \text{Heaviside step function}$$

and

$$E(t - R/V) = \int_{R/V}^{t} H(t - R/V)dt$$

$$= H(t - R/V)(t - R/V)$$

and

$$G(t - R/V) = \int_{R/V}^{t} E(t - R/V)dt$$

$$= \frac{1}{2} H(t - R/V)(t - R/V)^2 \quad . \tag{1.3}$$

It is clear that the P and S waves grow in time without limit. This should not be surprising since the static field consists of the stationary balance of compressional and shear stresses. Unusual waves must be present if our travelling wave solution is to create this balance. If we complete the calculation to find u_i, we find that indeed the P and S waves do cancel (or balance) and the solution can be written (after some algebra) for $D(t) = H(t)$:

$$u_R = \begin{cases} 0 & ; \quad t < R/\alpha \\ \dfrac{\mu R_{R(\delta,\lambda)}}{4\pi\rho\alpha^3}\left[\dfrac{\delta(t-R/\alpha)}{R} - \dfrac{\alpha}{2R^2} + \dfrac{9\alpha^3 t^2}{2R^4}\right] & ; \quad R/\alpha < t < R/\beta \\ \dfrac{1}{8\pi}\dfrac{(3\lambda+5\mu)}{(\lambda+2\mu)}\dfrac{R_{R(\delta,\lambda)}}{R^2} & ; \quad t > R/\beta \end{cases} \tag{1.4}$$

$$u_\xi = \begin{cases} 0 & ; \quad t < R/\alpha \\ \dfrac{\mu R_{\xi(\delta,\lambda)}}{4\pi\rho\alpha^2}\left[\dfrac{1}{R^2} + \dfrac{3\alpha^2 t^2}{R^4}\right] & ; \quad R/\alpha < t < R/\beta \\ \dfrac{1}{4\pi}\dfrac{\mu}{(\lambda+2\mu)}\dfrac{R_{\xi(\delta,\lambda)}}{R^2} & ; \quad t > R/\beta \end{cases}$$

where ξ denotes either θ or ζ .

Thus although the P and S waves grow without bound, the total displacement becomes constant after the S wave arrival time. When we solve the layered problem, the solution is written in terms of P and S waves and again the near-field terms will grow without bound. In that case, we have no analytic solution and we are forced to calculate the P and S waves numerically. It is easy to anticipate numerical instabilities associated with trying to balance terms which become large with time.

Unfortunately, the generalization to a layered model is not possible in spherical coordinates and we switch to cylindrical coordinates where the boundary value problem can be solved. The coordinate system

is shown in Figure 1.2. Harkrider (1964,1976) has shown that the displacements in cylindrical coordinates can be expressed in terms of a P potential (ϕ), a SV potential (ψ), and a SH potential (χ). In the frequency domain, i.e., time Fourier transformed to ω, he defines

$$\underset{\sim}{\bar{U}} = \text{grad } \bar{\phi} + \text{curl curl } (0,0,\bar{\psi}) + \text{curl } (0,0,\bar{\chi}) \tag{1.5}$$

or $\underset{\sim}{\bar{U}} = (\bar{Q},\bar{V},\bar{W})$, where

$$\bar{W}(r,z,\theta,\omega) = \frac{\partial\bar{\phi}}{\partial z} - \frac{1}{r}\frac{\partial}{\partial r}\left(r\frac{\partial\bar{\psi}}{\partial r}\right) + \frac{1}{r^2}\frac{\partial^2\bar{\psi}}{\partial\theta^2}$$

$$\bar{V}(r,z,\theta,\omega) = \frac{1}{r}\frac{\partial\bar{\phi}}{\partial\theta} + \frac{1}{r}\frac{\partial^2\bar{\psi}}{\partial z\partial\theta} - \frac{\partial\bar{\chi}}{\partial r} \tag{1.6}$$

$$\bar{Q}(r,z,\theta,\omega) = \frac{\partial\bar{\phi}}{\partial r} + \frac{\partial^2\bar{\psi}}{\partial r\partial z} + \frac{1}{r}\frac{\partial\bar{\chi}}{\partial\theta}$$

and where

$$\bar{u}(\omega) \equiv \int_{-\infty}^{\infty} u(t)\,\exp(-i\omega t)dt \ .$$

The Fourier time-transformed vector equation of motion for an isotropic elastic solid is

$$(\lambda + 2\mu)\text{grad div } \underset{\sim}{\bar{U}} - \mu \text{ curl curl } \underset{\sim}{\bar{U}} = -\omega^2\rho\,\underset{\sim}{\bar{U}} \quad . \tag{1.7}$$

Taking the divergence of (1.5),

$$\text{div } \underset{\sim}{\bar{U}} = \nabla^2\bar{\phi} + \text{div curl}[\text{ curl } (0,0,\bar{\psi}) + (0,0,\bar{\chi})]$$

$$= \nabla^2\bar{\phi} \ . \tag{1.8}$$

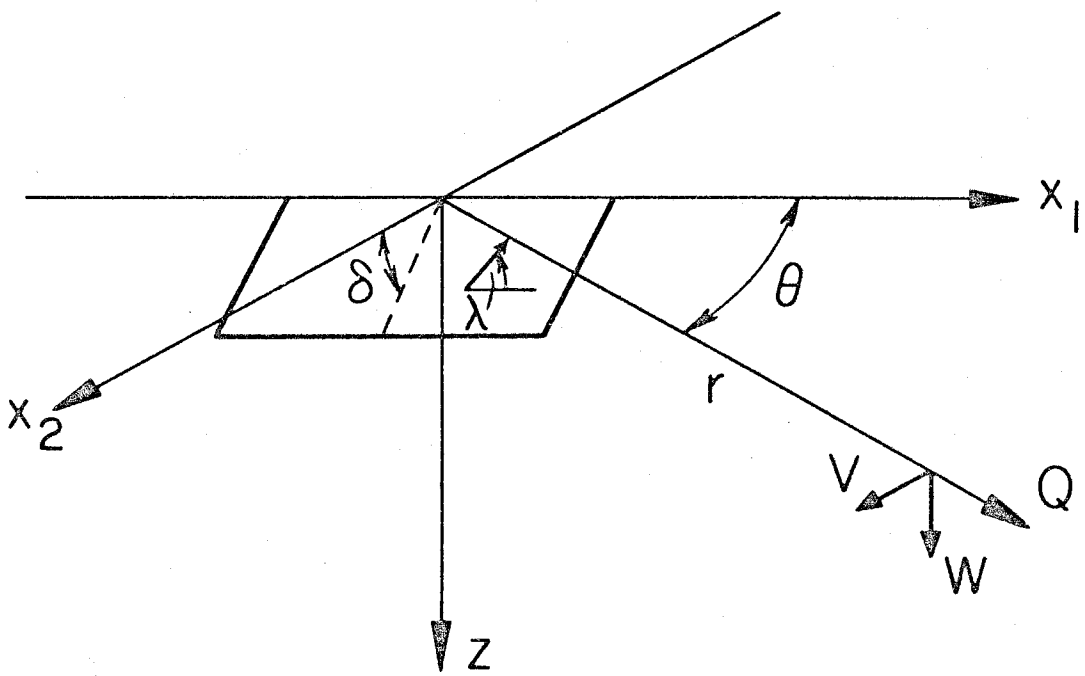

Figure 1.2. Cylindrical coordinate system showing orientation of point dislocation.

Thus we can rewrite (1.7) as

$$k_{\alpha}^{-2} \text{ grad } \nabla^2\bar{\phi} - k_{\beta}^{-2} \text{ curl curl } \underset{\sim}{\bar{U}}$$

$$= \text{grad } \bar{\phi} + \text{curl curl } (0,0,\bar{\psi}) + \text{curl } (0,0,\bar{\chi}) \quad , \tag{1.9}$$

where

$$k_{\alpha} \equiv \frac{\omega}{\alpha} \quad \text{and} \quad k_{\beta} \equiv \frac{\omega}{\beta} \, .$$

Taking the divergence of (1.9), we find

$$\text{div grad } \nabla^2\bar{\phi} = k_{\alpha}^{2} \text{ div grad } \bar{\phi} \quad ,$$

or

$$\nabla^2\bar{\phi} = k_{\alpha}^{2} \, \bar{\phi} \quad . \tag{1.10}$$

Now we can also show that the wave equation (1.7) is satisfied if $\bar{\psi}$ and $\bar{\chi}$ are solutions of

$$\begin{aligned} \nabla^2\bar{\psi} &= -k_{\beta}^{2}\bar{\psi} \\ \nabla^2\bar{\chi} &= -k_{\beta}^{2}\bar{\chi} \quad . \end{aligned} \tag{1.11}$$

Now if we recall that

$$\nabla^2 = \frac{1}{r}\frac{\partial}{\partial r}\left(r \frac{\partial}{\partial r}\right) + \frac{1}{r^2}\frac{\partial^2}{\partial \theta^2} + \frac{\partial^2}{\partial z^2} \quad ,$$

then we can use equations (1.10) and (1.11) to rewrite (1.6) as

$$\bar{W}(r,z,\theta,\omega) = \frac{\partial\bar{\phi}}{\partial z} + \frac{\partial^2\bar{\psi}}{\partial z^2} + k_\beta{}^2\bar{\psi}$$

$$\bar{V}(r,z,\theta,\omega) = \frac{1}{r}\frac{\partial\bar{\phi}}{\partial\theta} + \frac{1}{r}\frac{\partial^2\bar{\psi}}{\partial z\partial\theta} - \frac{\partial\bar{\chi}}{\partial r} \qquad (1.12)$$

$$\bar{Q}(r,z,\theta,\omega) = \frac{\partial\bar{\phi}}{\partial r} + \frac{\partial^2\bar{\psi}}{\partial r\partial z} + \frac{1}{r}\frac{\partial\bar{\chi}}{\partial\theta} \quad .$$

The task now is to find expressions for $\bar{\phi}$, $\bar{\psi}$, and $\bar{\chi}$ such that they describe a point dislocation of arbitrary orientation. In his 1976 paper, Harkrider derives these expressions and we will summarize his derivation. He begins by noting that the Cartesian displacements due to a horizontal double-couple can be written as

$$\bar{u}_i(\omega,x,y,z) = -\frac{\mu\bar{D}(\omega)}{4\pi\rho\omega^2}\left\{\frac{2\partial^3(A_\beta - A_\alpha)}{\partial x_i\,\partial x_1\,\partial x_2} + k_\beta{}^2(\delta_{i1}\frac{\partial}{\partial x_2} + \delta_{i2}\frac{\partial}{\partial x_1})\,A_\beta\right\}, \qquad (1.13)$$

where (x_1,x_2,x_3) = Cartesian coordinates at which $\bar{u}_i$ is to be evaluated,

$$A_v = \frac{\exp(-i\,k_v R)}{R} \quad ,$$

v = seismic velocity, either α or β ,

$$k_v = \omega/v \quad ,$$

$$R = (x_1{}^2 + x_2{}^2 + x_3{}^2)^{\frac{1}{2}} \quad ,$$

and

$D(t)$ = displacement time history of dislocation.

The next step is to perform coordinate rotations on (1.13) such that we are now viewing the fault from an arbitrary orientation. The rotation angles are θ, λ, and δ and are shown in Figure 1.2. This rotated expression is then transformed to cylindrical coordinates. In addition, we use the fact that cylindrical and spherical waves can be related by the Sommerfeld integral, or

$$A_v = \frac{\exp\{-i k_v R\}}{R} = \int_0^\infty \frac{k J_0(kr) \exp(-\nu_v |z - h|)\, dk}{\nu_v} ,$$

where

$$r^2 = x^2 + y^2$$

$$\nu_v = \begin{cases} (k^2 - k_v^2)^{\frac{1}{2}} & ; \quad k > k_v \\ i(k_v^2 - k^2)^{\frac{1}{2}} & ; \quad k < k_v \end{cases} .$$

Once expressions for the cylindrical displacements are obtained, the corresponding potentials can be found by inspection. All of this may sound straightforward, but you should realize that the algebra is indeed horrible. Harkrider's final result is

$$\bar{\phi} = - K \int_0^\infty k^2 F_\alpha J_2(kr)dk \cdot A_1(\theta,\lambda,\delta)$$

$$+ K \int_0^\infty 2k\varepsilon F_\alpha \nu_\alpha J_1(kr)dk \cdot A_2(\theta,\lambda,\delta)$$

$$+ K \int_0^\infty (2k_\alpha^2 - 3k^2) F_\alpha J_0(kr)dk \cdot A_3(\theta,\lambda,\delta)$$

$$\bar{\psi} = - K \int_0^\infty \varepsilon \nu_\beta F_\beta J_2(kr)dk \cdot A_1(\theta,\lambda,\delta)$$

$$- K \int_0^\infty \frac{(k_\beta^2 - 2k)}{k} F_\beta J_1(kr)dk \cdot A_2(\theta,\lambda,\delta) \qquad (1.14)$$

$$- K \int_0^\infty 3\varepsilon F_\beta \nu_\beta J_0(kr)dk \cdot A_3(\theta,\lambda,\delta)$$

$$\bar{\chi} = + K \int_0^\infty k_\beta^2 F_\beta J_2(kr)dk \cdot A_4(\theta,\lambda,\delta)$$

$$- K \int_0^\infty \frac{k_\beta^2}{k} \varepsilon F_\beta \nu_\beta J_1(kr)dk \cdot A_5(\theta,\lambda,\delta) \quad ,$$

where

α = compressional wave velocity

β = shear wave velocity

$k_v = \omega/v$

$\nu_v = (k^2 - k_v^2)$

$$F_v = \frac{ke^{-\nu_v|z-h|}}{\nu_v}$$

h = depth to source

μ = shear modulus at the source

ρ = density at the source

$$\varepsilon = \begin{cases} +1 & z > h \\ -1 & z < h \end{cases}$$

$$A_1(\theta,\lambda,\delta) = \sin 2\theta \cos\lambda \sin\delta + \frac{1}{2}\cos 2\theta \sin\lambda \sin 2\delta$$

$$A_2(\theta,\lambda,\delta) = \cos\theta \cos\lambda \cos\delta - \sin\theta \sin\lambda \cos 2\delta$$

$$A_3(\theta,\lambda,\delta) = \frac{1}{2}\sin\lambda \sin 2\delta \qquad (1.15)$$

$$A_4(\theta,\lambda,\delta) = \cos 2\theta \cos\lambda \sin\delta - \frac{1}{2}\sin 2\theta \sin\lambda \sin 2\delta$$

$$A_5(\theta,\lambda,\delta) = -\sin\theta \cos\lambda \cos\delta - \cos\theta \sin\lambda \cos 2\delta$$

θ = strike from the end of the fault plane

λ = rake angle

δ = dip angle

M_o = seismic moment

$K = -M_o/4\pi\rho\omega^2$

and we have assumed a step dislocation with unit magnitude.

Notice that if $\lambda = 0$ and $\delta = \pi/2$ (i.e., vertical strike-slip dislocation), then A_2, A_3 and A_5 are all zero. Thus the first term of the P and S potentials (1.14) corresponds to the response of a vertical strike-slip dislocation. Similar reasoning shows that the second term is the response of a vertical dip-slip dislocation. These two terms are all that is necessary to represent the SH potential, but the P and SV potentials require a third term. Since A_1 and A_2 are zero when $\theta = \pi/4$ and $\delta = \pi/4$, we conclude that this corresponds to the solution for a 45°-dipping fault observed at an angle 45° from the fault strike. The order of these terms will be kept throughout this thesis.

The task now is to find a way to evaluate the integrals in (1.14) and to then take the inverse Fourier transform. This could be done by numerically performing the double integral. Instead of this approach, we will transform these potentials such that the Cagniard-de Hoop technique can be used. The transformation is the same one that is discussed in Appendix A. It will allow us to transform this double integration over

spatial and time variables, k and ω, to a double integration over the variables p and t. A later change of variables will allow us to reduce the double integration to a single integration which, for high frequencies, can be performed by inspection. As an example, consider the function

$$\bar{\zeta}_n(r,z,\omega) = - \int_0^\infty F_\nu J_n(kr)dk \ . \tag{1.16}$$

Now perform the transformation,

$$\omega = is \quad \text{and} \quad k = -isp \tag{1.17}$$

where s is now a Laplace-transformed time variable. (1.16) becomes

$$\hat{\zeta}_n(r,z,s) = \frac{2}{\pi} s \ Im \int_0^{i\infty} \frac{p}{\eta_\nu} K_n(spr) e^{-s\eta_\nu |z-h|} dp \tag{1.18}$$

where

$$\hat{\zeta}(s) = \int_0^\infty \zeta\ (t)\ e^{-st}\ dt \ ,$$

$$\eta_\nu = (\frac{1}{\nu^2} - p^2)^{\frac{1}{2}} \quad ,$$

and K_n is a modified Bessel function. From what we have given here, it is not obvious how (1.18) appears from this transformation. In Appendix D, a similar transformation is demonstrated in greater detail.

Unfortunately the functions, K_1 and K_2, have simple poles at p = 0, and there is a residue contribution to the integral. If ϵ is a vanishing small real number, then (1.18) can be written,

$$\hat{\zeta}_n(v,z,s) = \frac{2}{\pi} s \; Im \int_{0+\epsilon}^{i\infty+\epsilon} \frac{P}{\eta_v} K_n(spr) e^{-s\eta_v|z-h|} dp + \hat{R}_n(r,z,s), \quad (1.19)$$

where the remainder term, $\hat{R}_n(r,z,s)$, represents the residue contribution of the integral. As it turns out, once the potentials are differentiated and summed to form displacements, all of these residue contributions vanish. Furthermore, the residue contributions make the potentials noncausal. These difficulties have been discussed by Harkrider (1976). Because the residue contributions separate explicitly in the P and S domain, they can be eliminated. This is discussed by Harkrider and Helmberger (1977). From this point on, we will implicitly assume that

$$\frac{2}{\pi} s \; Im \int_{0}^{i\infty} \frac{P}{\eta_v} K_n(spr) e^{-s\eta_v|z-h|} dp$$

really signifies

$$\frac{2}{\pi} s \; Im \int_{0+\epsilon}^{i\infty+\epsilon} \frac{P}{\eta_v} K_n(spr) e^{-s\eta_v|z-h|} dp \quad .$$

If we perform the transformation (1.17) on the potentials (1.14) we obtain

P-wave:

$$\hat{\phi} = + \frac{M_o}{4\pi\rho} \frac{2}{\pi} Im \int_0^{+i\infty} C_1(p) \frac{p}{\eta_\alpha} \exp(-s\eta_\alpha |z-h|) K_2(spr) dp \cdot A_1(\theta,\lambda,\delta)$$

$$+ \frac{M_o}{4\pi\rho} \frac{2}{\pi} Im \int_0^{+i\infty} C_2(p) \frac{p}{\eta_\alpha} \exp(-s\eta_\alpha |z-h|) K_1(spr) dp \cdot A_2(\theta,\lambda,\delta)$$

$$+ \frac{M_o}{4\pi\rho} \frac{2}{\pi} Im \int_0^{+i\infty} C_3(p) \frac{p}{\eta_\alpha} \exp(-s\eta_\alpha |z-h|) K_o(spr) dp \cdot A_3(\theta,\lambda,\delta).$$

SV-waves:

$$\hat{\Omega} = + \frac{M_o}{4\pi\rho} \frac{2}{\pi} Im \int_0^{+i\infty} SV_1(p) \frac{p}{\eta_\beta} \exp(-s\eta_\beta |z-h|) K_2(spr) dp \cdot A_1(\theta,\lambda,\delta)$$

$$+ \frac{M_o}{4\pi\rho} \frac{2}{\pi} Im \int_0^{+i\infty} SV_2(p) \frac{p}{\eta_\beta} \exp(-s\eta_\beta |z-h|) K_1(spr) dp \cdot A_2(\theta,\lambda,\delta) \quad (1.20)$$

$$+ \frac{M_o}{4\pi\rho} \frac{2}{\pi} Im \int_0^{+i\infty} SV_3(p) \frac{p}{\eta_\beta} \exp(-s\eta_\beta |z-h|) K_o(spr) dp \cdot A_3(\theta,\lambda,\delta) .$$

SH-waves:

$$\hat{\chi} = + \frac{M_o}{4\pi\rho} \frac{2}{\pi} Im \int_0^{+i\infty} SH_1(p) \frac{p}{\eta_\beta} \exp(-s\eta_\beta |z-h|) K_2(spr) dp \cdot A_4(\theta,\lambda,\delta)$$

$$+ \frac{M_o}{4\pi\rho} \frac{2}{\pi} Im \int_0^{+i\infty} SH_2(p) \frac{p}{\eta_\beta} \exp(-s\eta_\beta |z-h|) K_1(spr) dp \cdot A_5(\theta,\lambda,\delta) ,$$

where we changed the definition of the SV potential $\hat{\Omega} \equiv -sp\hat{\psi}$.

The vertical radiation patterns, as will become apparent shortly, are defined by

$$
\begin{aligned}
C_1 &= -p^2 & SV_1 &= -\varepsilon p \eta_\beta & SH_1 &= \frac{1}{\beta^2} \\
C_2 &= 2\varepsilon p \eta_\alpha & SV_2 &= (\eta_\beta^{\,2} - p^2) & SH_2 &= -\frac{\varepsilon}{\beta^2}\frac{\eta_\beta}{p} \\
C_3 &= (p^2 - 2\eta_\alpha^{\,2}) & SV_3 &= 3\varepsilon p \eta_\beta \quad .
\end{aligned}
\tag{1.21}
$$

The corresponding displacements become

$$
\begin{aligned}
\hat{W} &= \frac{\partial \hat{\phi}}{\partial z} + sp\hat{\Omega} \\
\hat{V} &= \frac{1}{r}\frac{\partial \hat{\phi}}{\partial \theta} - \frac{1}{spr}\frac{\partial^2 \hat{\Omega}}{\partial z \partial \theta} - \frac{\partial \hat{\chi}}{\partial r} \\
\hat{Q} &= \frac{\partial \hat{\phi}}{\partial r} - \frac{1}{sp}\frac{\partial^2 \hat{\Omega}}{\partial r \partial z} + \frac{1}{r}\frac{\partial \hat{\chi}}{\partial \theta} \quad .
\end{aligned}
\tag{1.22}
$$

The nature of the variable changes and SV potential transformation is described in Helmberger (1974). There are several noteworthy aspects of the form of the solution given above. Note that the A_i terms correspond to an azimuthal radiation. These A_i's can be brought outside of any integrals used to calculate the potentials. Although we are dealing with a three-dimensional problem, the third dimension, azimuth, can be introduced in a simple manner after the solution of the integrals. This effectively reduces a three-dimensional problem to a two-dimensional

problem. This allows us to evaluate the integrals by complex variable techniques. Notice that $dA_1/d\theta = A_4$, $dA_2/d\theta = A_5$, and $dA_3/d\theta = 0$. Also $dA_4/d\theta = A_1$ and $dA_5/d\theta = A_2$. This means that we could write (1.22) as

$$W = W_{SS}A_1 + W_{DS}A_2 + W_{45°}A_3$$

$$V = V_{SS}A_4 + V_{DS}A_5 \qquad (1.23)$$

$$Q = Q_{SS}A_1 + Q_{DS}A_2 + Q_{45°}A_3$$

where the subscripts SS, DS and 45° corresponds to displacements due to vertical strike-slip, vertical dip-slip and 45°-dipping faults respectively. Thus we see that the separation of the azimuthal radiation pattern is complete. This separation of the azimuthal dependence also allows us to easily identify near-field terms which correspond to azimuthal changes in amplitude along the wavefront of a given wave type. Any terms in (1.22) which involve a derivative with respect to θ are near-field terms. There are, however, other near-field terms included in (1.22) which are hidden within the integral. Thus, unlike the solution in spherical coordinates (1.1) and (1.2), it is not easy to distinguish all near-field versus far-field phenomena.

As stated before, the purpose of the transformation to the p and s domain is to allow us to apply the Cagniard-de Hoop technique. Consider again the field function given in (1.18). A deformation of the contour from $p = 0$ to $p = i\infty$ to the contour, Γ, yields,

$$\hat{\zeta}_n(r,z,s) = \frac{2}{\pi} s \; Im \int_{\Gamma} \frac{p}{\eta_v} K_n(spr) e^{-s\eta_v|z-h|} \, dp \qquad (1.24)$$

where Γ is the Cagniard contour, defined to be such that $\tau(p)$ is real where,

$$\tau(p) = pr + \eta_v|z-h| \; . \qquad (1.25)$$

The geometry and contour, Γ, are shown in Figure 1.3. Motivation for the contour deformation is given in the Appendices. The integral in (1.24) can be written in terms of the real and increasing parameter $\tau(p)$.

$$\hat{\zeta}_n(r,z,s) = \frac{2}{\pi} s \; Im \int_{\tau(o)}^{\infty} \frac{p(\tau)}{\eta_v(\tau)} K_n(sp(\tau)r) e^{-s\eta_v(\tau)|z-h|} \frac{dp}{d\tau} \, d\tau \; . \qquad (1.26)$$

The inverse Laplace transform of (1.26) can be evaluated directly by using the formula (Erdelyi, 1954)

$$\mathcal{L}p^{-1} \left\{ e^{ap} K_n(ap) \right\}$$

$$= (t^2 + 2at)^{-\frac{1}{2}} \cosh[a \cosh^{-1}(1 + \frac{t}{a})]$$

where $|\arg a| < \pi$. By also using the shift rule and by recognizing multiplication by s to be equivalent to differentiation with respect to t, we can rewrite (1.26) as

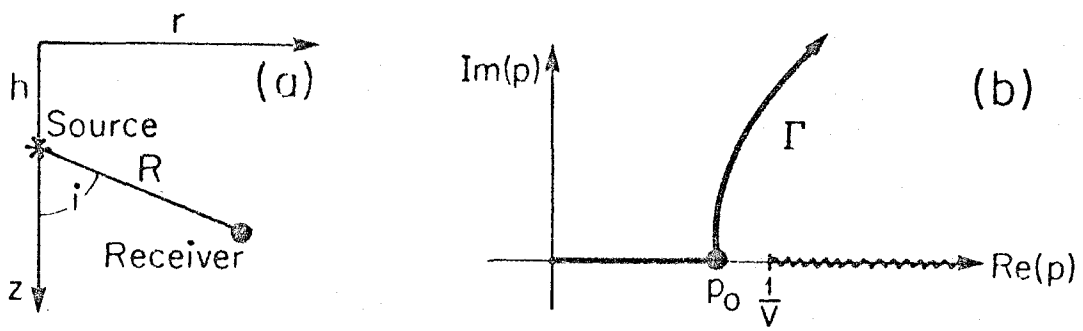

Figure 1.3. Source-receiver geometry and complex (p) plane with branch cut starting at (1/v) and running out along the real (p) axis.

$$\zeta_n(r,z,t) = \frac{2}{\pi}\frac{\partial}{\partial t} \; Im \int_0^t \frac{c_n(t,\tau)}{(t-\tau)^{\frac{1}{2}}\,(t-\tau+2pr)^{\frac{1}{2}}} \left(\frac{dp}{d\tau}\right)\frac{p(\tau)}{\eta_v}\, d\tau \;, \qquad (1.27)$$

where

$$c_n(t,\tau(p)) = \cosh\left(n \cosh^{-1}\left(\frac{t-\tau+pr}{pr}\right)\right) \;.$$

Solving (1.25) for $p(\tau)$, we obtain

$$p(\tau) = \frac{r}{R^2}\tau + i\left(\tau^2 - \frac{R^2}{v^2}\right)^{\frac{1}{2}} |z-h| \qquad (1.28)$$

and

$$\eta(\tau) = \frac{|z-h|\tau}{R^2} - i\left(\tau^2 - \frac{R^2}{v^2}\right)^{\frac{1}{2}} \frac{r}{R^2} \qquad (1.29)$$

and

$$\frac{dp(\tau)}{d\tau} = \frac{i\,\eta_v(\tau)}{(\tau^2 - R^2/v^2)^{\frac{1}{2}}} \;, \qquad (1.30)$$

where

$$R^2 = r^2 + |z-h|^2 \;.$$

Note that the integrand is real until

$$p = p_o = \frac{r}{Rv} = \frac{\sin i}{v}$$

which is the ray parameter corresponding to Snell's law. Because the whole-space problem has already been solved exactly, we can demonstrate the solution to the integral in (1.27). By comparing with Harkrider's (1976) solution in the (ω,k) domain, it can be shown that

$$\zeta_2(r,z,t) = \frac{\partial}{\partial t}\left\{\left[\frac{1}{R} + \frac{2V}{r^2}(\tau - R/v)\right] H(\tau - R/v)\right\}$$

$$= \frac{\delta(\tau - R/v)}{R} + \frac{2\, H(\tau - R/v)(\tau - R/v)}{r^2} \quad . \qquad (1.31)$$

Note that the first and second terms of (1.31) correspond to far-field and near-field terms, respectively.

In the general layered problem, integrals similar to (1.26), but with more complicated integrands, must be solved. Later we will discuss approximations which allow us to evaluate the integral by inspection. In order to find the exact solution, though, these integrals must be evaluated numerically. Notice that in the integral (1.27) there are singularities associated with the terms, $(t-\tau)^{-1/2}$ at $t=\tau$ and dp/d_τ at $\tau = R/v$. These singularities create problems with any numerical integration scheme and can be removed by a change of variables as proposed by Helmberger (1968). In (1.27) the integrand is real until $p = p_o$ (i.e., $t = R/v$), and thus by substituting (1.3) into (1.27), we obtain

$$\zeta_n(r,z,t) = \frac{2}{\pi}\frac{\partial}{\partial t}\,\mathrm{Re}\int_{t=R/v}^{t} \frac{c_n(t,\tau)\; p(\tau)\; d\tau}{(t-\tau)^{\frac{1}{2}}(t-\tau+2pr)^{\frac{1}{2}}\;(\tau^2-R^2/\,v^2)^{\frac{1}{2}}} \quad . \tag{1.32}$$

If we define a change at variables

$$\theta = \sin^{-1}\left(\frac{t-\tau}{t-R/v}\right)^{\frac{1}{2}} \quad , \tag{1.33}$$

then (1.32) becomes

$$\zeta_n(r,z,t) = \frac{4}{\pi}\frac{\partial}{\partial t}\,\mathrm{Re}\int_{0}^{\pi/2} F(\theta)\; d\theta \quad , \tag{1.34}$$

where

$$F(\theta) = \frac{p(\tau(\theta))\; C_n(t(\theta),\, \tau(\theta))}{(\tau(\theta)+R/v)^{\frac{1}{2}}\;(t(\theta)-\tau(\theta)+2p(\tau(\theta))r)^{\frac{1}{2}}} \quad . \tag{1.35}$$

The integral in (1.34) can now be treated numerically. Although the integral, (1.34), applies only to the whole-space problem, we will later see that similar methods can be used to compute the exact solution to the layered problem.

We will now demonstrate several approximate methods for determining integrals of the type given by (1.27). We will expand the integrand in terms of $(t-\tau)^{-\frac{1}{2}}$. Some rather messy algebra shows that

$$c_n(t,\tau,p) = \frac{1}{2}\left[\frac{(y+(y^2-1)^{\frac{1}{2}})^{2n}+1}{(y+(y^2-1)^{\frac{1}{2}})^n}\right] \quad , \tag{1.36}$$

where

$$y = \frac{t-\tau+pr}{pr}$$

and

$$\frac{c_n(t,\tau,p)}{(t-\tau+2pr)^{\frac{1}{2}}} \approx \frac{1}{\sqrt{2pr}} \tag{1.37}$$

to first order. Thus, we can approximate (1.27) by

$$\zeta_n(v,z,t) = \frac{2}{\pi}\frac{2}{\alpha t} Im \int_0^t \frac{1}{\sqrt{2pr}} \frac{1}{(t-\tau)^{\frac{1}{2}}} \frac{dp}{dt} \frac{p}{\eta_v} d\tau$$

$$= \frac{\partial}{\partial t}\left[\frac{H(\tau)}{\sqrt{t}} * Im\left(\sqrt{\frac{2}{r}}\frac{1}{\pi}\frac{\sqrt{p}}{\eta_v}\frac{dp}{dt}\right)\right] \quad , \tag{1.38}$$

when treating a high-frequency source with duration, T, such that $T \ll 2pr$ (i.e., $t-\tau \ll 2pr$). The solution can be further approximated for times close to the geometric ray arrival time. If $t - R/v$ is small, then

$$\frac{dp}{dt} \approx i \frac{\eta_v}{(t - R/v)^{\frac{1}{2}} (2\frac{R}{v})^{\frac{1}{2}}}$$

and also $p \approx p_o = r/Rv$ and (1.38) reduces to

$$\zeta_n(r,z,t) = \frac{\delta(t - R/v)}{R} \quad .$$

This is called the first-motion approximation and is appropriate for problems in which the ratio of travel time to source duration is of the order of 100 or greater. It corresponds to geometric ray theory and is useful for modeling teleseismic body-waves (Langston and Helmberger, 1975).

Another high-frequency approximation is called the asymptotic approximation. We return to equation (1.26) which states,

$$\hat{\zeta}_n(r,z,s) = \frac{2}{\pi} s \, Im \int_{\tau(0)}^{\infty} \frac{p(\tau)}{\eta_v(\tau)} K_n(sp(\tau)r) e^{-s\eta_v(\tau)|z - h|} \frac{dp}{dt} d\tau \quad . \tag{1.39}$$

Now for spr large,

$$K_n(spr) = (\frac{\pi}{2spr})^{\frac{1}{2}} e^{-spr} [1 + \frac{4n^2 - 1}{8spr} + \ldots] \tag{1.40}$$

and recall that

$$\tau = pr + \eta_v|z - h| \quad ,$$

so (1.39) can be approximately written

$$\hat{\zeta}_n(r,z,s) = \left(\frac{2}{\pi rs}\right)^{\frac{1}{2}} s \; Im \int_0^\infty \frac{H(\tau - \tau(0))\sqrt{p(\tau)}}{\eta_v(\tau)} \; e^{-s\tau} \frac{dp}{d\tau} \, d\tau$$

$$+ \left(\frac{2}{\pi rs}\right)^{\frac{1}{2}} \left(\frac{4n^2 - 1}{8r}\right) Im \int_0^\infty \frac{H(\tau - \tau(0))}{\eta_v(\tau)\sqrt{p(\tau)}} \; e^{-s\tau} \frac{dp}{d\tau} \, d\tau$$

$$+ \ldots \quad . \tag{1.41}$$

Now recall the definition of Laplace transform,

$$\hat{\zeta}_n(r,z,s) = \int_0^\infty \zeta_n(r,z,t) \; e^{-st} \, dt$$

and thus (1.41) can be solved by inspection

$$\zeta_n(r,z,t) = \frac{d}{dt} \left\{ \frac{H(t)}{\sqrt{t}} * Im \left(\sqrt{\frac{2}{r}} \; \frac{1}{\pi} \; \frac{\sqrt{p}}{\eta_v} \frac{dp}{dt} \right) \right\}$$

$$+ \frac{H(t)}{\sqrt{t}} * Im \left(\sqrt{\frac{2}{r}} \; \frac{(4n^2 - 1)}{8\pi v} \; \frac{1}{\eta_v \sqrt{p}} \frac{dp}{dt} \right) + \ldots . \tag{1.42}$$

Notice that the first term of (1.42) corresponds to the approximate solution (1.38). This asymptotic scheme is appealing because no numerical integration is performed and because additional terms can be computed easily. Realize however, that in more general problems, the inversion of $\tau(p)$ to find $p(\tau)$ must be done numerically. Also the

asymptotic approximation is not uniformly convergent in spr. That is, for small spr, the series does not converge to the modified Bessel function. Thus for small spr, the asymptotic series cannot be expected to be correct, regardless of the number of terms included in the expansion. This means that the estimation of the integral is poor when computing waves whose period is larger than the travel time, or when computing at small ranges. In practice, the asymptotic approximation seems to work surprisingly well, even as spr becomes moderately small (see Helmberger and Harkrider, 1978). Although the individual asymptotic solutions for P and S potentials may not approach the exact solutions, it appears that when these asymptotic solutions are differenced to form displacements, the asymptotic and exact solutions for displacement compare well. In general, though, if static offsets are an important part of a synthetic record, then it seems best to use the exact solution.

High-Frequency Solution for a Point Source in a Layered Space

The whole-space solution can be generalized to a layered space by applying the method of generalized reflection and transmission coefficients (Spencer, 1960). This method is demonstrated in Appendix C. The solution is represented as the infinite sum of all possible generalized rays between source and receiver. Each generalized ray is characterized by the interfaces with which it interacts and the response of each ray is evaluated using the Cagniard-de Hoop technique. Consider the layered stack in Figure 1.4. The source and receiver are on the bottom of the m^{th} and ℓ^{th} interfaces. The solution can be written,

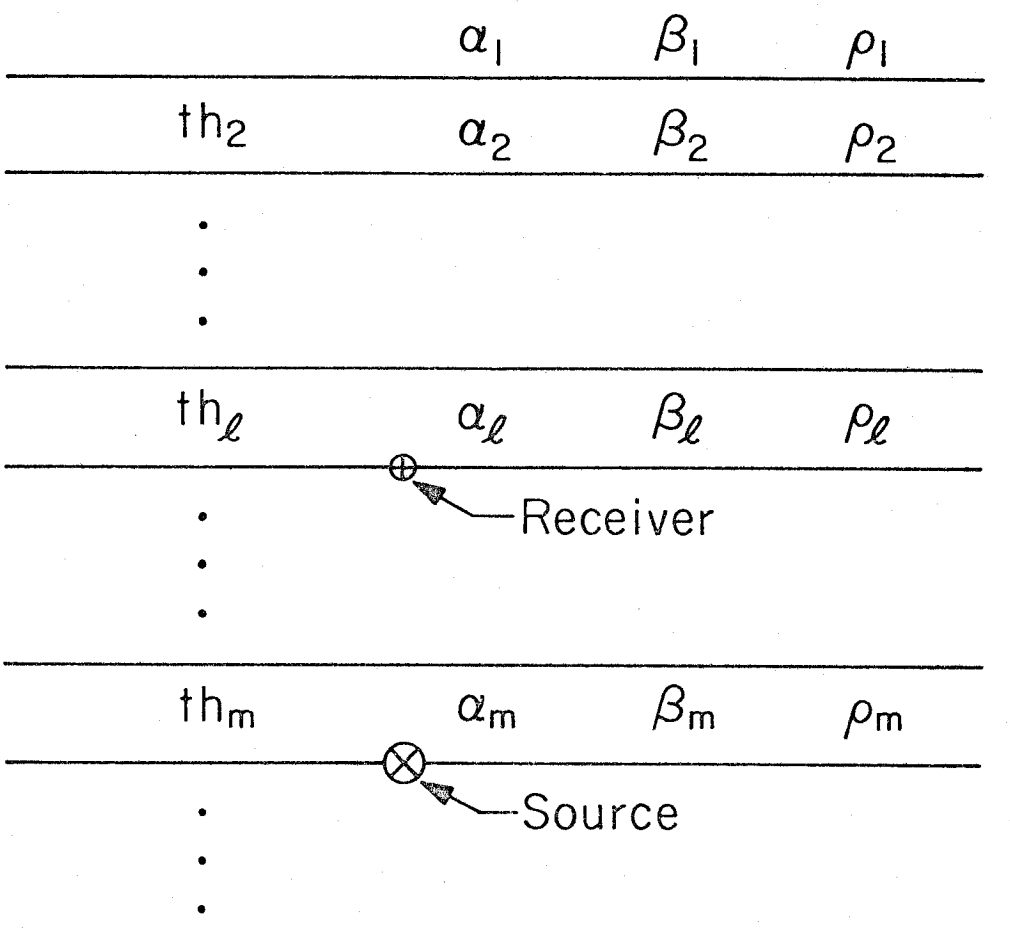

Figure 1.4. Layered medium with source at the bottom of the m^{th} layer and receiver at the bottom of the ℓ^{th} layer. Unless source and receiver coefficients are specifically included, the source and receiver must lie on boundaries across which elastic parameters do not vary.

$$\hat{\phi} = \frac{M_o}{4\pi\rho_m}\frac{2}{\pi}\sum_{i=1}^{3} A_i(\theta,\lambda,\delta) \sum_{k=1}^{\infty} Im \int_0^{i\infty} P\,\Xi_{ki}^{C}(p)\,\exp(-sg_k^{C}(p))$$

$$\cdot K_{3-i}(spr)\,dp \qquad (1.43)$$

$$\hat{\Omega} = \frac{M_o}{4\pi\rho_m}\frac{2}{\pi}\sum_{i=1}^{3} A_i(\theta,\lambda,\delta) \sum_{k=1}^{\infty} Im \int_0^{i\infty} P\,\Xi_{ki}^{SV}(p)\,\exp(-sg_k^{SV}(p))$$

$$\cdot K_{3-i}(spr)\,dp \qquad (1.43)$$

$$\hat{\chi} = \frac{M_o}{4\pi\rho_m}\frac{2}{\pi}\sum_{i=1}^{2} A_{i+3}(\theta,\lambda,\delta) \sum_{k=1}^{\infty} Im \int_0^{i\infty} P\,\Xi_{ki}^{SH}(p)\,\exp(-sg_h^{SH}(p))$$

$$\cdot K_{3-i}(spr)\,dp \quad ,$$

where k denotes the summation over all possible generalized rays (there are countably many). Suppose the path of the k^{th} generalized ray is characterized by $P_k^{(C,SV,SH)}$ where P is of the form

$$P_k^{C} = (m,{}_{SV}^{C}),\ (m+1,{}_{SV}^{C}),\ \ldots\ ,\ (\ell,C)$$

meaning that the ray has traversed the layers whose numbers are given

in the mode given. P^C and P^{SV} may have either compressional or shear modes along any leg, but the last leg must be a compressional wave for P^C and a shear wave for P^{SV}. P^{SH} has all of its legs consisting of shear waves. Now if the k^{th} ray has n legs and the q^{th} leg is described by $P_{kq}^{(C,SV,SH)}$ then

$$g_k(p) = \sum_{q=1}^{n} Th_{P_{kq}} \eta_{P_{kq}} + pr \quad . \tag{1.44}$$

This g contains travel time information about the k^{th} ray. Ξ contains information about the nature of reflections and transmissions through these layers. It also contains the source vertical radiation pattern.

$$\Xi_{ki}^{C} = \frac{1}{\eta_{P^C k_1}} \begin{Bmatrix} C_i(p) \\ SV_i(p) \end{Bmatrix} \Pi_k^C (p)$$

$$\Xi_{ki}^{SV} = \frac{1}{\eta_{P^{SV} k_1}} \begin{Bmatrix} C_i(p) \\ SV_i(p) \end{Bmatrix} \Pi_k^{SV} (p) \tag{1.45}$$

$$\Xi_{ki}^{SH} = \frac{1}{\eta_{\beta_m}} SH_i(p) \; \Pi_k^{SH} (p) \quad ,$$

where $\Pi_k^{(P,SV,SH)}$ is the product of all reflection and transmission coefficients involved with the propagation of the k^{th} ray. These reflection coefficients are those defined by Helmberger (1968) and are

only compatible with the Ω definition of the SV potential. This is why the transformation $\hat{\Omega} = -sp\bar{\psi}$ was made earlier in the whole-space solution. The transmission and reflection coefficients for a compressional or SV wave travelling in the i^{th} medium and reflecting off of or travelling into the j^{th} medium are given by

$$
\begin{aligned}
R_{P_iP_j} &= (-Q_1 + Q_2 + Q_3 - Q_4 - Q_5 + Q_6)/D \\
R_{P_iS_j} &= 2p\eta_{\alpha i}[(k_j - p^2)(k_r - p^2) - \eta_{\alpha j}\,\eta_{\beta j}\,(k_i - p^2)]/D \\
T_{P_iP_j} &= 2k_i\eta_{\alpha i}[\eta_{\beta j}(k_i - p^2) - \eta_{\beta i}(k_j - p^2)]/D \\
T_{P_iS_j} &= 2k_ip\eta_{\alpha i}[\eta_{\beta i}\eta_{\alpha j} - (k_r - p^2)]/D \\
R_{S_iS_j} &= (-Q_1 + Q_2 + Q_3 - Q_4 + Q_5 - Q_6)/D \\
R_{S_iP_j} &= [-2p\eta_{\beta i}\,(k_j - p^2)(kr - p^2) - \eta_{\alpha j}\,\eta_{\beta j}\,(k_i - p^2)]/D \\
T_{S_iS_j} &= -2k_i\eta_{\beta i}[\eta_{\alpha i}(k_j - p^2) - \eta_{\alpha j}(k_i - p^2)]/D \\
T_{S_iP_j} &= 2k_ip\eta_{\beta i}[(k_r - p^2) - \eta_{\alpha i}\,\eta_{\beta j}]/D \quad ,
\end{aligned}
\tag{1.46}
$$

where

$$k_i = \frac{1}{2\beta_i^2}\left(\frac{\rho_i\beta_i^2}{\rho_i\beta_i^2 - \rho_j\beta_j^2}\right)$$

$$k_j = \frac{1}{2\beta_j^2}\left(\frac{\rho_j\beta_j^2}{\rho_j\beta_j^2 - \rho_i\beta_i^2}\right)$$

$$k_r = k_i + k_j \quad ,$$

and where

$$Q_1 = p^2(k_r - p^2)^2$$

$$Q_2 = \eta_{\alpha i}\,\eta_{\alpha j}\,\eta_{\beta i}\,\eta_{\beta j}\,p^2$$

$$Q_3 = \eta_{\alpha i}\,\eta_{\beta i}\,(k_j - p^2)^2$$

$$Q_4 = \eta_{\alpha j}\,\eta_{\beta j}\,(k_i - p^2)^2$$

$$Q_5 = \eta_{\alpha i}\,\eta_{\beta j}\,k_i k_j$$

$$Q_6 = \eta_{\alpha j}\,\eta_{\beta i}\,k_i k_j$$

and

$$D = Q_1 + Q_2 + Q_3 + Q_4 - Q_5 - Q_6 \quad .$$

The corresponding reflection and transmission coefficients for SH waves are considerably simpler and are given by

$$R_{SH_{ij}} = \frac{\mu_i \eta_{\beta i} - \mu_j \eta_{\beta j}}{\mu_i \eta_{\beta i} + \mu_j \eta_{\beta j}}$$

$$T_{SH_{ij}} = \frac{2\mu_i \eta_{\beta i}}{\mu_i \eta_{\beta i} + \mu_j \eta_{\beta j}} \quad , \tag{1.47}$$

where μ_i is the shear modulus of the i^{th} layer. If the receiver lies on a boundary (e.g., the free surface), then the integrand must also contain a receiver coefficient which will be described shortly.

The general solution just given involves such messy and vague notation, that it is difficult to visualize how it is actually used to compute synthetic seismograms. We will now present some simple examples of how high-frequency approximations to the general solution can be used. In Chapters 2 and 3 we model SH waves recorded at moderate ranges in a sedimentary basin. If we retain only the far-field term and use the first-order asymptotic approximation (see equation (1.42)), then the approximate high-frequency solution as observed at the surface is given by

$$V(r,0,\theta,t) = \frac{M_o}{4\pi\rho_o} \frac{d}{dt} \left[\dot{D}(t) * \sum_{j=1}^{2} A_{j+3}(\theta,\lambda,\delta)\, V_j(t) \right] \quad , \tag{1.48}$$

where

$$V_j(t) = \frac{2}{r}\frac{1}{\pi}\frac{H(t)}{\sqrt{t}} * Im\left[\sum_{i=1}^{n}\left(\frac{\sqrt{p}}{\eta_\beta} SH_j(p)\pi_i(p)\ P\ \frac{dp}{dt}\right)_i\right] \qquad (1.49)$$

$\dot{D}(t)$ = far-field time function

V_1 = tangential displacement for vertical strike-slip fault

V_2 = tangential displacement for vertical dip-slip fault .

$\pi_i(p)$ = product of reflection and transmission coefficients and the summation is over contributing rays. Only a finite number of rays is necessary to closely approximate the solution. The number of rays necessary is a function of source to receiver geometry and is found by trial and error. A factor of 2 has been introduced in the solution (1.49) by the SH free surface receiver coefficient. The far-field step function response for a pure strike-slip event, $V_1(t)$, is given in Figure 1.5, where the model is included as an inset for various values of source depth. The corresponding half-space response is the simple step displayed on each trace. When the source is embedded within the upper layer, one obtains the well-known Love wave dispersion with the first few seconds of motion produced by the classical head wave contribution. Each ray in the solution must be evaluated along its own contour which is determined by inverting polynomial equations of the form (1.44). For instance, for sources beneath the layer, the contour appropriate for the direct generalized ray is found by inverting

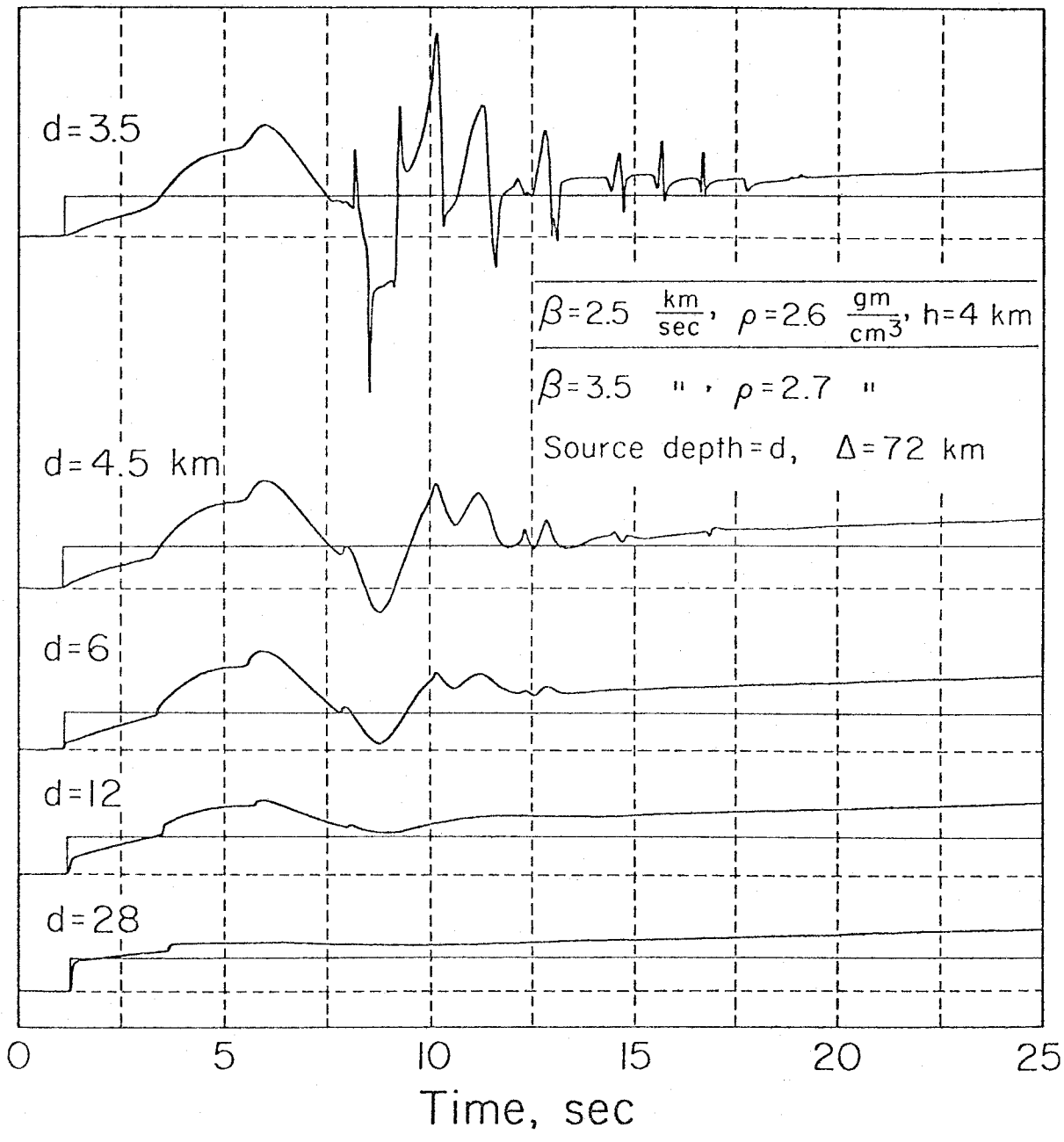

Figure 1.5. SH step function responses at the surface assuming a point strike-slip dislocation situated at various depths. The amplitudes are scaled relative to the top trace with the step response for a homogeneous half-space (bottom properties) displayed for comparison.

$$t = pr + \eta_2(d - h) + \eta_1(h) \qquad (1.50)$$

for p as a function of t, where t is positive real and increasing. The contours used to compute the direct rays for Figure 1.5 are shown in Figure 1.6. Now *Im* (dp/dt) is an extremely important variable in the solution (1.49). The parameter time is also plotted along these contours and it is easy to see that abrupt increases in *Im* (dp/dt) occur where the contour abruptly increases its slope. From equation (1.30) we see that when the contour leaves the real p axis, there is actually a singularity in *Im* (dp/dt). This corresponds to the geometric ray arrival. For large source depths, the contour is near vertical and the synthetic waveform closely resembles the geometric ray response. As the depth decreases the initial values of *Im* (dp/dt) become smaller and a later change in *Im* (dp/dt) develops near $p = 1/\beta_1$. This later arrival is a diffracted phase and does not have a well-defined arrival time. The interpretation of this diffracted phase is as follows. As the source moves close to the boundary, the curvature of the incident wave-front upon the boundary greatly increases. For a long-period wave, this tightly curved wave-front appears as if it were a source located on the boundary. Waves from this imaginary long-period source then travel in the upper layer with velocity β_1 and with a ray parameter appropriate for a source located on the boundary. Were it not for this diffraction, there could be no Love waves generated by a source exterior to the waveguide. The physical interpretation of this phenomenon is discussed further in Chapters 2 and 3.

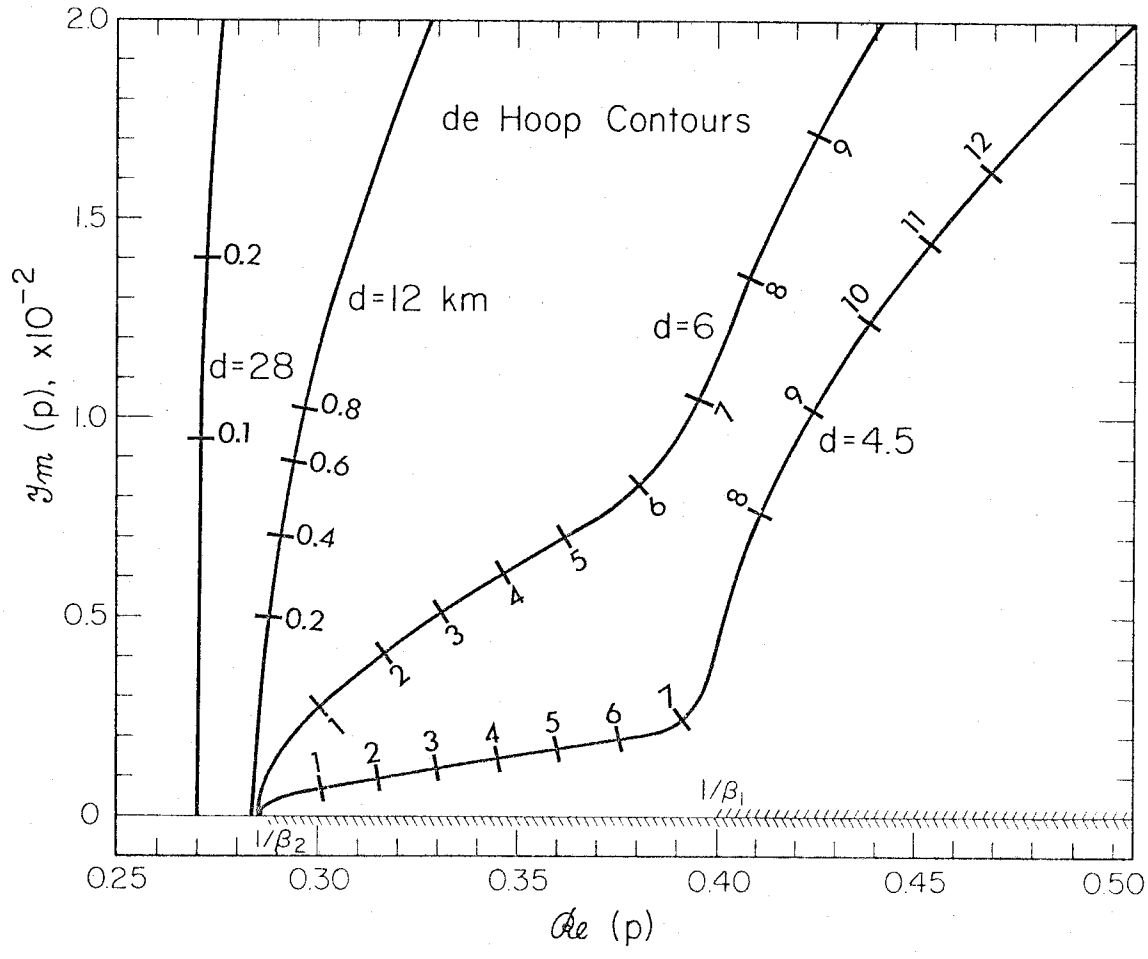

Figure 1.6. Contours of *Im*(p) versus Re(p) for the direct rays shown in Figure 1.5. The branch cuts run along the Re(p) coordinate, starting at $1/\beta_2$ and $1/\beta_1$, respectively. The parameter time is marked along each contour.

When the source is located within the layer, there is a strong arrival corresponding to the first reflection which occurs when the contour leaves the real p axis near $1/\beta_1$. This, however, is not the first arrival for this generalized ray. When the contour reaches the branch point at $1/\beta_2$, the reflection coefficient, given by

$$R_{12}(p) = \frac{\mu_1\eta_1 - \mu_2\eta_2}{\mu_1\eta_1 + \mu_2\eta_2} \quad ,$$

becomes complex. This corresponds to the head wave arrival. A more detailed discussion of head waves and critical reflections is given in Appendix B.

The high-frequency solutions for the vertical and radial components of motion are considerably more complex than the corresponding transverse component solution. The solution is constructed in the same manner as (1.49), but now P to S and S to P conversions must be considered. The notation for the multilayered problem is unwieldy and we will only explicitly show the half-space solution. This will allow us to discuss the receiver coefficient and demonstrate the existence of Rayleigh waves. First consider a pure strike-slip source, at depth z, which emits only P waves. The solution will consist of the sum of the three generalized rays shown in Figure 1.7. The solution for the P potential can be written as the sum of the direct and reflected P waves and is given by

$$\bar{\phi}(r,z,\theta,s) = -\frac{M_o}{4\pi\rho}\frac{2}{\pi} Im \int_0^{i\infty} p^2 N_\alpha \frac{p}{\eta_\alpha} K_2(spr) \sin 2\theta \, dp \quad , \qquad (1.51)$$

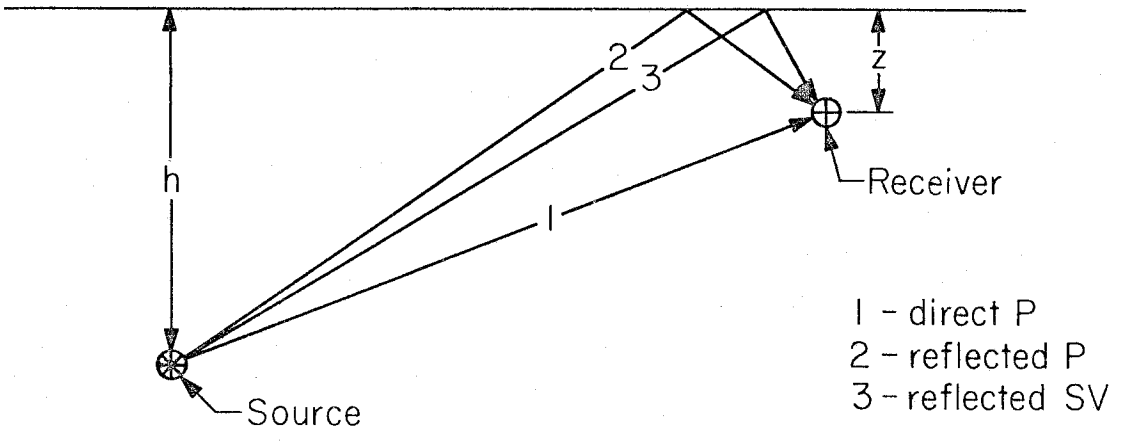

Figure 1.7. Three contributing generalized rays for a compressional source located in a half-space.

where

$$N_\alpha = \exp(-s\eta_\alpha |z - h|) + R_{pp} \exp(-s\eta_\alpha (z + h)) \quad ,$$

where h is the source depth.

The expression for the reflected SV potential is

$$\bar{\Omega} = - \frac{M_o}{4\pi\rho} \frac{2}{\pi} Im \int_0^{i\infty} p^2 N_\beta \frac{p}{\eta_\beta} K_2(spr) \sin 2\theta \, dp \quad , \tag{1.52}$$

where

$$N_\beta = R_{PS} \exp[-s(\eta_\alpha h + \eta_\beta z)] \quad .$$

The reflection coefficients at the free surface can be found by using expression (1.46) and by letting one of the solids become a vacuum. The free surface reflection coefficients are,

$$R_{PP} = \frac{4\beta^4 p^2 \eta_\alpha \eta_\beta - (1 - 2\beta^2 p^2)^2}{D(p)}$$

$$R_{PS} = \frac{4\beta^2 \eta_\alpha \, p(1 - 2\beta^2 p^2)^2}{D(p)}$$

$$R_{SP} = - \frac{4\beta^2 \eta_\beta \, p(1 - 2\beta^2 p^2)}{D(p)} \tag{1.53}$$

$$R_{SS} = R_{PP} \quad ,$$

where

$$D(p) = 4\beta^4 p^2 \eta_\alpha \eta_\beta + (1 - 2\beta^2 p^2)^2 \quad . \tag{1.54}$$

As z goes to zero (i.e., placing the receiver on the free surface), the travel paths for these three rays coincide. The displacement due to an incoming P wave can be found by substituting (1.51) and (1.52) into (1.22) and taking the limit as z goes to zero. The solution for the vertical displacement becomes

$$\bar{W}_\phi(r,o,\theta,s) = - \frac{M_o}{4\pi\rho} \frac{2}{\pi} s \; Im \int_o^{i\infty} (p^2) \frac{p}{\eta_\alpha} K_2(spr) \exp(-s\eta_\alpha h) R_{PZ} \, dp \sin 2\theta \quad , \tag{1.55}$$

where

$$R_{PZ} = \frac{2\eta_\alpha(\eta_\beta^2 - p^2)}{\beta^2 R(p)} \tag{1.56}$$

and

$$R(p) = (\eta_\beta^2 - p^2)^2 + 4p^2 \eta_\alpha \eta_\beta \; . \tag{1.57}$$

R(p) is called the Rayleigh denominator. R_{PZ} is called the receiver function and describes the interaction of P and SV waves at the free surface.

The radial displacement produced by the ϕ potential becomes

$$\bar{Q}_{\phi}(r,o,\theta,s) = - \frac{M_o}{4\pi\rho} \frac{2}{\pi} s \, Im \int_o^{i\infty} (p^2) \, M_{\alpha} \exp(-s\eta_{\alpha} h) \, R_{PR} \, dp \sin 2\theta \, , \tag{1.58}$$

where

$$R_{PR} = - \frac{4\eta_{\alpha}\eta_{\beta}P}{\beta^2 R(p)} \tag{1.59}$$

and

$$M_v = \frac{P}{\eta_v} [K_1(spr) + \frac{2}{spr} K_2(spr)] \quad . \tag{1.60}$$

The extra complication in M_v is introduced by taking the radial derivative

$$\frac{\partial}{\partial r} K_2(spr) = -sp[K_1(spr) + \frac{2}{spr} K_2(spr)] \quad . \tag{1.61}$$

In general, there is also a near-field transverse motion generated by the P and SV waves, but we will save discussion of this until we demonstrate the exact solution in the next section.

The solution for an SV wave from a vertical strike-slip source as observed at the surface can be generated in a similar manner and is given by

$$\bar{W}_{\Omega}(r,o,\theta,s) = \frac{M_o}{4\pi\rho} \frac{2}{\pi} s \, Im \int_o^{i\infty} (p\eta_{\beta}) R_{SZ} \frac{p}{\eta_{\beta}} \exp(-s\eta_{\beta} h) \, K_2(spr) \, dp \sin 2\theta \, , \tag{1.62}$$

where

$$R_{SZ} = \frac{4p\ \eta_\alpha \eta_\beta}{\beta^2 R(p)} \tag{1.63}$$

and

$$\bar{Q}_\Omega = \frac{M_o}{4\pi\rho}\frac{2}{\pi}\, s\ Im \int_0^{i\infty} (p\eta_\beta)\ R_{SR}\ M_\beta\ \sin 2\theta\ \exp(-s\eta_\beta h)\ dp \quad , \tag{1.64}$$

where

$$R_{SR} = \frac{2\eta_\beta(\eta_\beta^2 - p^2)}{\beta^2 R(p)} \quad . \tag{1.65}$$

If we keep only far-field terms and apply the first-order asymptotic expansion to the solutions just given, then we can write the high frequency half-space solution as

$$\begin{aligned} W(r,o,\theta,t) &= \frac{M_o}{4\pi\rho}\frac{d}{dt}\left[\dot{D}(t) * \sum_{j=1}^{3} A_j(\theta,\lambda,\delta)\ W_j\right] \\ Q(r,o,\theta,t) &= \frac{M_o}{4\pi\rho}\frac{d}{dt}\left[\dot{D}(t) * \sum_{j=1}^{3} A_j(\theta,\lambda,\delta)\ Q_j\right] \quad , \end{aligned} \tag{1.66}$$

where the index j = 1, 2, 3 corresponds to strike-slip, dip-slip, and 45° solutions, respectively. The far-field step function responses are

$$W_j(t) = \sqrt{\frac{2}{r}}\ \frac{1}{\sqrt{t}} * \left\{ Im\left(\frac{\sqrt{p}}{\eta_\alpha} C_j(p)\ R_{PZ}(p)\ \frac{dp}{dt} \right) + Im\ \frac{\sqrt{p}}{\eta_\beta} SV_j(p)\ R_{SZ}(p)\ \frac{dp}{dt} \right\}$$

and (1.67)

$$Q_j(t) = \sqrt{\frac{2}{r}}\ \frac{1}{\sqrt{t}} * \left\{ Im\left(\frac{\sqrt{p}}{\eta_\alpha} C_j(p)\ R_{PR}(p)\ \frac{dp}{dt} \right) + Im\left(\frac{\sqrt{p}}{\eta_\beta} SV_j(p)\ R_{SR}(p)\ \frac{dp}{dt} \right) \right\}.$$

In the half-space problem, inversion of $\tau(p)$ to find $p(\tau)$ is trivial and the contours along which the P and SV parts of (1.67) are to be evaluated are

$$p(t) = \frac{r}{R^2}\, t - \left(\frac{R^2}{\alpha^2} - t^2\right)^{\frac{1}{2}} \frac{h}{R^2}$$

and (1.68)

$$p(t) = \frac{r}{R^2}\, t - \left(\frac{R^2}{\beta^2} - t^2\right)^{\frac{1}{2}} \frac{h}{R^2} \quad ,$$

respectively. We can also write η_α and η_β explicitly as

$$\eta_\alpha = \frac{h}{R^2}\, t + \left(\frac{R^2}{\alpha^2} - t^2\right)^{\frac{1}{2}} \frac{r}{R^2}$$

and (1.69)

$$\eta_\beta = \frac{h}{R^2}\, t + \left(\frac{R^2}{\beta^2} - t^2\right)^{\frac{1}{2}} \frac{r}{R^2} \quad .$$

Let us now examine the SV solution in more detail. The contours for SV waves at several ranges are shown in Figure 1.8 and corresponding vertical strike-slip fault synthetics which include both the P and SV waves are shown in Figure 1.9. First notice that there is a branch cut at $1/\alpha$ and that the contour becomes imaginary at $p = r_\beta/R$. Thus η_α can become imaginary before p(t) does. Because η_α is involved in all of the receiver functions, the SV response can begin before the arrival of the direct S wave. It is this complex reflection coefficient which gives rise to the S to P head wave. Since this wave is a diffracted P wave which travels at a shallow angle with respect to the surface, it appears much larger on the radial component of motion.

The receiver function causes another important arrival in the synthetics. Notice that the Rayleigh denominator R(p) can have a zero when

$$(\eta_\beta^2 - p^2)^2 = 4\beta^4 p^2 \eta_\beta \eta_\alpha \quad . \tag{1.70}$$

It can be shown that (1.70) is satisfied when p equals the reciprocal of the Rayleigh wave velocity. Thus all of the receiver functions have simple poles at p = 1/(Rayleigh velocity). This pole is not included within the contour and hence there is no residue contribution to the integral. Nevertheless, when the ratio of range to depth becomes large, the contour passes close to this pole. When this happens, the receiver function becomes large and changes quickly as a function of p (also time) and the result is a Rayleigh wave.

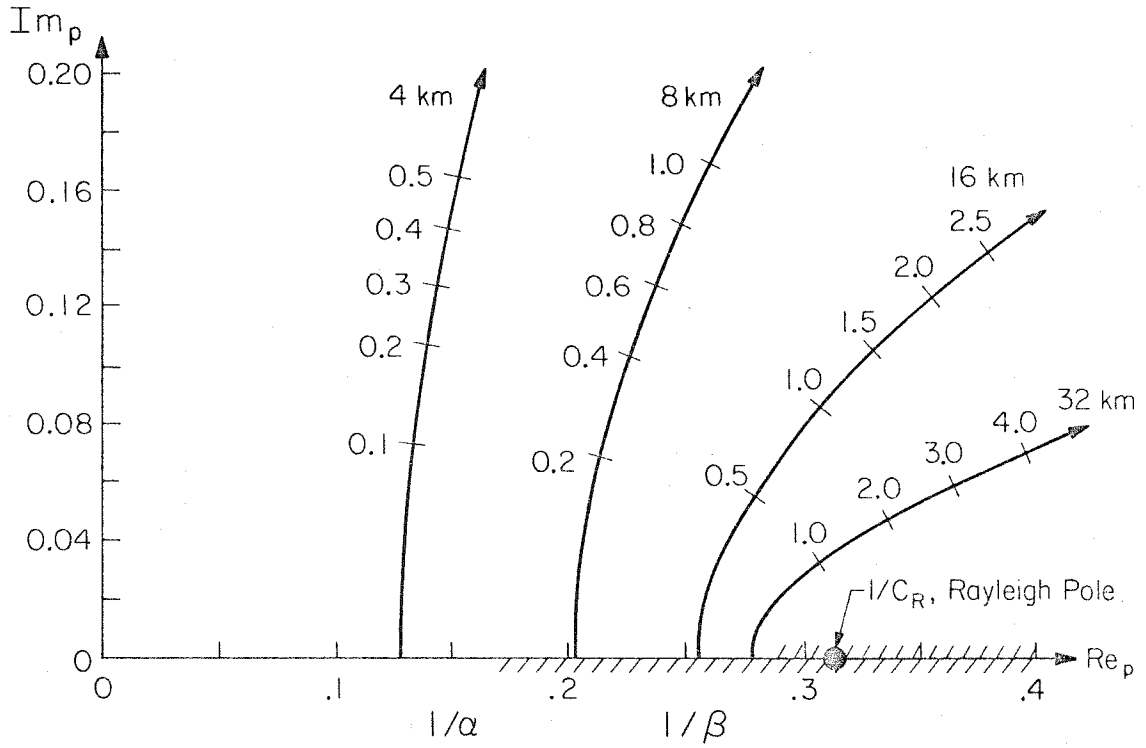

Figure 1.8. Contours for SV waves of half-space synthetics which are shown in Figure 1.9 The parameter time is marked along each contour.

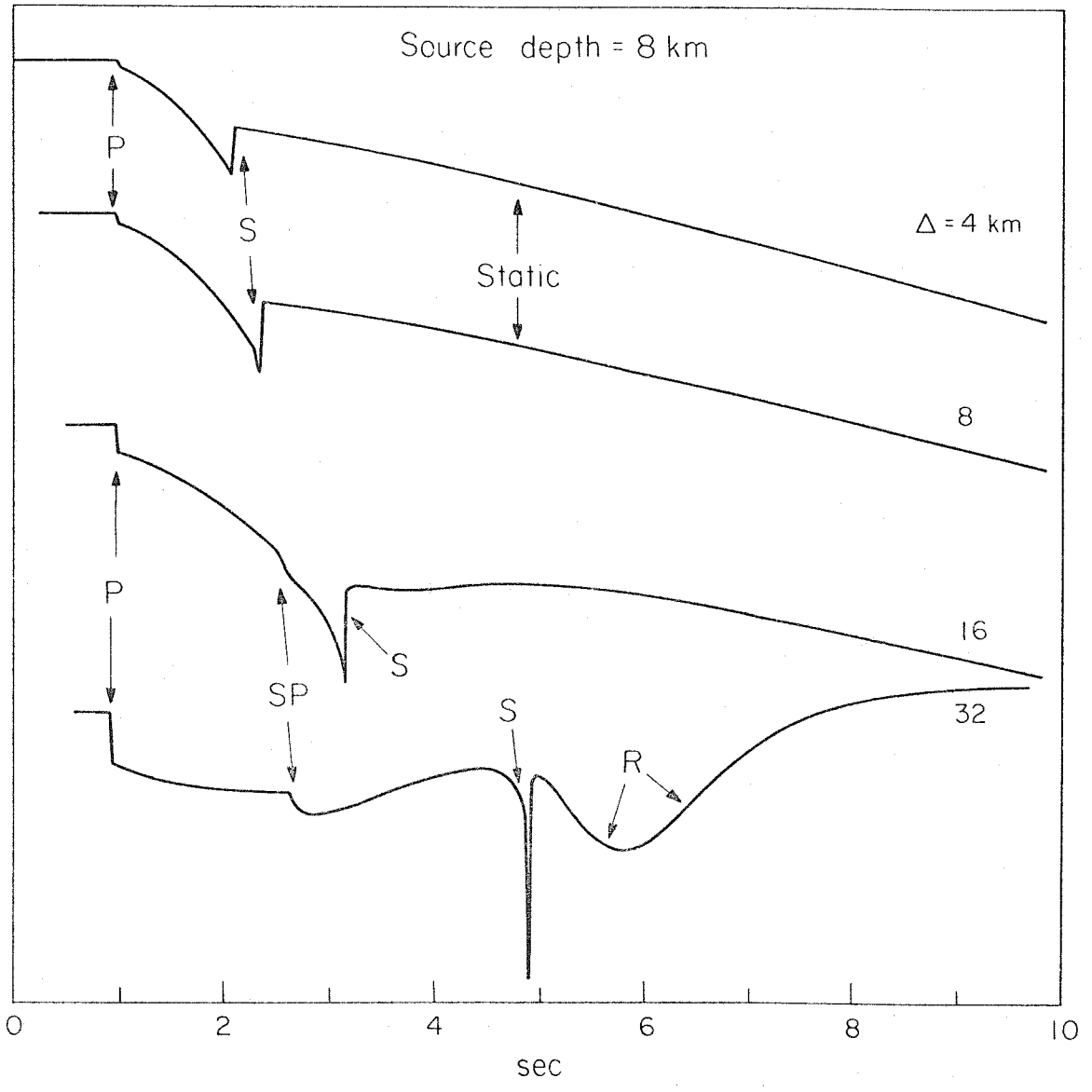

Figure 1.9 . Vertical component step function response for a vertical strike-slip point dislocation in a half-space (exact solution). The phases corresponding to the P wave, the S to P head wave, the S wave, and the Rayleigh wave are all identified.

Exact Half-Space Solution

When the ratio of source duration to travel time becomes large, asymptotic approximations become very poor. Equation (1.32) demonstrated the type of solution which can be used for the exact whole-space solution. Using our discussion in the preceding section, we will now generalize the exact whole-space answer to the exact half-space solution. By following the technique for solving layered problems which we have just described, it is possible to generalize the exact solution to any layered problem. Since the general solution is so clumsy to work with, we will restrict ourselves to the half-space problem. The solution is very similar to our high-frequency solution for this problem. However, now the near-field terms must be included and the inverse transform integral must be solved numerically. Let us first consider the vertical displacement which is given by

$$W(r,z,\theta,t) = \frac{M_o}{4\pi\rho_o} \frac{d}{dt} \left[\dot{D}(t) * \sum_{j=1}^{3} A_j W_j\right] \quad , \tag{1.71}$$

where W_1, W_2 and W_3 correspond to pure strike-slip, dip-slip, and 45°-dip-slip dislocations, respectively. By using the same logic we used to derive the high-frequency solution (1.67), we can also deduce that

$$W_j(r,z,t) = \frac{2}{\pi} Im \int_o^t g_\alpha(3-j)\, C_j\, R_{PZ}\, d\tau + \frac{2}{\pi} Im \int_o^t g_\beta(3-j)\, SV_j\, R_{SZ}\, d\tau \quad , \tag{1.72}$$

where

$$g_V(n) \equiv C_n(t,\tau,p)\ \frac{p}{\eta_V}\ \left(\frac{dp}{dt}\right)(t-\tau+2pr)^{-\frac{1}{2}}(t-\tau)^{-\frac{1}{2}} \qquad (1.73)$$

and where C_n was given in equation (1.36). Remember that this integral occurs along the Cagniard contour, thus specifying p as a function of t. C_j and SV_j are vertical radiation patterns given by equation (1.21). We just defined R_{PZ} and R_{SZ} in the last section, and for a receiver on the free surface, they are given by equations (1.56) and (1.63), respectively. For a receiver in a whole space, $R_{PZ} = \eta_\alpha$ and $R_{SZ} = p$. Notice that equation (1.72) contains no explicit near-field terms. All near-field phenomena which are on the vertical component are calculated within the integral and are thus more difficult to recognize.

The expression for the tangential displacement is more complicated since many of the near-field terms are explicitly separated.

$$V(r,z,\theta,t) = \frac{M_o}{4\pi\rho_o}\ \frac{d}{dt}\left[\dot{D}(t) * \sum_{j=1}^{2} A_{j+3}\ V_j\right] \quad , \qquad (1.74)$$

where

$$V_i(r,z,t) = \frac{2}{\pi} Im \int_0^t g_\beta(2-j)\ SH_j\ R_T\ d\tau$$

$$+ \frac{(1+\delta_{ij})}{\pi} Im \iint_0^t g_\beta(3-j)\ SH_j\ R_T(\frac{2}{pr})\ d\tau\ dt$$

$$+ \frac{(1+\delta_{ij})}{\pi} Im \iint_0^t g_\alpha(3-j)\ C_j\ R_{PT}(\frac{2}{r})\ d\tau\ dt$$

$$+ \frac{(1+\delta_{ij})}{\pi} Im \iint_0^t g_\beta(3-j)\ SV_j\ R_{ST}(\frac{2}{r})\ d\tau\ dt\ , \qquad (1.75)$$

where

$$\delta_{ij} = \begin{cases} 0 & j \neq 1 \\ 1 & j = 1 \end{cases}$$

and when the receiver is on the free surface, then

$$R_T = 2p$$

$$R_{PT} = \frac{4\eta_\alpha \eta_\beta}{\beta^2 R(p)} \qquad (1.76)$$

$$R_{ST} = \frac{-2\eta_\beta}{p} \frac{(\eta_\beta^2 - p^2)}{\beta^2 R(p)} \ .$$

When the receiver is in a whole-space, then

$$R_T = p, \quad R_{PT} = 1, \quad R_{ST} = -\eta_\beta/p \ .$$

The last three terms of (1.75) are near-field terms and involve an extra time integral. Notice that the last two terms contain R(p), the Rayleigh denominator, and thus we see that it is possible for the tangential component to have near-field Rayleigh waves.

Finally, the radial component is given by

$$Q(r,z,\theta,t) = \frac{M_o}{4\pi\rho_o} \frac{d}{dt} [\dot{D}(t) * \sum_{j=1}^{3} A_j Q_j] \quad , \tag{1.77}$$

where

$$\begin{aligned} Q_j(r,z,t) = {} & \frac{2}{\pi} \int_0^t g_\alpha(2-j)\, C_j\, R_{PR}\, d\tau + \frac{2}{\pi} \int_0^t g_\beta(2-j)\, SV_j\, R_{SR}\, d\tau \\ & + \frac{(1+\delta_{ij})}{\pi} \iint_0^t g_\alpha(3-j)\, C_j\, R_{PR}\left(\frac{2}{pr}\right) d\tau\, dt \\ & + \frac{(1+\delta_{ij})}{\pi} \iint_0^t g_\beta(3-j)\, SV_j\, R_{SR}\left(\frac{2}{pr}\right) d\tau\, dt \\ & - \frac{(1+\delta_{ij})}{\pi} \iint_0^t g_\beta(3-j)\, SH_j\left(\frac{2}{r}\right) d\tau\, dt \end{aligned} \tag{1.78}$$

for j = 1, 2 and for j = 3,

$$Q_3(r,z,t) = \frac{2}{\pi} \int_0^t g_\alpha(1)\, C_3\, R_{PR}\, d\tau + \frac{2}{\pi} \int_0^t g_\beta(1)\, SV_3\, R_{SR}\, d\tau \quad , \tag{1.79}$$

where R_{SR} is given by equation (1.65) and R_{PR} is given by equation (1.59) if the receiver is located on the free surface. For a receiver in a whole-space, $R_{PR} = -p$ and $R_{SR} = \eta_\beta$.

You might recall that earlier we had problems with integrals of the form which we have just written. An example of how to treat similar integrals was given in equations (1.32) through (1.35). There was a singularity beginning at the time which corresponds to the direct arrival of P and S waves. For the layered problem, we face even greater difficulties. Because of the possibility of head waves and critical reflections, the response of a generalized ray may begin before the direct arrival time. The integral must be broken into that part which occurs before the direct arrival and that part which occurs after.

By analogy to equation (1.32), we will now have to integrate equations of the form

$$\zeta_n(r,z,t) = \frac{2}{\pi}\frac{\partial}{\partial t} Im \int_0^t \frac{R(p)\ C_n\ (t,\tau)}{(t-\tau)^{\frac{1}{2}}(t-\tau+2pr)^{\frac{1}{2}}} \left(\frac{dp}{dt}\right) \frac{p}{\eta_v}\, d\tau \quad , \qquad (1.80)$$

where now R(p) is some complex reflection, transmission or receiver coefficient which is a function of p(t). Just as in the head wave problem, R(p) can become imaginary before dp/dt does. Refer back to Figure 1.9. If $p_o < 1/\alpha$, then R(p) is a real function and the integral may be solved in the manner demonstrated by equations (1.32) through (1.35). If $p_o > 1/\alpha$ and if R(p) becomes complex, then a head wave will result. In this case the integral in (1.80) can be broken into two parts

$$\zeta_n = \zeta_n^{\,1} \qquad t < t(p_o)$$

$$\zeta_n = \zeta_n^{\,2} + \zeta_n^{\,3} \qquad t > t(p_o) \quad ,$$

where

$$\zeta_n^{\,1}(r,z,t) = \frac{2}{\pi} \frac{\partial}{\partial t} Im \int_o^t \frac{R(p)\ C_n\ (t,\tau)}{(t-\tau)^{\frac{1}{2}}(t-\tau+2pr)^{\frac{1}{2}}} \left(\frac{dp}{dt}\right) \frac{p}{\eta_v}\, d\tau \qquad (1.81)$$

$$\zeta_n^{\,2}(r,z,t) = \frac{2}{\pi} \frac{\partial}{\partial t} Im \int_o^{t(p_o)} \frac{R(p)\ C_n\ (t,\tau)}{(t-\tau)^{\frac{1}{2}}(t-\tau+2pr)^{\frac{1}{2}}} \left(\frac{dp}{dt}\right) \frac{p}{\eta_v}\, d\tau \qquad (1.82)$$

$$\zeta_n^{\,3}(r,z,t) = \frac{2}{\pi} \frac{\partial}{\partial t} Im \int_{t(p_o)}^t \frac{R(p)\ C_n\ (t,\tau)}{(t-\tau)^{\frac{1}{2}}(t-\tau+2pr)^{\frac{1}{2}}} \left(\frac{dp}{dt}\right) \frac{p}{\eta_v}\, d\tau \quad . \qquad (1.83)$$

$\zeta_n^{\,3}$ is solved in the same manner as the exact whole-space solution; see equations (1.32) through (1.35). $\zeta_n^{\,1}$ and $\zeta_n^{\,2}$ can be numerically integrated by employing the following change of variables:

$$\theta = \sin^{-1} (\tau/t)^{\frac{1}{2}} \quad . \qquad (1.84)$$

Equations (1.81) and (1.82) become

$$\zeta_n^{\,1}(r,z,t) = \frac{4}{\pi} \int_{\theta_c}^{\pi/2} F(\theta)\, d\theta \quad , \qquad (1.85)$$

where

$$F(\theta) = Im\left[R(p)\,\frac{p}{\eta_v}\,\frac{dp}{dt}\right]\frac{\sqrt{\tau}}{(t-\tau+2pr)^{\frac{1}{2}}} \tag{1.86}$$

and where

$$\theta_c = \sin^{-1}\left(\frac{t_h}{t}\right)^{\frac{1}{2}} \tag{1.87}$$

$$t_h \equiv t(p = 1/\alpha)$$

and

$$\zeta_n^{\,2}(r,z,t) = \frac{4}{\pi}\int_{\theta_{c_o}}^{\pi/2} F(\theta)\,d\theta \quad , \tag{1.88}$$

where

$$\theta_{c_o} = \sin^{-1}\left(\frac{t_h}{t(p_o)}\right)^{\frac{1}{2}} \quad . \tag{1.89}$$

In order to obtain the exact solution for a point dislocation in a half-space, 26 numerical integrations must be performed for each time point in the solution. Recall also, that as the epicentral range, r, becomes small, very large numbers must be differenced to find the static solution. This means that as r becomes small, these 26 integrations per time point must be computed with special care. Numerous examples of this half-space solution are given in Chapter 4 when we construct models of the San Fernando earthquake.

Three-Dimensional Finite Fault

We have now demonstrated techniques which allow us to calculate the response of a layered half-space to a point shear dislocation. However, it is clear that the earthquakes we wish to model occurred on planes of finite area. Consider the rectangular plane which includes the plane which breaks during any one particular earthquake. Let the coordinates x and y be along the fault strike and down the fault dip, respectively. Consider a receiver which records three components of ground motion, $\underset{\sim}{U}$, in the frame north, east, and up. Now by using the results of the previous sections, we can compute the displacement due to any point on the fault. In order to find the solution for a finite fault, we need merely integrate these responses over the fault surface. Consider the motion due to one point (x,y) on the fault. The motion, $\underset{\sim}{U}$, is given by

$$U_1(x,y,t) = Q(r,z,\theta,t) \cos \nu - V(r,z,\theta,t) \sin \nu$$

$$U_2(x,y,t) = Q(r,z,\theta,t) \sin \nu + V(r,z,\theta,t) \cos \nu$$

$$U_3(x,y,t) = W(r,z,\theta,t) \quad , \tag{1.90}$$

where $\nu(x,y)$ is the backazimuth of the point source as measured clockwise from north. r, z, and θ are functions of x and y and are shown back in Figure 1.2. The task now is to simply integrate (1.90) over x and y. Of course, this task is not so simple. In general, we have no analytic expressions for Q, V and W. In fact, as we have just seen, these solutions

can be very complex. We will begin by writing a general expression for this integration, and then we will see in what instances we can make simplifying assumptions.

$$U_i = \int_{x_1}^{x_2} \int_{y_1}^{y_2} U_i(x,y,t)\, d\, y\, dx \quad . \tag{1.91}$$

We can solve (1.91) as accurately as we please if we are willing to endure the massive numerical calculations involved. We merely subdivide the fault into a fine gridwork. We sum the responses of each point on the fault. The response of each point can be computed using the full Cagniard solution. Of course, the source to receiver geometry is different for each point on the fault. In general, each point source will have a different time history. In fact, the general answer has so many variables, it would be pointless to try and write expressions which show all the variables. In Chapter 4, we will show some examples of how to construct such solutions.

Because our integration contains a numerical function U_i, there is no hope to find an exact analytic expression of the integral (1.91). Every approximation which we will make depends upon the ability to bring the numerically computed part of U_i outside of the integral. Of course, the way to do this is to require that these numerical parts be slowly varying functions of x and y relative to the limits of integration. If there are large changes of the numerical responses within the limits, then simply subdivide the fault into smaller areas until the numerical responses change little within the dimensions of the subfault. In the

next three chapters we will demonstrate how these approximations are made and we will investigate records taken at small, medium and large ratios of source dimension to receiver distance.

Chapter 2

Modeling the M 4.9 November 4, 1976 Brawley Earthquake: Predictability of Strong Ground Motion in the Imperial Valley

Introduction

Both Chapters 2 and 3 are taken, with slight modification, from two papers by Heaton and Helmberger (1977, 1978). In truth, Chapter 3 was written before Chapter 2 and thus there is some loss in logical continuity. However, I believe that it is appropriate to discuss the Brawley study first since it represents the case of a simple source located in a structure which can be understood. We will save studying more complex sources for later.

The Imperial Valley of Southern California is unusual in that it has the rare combination of flat-lying sediments and earthquakes. Furthermore, the upper crustal velocity structure has been studied extensively by Biehler (1964). The Imperial Valley is thus particularly well-suited for waveform modeling studies of strong ground motion from local earthquakes. In this Chapter, we will examine the tangentially polarized ground motion from a M_L 4.9 earthquake which occurred on November 4, 1976. Our approach will be to use a velocity structure model which is based on Biehler's work, along with the calculated hypocentral location and fault plane solution, to predict the tangentially polarized ground motion observed for this earthquake. Previous modeling of local SH waveforms (Helmberger and Malone, 1975; Heaton and Helmberger, 1977, i.e., Chapter 3) has been somewhat unsatisfying because velocity structure

as well as source model parameters have been constrained primarily by the condition that synthetic and observed waveforms match each other. Obviously, any successful model must satisfy this constraint, but due to questions of uniqueness and the applicability of plane-layered structure models to complexly faulted regions, one cannot help but feel that the choice of model parameters seemed somewhat ad hoc. In view of this objection, we pose the following question: Is it possible to predict the motion from an earthquake using a model whose velocity structure parameters are determined independently of the waveform modeling? We will show that the answer in this particular case is yes! Thus we will demonstrate a model which is consistent with both the observed waveforms and the independent constraints on velocity structure and epicentral location.

We will also investigate the effect of changes in the model parameters on the synthetic waveforms. Since we used generalized ray theory to generate the synthetics, it is possible to associate arrivals on the record with specific travel paths. Although we prefer to view our models in the time domain, we will also present Fourier amplitude spectra of our synthetics. We will show that synthetic amplitude spectra for a layered half-space are significantly different than spectra calculated for a homogeneous half-space. The effects of structure must be included when making estimates of source parameters or seismic wave attenuation.

The November 4 Brawley Earthquake

During the period from November 3 through November 8, 1976, a swarm of more than 400 earthquakes was recorded by the U.S. Geological

Survey Imperial Valley short period seismic array. This swarm occurred approximately 15 km northwest of a well-studied swarm which occurred along the Brawley fault in February of 1975 (Johnson and Hadley, 1976). Unlike the February 1975 swarm, which produced significant surface deformation (Sharp, 1976), no surface deformation has yet been associated with the November 1976 swarm. The largest event in the November 1976 swarm occurred at 10:41 GMT on November 4 and was assigned a magnitude of 4.9. By using P wave arrival times from the Imperial Valley seismic array, the epicentral location (shown in Figure 2.1) was determined by the U.S. Geological Survey to be 33°05' North latitude and 115°36' West longitude (Madeline Schnapp and Gary Fuis, personal communication). The USGS hypocentral depth was 4-1/2 km with low P residuals. However, we prefer a depth of 7 km based on our modeling of strong-motion waveforms. Since the hypocenter is only loosely constrained by P for these solutions, this difference does not appear significant. Assuming a hypocentral depth of 7 km, we computed a focal mechanism using P wave first motion data from 68 stations in the joint Caltech-USGS Southern California seismic array. The focal mechanism, which is shown in Figure 2.2, indicates predominantly right-lateral faulting along a steeply dipping fault which trends N-NW. Because the motion is mostly strike-slip along a vertical plane, this solution is relatively insensitive to changes in the assumed hypocentral depth.

Two long-period strong-motion seismic stations were triggered during the swarm sequence. A three-component 4X torsion seismometer with a free period of 10 seconds was located at Imperial Valley College (IVC)

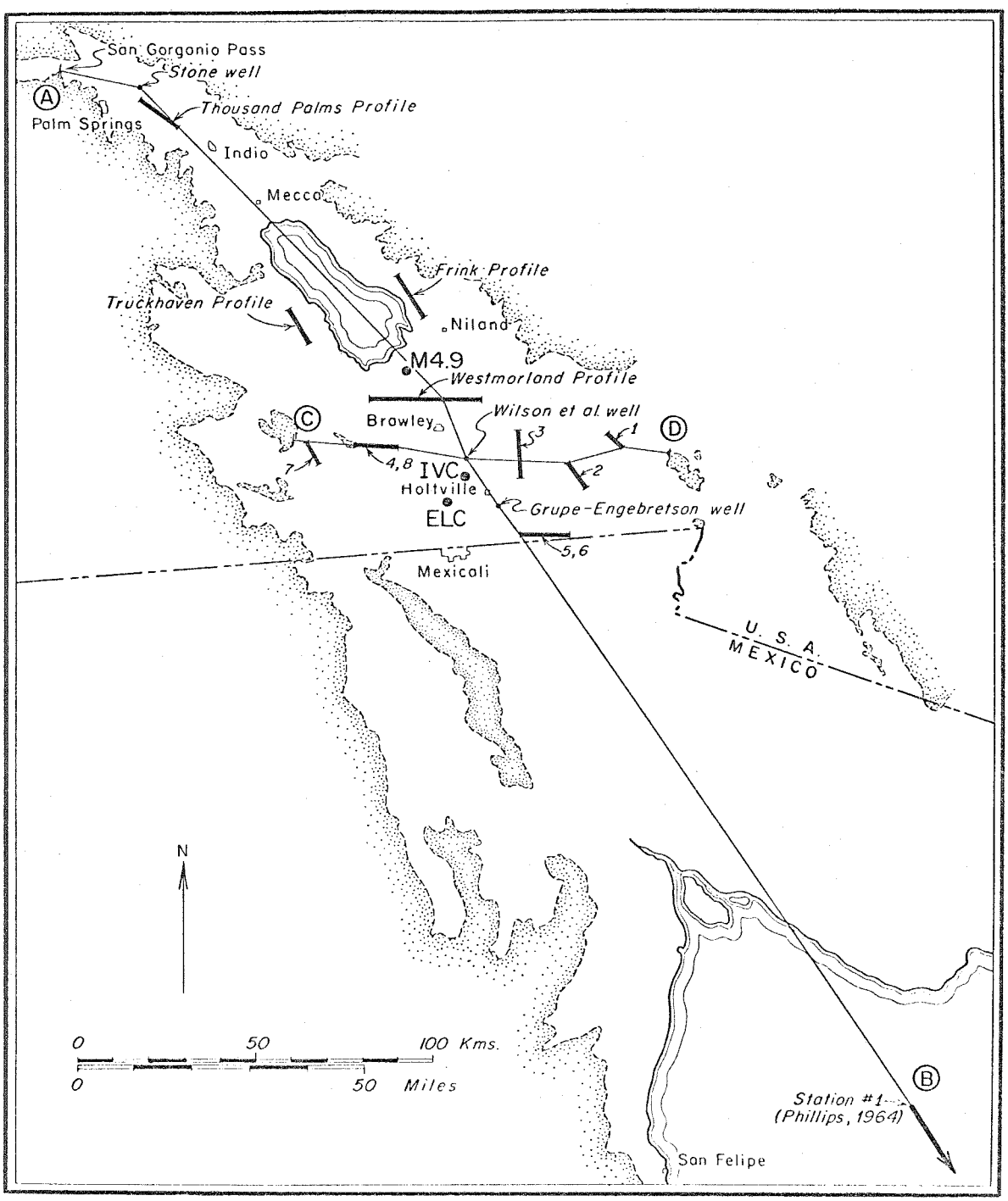

Figure 2.1. Index map of Salton Trough showing locations of seismic refraction profiles and cross-section lines A-B (Fig. 2.5a) and C-D (Fig. 2.5b). Also shown are the long-period strong-motion stations, IVC and ELC, and the epicenter of the M 4.9, November 4, 1976 earthquake. Stippling indicates generalized outline of pre-Tertiary crystalline rocks bordering the Salton Trough. This figure has been modified from Biehler, Kovach and Allen (1964).

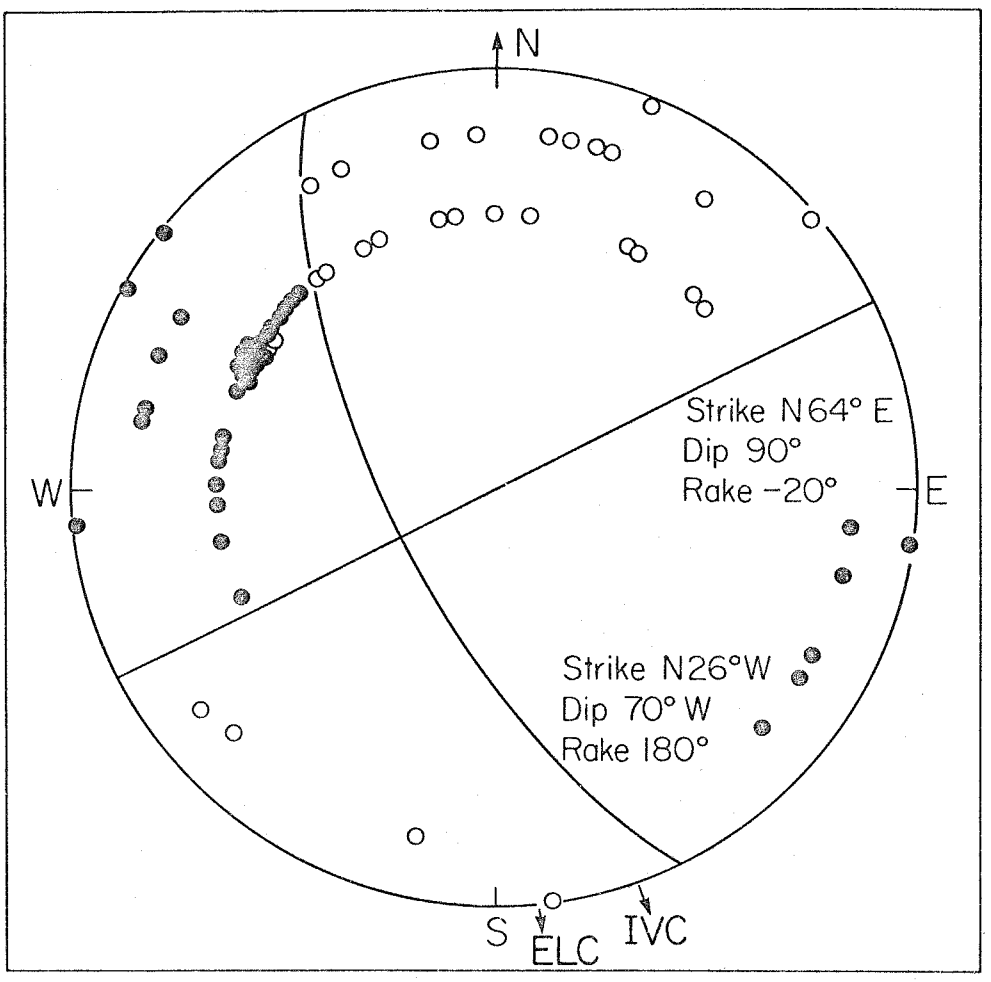

Figure 2.2. Focal mechanism for the M 4.9, November 4 earthquake determined from P wave first motions observed at 68 stations in the joint Caltech-USGS Southern California seismic array. The azimuths of the stations, IVC and ELC, are also shown.

at a distance of 33 km from the epicenter (see Figure 2.1). This instrument records on photographic paper on a revolving drum for a full 24 hours after being triggered. The instrument triggered 6 hours before the M 4.9 quake being studied in this paper and thus the entire wave-train of the earthquake was well recorded. Shown in Figure 2.3 are the records from IVC. The instrument response has been deconvolved and the resulting ground motion has been heavily filtered at periods longer than 20 seconds with an Ormsby filter (Hudson et al., 1971). Unfortunately, the vertical torsion recording shows a long-period drift near the onset of motion which seems to have a positive net area. This indicates some nonlinearity in the instrument response which made deconvolution impossible. Despite this, it seems clear from the original records that horizontal ground motion was much larger than vertical ground motion. Also shown in Figure 2.3 are the displacements rotated into radial and tangential directions. An inspection of these rotated motions clearly shows that the ground motion at IVC was dominated by transversely polarized shear waves, as would be expected, since IVC lies near a P-SV node (Figure 2.2).

A second recording of ground motion was made by the horizontal Carder displacement meters located in El Centro at a distance of 36 km. No long-period vertical instrument is present at this station. The horizontal instruments have a static magnification of 1.0 with free periods near 6 seconds. These instruments appear to have triggered near the start of the S wave and thus the beginning of the record is lost. The records from ELC are shown in Figure 2.4. Also shown is the ground motion obtained by deconvolution of the instrument response and Ormsby

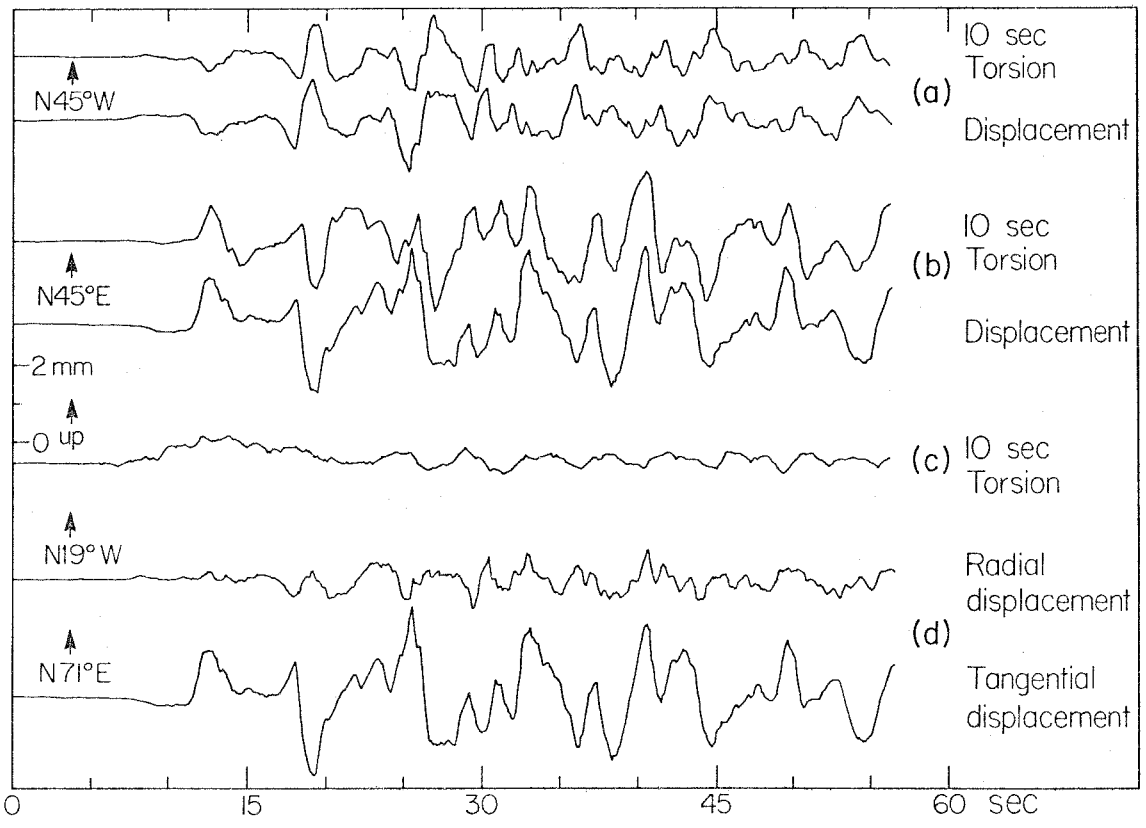

Figure 2.3. Summary of ground motion observed at IVC. (a) NW component of ground motion with and without the instrument response. (b) NE component of ground motion with and without instrument response. (c) Vertical component of ground motion with the instrument response. The instrument response could not be deconvolved because of the long period arrival which appears to have a net positive area. (d) Ground motion rotated into radial and tangential components.

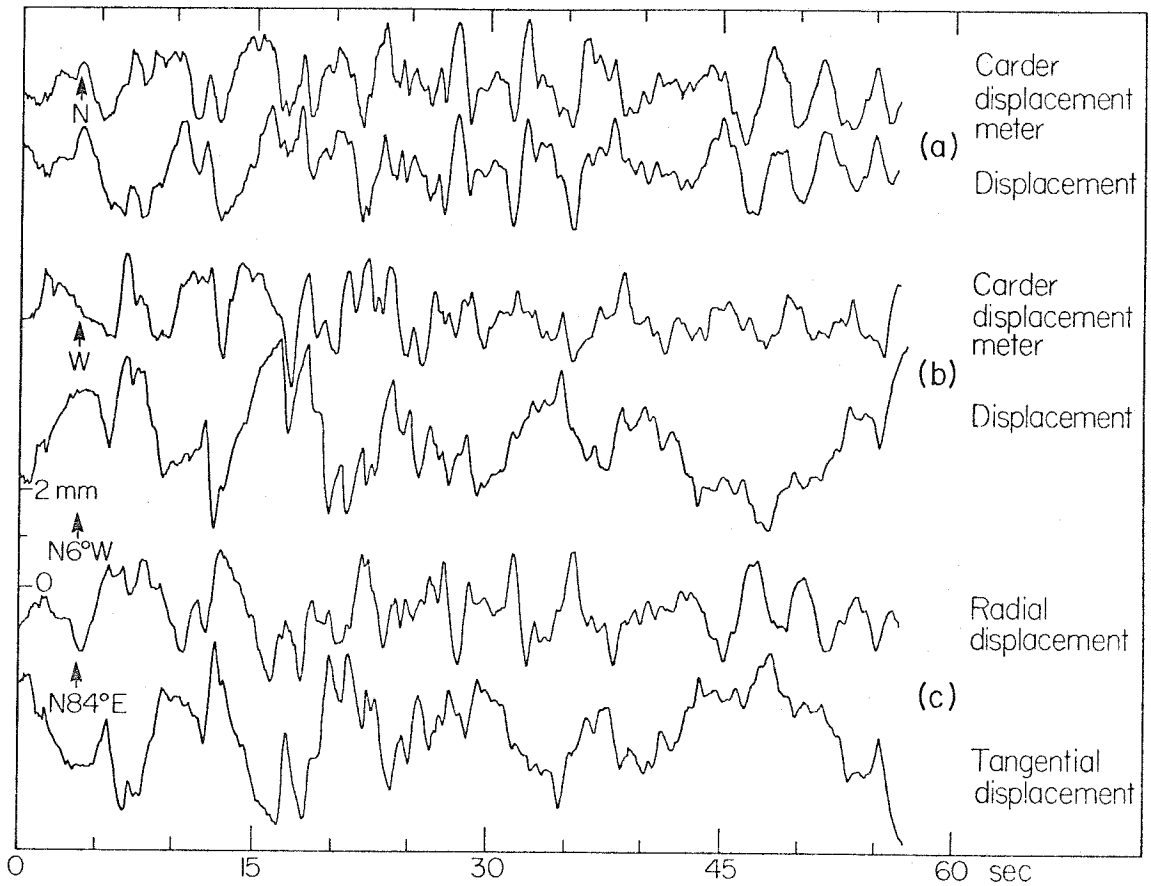

Figure 2.4. Summary of ground motion observed at ELC. Since this instrument was probably triggered by the direct S wave, the beginning of the record is lost. (a) North component of ground motion with and without instrument response. (b) West component of ground motion with and without instrument response. (c) Ground motion rotated into radial and tangential components. No long-period vertical strong-motion instrument is present at this station.

filtering of periods beyond 15 seconds. Since the beginning of the record was lost, the deconvolution of the first pulse on the record is questionable. Rotation of the displacements indicates that there were much larger radial displacements at ELC than there were at IVC. The fact that the radial and tangential waveforms are quite dissimilar suggests that this change in amplitude ratios is not due to a poor rotation of predominately transverse motions. The difference in the magnitude of radial displacements between ELC and IVC is consistent with the fact that the azimuth of ELC is further from the P and SV node shown in Figure 2.2. Notice that there is a remarkable degree of coherence between the tangential waveforms recorded at IVC and ELC. This is as it should be since the differences in range and azimuth between ELC and IVC are only 3 km and 13°, respectively.

Crustal Structure in the Salton Trough

The Salton Trough is a structural depression which is the northward continuation of the Gulf of California. This depression is underlain and bounded by Mesozoic and older crystalline rocks. As much as 6 km of upper Tertiary and Quaternary marine and nonmarine sediments fill this depression. Also present in the Salton Trough are several major active right-lateral fault zones, recent volcanism, and potential geothermal reserves. The November 1976 Brawley swarm as well as the stations, IVC and ELC, lie near the axis of this depression. The work of Biehler, Kovach and Allen (1964) on P wave refraction profiles indicates that there is very little variation in upper crustal velocity structure along

the axis of the Salton Trough. This is illustrated by the cross section A-B which is shown in Figure 2.5a. Although the total thickness of sediments varies considerably as one travels perpendicular to the axis of the trough, the depths of individual layers within the sediments are amazingly consistent as one crosses the Salton Trough. This can be seen in the cross section C-D shown in Figure 2.5b. Thus the overall impression of sedimentary structures down the axis of the trough is one of relatively plane layers.

Unfortunately, there are several reasons why the velocity models calculated by Biehler et al. (1964) cannot be used directly in our modeling. Most importantly, we need to know shear wave velocities and the refraction studies were for only compressional waves. Also, a model which consists of five layers over a half-space requires the computation of too many generalized rays to be practical. Shawn Biehler (personal communication) has indicated that the interfaces above and below the layer with a compressional wave velocity of 2.6 km/sec were the sharpest and most consistently observed interfaces found in the region. He also believes that the sediment to basement velocity contrast is very sharp. We thus condensed the five-layered model into one with three layers by combining layers one and two and also layers four and five. This is shown in Table II.1. In order to convert these compressional wave velocities to shear wave velocities, we chose a Poisson ratio of 0.25 for everything except the uppermost layer. A Poisson ratio of 0.35 was assumed for the uppermost kilometer of very soft sediments as suggested by Ronald Scott (personal communication). The S wave model given in Table II.1 is the one which was used throughout this study.

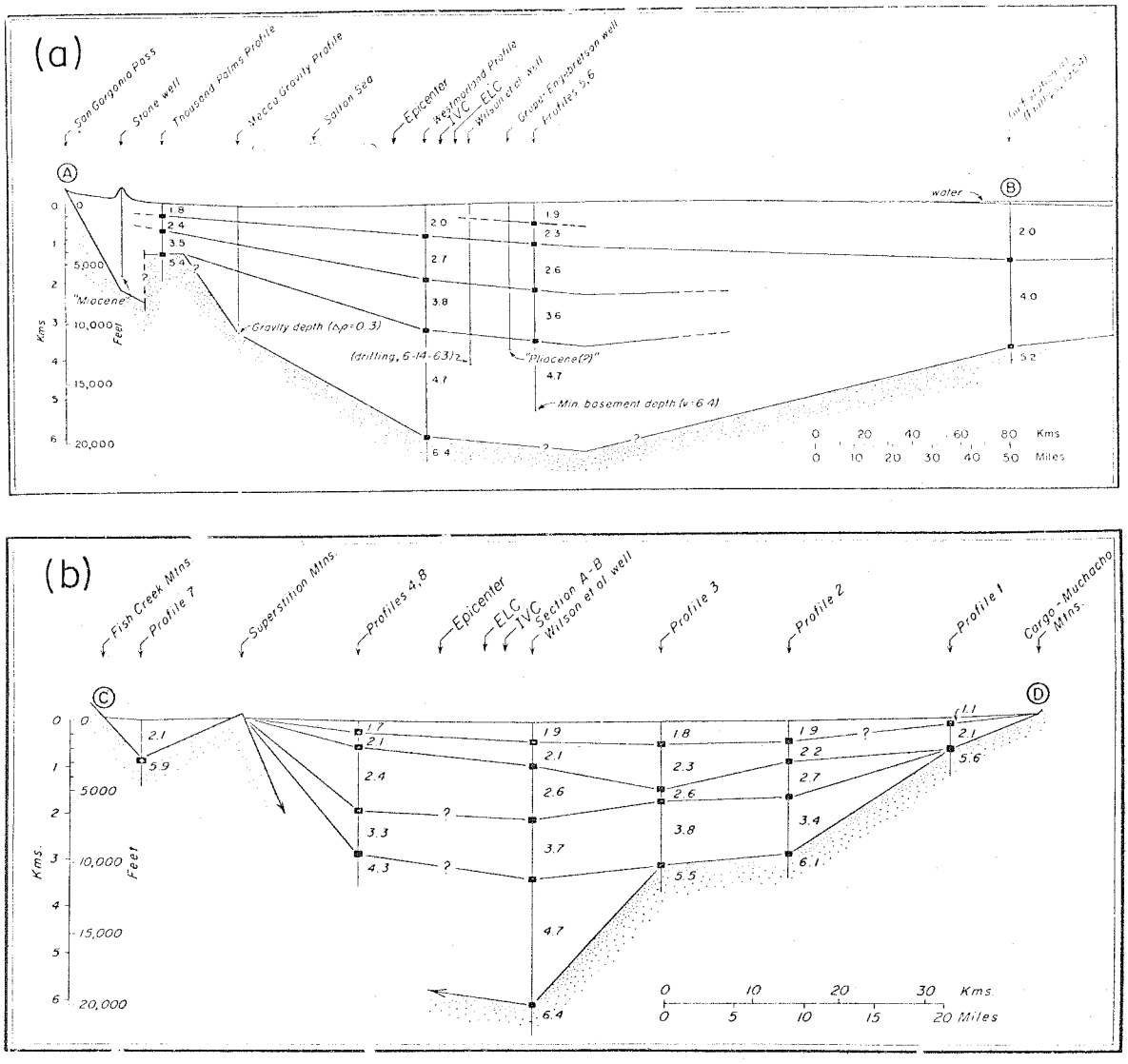

Figure 2.5. (a) Seismic cross-section along line A-B of Figure 2.1. Numbers indicate velocities in km/sec. (b) Seismic cross-section along line C-D of Figure 2.1. Note that the ratio of horizontal to vertical scales is different on part (a) than on part (b). Also notice that the structure is relatively flat along the paths from the epicenter to the stations, IVC and ELC. These figures have been modified by Biehler, et al. (1964).

TABLE II.1

Velocity Structure for Imperial Valley Sediments

Thickness (km)	P Velocity (km/sec)	Thickness (km)	P Velocity (km/sec)	S Velocity (km/sec)	Density (g/cc)
0.45	1.7	0.95	2.0	0.88	1.8
0.5	2.1				
1.15	2.6	1.15	2.6	1.5	2.35
1.3	3.7	3.8	4.2	2.4	2.6
2.5	4.7				
	6.4		6.4	3.7	2.8

Description of the Modeling Technique

Our basic modeling tool will be the Green's function, $V_j(t)$, which represents the transverse response of a layered elastic half-space to a point shear dislocation. The response is calculated by using the generalized ray method. The solution is represented by the sum of the responses of individual generalized rays, each of which traverses a different path which is characterized by the interfaces it contacts. The response of each generalized ray was computed by using the Cagniard-de Hoop technique. In Chapter 1, we reviewed our technique for computing these point source responses. The complete solution containing both near-field and far-field terms for dislocation sources embedded in a layered half-space has been discussed by Helmberger (1974) and Vered and Ben-Menahem (1974). For the periods and station ranges of interest in this study, it is sufficient to model only the far-field term so that the asymptotic solution can be used (see Helmberger and Malone, 1975). These approximations become progressively better for shorter periods. We have found it convenient to view our responses in terms of the displacement, $V_j(t)$, due to a dislocation time history which consists of a ramp function (far-field step function response). The surface tangential component of motion produced by an arbitrarily oriented point dislocation as described by Langston and Helmberger (1975) is given by

$$V(r,\theta,0,t) = \frac{M_o}{4\pi\rho_o} F(t) * \frac{d}{dt} \sum_{j=1}^{2} A_j+3\ V_j(t) \quad , \tag{2.1}$$

where M_o is fault moment, ρ_o is density at the source, F(t) is the far-field time history, (dS(t)/dt), and S(t) is the dislocation time history. Also,

$$A_4(\theta,\lambda,\delta) = \cos 2\theta \cos \lambda \sin \delta - 1/2 \sin 2\theta \sin \lambda \sin 2\delta \qquad (2.2)$$

and

$$A_5(\theta,\lambda,\delta) = -\sin \theta \cos \lambda \cos \delta - \cos \theta \sin \lambda \cos 2\delta \qquad (2.3)$$

where θ is the angle between receiver azimuth and fault strike, λ is the rake angle, and δ is the dip angle. V_1 and V_2 are the far-field step function responses for a vertical strike-slip source and a vertical dip-slip source, respectively. Expressions for V_1 and V_2 are given by Helmberger and Malone (1975) and by equation (1.49) of this thesis. Because the far-field delta function response, $\dot{V}_j(t)$, is dominated by high frequency reflections, we choose to display the far-field step function response, $V_j(t)$ in our figures.

When one or more layers are present, an infinite number of generalized rays are necessary to give an exact representation of the solution at all times. The number of rays which are necessary to give a close approximation is a function of both source to receiver geometry and the length of record to be modeled. In order to model the first 25 seconds of ground motion for three layers over a half-space and a range of 33 km, we found it necessary to include over 100 generalized rays.

This number grows rapidly for an increased number of layers. Shown in Figure 2.6 is the strike-slip far-field step function response, $V_1(t)$, given as a function of a number of rays used in the synthetic. The number of non-degenerate rays necessary to describe responses which include rays having up to 1, 2, 3, 4 and 5 internal reflections are 4, 13, 31, 65 and 104, respectively. Here, an internal reflection is any reflection which does not occur at the free surface. It can be seen that as extra rays are added, the beginning of the response changes very little, but the latter portion of the response changes as more complex rays are added. The final summation of rays seems adequate to approximate the first 25 seconds of record. Not all of these rays are of equal importance. Also shown in Figure 2.6 are the first arrival times and a schematic description of the 18 most prominent phases.

Throughout this study we will stress the importance of diffraction in these models. According to Sommerfeld (1949), "Any deviation of light rays from rectilinear paths which cannot be interpreted as reflection or refraction is called diffraction." Thus head waves and the excitation of Love waves by a source exterior to the waveguide are examples of diffraction phenomena. The diffraction of spherical wavefronts can be seen in Figure 2.6. If geometric ray theory had been used to calculate these responses, then they would consist of a series of steps. However, our computed responses do not consist of such sharp steps because of the inherent frequency dependence of wave propagation due to diffraction. This can be seen in the direct wave (arrival 1) which is depleted in short periods relative to long periods. This observation is important

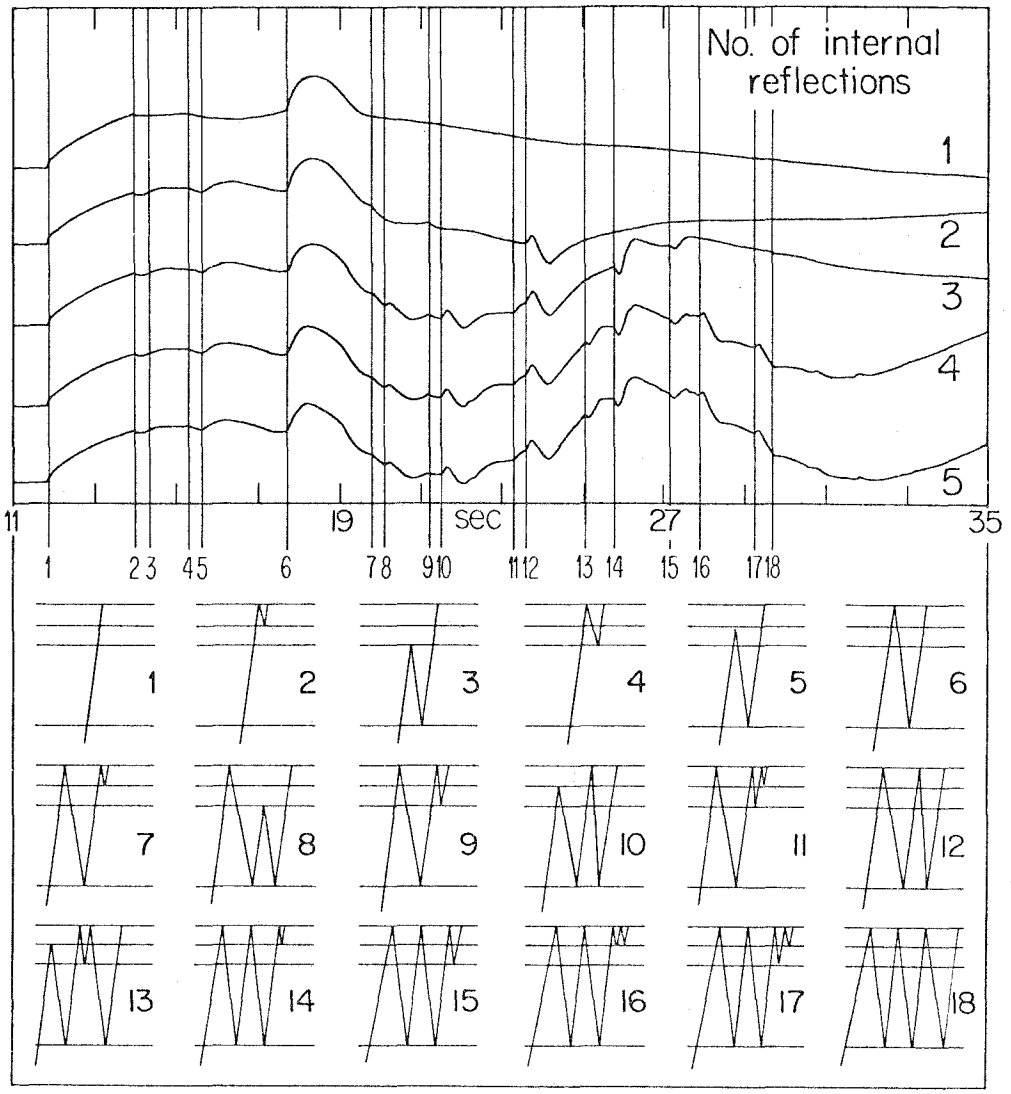

Figure 2.6. Strike-slip far-field step function response as a function of the number of rays used. An internal reflection is any reflection which does not occur at the free surface. First arrival times and schematic description of the most prominent rays are also shown. Source depth is 6.9 km and the range is 33 km.

in the understanding of the spectra which we present later in this Chapter.

In this study, we know very little about the time history of dislocations which occurred on the fault plane of this earthquake. Because of this, we choose to consider models consisting of a single point dislocation which have time functions which give a reasonable comparison between synthetic and observed ground motion. Clearly, an earthquake is not a point dislocation. However, the differences in ground motion between finite source models and point source models are for practical purposes unresolvable for this type of source to receiver geometry. The reasons for this poor resolution can be understood by examining the step function responses, V_1 and V_2, as a function of source depth and epicentral range. Figure 2.7 demonstrates that at a constant source depth of 6.9 km, the response is a slowly varying function of range. Figure 2.8 shows that although the response changes more rapidly as a function of source depth, it is still a slowly changing function for depth variations of several kilometers. This generalization is particularly valid for sources occurring below the sediment layers. For sources in the sediment layers, there is a complex interference of multiple reflected rays which propagate upward and downward from the source. Thus, short-period arrivals change fairly rapidly with depth when the source occurs in the sediment layers.

A curious effect can be seen in the dip-slip responses, $V_2(t)$, displayed in Figure 2.8. Notice that the first motion for every response except No. 5 is negative. Now there is a radiation node for SH waves

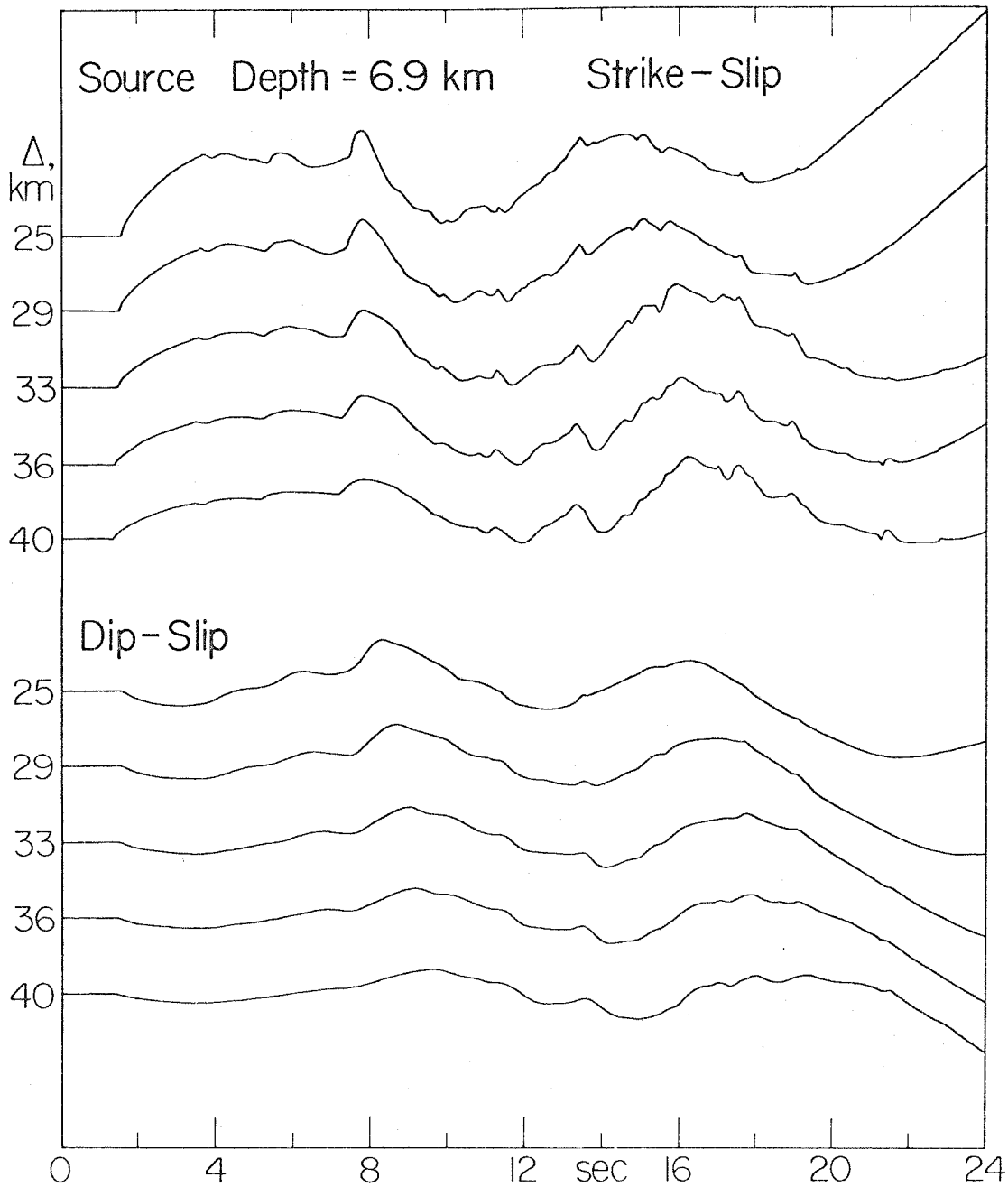

Figure 2.7. Far-field step function response as a function of range. Amplitudes are scaled in relation to the top trace.

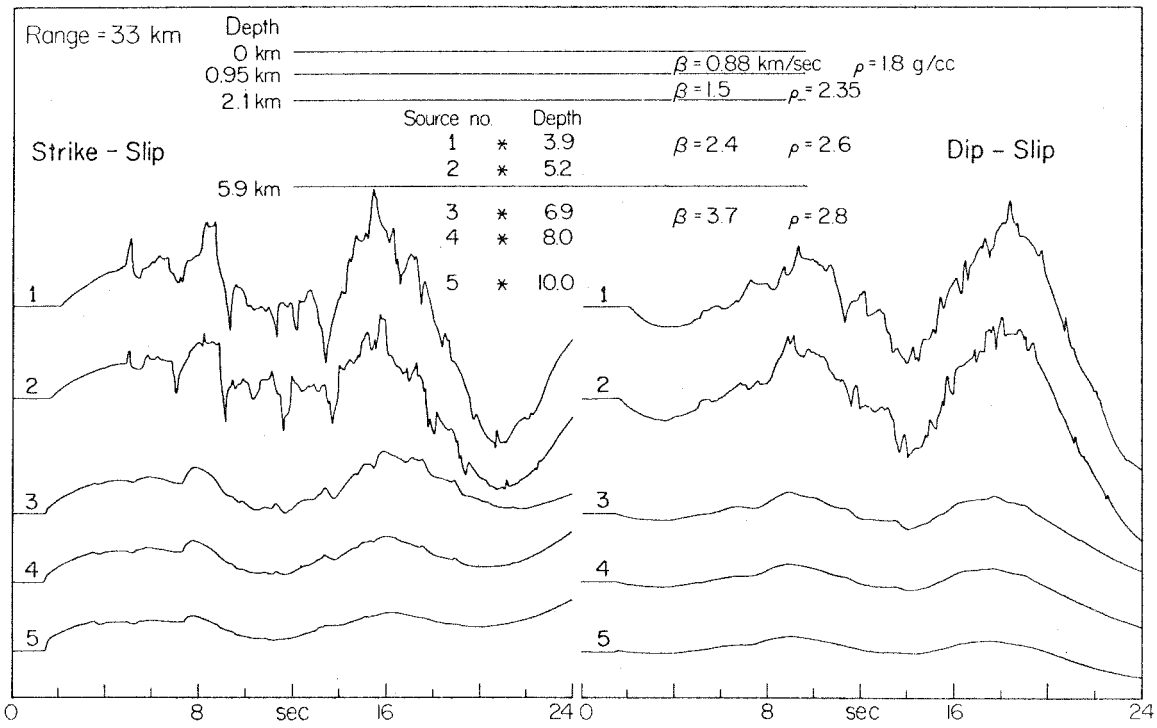

Figure 2.8. Far-field step function response as a function of source depth. Amplitudes are scaled in relation to the top trace. Notice that the long-period nature of the signal changes slowly with depth, whereas short-period arrivals for sources in the sediments change rapidly.

travelling horizontally from a vertical dip-slip fault. Rays which travel upward should be positive and rays which travel downward should be negative. The first arrivals from sources in the sediment, Nos. 1 and 2, are head waves and should be negative. The first arrivals from sources in the half-space, Nos. 3, 4 and 5, are direct waves and should be positive. Yet, first arrivals for sources 3 and 4 appear to be negative, and the waveform for source 5 quickly becomes negative. Somehow energy which has travelled downward into the half-space affects the direct wave observed above the half-space. What is happening is that down-going energy is diffracted into the sediment layers much as down-going waves are diffracted back upward in the head wave problem. If we examine the first arrival for source 3 in more detail, we find that it does actually break upwards, but the size and duration of this first arrival are exceedingly small. The direct wave is dominated by down-going energy which diffracted upward. Thus, where geometric ray theory would have predicted a small positive first arrival, we would actually see a fairly clear negative arrival. This example dramatically demonstrates the shortcomings of geometric ray theory for this type of problem.

Although the short-period arrivals can change rapidly with depth as mentioned earlier, the long-period character of the response is fairly stable with depth, even when the source occurs in the sediment layers. Thus, except for a travel time correction, the response does not vary greatly along the fault plane if the dimensions of the fault are small. This observation allows us to make a formal statement which justifies modeling this earthquake with a single point source. That is, consider

a fault plane with dimensions $o < x < \ell$, $o < y < h$, where x runs along the fault strike and y is down the fault dip. The tangential displacement at a receiver, V(t), due to a planar fault of arbitrary time history can be written as

$$V(t) \simeq \frac{\beta_o^2}{4\pi} \sum_{j=1}^{2} A_{j+3} \int_o^{\ell} \int_o^{h} \dot{D}[x,y,t-\tau(x,y)] * \dot{V}_j(x,y,t)\, dy\, dx \quad , (2.4)$$

where $\dot{V}_j(x,y,t)$ is the far-field delta function response of the medium, β_o is the shear velocity in the source region, $\dot{D}[x,y,t-\tau(x,y)]$ is the time derivative (far-field response) of the dislocation history on the fault, and $\tau(x,y)$ is the time lag between the origin time of the earthquake and the initiation of rupture at the point (x,y). Equation (2.4) is valid as long as the source to receiver distance is much larger than the fault dimensions, thus insuring that the azimuth angle from each point on the fault to the receiver is approximately constant.

Now from our previous discussion of the behavior of the point source response, $\dot{V}_j$, for small variations in x and y, we make the following approximation:

$$\dot{V}_j(x,y,t) \approx \dot{V}_j[x_o,y_o,t-T(x,y)], \qquad (2.5)$$

where

$$o < x_o < \ell, \quad o < y_o < h.$$

$T(x,y)$ is the difference in travel times between $\dot{V}_j(x,y,t)$ and $\dot{V}_j(x_o,y_o,t)$. It can easily be shown that

$$\dot{D}[x,y,t-\tau(x,y)] * \dot{V}_j[x_o,y_o,t-T(x,y)]$$

$$= \dot{V}_j(x_o,y_o,t) * \dot{D}[x,y,t-\tau(x,y)-T(x,y)] \quad . \qquad (2.6)$$

Thus, from expressions (2.4), (2.5) and (2.6), we conclude that

$$V(t) \quad \frac{M_o}{4\pi\rho} \sum_{j=1}^{2} A_{j+3} \, [F(t) * \dot{V}_j(x_o,y_o,t)] \, ,$$

where

$$F(t) \equiv \frac{1}{\ell h \bar{D}} \int_0^{\ell} \int_0^{h} \dot{D}[x,y,t-\tau(x,y)-T(x,y)] \, dy \, dx \quad . \qquad (2.7)$$

$\bar{D}$ is the average dislocation on the fault surface. Since $V(t)$ and $V_j(x_o,y_o,t)$ are known, we can obtain some estimate for $F(t)$ through our modeling studies. Unfortunately, there is no way to deduce ℓ, h or $D(x,y,t)$ from a knowledge of $F(t)$. Even though a knowledge of $F(t)$ does put constraints on these parameters, any models which specify ℓ, h and $D(x,y,t)$ require ad hoc parameterizations of these variables.

Modeling the November 4 Brawley earthquake

We will model the November 4 earthquake with a point source located in the velocity model given in Table II.1. Because of the focal

mechanism given in Figure 2.2 and because ground motion at IVC was almost entirely tangentially polarized, we will assume that the earthquake was a pure strike-slip event occurring on a vertical plane directed towards the station, IVC. We also know that the stations IVC and ELC lie at distances of 33 km and 36 km, respectively, from the eipcenter. We do not have good independent constraints on either the hypocentral depth or the far-field time function, F(t). We will first constrain the depth to be 6.9 km and then try to estimate F(t). Even though depth and source time function do not produce strictly independent effects in our synthetics, it is sufficient for our purposes to first estimate F(t) and then to try and resolve the depth. Shown in Figure 2.9 are comparisons of the observed IVC tangential ground motion and synthetics with a variety of source time functions. For simplicity, we assumed that the time function was an isosceles triangle where duration was the independent parameter. Considering the simplistic nature of the assumptions we have made about velocity structure and source finiteness, it seems counter productive to attempt more detailed modeling of the source time function. In Figure 2.9 it can be seen that a duration of 1.5 seconds gives the best overall fit to the observed record. Durations of 0.6 seconds and 3.0 seconds are definitely too short and too long, respectively. A moment of 3.2×10^{23} ergs is inferred if the time function is a 1.5 second triangle. These quantities are consistent with the observations of Helmberger and Johnson (1977) concerning the empirical relationship between moment and time function duration.

In Figure 2.10 we show several comparisons of the tangential ground motions at IVC and ELC with our synthesized records. Since the

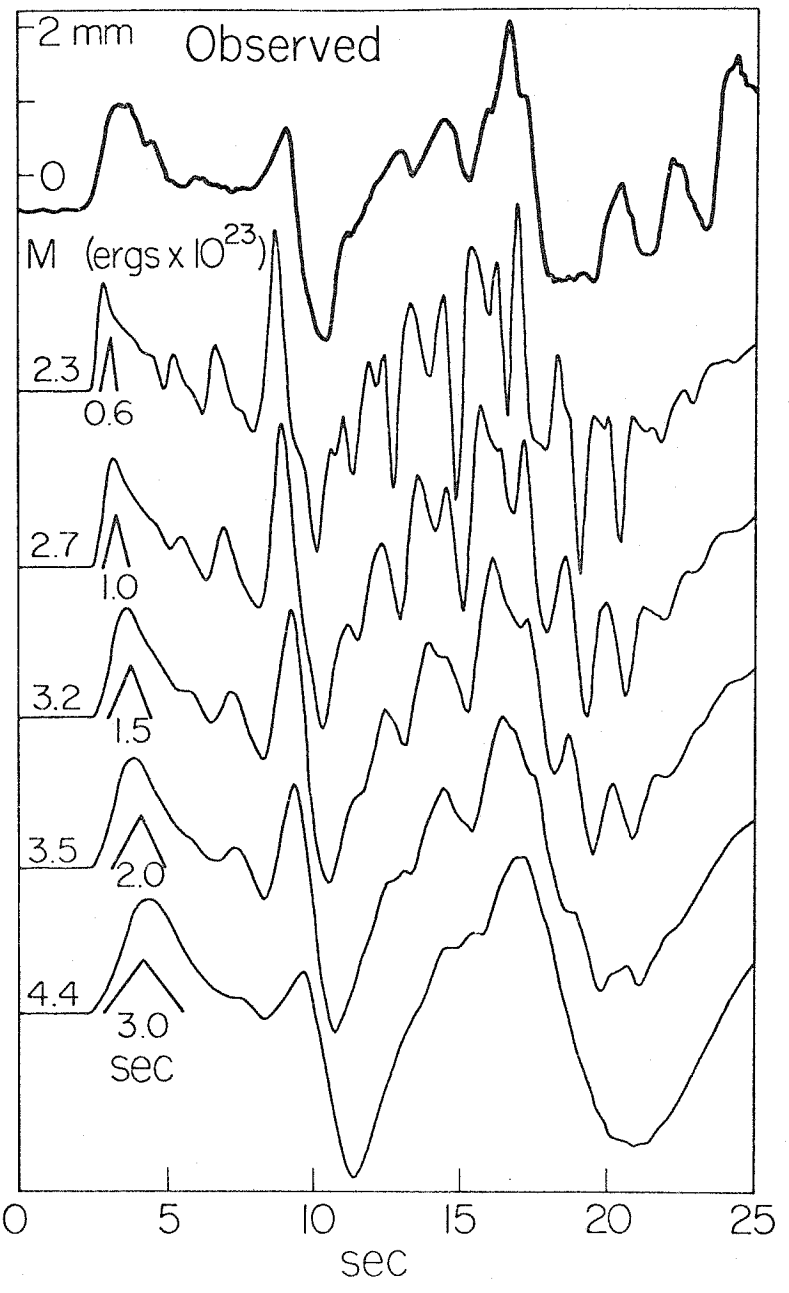

Figure 2.9. Comparison of IVC tangential ground motion with synthetics which have different duration triangular far-field time functions. The far-field time functions are displayed directly under the first pulse in the corresponding synthetic. A strike-slip point source with a depth of 6.9 km and a range of 33 km was used in all of these synthetics.

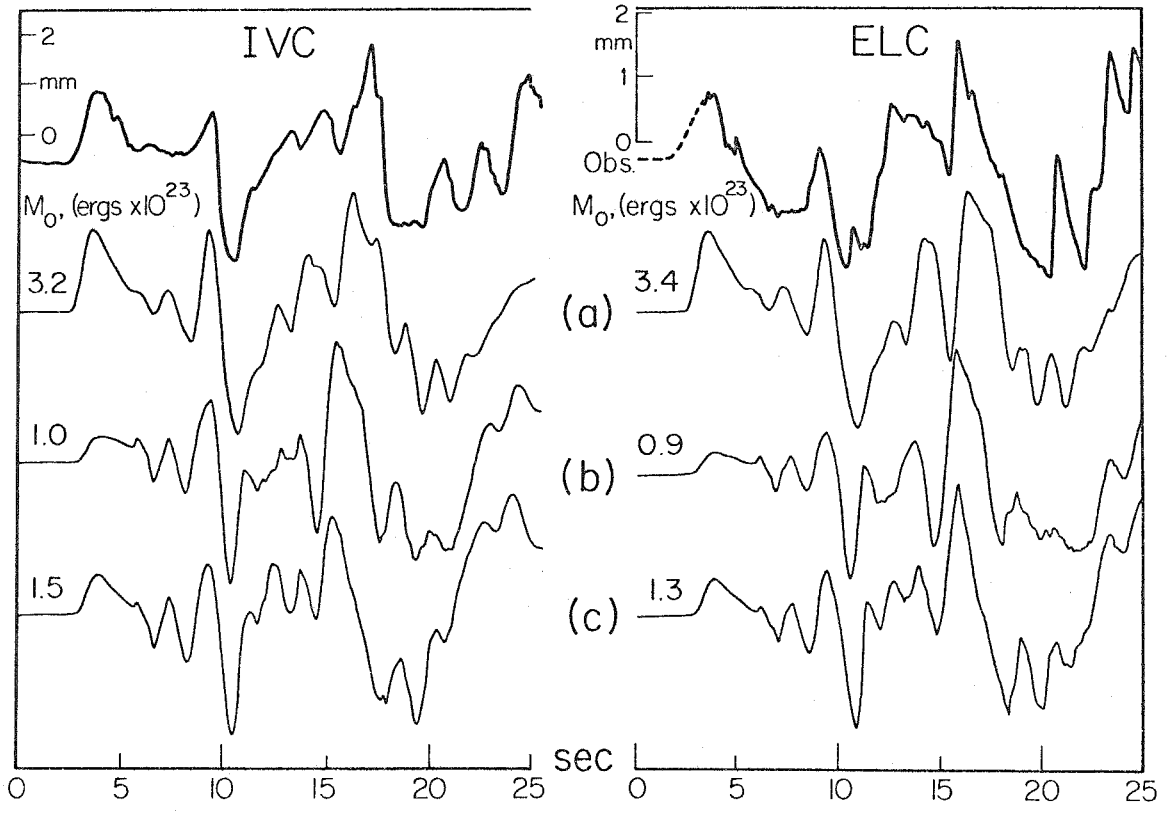

Figure 2.10 Comparisons of IVC and ELC tangential ground motions with synthetics. IVC and ELC are assumed to be at ranges of 33 and 36 km, respectively. A triangular far-field time function with a duration of 1.5 sec is used throughout. (a) Pure strike-slip with source depth of 6.9 km. (b) Pure strike-slip with source depth of 3.9 km. (c) Source depth of 3.9 km and source striking N39°W, dipping 60°SW, and with a rake of 120°.

beginning of the motion at ELC was not recorded, we have dotted in our guess of its shape. A far-field time function consisting of an equilateral triangle with a duration of 1.5 seconds was used in the three models shown. The source depth is 6.9 km in synthetic (a) and 3.9 km in synthetic (b).

Model (a) seems to provide a good fit to both the timing and amplitudes of the major arrivals seen on the actual records. In model (a) we assumed that the source was pure strike-slip on a vertical plane directed towards IVC. Because the U.S. Geological Survey's computed hypocentral depth indicated that the source may have been somewhat shallower, in model (b) we have shown the same source that was used in model (a), but with a depth of 3.9 km. Clearly, model (b) does not fit the observed as well as model (a). The first arrival, a head wave, is too small in amplitude. Furthermore, later arrivals come in too soon with respect to the first arrival. It is possible to improve the shallow source depth synthetic waveforms by changing the fault orientation. A fault plane striking at N39°W, dipping 60° to the SW, with a rake angle of 120°, and a depth of 3.9 km was assumed in model (c). This improves the fit, but the timing of arrivals is still inferior when compared to model (a). Furthermore, model (a) is consistent with the change in amplitude ratios of tangential to radial ground motion seen between IVC and ELC. Model (c) is consistent with neither of these ratios nor with the focal mechanism given in Figure (2.2). For this reason, we prefer model (a) with a focal depth of 6.9 km.

At this point, let's step away from all these modeling details and try to evaluate where we have been. We have approximated the shear

wave velocities of a 6 km thick stack of sediments with three planar layers over a half-space. Our simplified shear wave model is based on compressional wave refraction studies. We argued that, in this case, a M 4.9 earthquake could be approximated by a point source with the appropriate time function. The distances between source and receiver are well-constrained by the U.S. Geological Survey's epicentral solution. Our focal mechanism constrains our dislocation model to be predominately strike-slip on a vertical plane. The source time function and depth are variables which we were able to constrain only through our modeling studies. Although a fairly large suite of models could be constructed by varying the depth and time function, it seems clear that the match between model (a) and the observed ground motion was not a mere coincidence. Apparently, the assumptions which led to model (a) were sufficiently valid to predict the tangential ground motions seen at ELC and IVC. We could even argue that, given the moment, the time function would have been predicted accurately by the moment versus duration plot given by Helmberger and Johnson (1977). Considering this success, we feel that it should be possible to make predictions of the tangential ground motions seen in the Imperial Valley. Because one must a priori know such variables as hypocentral location, fault mechanism, and source time function, there is some question about the practical applications of such predictions. Our simplistic modeling of source and structure necessarily limits such predictions to longer period motions. In order to model large earthquakes, source finiteness would also have to be considered. As we have already seen, the ability to predict the effects

of structure provides valuable insight into the problem of determining source depth and time function.

Now that you are thoroughly tired of hearing our inflated claims of success, we will discuss our failures. We say that we have constructed a model to explain the first 25 seconds of observed motion. What about motions occurring 60 seconds into the record? Here we fail, for our model would predict practically no motion after 35 seconds. Long duration codas are routinely observed on nearly all local earthquake records. Their causes are not well understood. Long period P waveforms recorded at several Canadian stations show a relatively simple pulse for the P wave of this earthquake. Thus, there seems to be no justification for producing this coda by assuming that this earthquake was a complicated multiple event. Perhaps the coda is due to surface waves which are reflected by lateral variations in structure. In Figure 2.3, it can be seen that at IVC, even the coda is tangentially polarized with respect to the epicentral location. This observation is hard to understand if the coda is due to waves which are reflected off the boundaries of the Salton Trough since we would presumably see a Rayleigh wave contribution along with the Love waves.

Synthetic Fourier Spectra

We will now discuss the effects of plane-layered velocity structure upon the Fourier amplitude spectra of ground displacement. In a homogeneous half-space, the far-field SH response to a point step dislocation is simply a delta function whose Fourier amplitude spectrum

is some constant value at all frequencies. If the earth were this simple, then the amplitude spectra of SH ground motion would accurately reflect the amplitude spectra of only the source. As we have already seen, the introduction of layering produces profound changes in the far-field delta function response. It has been commonly assumed that the effects of structure do not change the overall shape of amplitude spectra (for examples, see Johnson and McEvilly, 1974, or Tucker and Brune, 1973). The justification given is that all of the arrivals on a seismogram are caused by the same source and thus each arrival contains the spectral characteristics of the source. Interference between various arrivals should introduce irregularities into the spectra (spectral scalloping), but this interference phenomena should not change the overall shape of the spectra. In order to test the validity of this assumption, we have computed the Fourier amplitude spectra of the SH far-field delta function responses of point sources located in the layered half-space which is described in Table II.1. If the above assumption is correct, then the synthetic spectra should be basically flat. In Figure 2.11, we show synthetic spectra for a point source located at a range of 33 km and at depth 3.9, 6.9 and 10 km. Here we have plotted the function, $||\text{F.T.}\ (\dot{V}_j)||$, where $\dot{V}_j(t)$ is the far-field delta function response used in equation (2.1). Spectra of both strike-slip and dip-slip terms are shown. The corresponding spectra for a homogeneous half-space are given by the straight dotted lines. When the source is in the sedimentary layers, the spectra appear to be relatively flat with complicated scalloping. In the strike-slip case, the layered space produces a long

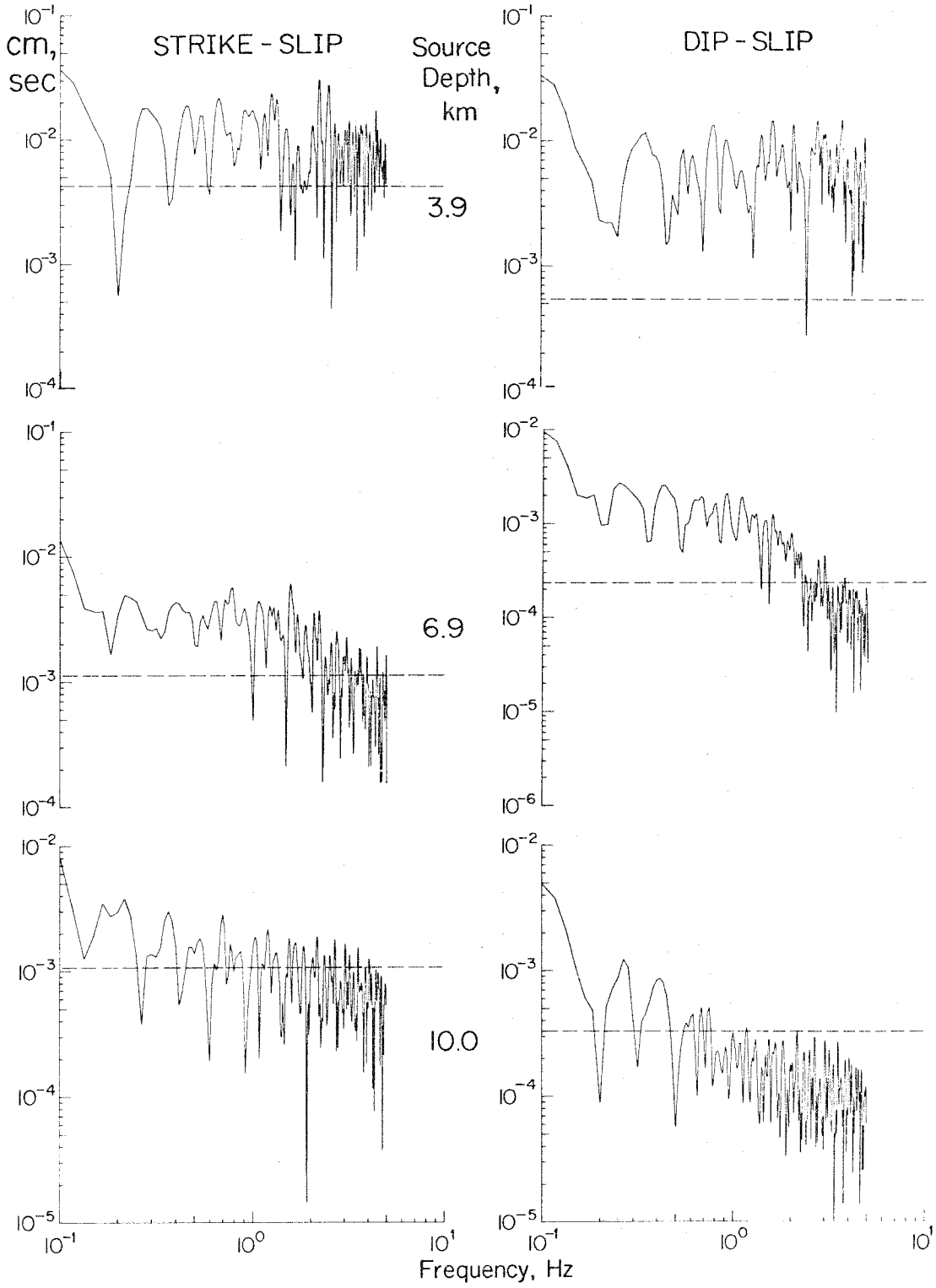

Figure 2.11. Synthetic far-field delta function responses as a function of source depth, where the range is 33 km. Dotted lines indicate corresponding half-space responses.

period level which is 2 or 3 times the level computed for a homogeneous half-space. The sedimentary layers have trapped energy of all frequencies. In the dip-slip case, the layered space produces a long-period level which is an order of magnitude higher than is produced by the homogeneous half-space. This discrepancy is primarily caused by the fact that, in the homogeneous case, the direct SH ray is very near a radiation node. Waves which are reflected within the sediments traverse paths which are much farther from this node. When the source is moved to a depth of 6.9 km (1 km beneath the sediments), the spectra no longer look flat. In fact, it appears that we could pick corner frequencies in these spectra. This is remarkable when one realizes that these are delta function responses! There appears to be an ω^{-1} and ω^{-2} falloff in the high frequencies for the strike-slip and dip-slip cases, respectively. The reason for this behavior is hard to understand from the viewpoint of geometric ray theory. What we see here is actually a diffraction effect. Long-period energy is diffracted into and trapped within the sediment layers, while shorter period energy is reflected off the bottom of the sediments. When the source is moved to a depth of 10 km, we see another dramatic change in the shape of the spectra. Diffraction effects are responsible for the slope seen for longer periods. For this depth, geometric ray theory is probably adequate to explain very short-period waveforms. This is consistent with the fact that the spectra become relatively flat for short periods. Our interpretations are further complicated by the effects of radiation pattern.

We have seen that, at a constant epicentral range, the effects of depth are dramatic. In Figure 2.12, we show spectra for sources at

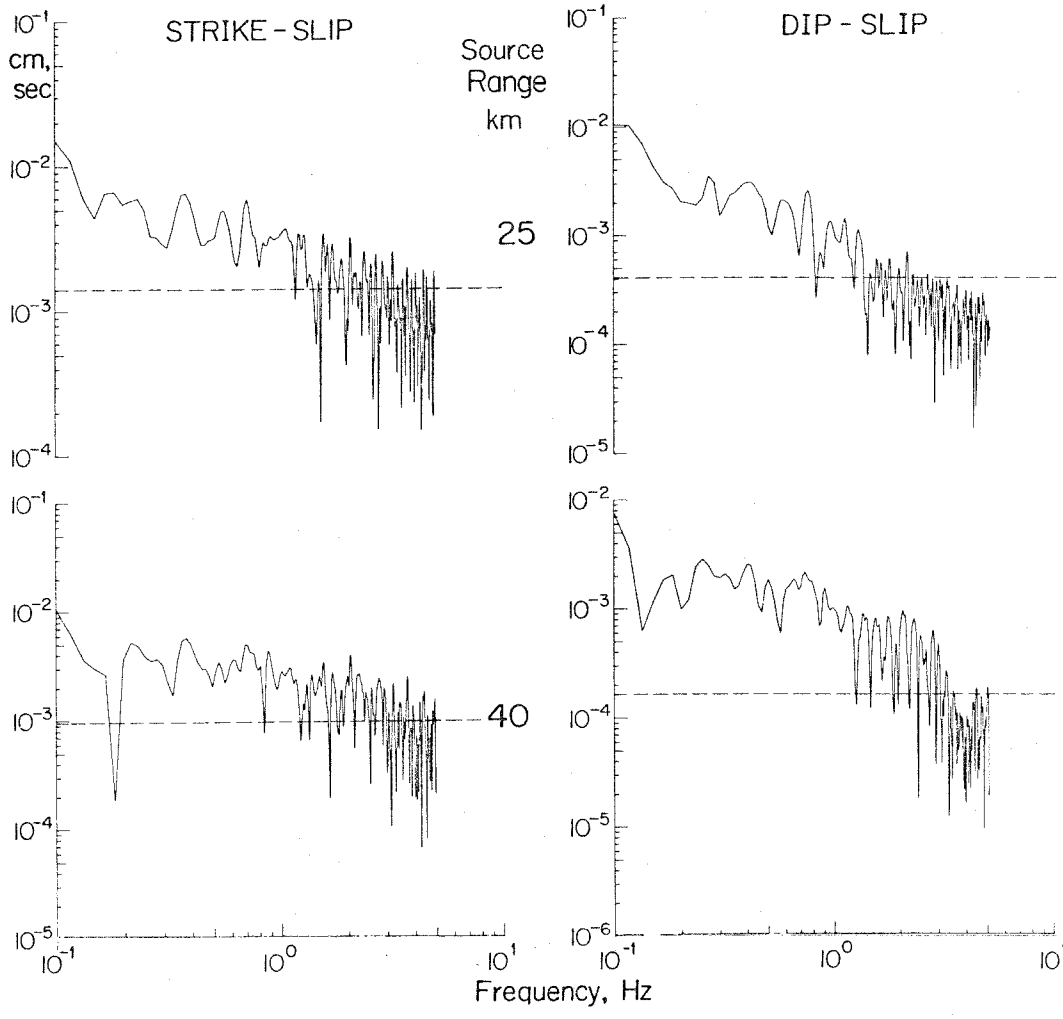

Figure 2.12. Synthetic far-field delta function responses as a function of range. Source depth is 6.9 km. Dotted lines indicate corresponding half-space responses.

a constant depth of 6.9 km and at ranges of 25 km to 40 km. Apparently range also has a large effect upon the overall spectral shape. Clearly this has implications for seismic wave attenuation studies as well as seismic source studies. Remember, there is no anelasticity built into our synthetic models.

In the case of SH waves, we have seen that the introduction of layering can do far more than simply add scalloping to a spectrum. The exact effect is a complicated function of the source location and focal mechanism. Although we have only demonstrated this to be true for whole-record spectra, the spectra of individual arrivals should also be affected by diffraction phenomena. Even if the direct S wave could be isolated, there is no guarantee that the waveform has not been altered by diffraction effects. This can be seen by noticing that the step function responses of the direct S waves do not consist of a simple step. Furthermore, if one desires to understand the high-frequency characteristics of the source, then one must understand the high-frequency effects of wave propagation. This means that one must know the details of the velocity structure along with a good estimate of source location. Because the effects of wave propagation are so complicated, we prefer to do our modeling in the time domain. Although ambiguities are still present when trying to sort out the relative effects of source and structure, there is some hope of understanding the effects of wave propagation when modeling in the time domain. We anticipate that the phenomena which we have observed for SH waves should also be seen for P and SV waves. Because of the existence of mode conversions and Rayleigh waves, the

effects of wave propagation will be even more complicated for radial and vertical motions.

Conclusions

The sedimentary structure which lies between the M 4.9 November 4, 1976 earthquake and the stations, IVC and ELC, is relatively flat. A simplified model of shear wave velocities was derived from the compressional wave refraction studies of Biehler et al. (1964). The epicentral solution and focal mechanism were determined by P wave first arrival studies. Using these constraints, we determined a hypocentral depth of about 7 km by modeling the tangentially polarized ground motions observed at IVC and ELC. An infinitesimal dislocation source with a triangular time function was sufficient to model the first 25 seconds of observed ground motion. We determined the moment to be approximately 3×10^{23} ergs and the far-field time function had a duration of about 1.5 seconds. Because of our success in modeling these records, we feel that propagational effects on longer period tangential ground motions are predictable in the Imperial Valley. We also found that our layered half-space model was unable to explain the long duration codas seen at IVC and ELC.

By studying the Fourier amplitude spectra of the far-field delta function responses computed for our layered half-space model, we demonstrated that wave propagation effects should be included in studies of source spectra. Diffraction phenomena can produce corners which have nothing to do with source spectral characteristics. The effects of structure must also be included when making estimates of the moment from

the long-period level of amplitude spectra. Finally, the effects of diffraction should be considered in studies of seismic wave attenuation.

Chapter 3

A Study of the Strong Ground Motion of the Borrego Mountain, California, Earthquake of April 9, 1968

Introduction

The Borrego Mountain strong-motion records provide an opportunity to study a larger earthquake which occurred in a similar setting as the Brawley earthquake which was discussed in the last chapter. Furthermore, Burdick and Mellman (1976) studied the teleseismic body waveforms for this earthquake. Thus we are able to study the compatibility of teleseismic and local modeling results.

In many situations the seismic waves recorded in the local field travel more nearly horizontal paths than waves which are recorded at teleseismic distances. This allows us to sample waves from earthquakes which leave the source area in directions which are inaccessible to researchers studying the waveforms of teleseismic records. Unfortunately, the fact that energy in the local field travels nearly horizontal paths implies that reflections from horizontal crustal layers are both large and complicated. In the local field, a clear distinction between body waves and surface waves is not possible. Thus, in many respects, interpreting the relative effects of source and earth structure is a more tractable problem for teleseismic modeling than for local field modeling. Yet, as we will show, it is possible to model local observations of moderate size earthquakes with realistic source and crustal structure models. Obviously, it is important to construct earthquake source models

which are compatible with both local and teleseismic waveforms. This test of compatibility is especially important with respect to the assumed Q structure of the earth which must be used when correcting teleseismic observations. Thus, the inclusion of local observations into the data set in earthquake studies is becoming increasingly important.

In most previous waveform modeling of strong ground motion, researchers have circumvented the complications of horizontal layering by considering only records which are taken very close to the causative fault. Most studies of this nature approximate the earth response by the response of a homogeneous whole-space with an amplitude correction of two in order to approximate the free surface. Since only direct waves can be generated by such a model, simple source models will result in relatively simple pulse-like waveforms. Unfortunately, strong ground motion records displaying simple pulse-like waveforms are relatively rare. Some of the better examples are: 1) the Pacoima Dam recording of the 1971 San Fernando earthquake which has been modeled by Trifunac (1974) and which we model in Chapter 4; 2) the Cholame No. 2 recording of the 1966 Parkfield earthquake modeled by Aki (1968), Trifunac and Udwadia (1974), Kawasaki (1975), and Anderson (1974). Anderson and Richards (1975) have reviewed several of the different source models which have been used in modeling such records and they give some insight into the ambiguities which are present in modeling ground motion very close to an earthquake. They demonstrate that a variety of source models with quite different rupture motions, rupture geometries, rupture velocities, and rise times can produce very similar near-field motions in a

homogeneous whole-space. Things change considerably when horizontal layering is introduced into the problem. If the structure is not known, even greater ambiguity in source modeling exists due to the introduction of more variables. Things may not be as hopeless as they first appear though, since if the structure is known its effects can be used to advantage. That is, the response of a layered medium is unlike that of a homogeneous medium in that the response of the layered medium is a sensitive function of the position of the source within the layers. Thus if the structure is known, the complications due to that structure can help clear up ambiguities concerning the source. Consider the dilemma presented by any single displacement record taken in a homogeneous whole-space. It is practically impossible to distinguish a source composed of several point dislocations from another source which consists of only one point dislocation. This ambiguity is not as severe in a layered space since each of the several point sources will interact with the structure in a predictable fashion. A case will be made that the El Centro record of the Borrego Mountain earthquake cannot be adequately modeled with just one point dislocation. This distinction could not be made for homogeneous whole-space models.

The Borrego Mountain Earthquake

The Borrego Mountain earthquake occurred at 2:29 GMT on April 9, 1968 and has been assigned a magnitude of 6.4 (Allen and Nordquist, 1972). A surface rupture which extended nearly 31 km was recognized along three well-defined zones of fracture (north, central and south segments) which

comprise the Coyote Creek fault which is itself a segment of the San Jacinto fault zone of southern California. A maximum right-lateral offset of 38 cm was measured along the north segment and right-lateral offsets of 25-30 cm and 8-14 cm were measured on the central and south segments, respectively (Clark, 1972). The central and south segments are distinguished from the north segment in that approximately half the displacements measured were recognized to be due to post-earthquake creep (Burford, 1972). Surface ruptures of 1 to 2-1/2 cm were also reported by Allen et al. (1972) for segments of the Superstition Hills, Imperial and San Andreas faults. These displacements are presumed to be due to fault creep which was triggered by the Borrego Mountain earthquake. Figure 3.1 shows the spatial relationship of these various faults. Rupture appears to have initiated on the north segment. Aftershocks define a diffuse zone which is about 50 km in length (Allen and Nordquist, 1972). No conspicuous increase in seismicity could be found for the Superstition Hills, Imperial and San Andreas faults.

Faulting on the north segment of the Coyote Creek fault displays several features which clearly distinguish it from other fault segments which had rupture associated with the earthquake. Both the initiation of rupturing and the largest offsets occurred on the north segment. As compared with the central and south segments, the north segment had fewer aftershocks and very little post-seismic creep. Burdick and Mellman (1976) argue persuasively that these variations in the behavior of the fault segments reflect different behaviors deep in the earth. Their modeling of teleseismic waveforms seems to require a short duration

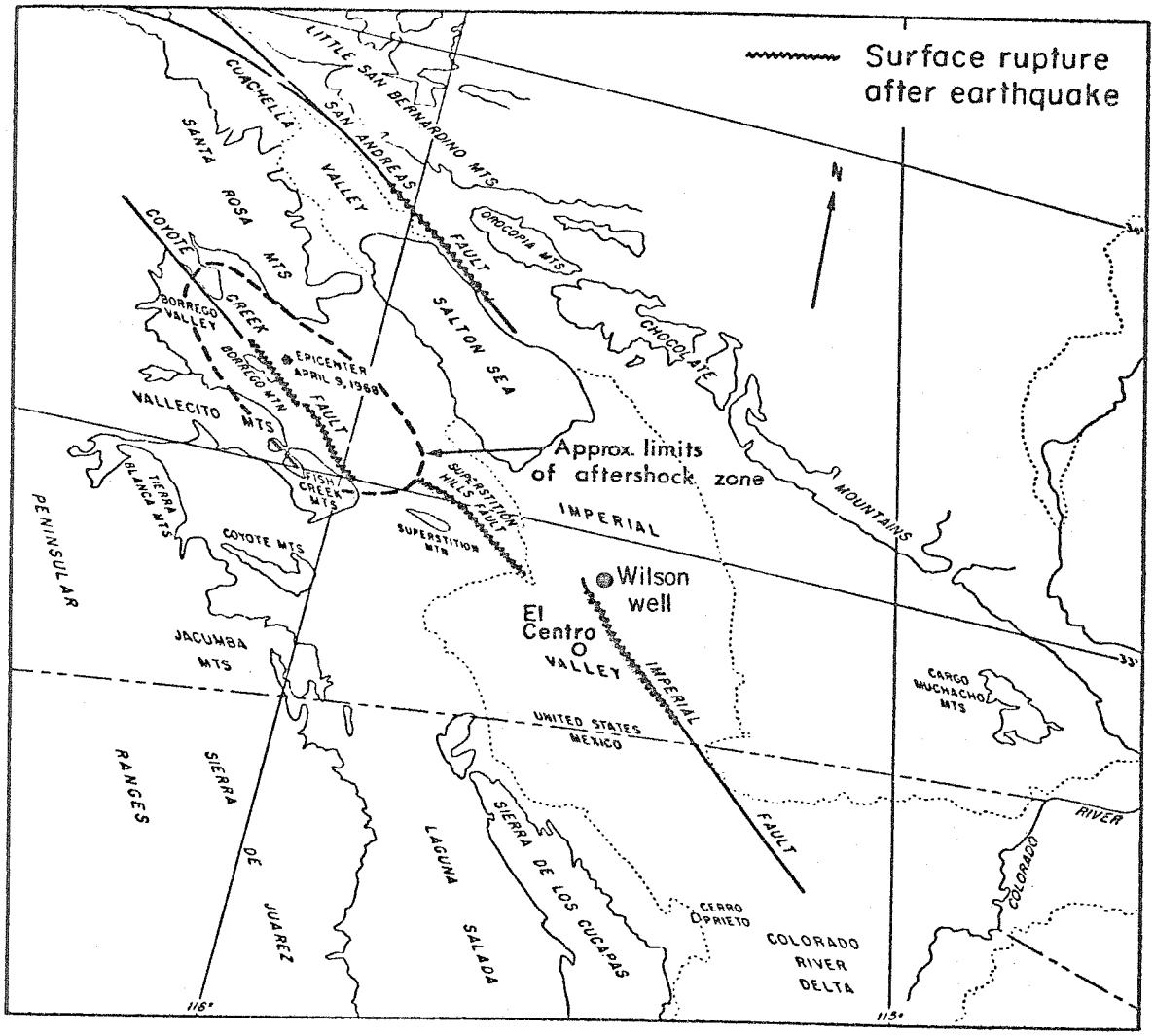

Figure 3.1. Oblique map of the Salton Trough. Lines within shaded areas indicate segments of faults that moved in association with the 1968 Borrego Mountain earthquake. The distance between meridians shown is 93.5 km along the 33°N parallel (figure modified from U.S. Geol. Survey Prof. Paper 787).

source time function and hence a small source dimension. They suggest a circular fault of radius 8 km. If indeed such a small source area is required, then clearly the north segment is the likely candidate.

The El Centro Strong Ground Motion Record

The Borrego Mountain earthquake triggered 114 strong-motion seismographs in southern California and southeastern Nevada (U.S. Coast and Geodetic Survey et al., 1968). Most of the instruments were located in the Los Angeles area which is approximately 200 km from the epicentral region. The closest strong-motion stations were located in El Centro, San Diego and Perris Dam which are at epicentral distances of 60 km, 100 km and 120 km, respectively. We chose to model only the El Centro recording because it was the closest station and was the only station located in the same geologic province (the Salton Trough) as the earthquake. Moreover, Carder displacement meters were located at El Centro, providing reliable information at periods beyond 8 seconds.

Figure 3.2 shows both displacement records as well as accelerograph records from El Centro. The accelerograph records have been integrated to obtain both ground velocity and displacement (Hudson et al., 1971). Figure 3.3 shows that the ground motion obtained by double integration compares favorably with the ground motion obtained by deconvolution of the instrument's response from the Carder displacement meter records. The Carder instruments have free periods of 6.4 seconds on the E-W component and 6.8 seconds on the N-S component. The deconvolved Carder records have been heavily filtered at periods beyond 14 seconds with an Ormsby-type

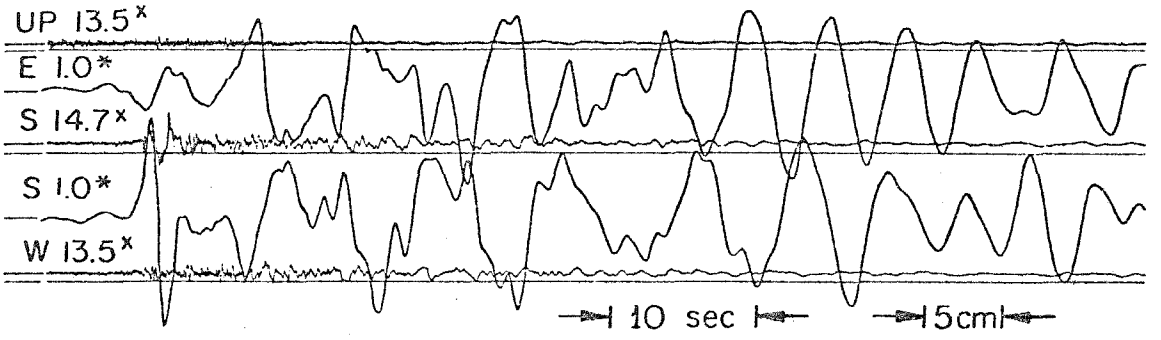

(x) Sensitivity in cm/g; (*) Static magnification.

Figure 3.2. El Centro accelerograph and Carder displacement meter record from the Borrego Mountain earthquake (U.S. Coast and Geodetic Survey, et al., 1968).

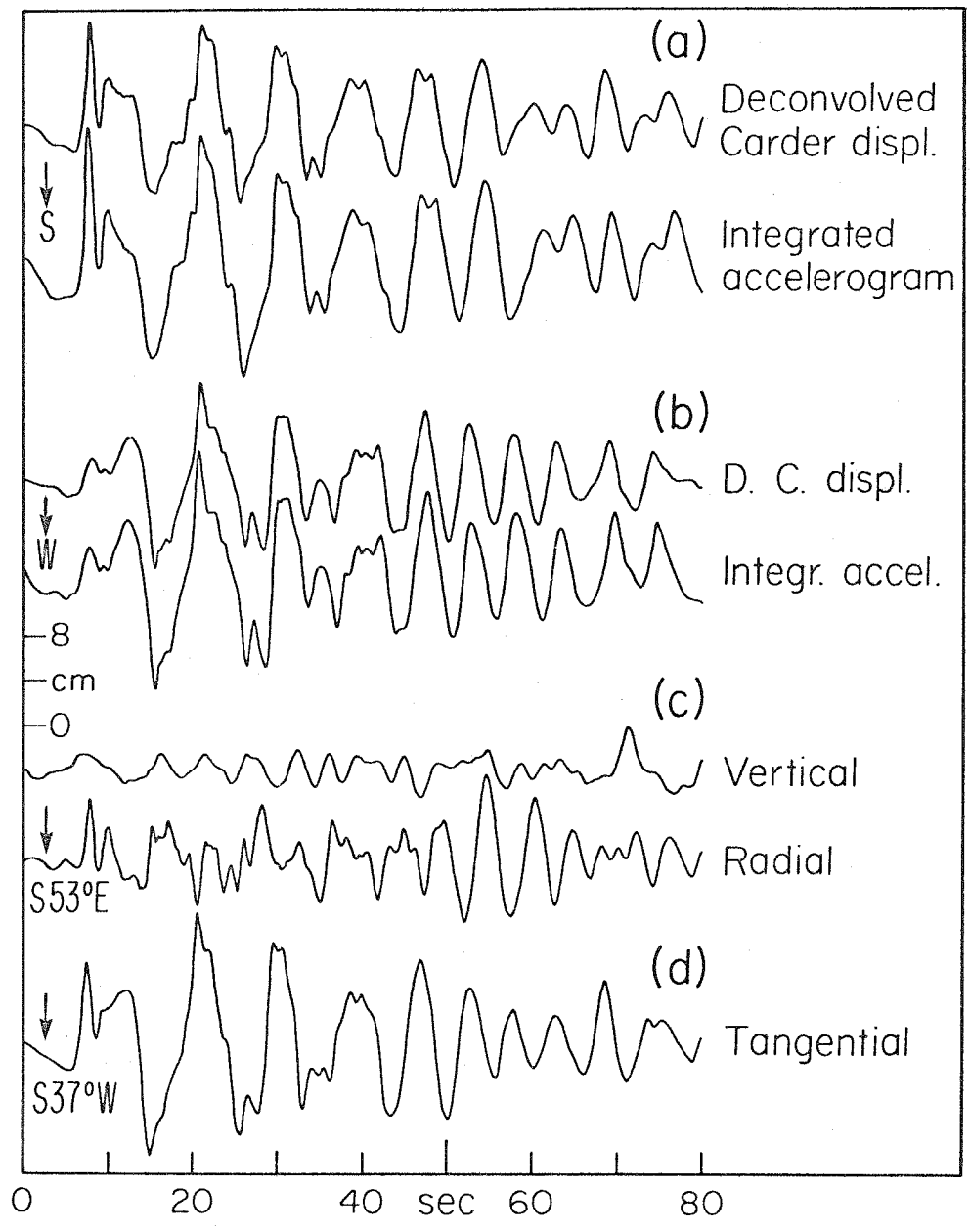

Figure 3.3. Summary of observed ground motion. (a) Comparison of deconvolved Carder displacement meter record and integrated accelerogram for N-S component. (b) Comparison of deconvolved Carder displacement meter record and integrated accelerogram for E-W component. (c) Ground motion rotated into vertical, radial and tangential components.

filter to avoid the inherent instability present in the deconvolution process. We believe that the deconvolved Carder record gives a very reliable representation of the ground motion at El Centro. The agreement between the integrated accelerogram and the deconvolved Carder record is remarkable when one realizes that the free periods of the accelerographs are about 0.067 seconds. However, there does appear to be significant disagreement in the absolute amplitude scales. This discrepancy raises questions about the reliability of the gains reported for these instruments.

El Centro is only 8° from being directly along the strike of the earthquake fault plane. Since the earthquake was strike-slip along a vertical fault, we expect to be very close to an SH radiation maximum and SV and P radiation nodes. The tangentially-polarized, radially-polarized and vertical components of ground motion are also shown in Figure 3.3. The vertical component is a doubly-integrated accelerogram (Hudson et al., 1971). The horizontal components were rotated such that the azimuth of the tangential and radial axes were S 37° W and S 53° E, respectively. The first 40 seconds of displacement are dominated by transversely-polarized motion as indicated in Figure 3.3c. Considerable radially-polarized motion is present in the next 40 seconds of ground motion. One possibility is that this departure from transverse polarization is due to lateral reflections of surface waves in the Salton Trough.

Crustal Structure in the Salton Trough

The Borrego Mountain earthquake occurred along the western side of the Salton Trough whereas El Centro lies close to the axis of the

depression. The work of Biehler (1964) and Hamilton (1970) indicates that considerable variation in upper-crustal velocity structure exists along the path from Borrego to El Centro. A summary of the crustal structure found by Hamilton (1970) for the Borrego vicinity is given in Table III.1. Also in Table III.1 is the upper-most crustal structure reported by Biehler (1964) for his closest refraction line to El Centro. Clearly, the thick layer of sediments underlying El Centro is not present in the epicentral region. In fact, basement rocks are exposed in the Superstition Hills which lie 20 km from El Centro and along the line between the epicenter and El Centro. Fortunately, the basin structure near El Centro consists of relatively flat, laterally homogeneous sediments. Experience has shown us that the major effect of sediments is to allow post critical angle multiple reflections to occur in the section. Furthermore, for a source beneath the sediments, reflection points for these multiple reflections occur near the receiver. Since our modeling technique is limited to plane layers, it is important that our structure model give a fair representation of the receiver sediment structure rather than the sediment structure at the source. For our purposes, we found that it was sufficient to model the sedimentary stack with only one low-velocity surface layer. Although modeling the complicated upper-crustal structure from Borrego to El Centro with a simple plane layer over a half-space does not seem entirely satisfying, it should be realized that this model retains the essential characteristic in that it traps SH waves in the upper layer. We believe that the Imperial Valley sediments also trap SH waves and that their response is approximated by that of a layer

Table III.1

Crustal Structure in the Epicentral Region

as Reported by Hamilton (1970)

Layer	Compressional Wave Velocity (km/sec)	Depth to Top (km)
1	2.5	0.0
2	5.1	0.4
3	6.0	2.9
4	7.1	14.0
5	7.9?	25.0?

Upper Crustal Structure as Reported by Biehler (1964)

for the Wilson et al. Well. Shown in Figure 1

Layer	Compressional Wave Velocity (km/sec)	Depth to Top (km)
1	1.9	0.0
2	2.1	0.4
3	2.6	1.0
4	3.7	2.0
5	4.7	3.4
6	6.4	6.0

over a half-space. This approximation probably becomes progressively worse for shorter-period waves. Finally, it should be pointed out that we chose the layer velocity and thickness such that they fit the observed Love waves. Even though this layer thickness and velocity was not determined directly from the refraction profiles such as Biehler's (1964), we feel that our model is compatible with the inferred depth of sediments in the Imperial Valley.

Our study of the Brawley earthquake further justifies our single-layer sediment model. Although the intermediate layers were important for short-period details, the most important interface was the sediment to basement contrast. Furthermore, Swanger and Boore (1978) subsequently repeated much of this study using surface wave mode techniques and a more complex sedimentary structure which was based upon Biehler's (1964) models. They concluded that the single-layered model adequately represented the response of the more complex structure at the periods which dominate the displacement records.

Because of the possibility of head waves and the reflection of downgoing rays, intermediate and deep crustal structure can have a significant effect on the beginning portion of the strong ground motion record. Hamilton (1970) has suggested that compressional wave velocities as high as 7.1 km/sec exist as shallow as 14 km and that the Moho may be only 25 km deep in this region. As will be seen later, it is not necessary to include intermediate and lower crustal structure in order to model the El Centro strong-motion record. Thus we will mainly concern ouselves with a structure model which consists of a simple layer over a half-space.

However, due to the possibility of relatively shallow high velocity layers, a structural model which includes these layers will also be considered.

The Modeling Technique

Our modeling technique is virtually identical to that which we used in the last chapter. Generalized ray theory, in conjuction with the Cagniard-de Hoop technique, is used to compute the response of a point shear dislocation. Once again, only the far-field SH waves are included and the first order asymptotic approximation of the Bessel function is used. Because of the simplicity of the structure, fewer than 20 generalized rays are necessary to approximate the response of a 3 km layer over a half-space at a range of 60 km.

Since the Borrego Mountain earthquake has much larger source dimensions than the Brawley event did, there are serious questions about the adequacy of a single point source model. In this chapter, we will approach the problem of the source from two directions. We will begin by attempting to find simple models which contain only one or two point sources. We will attempt to find the far-field time functions which will explain the observed motion. This is equivalent to finding the function, $F(t)$, which was given in equation (2.7). The actual faulting history need not be specified when modeling in this manner. The second approach is to specify fault displacements explicitly. By integrating point source responses over the entire fault plane, we directly calculate the finite fault response. Essentially we calculate $F(t)$ in a forward manner, instead of exploring what form $F(t)$ may have in order to fit the records.

Modeling with a Single Point Source

The first models which we will consider will be those consisting of a single point source. These models allow us to investigate the effect of structure in a fairly direct way. Figure 3.4 illustrates the step function response of a point source located at various depths within a layer over a half-space model. The upper layer's thickness and velocity have been defined such that they fit the long-period Love waves as recorded at El Centro. Theoretical ground motions are obtained by convolving the derivative of the step-function response with the far-field time function of the source. The particle motion of the point dislocation is the integral of the far-field time function. For shallower source depths, the direct wave is diffracted by the shallow layer and becomes less distinct and at the same time, Love waves are strongly developed. When the source is placed in the upper layer, the first arrivals are head waves with later arrivals being high-frequency critical reflections which are trapped in the upper layer. We see no evidence of these high-frequency critical reflections in the El Centro record and thus our sources will always be located beneath the surface layer. This conclusion is supported by the fact that the sediments directly above the earthquake are thin and also by the hypocentral depth of 8 km computed by Burdick and Mellman (1976).

Model B42, shown in Figure 3.5, is the ground motion which one expects for a point source with a simple triangular far-field time function which is located at a depth of 6 km in the layer over a half-space model. It does a fair job of fitting the Love waves, but does

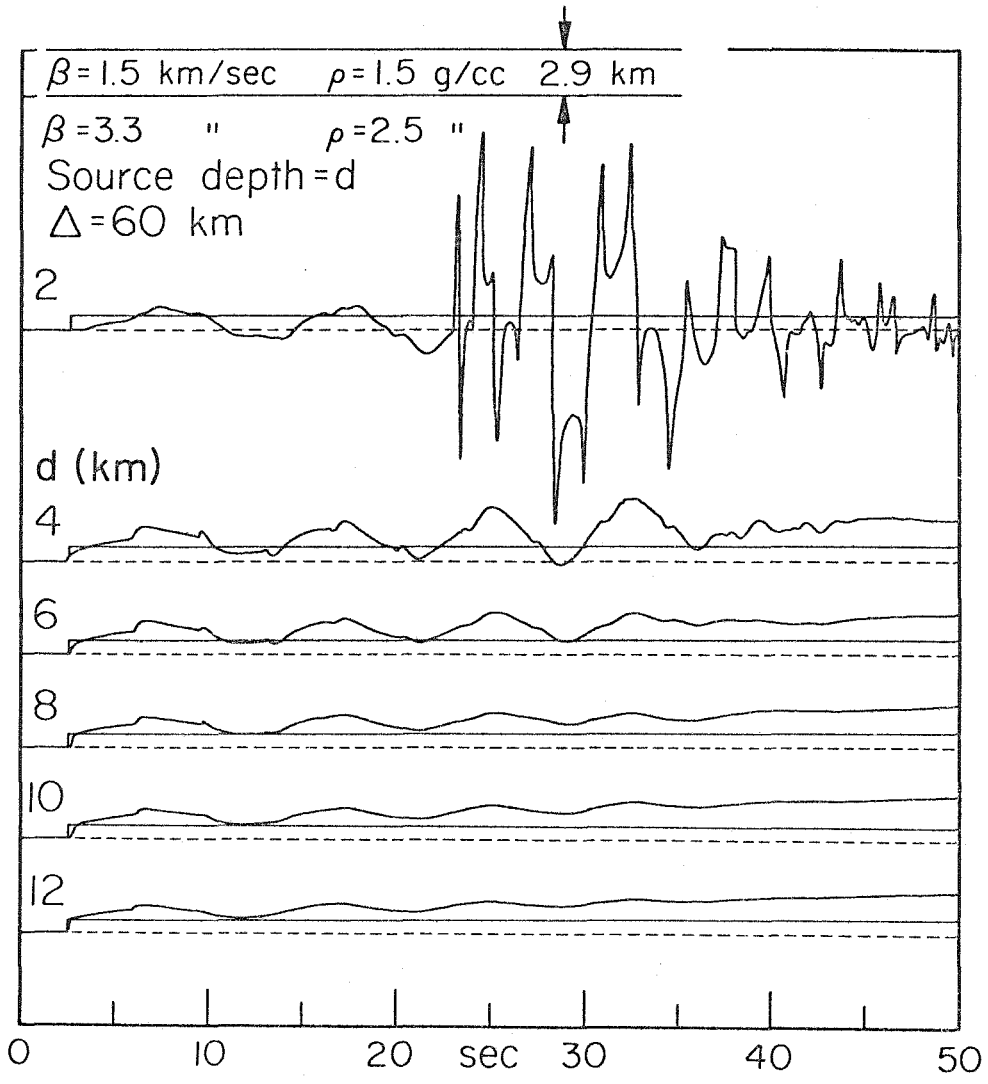

Figure 3.4. SH step function response at the surface assuming a point strike-slip dislocation located at various depths. The amplitudes are scaled in relation to the top trace with the step response for a homogeneous half-space displayed for comparison.

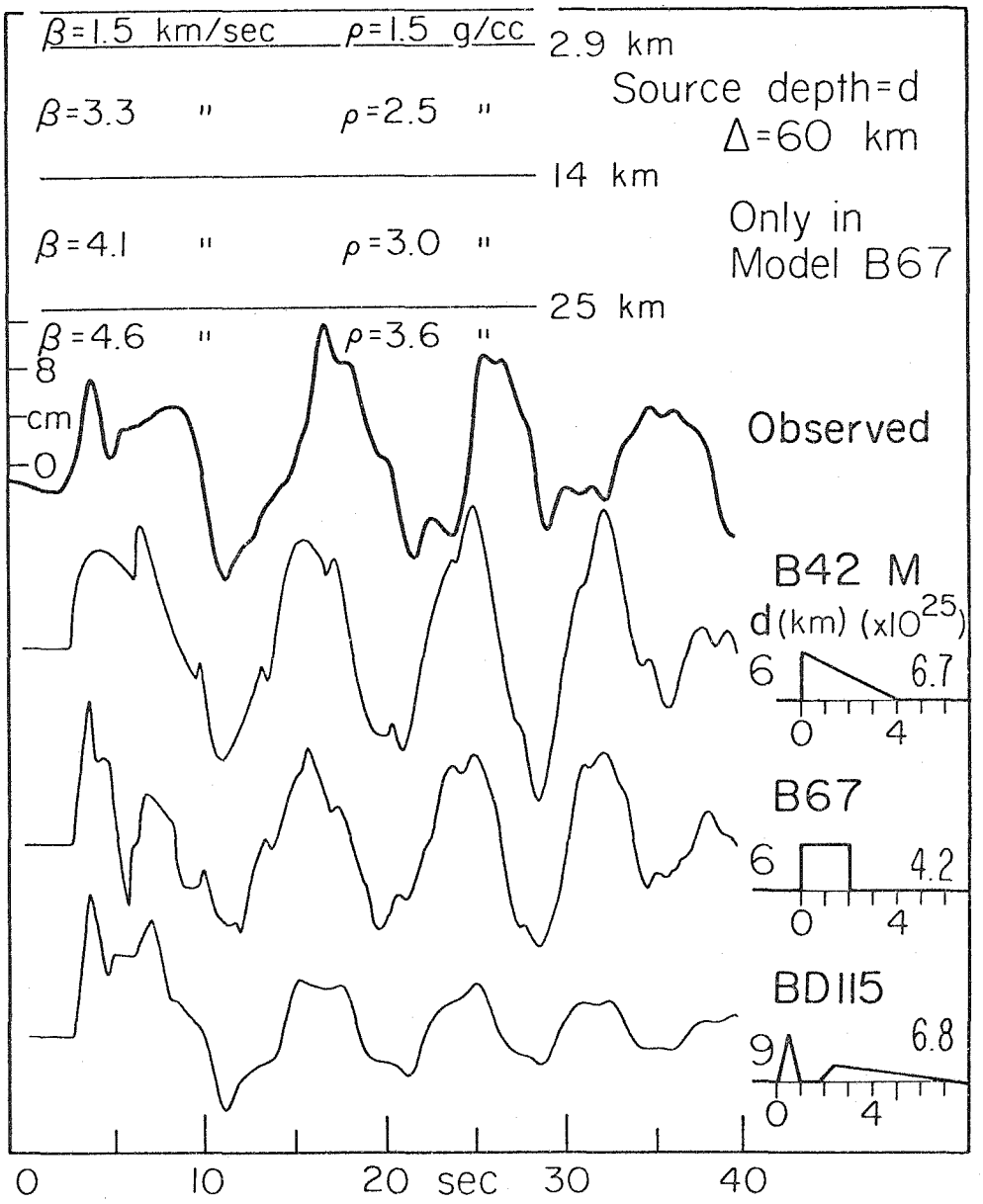

Figure 3.5. Comparison of observed with synthetic SH ground motion for models consisting of a single point dislocation source. Far-field source time functions are displayed on the right. Deep crustal layers were included in model B67 whereas a simple layer over a half-space was used for models B42 and BD115.

poorly for the first large SH pulse which is present on the record. We next investigated the possibility that the first SH pulse was actually due to a diving ray. By adding high-velocity lower-crustal layers it is possible to obtain near-critical angle reflections which introduce sharp pulses to the beginning of the synthetic and which have virtually no effect on the Love wave portion of the synthetic record. Model B67, which is shown in Figure 3.5, is the result of an attempt to model the first SH pulse with a diving ray. It matches the first pulse well, but does poorly on the broad second pulse. High shear wave velocities seem to be required at depths less than 20 km by such models. Even though Hamilton's work (1970) suggests a Moho at 25 km, the velocity model for B67 seems somewhat extreme. Although we are not entirely comfortable with the high velocities of model B67 and even though other models will be presented which fit the record better, we believe that a diving ray could well be an important contributor to the sharp pulse at the record's beginning. The advantage of model B67 is that a very simple point source time function is all that is necessary to produce both sharp body waves and a well-developed Love wave. All other models which will be presented in this study will consist of a simple layer over a half-space model, but will require more complex sources to fit both body waves and Love waves.

Model BD115, which is shown in Figure 3.5, is an example of a layer over a half-space with a point source which has a complicated time function. Since the source is relatively deep at 9 km, the direct shear wave is sharp and thus it was possible to model the first 10 seconds well.

Because of the depth, though, the Love wave is too small. This motivated us to investigate models with both a deep source and a shallow source.

Modeling with Two Point Sources

In the previous section we discussed the notion of fitting the Love waves with a fairly shallow source and then we invoked reflections from deeper layers to explain the sharp first arrivals. An alternative approach is to have a shallow source which produces mainly Love waves and a deep source which produces sharp body waves. We chose to model the record with a source at 9 km and another source at 4 km. Furthermore, we allowed these sources to have different time histories. Because of the large number of variables which are introduced into this model, it is not surprising that the record could be fit quite well. Figure 3.6 illustrates four of the models which gave good fits. These models vary in detail, but a common feature is a sharp time function for the deep source and a slower time function for the shallow source. The total moments for all these models seems to be approximately 7×10^{25} dyne-cm.

It seems fairly important to ask whether or not the models shown in Figure 3.6 are consistent with the teleseismic observations of the Borrego Mountain earthquake. Burdick and Mellman's (1976) inversion of teleseismic body waves for source parameters yielded a moment of 1.12×10^{26} dyne-cm which is somewhat larger than that of our two-source models. Our computed moment would be on the order of 10^{26} dyne-cm if the intergrated accelerograms were used in place of the Carder records. This is due to the previously mentioned discrepancy in amplitude found

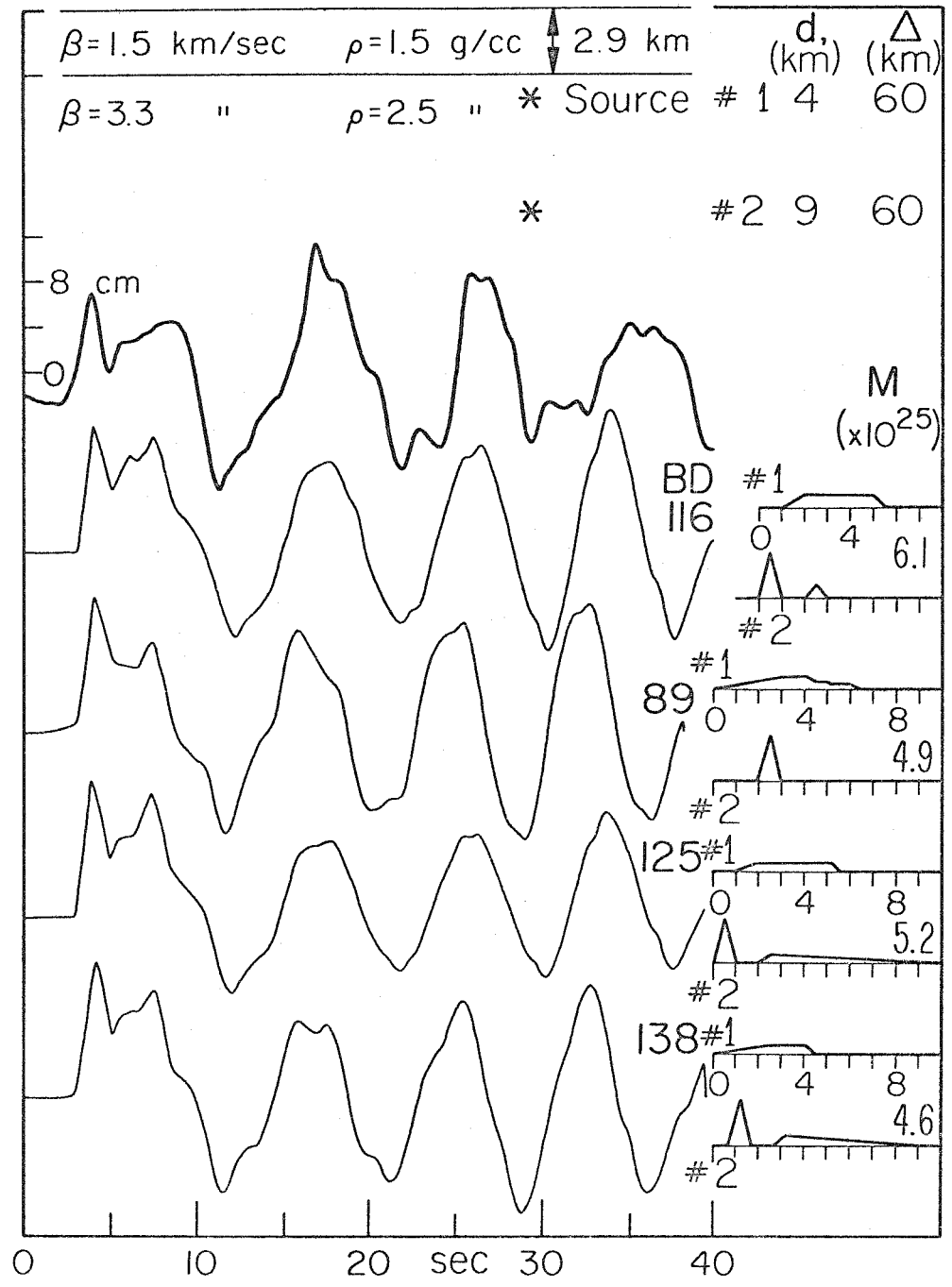

Figure 3.6. Comparison of observed with synthetic SH ground motion for models consisting of two point dislocation sources embedded in a half-space overlain by a single layer. Both shallow and deep far-field source time functions are displayed on the right.

between integrated accelerogram and displacement meter records. It should also be noted that Hanks, Hileman and Thatcher (1975) reported a moment of 6×10^{25} dyne-cm for the Borrego Mountain earthquake based on a combination of body wave spectra isoseismal maps, and extent of surface faulting.

Burdick and Mellman were also able to isolate the phase sP and then simultaneously deconvolve short- and long-period recordings of sP. From this procedure they obtained a detailed source time function appropriate for the phase sP. Figure 3.7 shows the sP time functions that would be predicted by our two-source models. Model BD116 agrees very well with the observed teleseismic sP time function. Model BD116 is thus very appealing in that it fits the El Centro strong SH ground motion and it is also consistent with the teleseismic observations. Unfortunately, it is rather obvious that the Borrego Mountain earthquake was not two point dislocations. How are we to relate model BD116 to the slip which occurred along the Coyote Creek fault? We will delay a closer examination of this question until the discussion section of this chapter.

Modeling with Finite Sources

In the previous section we have shown that it is possible to construct a relatively simple model which is consistent with the teleseismic recording and also the El Centro strong ground motion. Our main concern was to fit the seismic data and we gave relatively little consideration to our intuition that these seismic waves were due to an

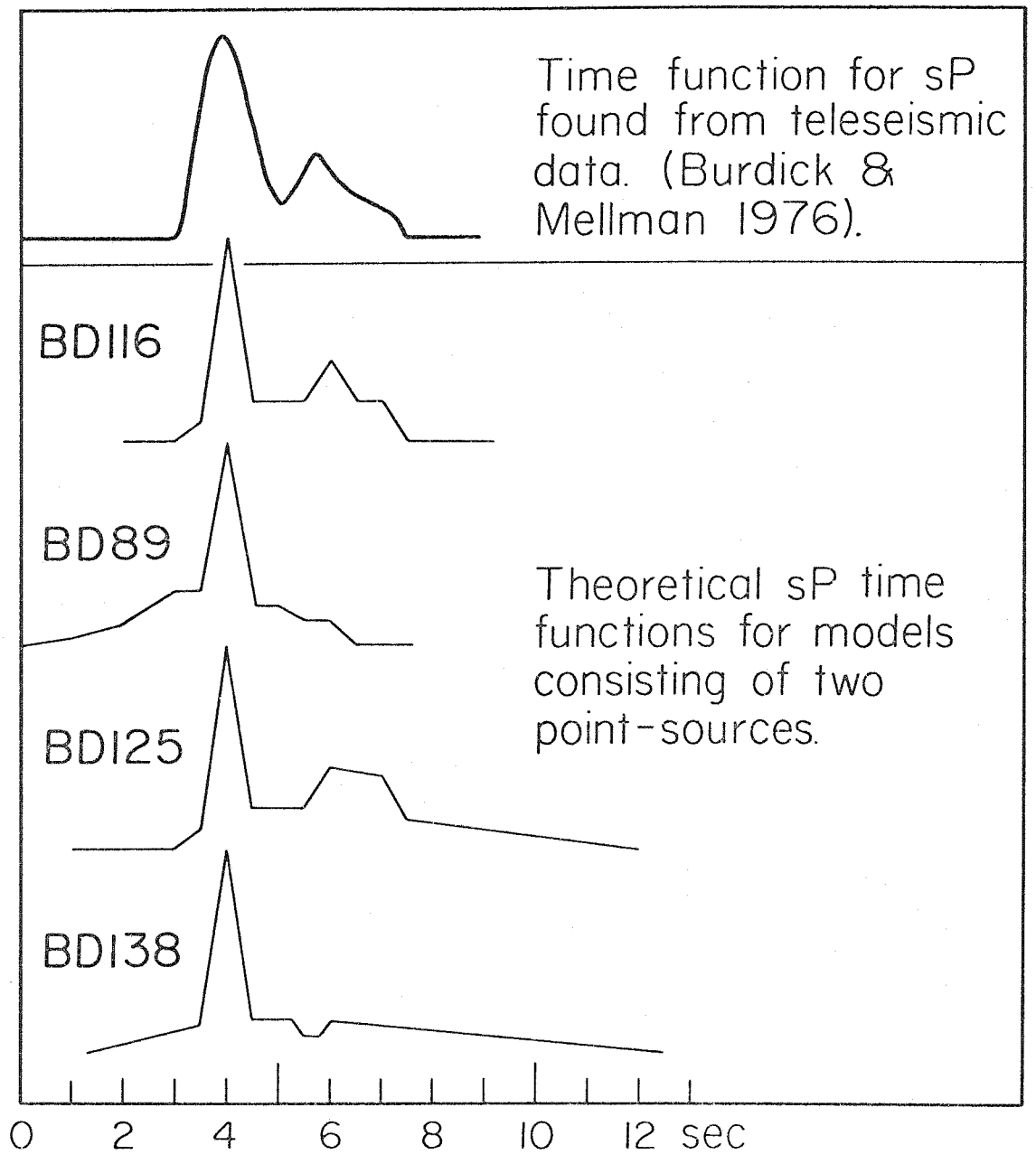

Figure 3.7. Comparison of teleseismic sP time function reported by Burdick and Mellman (1976) with sP time functions computed for our models consisting of two point sources.

offset along a two-dimensional surface which we call the Coyote Creek fault. Let us try a different approach in which we build several simple models of what we, a priori, think the earthquake should look like. We chose to model the earthquake as a radially-propagating, uniform dislocation which is confined to a vertical rectangular surface. Because of the success we had with the point-source models, we retained the layer over a half-space structure which was used in those models. Since we have no analytical expression for the point-source response of this structure model, it was not possible to analytically integrate the infinitesimal point-source response over the fault plane. Instead, each square kilometer of fault surface was approximated by a point dislocation source. Figure 3.8 shows that the step-function response is a slowly-varying function of range. Generalized ray theory was therefore used to compute only the response functions of sources which were spaced at intervals of 5 km horizontally and 2 km vertically. The remaining response functions were computed by simply interpolating between the response functions found by generalized rays. Response functions were then added with an appropriate time delay which was a function of only the rupture velocity and fault geometry. This sum of response functions was then convolved with a source time function which is the time derivative of the particle motion on the fault plane. Particle motion was assumed to be uniform everywhere on the fault plane. Displacements in a homogeneous whole-space have been analytically determined by Savage (1966) for similar types of fault models.

In Figure 3.9, synthetics are shown for an 11 km by 5 km rectangular fault with different hypocentral locations and rupture velocities. BNOR1

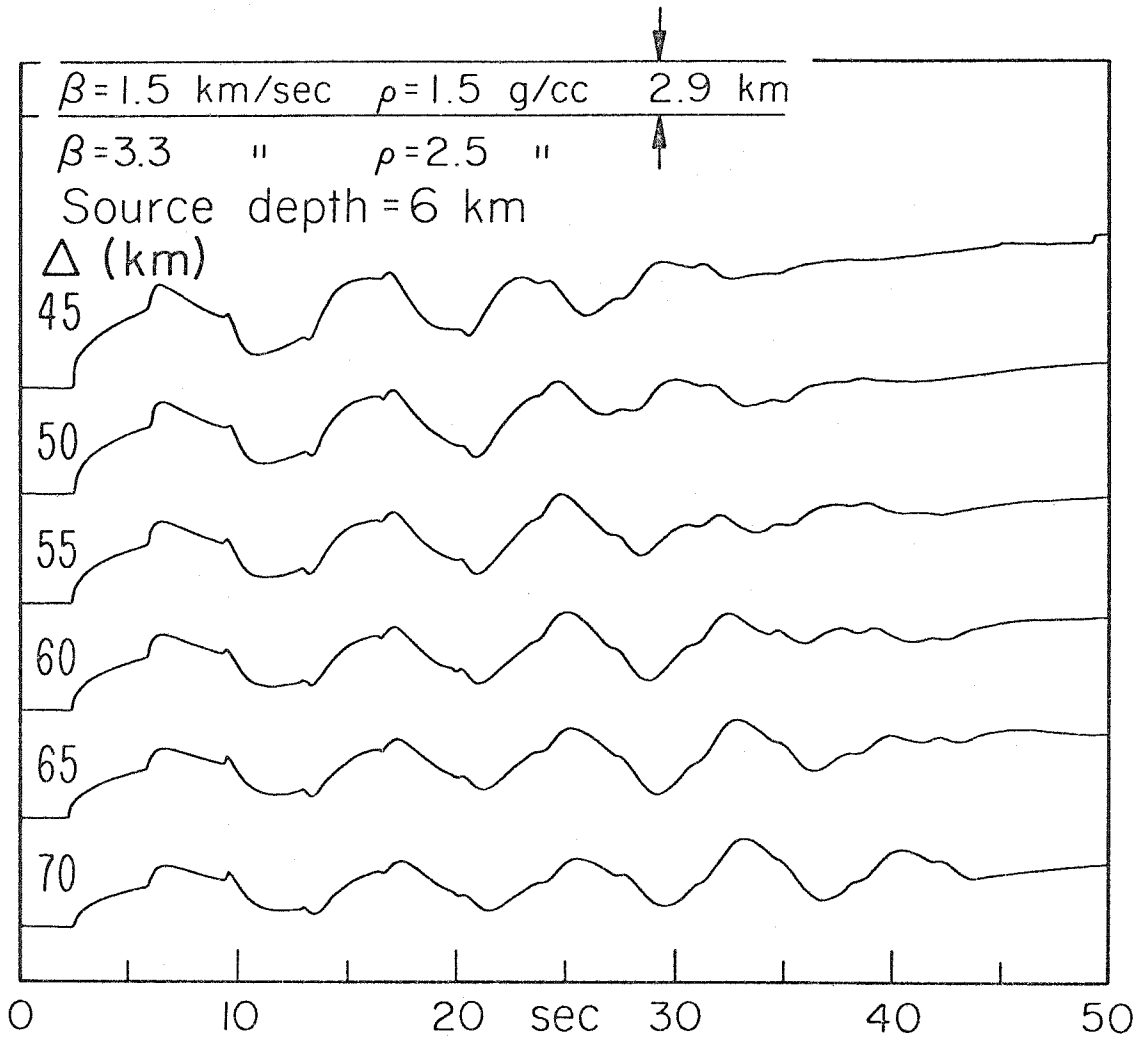

Figure 3.8. SH step function response as a function of distance and the constant depth of 6 km. The fact that the response changes very little with distance means that it is virtually impossible to resolve the difference between a horizontal line source and a point source convolved with the appropriate time function.

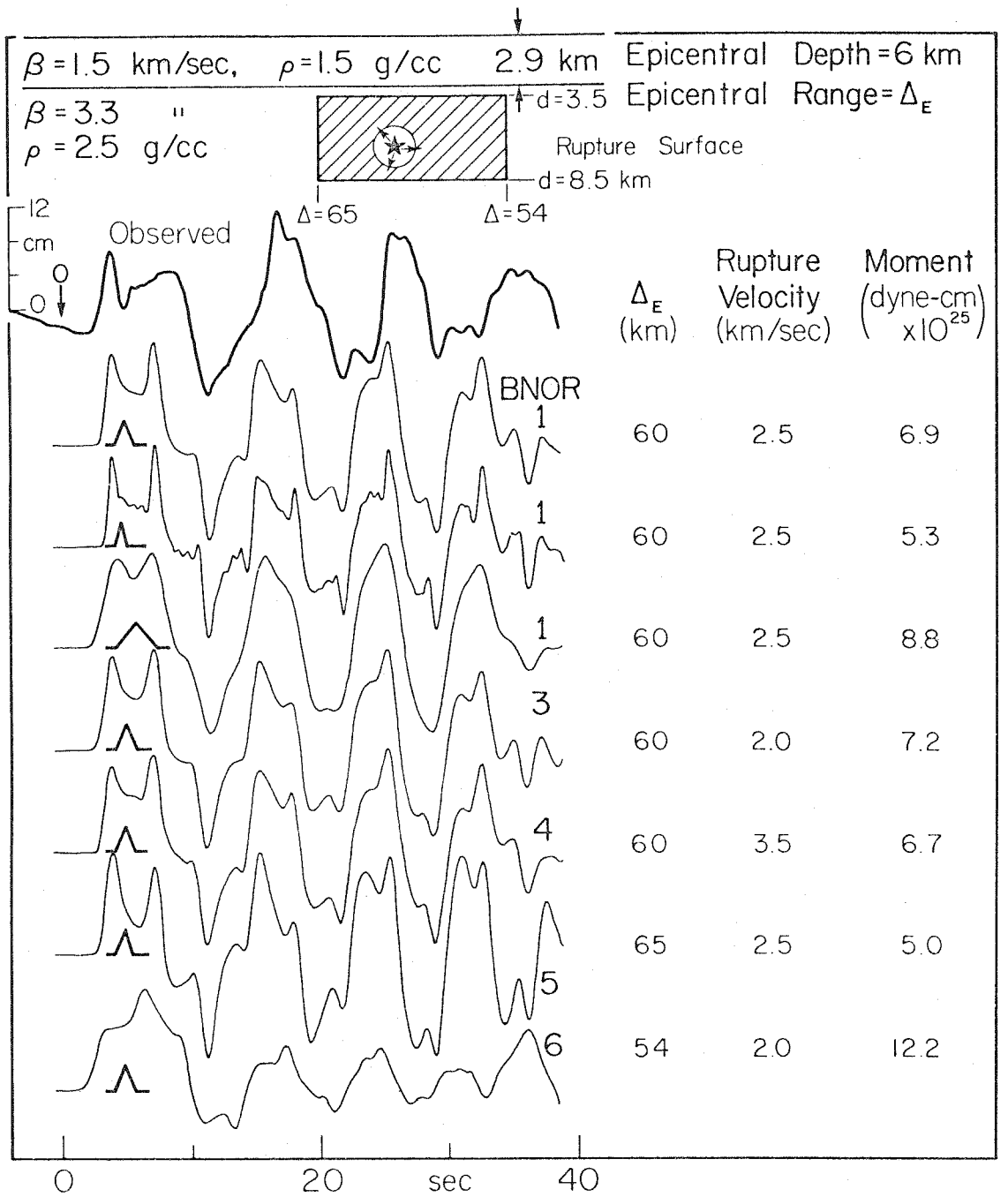

Figure 3.9. Comparison of observed with synthetic SH ground motion for models consisting of a rectangular fault with uniform offset which initiates at a point and propagates radially to the edge of the rectangle. In models BNOR5 and BNOR6 the rupture propagates unilaterally towards and away from El Centro, respectively. Rupture propagation is bilateral in the other models shown. The far-field time function for each point on the fault is displayed directly beneath the beginning of each synthetic.

is a model in which the rupture begins at the center of the rectangle and propagates radially with a rupture velocity of 2.5 km/sec. A triangular source time function was used and convolutions of BNOR1 with triangles of durations of 3.0 seconds, 1.5 seconds and 0.75 seconds are shown in Figure 3.9. The 1.5 second triangle clearly gave a superior fit and we have convolved this 1.5 second triangle with our other finite fault models. BNOR3 and BNOR4 which are also seen in Figure 3.9 are identical to BNOR1 except that the rupture velocities were 2.0 km/sec and 3.5 km/sec, respectively. The synthetics do not appear to be very sensitive to the rupture velocity for this size fault. Finally, Figure 3.9 shows BNOR5 and BNOR6 which are identical to BNOR1 except that rupture initiates on the far and near ends of the fault, respectively.

Model BNOR1 does a very respectable job of fitting the El Centro ground motion; particularly the character of the Love wave. This success is encouraging and we believe that it should be possible to construct a relatively simple finite source model which would fit the data just as well as our two-point source model. Model BNOR1 yielded a moment of 7×10^{25} dyne-cm. This would indicate an offset of about 500 cm and a stress drop which is near 500 bars. These estimates seem very large indeed. Figure 3.10 illustrates our attempts to decrease the fault offset by increasing the fault area. BNOR7 has a fault which is 26 km long by 9 km deep. Even with this much larger fault, the calculated offset would be about 110 cm, whereas the largest observed surface offset was only 38 cm. Moreover, BNOR7 has the problem that its body waves are too large compared to the Love waves. This can be alleviated by making the

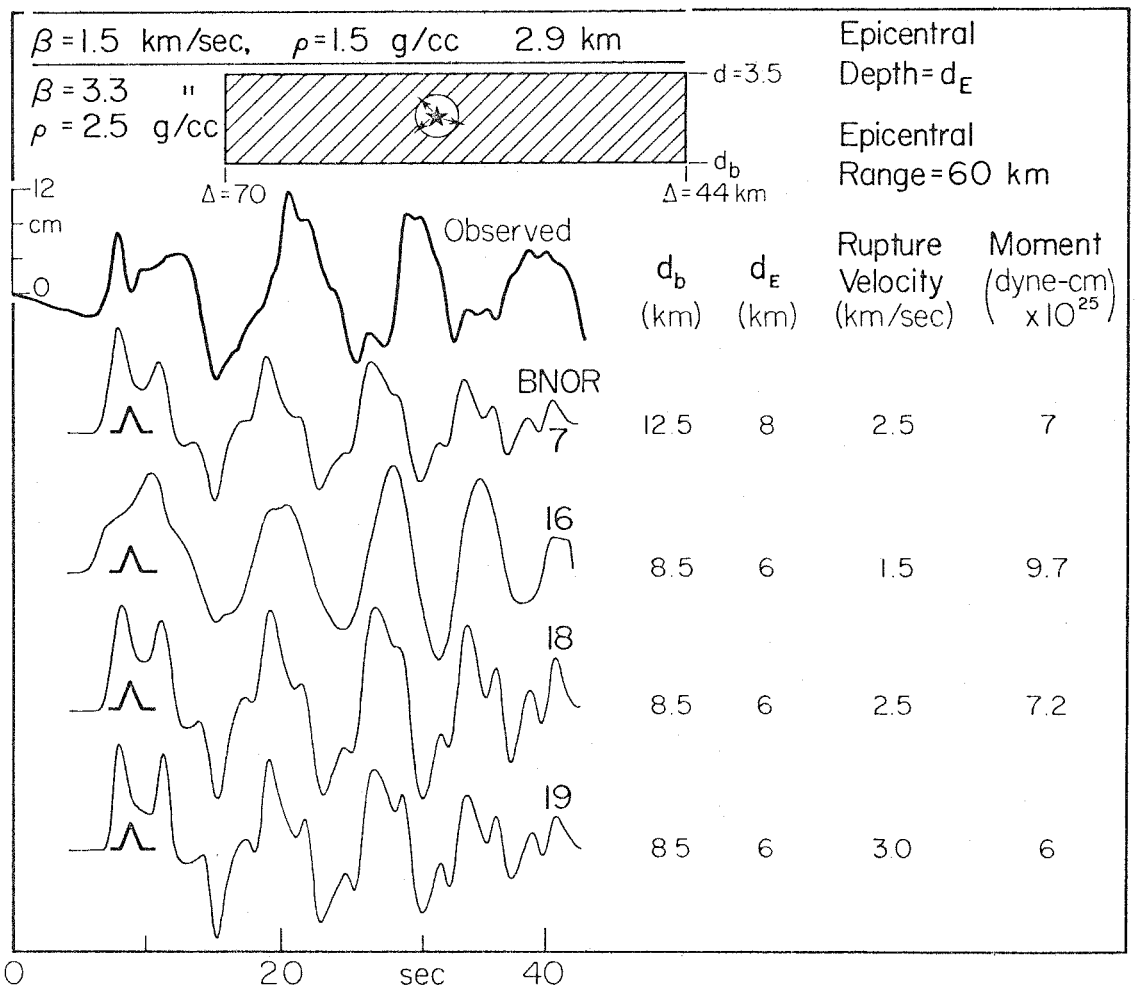

Figure 3.10. Comparison of observed synthetic SH ground motion for models consisting of a rectangular fault as described in Figure 3.8 except with a larger fault area. Notice that the direct arrival for BNOR7 is too large in relation to the Love wave. This situation is alleviated by making the fault plane shallower.

fault shallower. A fault which is 26 km long by 5 km deep was used in BNOR18 and BNOR19 which had rupture velocities of 2.5 km/sec and 3.0 km/sec, respectively. These models fit the actual record adequately, but the fault offsets must grow to about 200 cm. Part of this dilemma which we have encountered is due to the fact that we have not allowed the rupture to extend into the soft sediment layer because of the high-frequency reflections which our model will produce. In reality though, the sediments above the quake are probably very thin and discontinuous with the sedimentary stack at El Centro. Furthermore, we know that the earthquake ruptured clear to the surface. Yet our plane layer model does not allow us to model the contributions of the very shallow section of the fault plane. If we were able to model the upper 3 km of rupture, then we could also allow the fault to extend to depths below 10 km without disturbing the ratio of body wave amplitudes to Love wave amplitudes.

We have not drawn many conclusions regarding the earthquake from our attempts to model the El Centro record with a finite source. There does not appear to be enough information to resolve important parameters such as fault dimensions, rupture velocity and time history. What we have demonstrated is that it is possible to adequately fit the El Centro strong ground motion with simple finite source models embedded in a layer over a half-space structure model.

Discussion

It appears that the El Centro record can be successfully modeled by both finite source models and also by models which consist of only

two point sources. Is it possible to reconcile these different types of sources? If we were dealing with a homogeneous space, then it is obvious that it would be impossible to resolve the difference between a finite source and a point source with just one record. We could simply modify the time function for the point source such that it fit a single recording of any finite source. In general, this would not be true if we had to fit several recordings of the same event. The introduction of velocity structure is analogous to having several recordings of the earthquake in that the study of the interaction of seismic waves with the layers allows us to determine where those waves originated with respect to the layers. Figure 3.4 illustrates that it would be possible to resolve the difference between a vertical line source and a single point source for the case of a layer over a half-space. This is because the response changes with depth. Figure 3.8 shows that the response changes very little with the horizontal distance of the source (for our geometry). Thus it is very difficult for us to resolve the epicentral distance of a point source. In fact, it is virtually impossible for us to tell the difference between a point source and a finite horizontal line source. Thus the response of a finite vertical rectangular fault plane can be approximated by a vertical line source with an appropriate time function. In our case the response of the vertical line source is approximated by two point sources of different depth.

Conclusions

The strong ground motion recorded at El Centro for the 1968 Borrego Mountain earthquake is dominated by SH-type motion. Displacements

of up to 13 cm are indicated by the rotated deconvolved Carder displacement meter records. The thick sedimentary layer present in the vicinity of El Centro is modeled by a single 2.9 km thick layer. This layer traps SH waves allowing the formation of Love waves. In reality, there is considerable heterogeneity in the sediment structure along the path from the earthquake to El Centro, but the Love waves are formed in the flat-lying sediments relatively near El Centro.

It is possible to model the El Centro record with a single point source if relatively shallow high-velocity lower-crustal layers are introduced. If a simple layer over a half-space model is used, at least two point sources are necessary to provide an adequate fit to the record. Within the framework of this structure model, it appears to be possible to show that the majority of faulting extended from the free surface to a depth of not more than 12 km. A sharp time function with a 1 sec duration is indicated for the deeper segment at the fault, and a slower time function with a duration of greater than 4 sec is implied for the shallower parts of the fault. The horizontal dimension of the faulting does not appear to be resolvable. Considerable nonuniqueness is present in the models constructed and parameters such as fault geometry, hypocenter, rupture velocity and rise time do not appear to be resolvable. A model which is consistent with the teleseismic study done by Burdick and Mellman was demonstrated. The earthquake moment was found to be approximately 7×10^{25} dyne-cm.

Chapter 4

Synthesis of Strong Motion Recordings of the 1971 San Fernando Earthquake

Introduction

In the previous two chapters, we have examined ground motions which were profoundly affected by seismic velocity structure. Although source characteristics were important, relatively simple source models were all that were necessary to produce adequate synthetic records. However, since the San Fernando earthquake was well recorded by many close stations, a more detailed inspection of source processes is required. Several new complications are also introduced by the small source to receiver distances. Near-field terms can no longer be neglected. Fault finiteness requires that waves from differing parts of the fault must approach the receiver from differing directions. This means that the observed ground motion can no longer be rotated into radial and transverse directions. Thus we can no longer isolate SH waveforms and we are forced to consider P waves, SV waves and Rayleigh waves. For many reasons, life becomes more complicated as we move closer to the earthquake source. Fortunately, as the source to receiver distance becomes small, the effects of plane-layered structure become less dramatic. In an attempt to understand the most basic features of the interplay between source and structural effects, we choose to first model the San Fernando earthquake as a three-dimensional fault located in an elastic half-space.

The purpose of this chapter is two-fold. We would first like to understand the types of phenomena which should be expected from a three-dimensional fault which is located in a half-space. The second goal is to achieve a better understanding of the particular source processes of the San Fernando earthquake. The second goal is the more important and difficult to achieve. The San Fernando earthquake created a wealth of teleseismic body wave and surface wave data and also local static offset data. It thus provides a unique cross-check of several different techniques of studying the slip on the fault plane. Ultimately, we would like to find a single model which explains all of these observations. However, in this study we will not attempt to model these different data sets simultaneously. We will comment on the compatibility of our strong-motion models with models which have been derived by other authors.

A large number of papers have been written about the San Fernando earthquake and we will not attempt to summarize the results of all previous studies. However, there are several papers which we found very useful in constructing our models. The study of teleseismic body waves by Langston (1978), Alewine's (1974) inversion of static offset data and teleseismic surface wave data, Hanks' study of observed strong ground motion (1975), and the inversion of strong-motion data by Trifunac (1974) all proved very useful in our construction of San Fernando models. Although Trifunac's models were for a finite fault in a whole-space, we learned from his synthetic Pacoima Dam ground motion. Thus there are several similarities between our preferred fault model and Trifunac's final fault model.

The numerical calculations involved in our synthetics consist of several relatively laborious and expensive steps. Once a particular fault to station geometry is chosen, it is time and money consuming to change that geometry. We have chosen to model four stations and no attempt was made to find alternate stations or source to station geometries which might produce better synthetics. In retrospect, we would have ignored the station at Palmdale since a half-space seems to be a very poor approximation of earth structure near this station. Also it appears that a different fault dip versus depth relationship might have improved the comparison between synthetic and real data. However, it is not our purpose to discover the best half-space model. We would like to discover the gross features of the model which are required by the data. Because of the large number of parameters involved, a thorough search of the model space can result in an endless groping process. Until we learned the significance of different parameters, we were victims of this grope. The merits of this process are that much can be learned about what will not work.

We are now faced with the problem of showing the reader what we have learned from this process and why we have chosen the model presented in this thesis. It would be impractical and tedious to present all of our unsuccessful models. Thus our plan is to present several simple models and to then try and understand why they do not work and how they could be improved.

The Data

The 1971 San Fernando earthquake produced by far the largest single strong-motion data set yet available. Shown in Figure 4.1 are the locations of most of the accelerometers which recorded this event. We were faced with the choice of which records from this immense set we would model. Because we are using a half-space model, it is important that the stations be near the fault. In order to minimize redundant information, stations from different azimuths were chosen. The stations for which records were synthesized are Pacoima Dam (PAC), Jet Propulsion Laboratory (JPL), Lake Hughes Array Station No. 4 (LKH) and Palmdale Fire station (PLM). These stations are indicated in Figure 4.1 by the codes C041, G110, J142 and G114, respectively. These codes refer to the cataloguing system used in the series of strong-motion data reports published by the Earthquake Engineering Research Laboratory of the California Institute of Technology. It is from these reports that our observed ground displacement curves have been taken. In Figures 4.2 through 4.5 we show the corrected accelerograms, integrated ground velocity and displacement curves for these stations (Trifunac et al., 1973b). The processing of these accelerograms involves baseline corrections and Ormsby filtering. The basis for this processing can be found in papers by Trifunac (1971), Trifunac et al. (1973a) and Trifunac et al. (1973b).

It is impossible for an accelerometer to recover static or even very long-period ground displacement information and thus these integrated displacement curves are really displacements in which periods longer than 10 seconds have been heavily filtered. In fact, the baseline

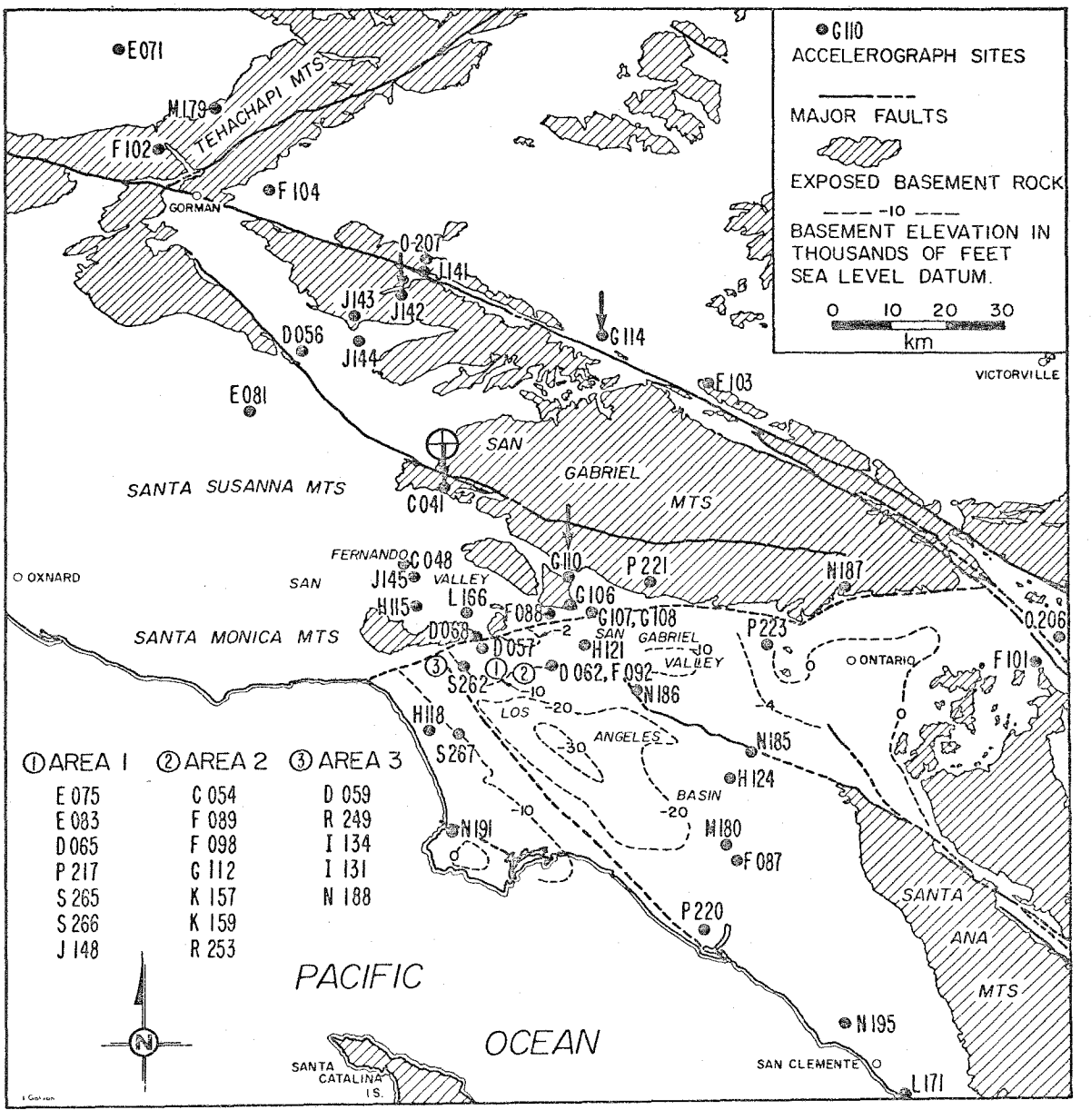

Figure 4.1. The site locations of accelerometer recordings of the San Fernando earthquake are superimposed on the gross geological and structural features of the area. The encircled cross is the Allen et al. (1973) epicenter and the arrows point to stations which are studied in this chapter (modified from Hanks, 1975).

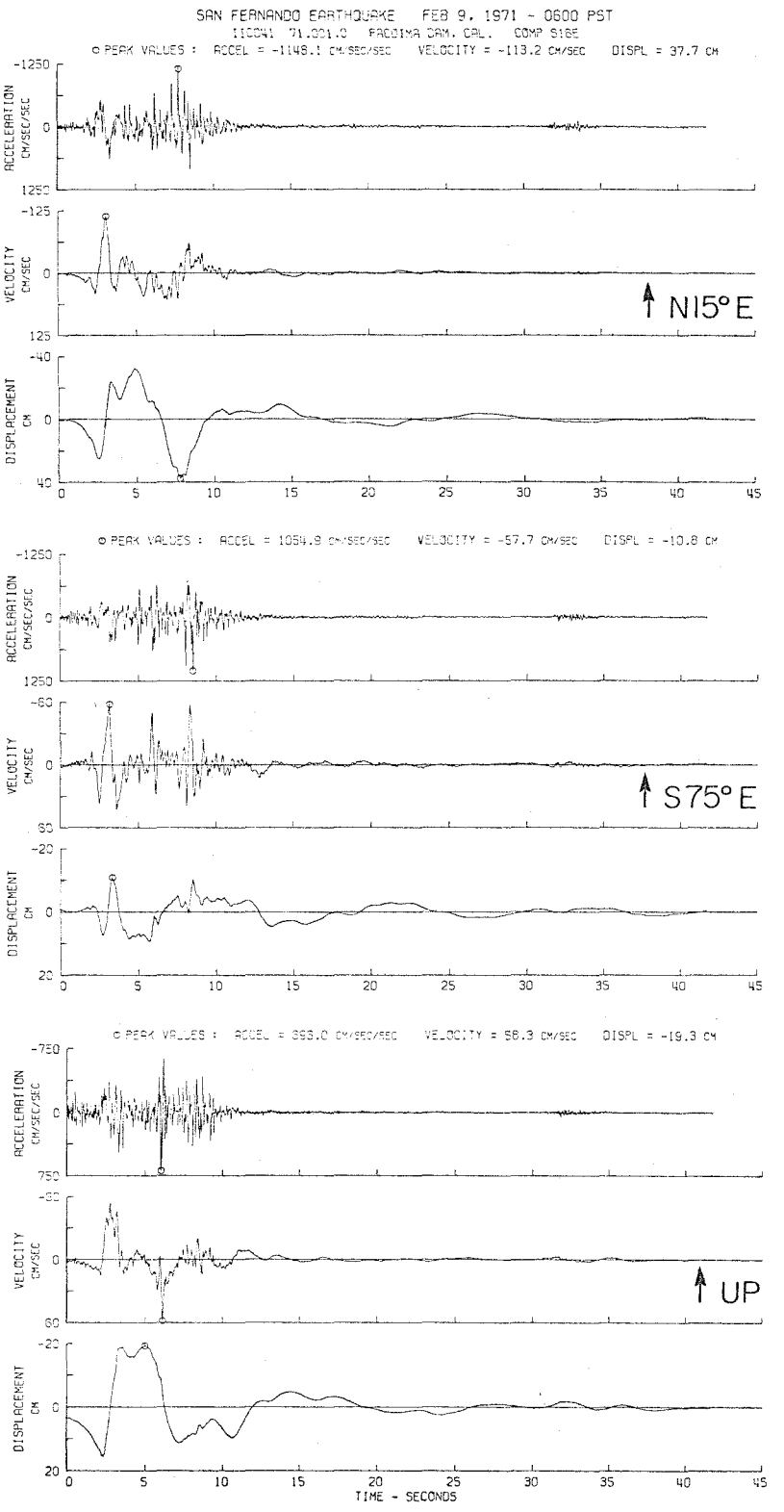

Figure 4.2. Corrected accelerograms, velocities and displacements for the San Fernando earthquake as recorded at Pacoima Dam (modified from Trifunac et al., 1973b).

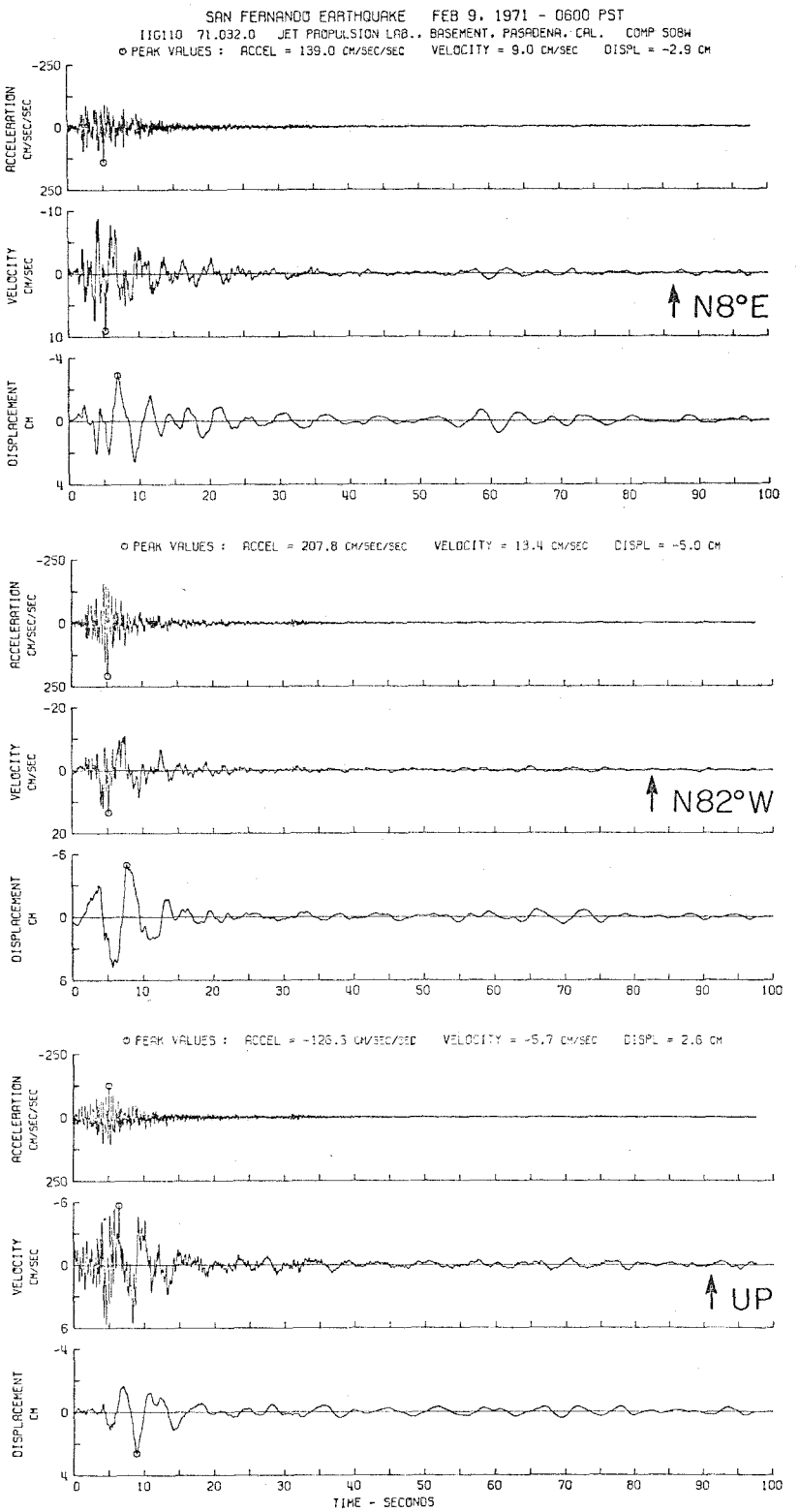

Figure 4.3. Corrected accelerograms, velocities and displacements for the San Fernando earthquake as recorded at the Jet Propulsion Laboratory (modified from Trifunac et al., 1973b).

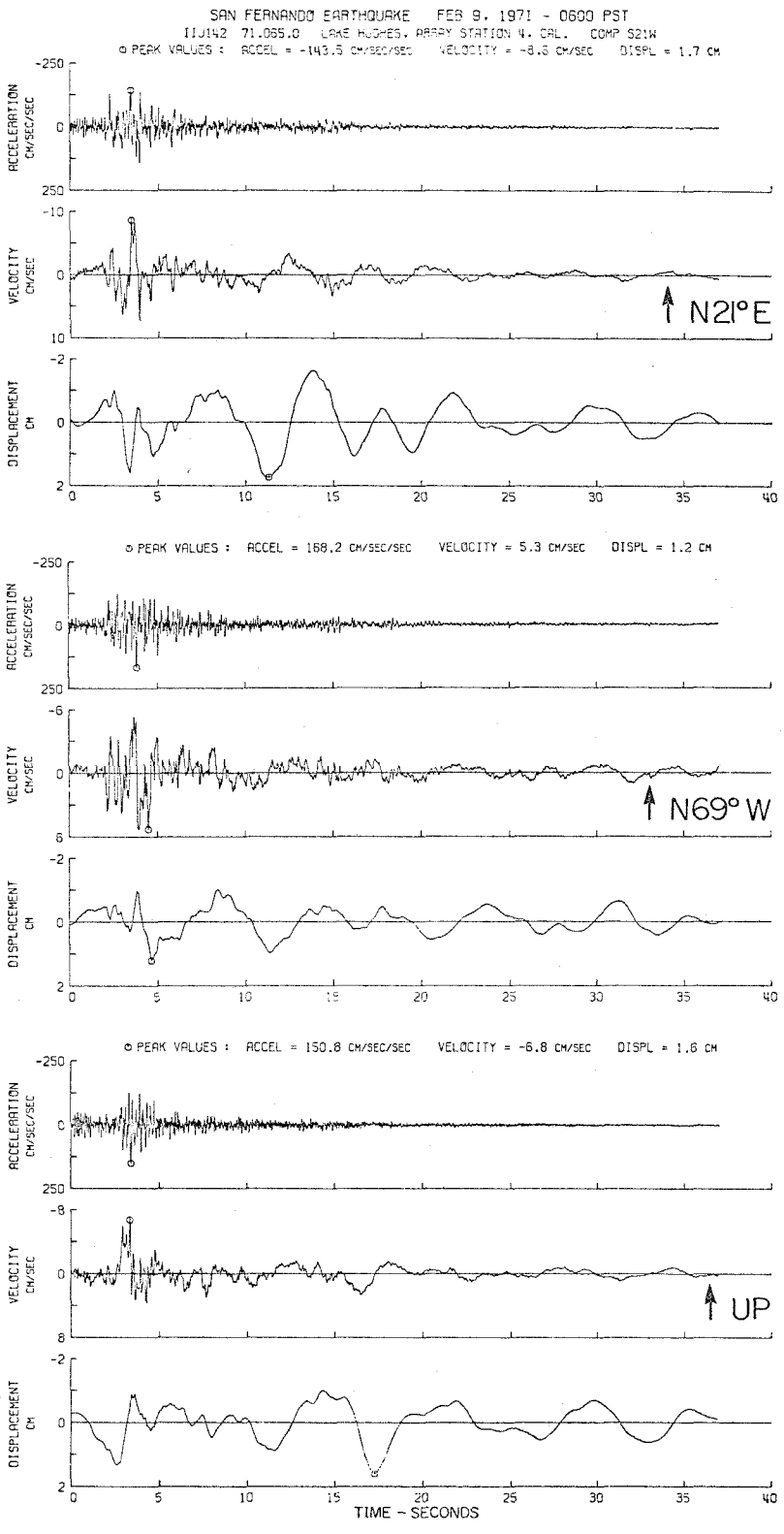

Figure 4.4. Corrected accelerograms, velocities and displacements for the San Fernando earthquake as recorded at the Lake Hughes Array Station No. 4 (modified from Trifunac et al., 1973b).

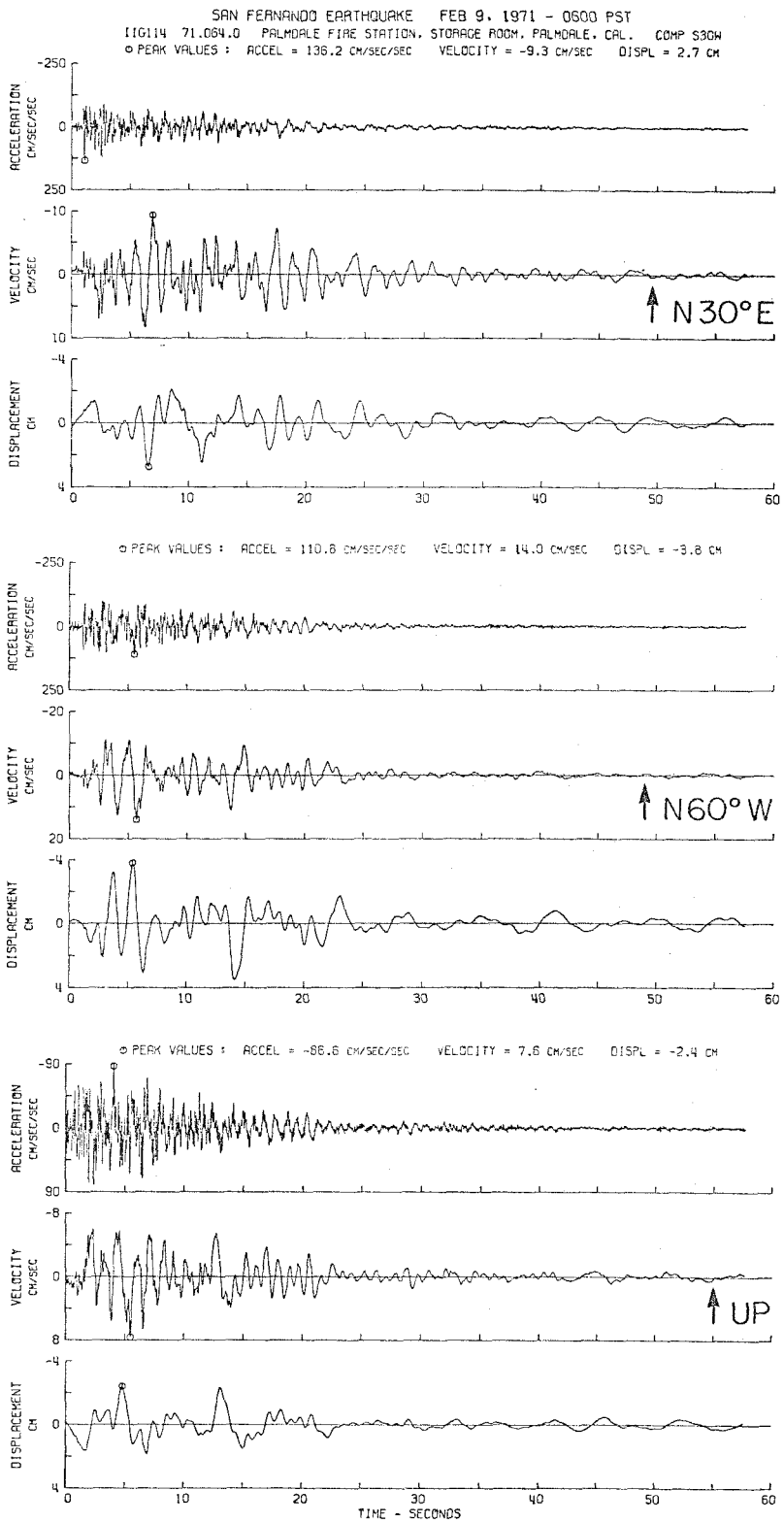

Figure 4.5. Corrected accelerograms, velocities and displacements for the San Fernando earthquake as recorded at the Palmdale Fire Station (modified from Trifunac et al., 1973b).

correction can effectively filter periods of less than 10 seconds. For instance, the Pacoima station probably experienced a large static offset which cannot be easily seen when simply viewing the displacement curves. Hanks (1975) has presented a relatively comprehensive discussion of the sources of long-period errors for this data set.

In his 1975 paper, Hanks also investigates the coherence of displacements between stations which are located near each other. In general, he finds this coherence to be very good. In particular, the records from stations in the Pasadena (i.e., JPL) area are very similar to each other. Also the records from stations in the Lake Hughes area look similar. This increases our confidence that waveform modeling of these records will yield physically meaningful results. Unfortunately, there are only two stations to the northeast and we chose Palmdale since it was closest. An inspection of the records for PLM shows a distinct "ringing" in the records with a period near 1 second. We feel that this is caused by local structure and that the Pearblossom records (F103) would have been more useful.

Hanks (1975) points out that both the intensity of shaking and amplitude of displacements were generally larger for regions south of the hypocenter. In particular, this is true of the stations which we have chosen to model. We will use this observation to try and pin down the slip on the fault plane.

The Model

Our model consists of a three-dimensional finite fault located in a half-space. A circular rupture front is assumed to propagate at

a given rupture velocity from the hypocenter. The slip angle and dislocation time history are assumed to be uniform throughout the fault plane. The Cagniard-de Hoop technique, together with a linear interpolation scheme, is used to compute the ground motions from point dislocations which are evenly distributed (0.5 km spacing) on the fault plane. These responses are summed with time lags which are determined by the assumed hypocentral solution and rupture velocity. Nonuniform fault displacement is modeled by varying the weights of individual point sources. We are thus using a numerical Green's function technique to integrate over the fault plane. This is very similar to the finite fault models which were constructed for the Borrego Mountain earthquake in Chapter 3. However, in this case, there are many added complexities due to the inclusion of P and SV waves, near-field terms and a more general fault to station geometry which dictates that waves arrive from different azimuths. This last complication has two effects, both of which are included, without approximation, in our models. The first effect originates from the fact that sources having different locations on the fault plane have different radiation patterns with respect to a fixed station. The second effect is to make the definition of radial and transverse directions a function of the position of the point on the fault being considered at any one time. As is discussed in Chapter 1, the importance of these effects is a function of the source's dimensions and the receiver's distance. These effects are particularly important in our Pacoima models.

Our total solution can be formally written

$$\underset{\sim}{U}(t) = \sum_{j=1}^{n} \sum_{k=1}^{m} m_{jk} \underset{\sim}{Y}_{jk}(t) * \dot{D}(t) \tag{4.1}$$

where $\underset{\sim}{U}(t)$ is the displacement at a station, j denotes the j^{th} source along the fault strike, k denotes the k^{th} source down the fault dip, m_{jk} is the moment of the j,k^{th} source, $\underset{\sim}{Y}_{jk}(t)$ is the response of the j,k^{th} source, and $\dot{D}(t)$ is the time derivation of the time history for any point on the fault. If we choose the coordinate frame ($\underset{\sim}{e}_1$, $\underset{\sim}{e}_2$, $\underset{\sim}{e}_3$) to be north, east and down, then

$$\underset{\sim}{Y}_{jk}(t) = (Q_{jk} \cos \nu_{jk} - V_{jk} \sin \nu_{jk})\underset{\sim}{e}_1 + (Q_{jk} \sin \nu_{jk} + V_{jk} \cos \nu_{jk})\underset{\sim}{e}_2 + W_{jk} \underset{\sim}{e}_3 \tag{4.2}$$

where we have used the notation

$$\begin{aligned} Q_{jk} &= Q(r_{jk}, h_{jk}, \theta_{jk}, \lambda, \tau) \\ V_{jk} &= V(r_{jk}, h_{jk}, \theta_{jk}, \lambda, \tau) \\ W_{jk} &= W(r_{jk}, h_{jk}, \theta_{jk}, \lambda, \tau) \end{aligned} \tag{4.3}$$

and where r_{jk} is the distance of the j,k^{th} source, h_{jk} is its depth, θ is its azimuth angle as defined from the fault strike, and λ is the rake. Q, V and W are the radial, transverse and vertical components of motion, respectively. They are given in equations (1.71), (1.74) and (1.77). ν_{jk} is the backazimuth angle of the j,k^{th} point source as measured clockwise from north.

Our method for determining individual point source responses is to start with a coarse gridwork on the fault. Responses for points located on the corners of this gridwork are computed by using the exact Cagniard solutions discussed in Chapter 1. These solutions are extremely broad band; that is, they are correct for the static as well as the very high-frequency parts of the solution. Just as in Chapter 3, we notice that responses from adjacent sources look very similar. It is thus possible to calculate other responses on a finer gridwork by interpolation. Our scheme is as follows. Responses from adjacent points are shifted in time such that their direct shear wave arrival times coincide. Then a simple linear interpolation is used to calculate the shape of the approximate solution for intermediate locations. The approximate solution is again shifted in time such that the shear wave arrival time for the approximate solution is exactly correct. Hartzell et al. (1978) have also devised a similar method for approximating intermediate point source responses.

The accuracy of the interpolated solutions is a function of frequency and the distance between coarse grid points. The solutions are very good at the longer periods which dominate the displacement records. Because the interpolation is based on shear wave arrival times, the approximation for the direct shear is quite good for all frequencies. However, the high-frequency parts of the solution for phases with different phase velocities than the direct shear wave are poorly approximated by this scheme. For instance, the direct compressional wave will appear as two sharp arrivals instead of just one. This is not a great worry

to us, however, since the largest high-frequency arrival is the direct shear wave and also because our synthetic displacements are rather insensitive to the details of the high frequencies anyway.

For stations except Pacoima, exact responses were computed every 4 km along the strike and every 2 km down the dip. Since Pacoima is so close to the fault, this spacing was halved for Pacoima. Interpolated responses were calculated at a 0.5 km spacing.

It is interesting to note that our interpolation technique could be replaced with a convolution technique such as the one employed by Wiggins and Frazier (1977). That is, instead of summing interpolated sources, we could sum only the coarse grid where each source would be convolved with a separate time function which would approximate the finiteness of that section of the fault. We can demonstrate this equivalence by considering one element of the gridwork on the fault. Consider the fault element shown in Figure 4.6, for which exact responses have been computed at the corners. For simplicity, consider this to be a scalar problem with the scalar displacement, u. u is given by:

$$u = \sum_{j=1}^{n} \sum_{k=1}^{m} Y_{jk}(t) \quad . \tag{4.4}$$

Now our linear interpolation technique says that the j,kth response can be approximated by

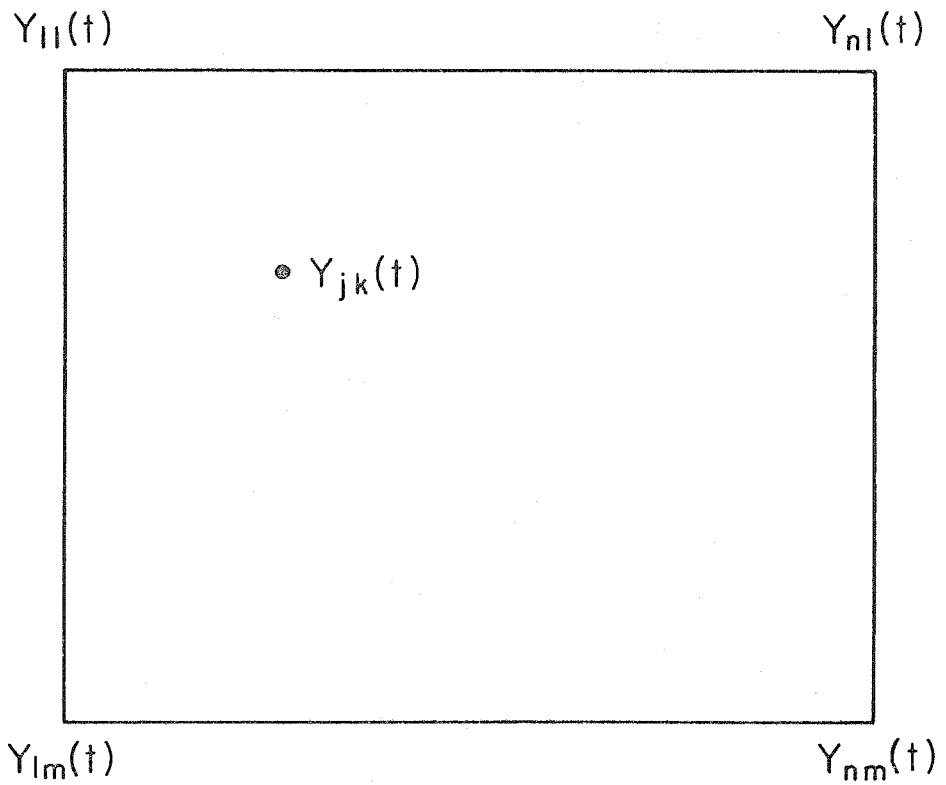

Figure 4.6. Schematic of one subdivision of a finite fault. Exact responses are computed at the corners and responses within the subdivision are then computed by linear interpolation.

$$Y_{jk} = a_{jk}^{11} Y_{11}(t-\tau_{ij}^{11}) + a_{jk}^{n1} Y_{n1}(t-\tau_{ij}^{n1}) + a_{jk}^{1m} Y_{1m}(t-\tau_{ij}^{1m})$$

$$+ a_{jk}^{nm} Y_{nm}(t-\tau_{ij}^{nm}) \quad , \tag{4.5}$$

where the a_{jk}^{nm} are interpolated constants, and the τ_{ij}^{nm}'s are time shifts which are used to insure that shear wave arrival times are aligned during interpolation. These time lags may also contain information about the rupture process. Noting that

$$Y_{11}(t-\tau_{ij}^{11}) = Y_{11}(t) * \delta(t-\tau_{ij}^{11}) \quad ,$$

we can write (4.4) as

$$U = Y_{11}(t) * A_{11}(t) + Y_{n1}(t) * A_{n1}(t) + Y_{1m}(t) * A_{1m}(t)$$

$$+ Y_{nm}(t) * A_{nm}(t) \quad , \tag{4.6}$$

where

$$A_{i\ell}(t) \equiv \sum_{j=1}^{n} \sum_{k=1}^{m} a_{jk}^{i\ell} \delta(t-\tau_{jk}^{i\ell}) \quad .$$

Thus we see that our interpolation scheme is a way of finding the appropriate far-field time functions for point sources located on our coarse gridwork. In our actual models, the interpolation technique includes the second order effects due to the variation in azimuth angle

between individual point sources and the receiver. These variations cannot be included in a convolution technique, but as long as the spacing of the coarse gridwork does not become too large, these azimuthal effects are very small. Finally, it is important to realize that both the interpolation and convolution techniques may poorly approximate the high-frequency behavior of phases other than the direct shear wave. As we have said before, this is not a severe problem for the half-space solution. However, some care should be taken when applying these techniques to a layered half-space problem, since there may be several other important high-frequency phases present.

In Figure 4.7 we show the fault and station geometry that was used in this study. Unfortunately, picking a fault geometry is largely guesswork. Allen et al. (1973) have argued that the fault dip increases with depth. They based this result on the discrepancy between the aftershock pattern and the teleseismic focal mechanism. Langston (1978) has concluded that the waveforms of teleseismic body waves require a depth-dependent dip. He found that he could adequately synthesize the teleseismic waveforms with a hinged fault in which the strike, dip and rake of the upper and lower planes are (θ_1 = N80°W, δ_1 = 29°, λ = 90°) and (θ_2 = N70°W, δ_2 = 53°, λ_2 = 76°), respectively. These two faults intersect at a depth of 5 km. We have incorporated these two planes in our solution. However, for the sake of simplicity, we have assumed that $\theta_1 = \theta_2$ = N75°W. Thus the fault geometry used in this study was chosen independently of the strong motion modeling results.

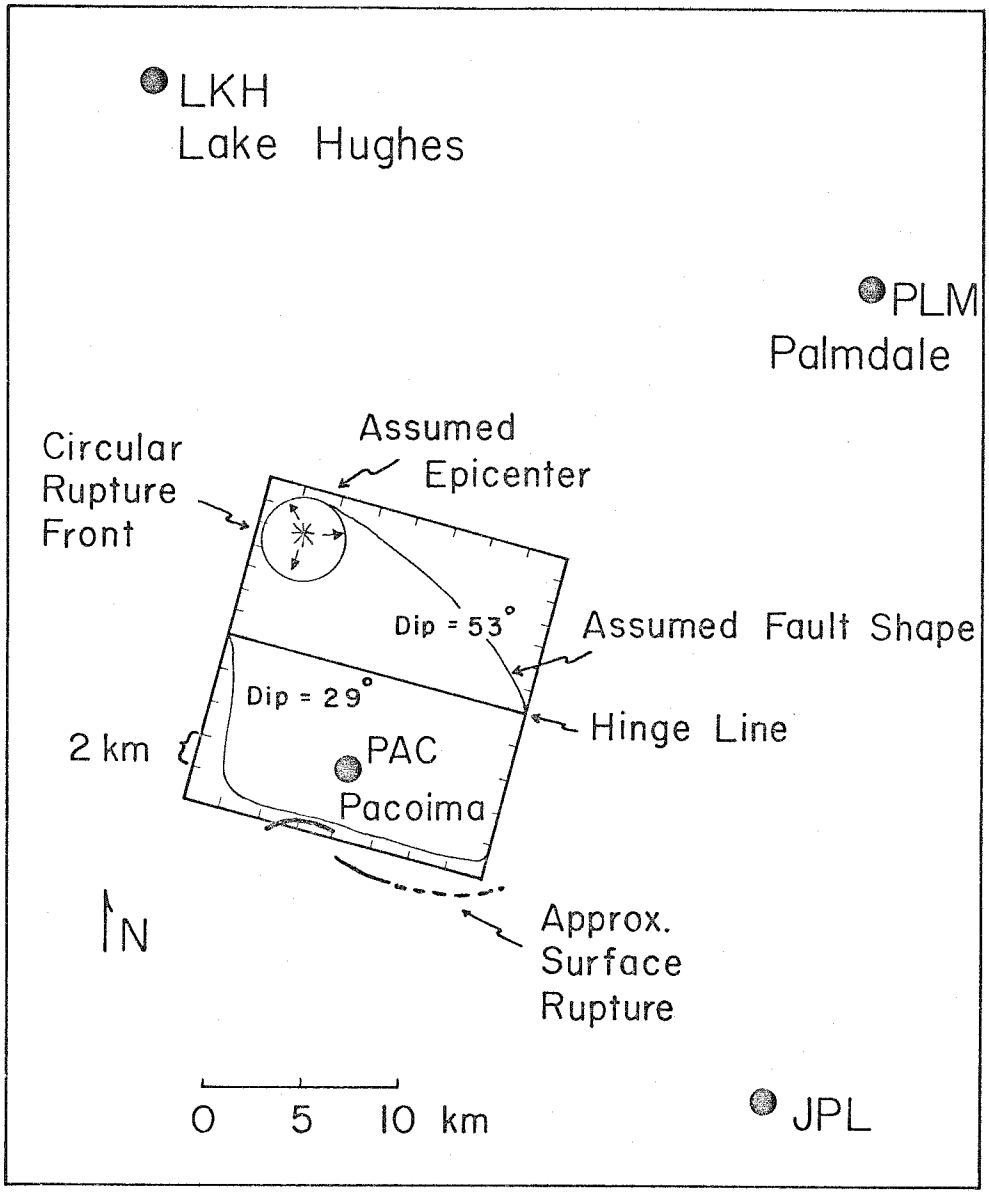

Figure 4.7. Assumed geometry for the San Fernando fault and receivers. Model consists of a three-dimensional fault in a half-space. A circular rupture front propagates from an assumed hypocenter and displacement magnitudes are prescribed on the fault surface. Notice that the fault changes dip at a depth of 5 km.

Modeling the Records

Our basic objective is to search through a model space in which the hypocentral solution, rupture velocity and distribution of faulting are allowed to vary. We would like to discover which models adequately explain the records we have chosen to model. Our model space is large and it is unreasonable for us to randomly search through it. It is important that we learn from the small number of models which we have the time to study. Langston (1978) and Hanks (1974) have both argued that the timing of the teleseismic pP phase indicates a hypocentral depth of 13 km. Hanks suggests that the hypocenter is located 13 km due north of Pacoima. A recent relocation by Hadley and Kanamori (1978) indicates that the hypocenter is several kilometers south of Hank's solution at a depth of 11.5 km. Langston found that a bilateral rupture on a uniform fault with a width of 10 km and upward and downward rupture velocities of 1.8 km/sec and 3.0 km/sec yielded a good fit to the teleseismic body waves. He also concluded that the moments of the upper and lower fault segments were 0.41×10^{26} ergs and 0.45×10^{26} ergs, respectively. In Figure 4.8 we show our attempt to approximate Langston's model. For the moment, we will not worry about the downgoing high rupture velocity feature of Langston's model. The contours in Figure 4.8 signify lines of equal fault slip in meters. The hypocenter is located in the region of maximum slip and the rupture velocity is 1.8 km/sec. The time derivative of the time history of slip for each point on the fault is an isosceles triangle with a duration of 0.8 seconds. The fault moment, 1.5×10^{26} ergs, is significantly larger than Langston's moment.

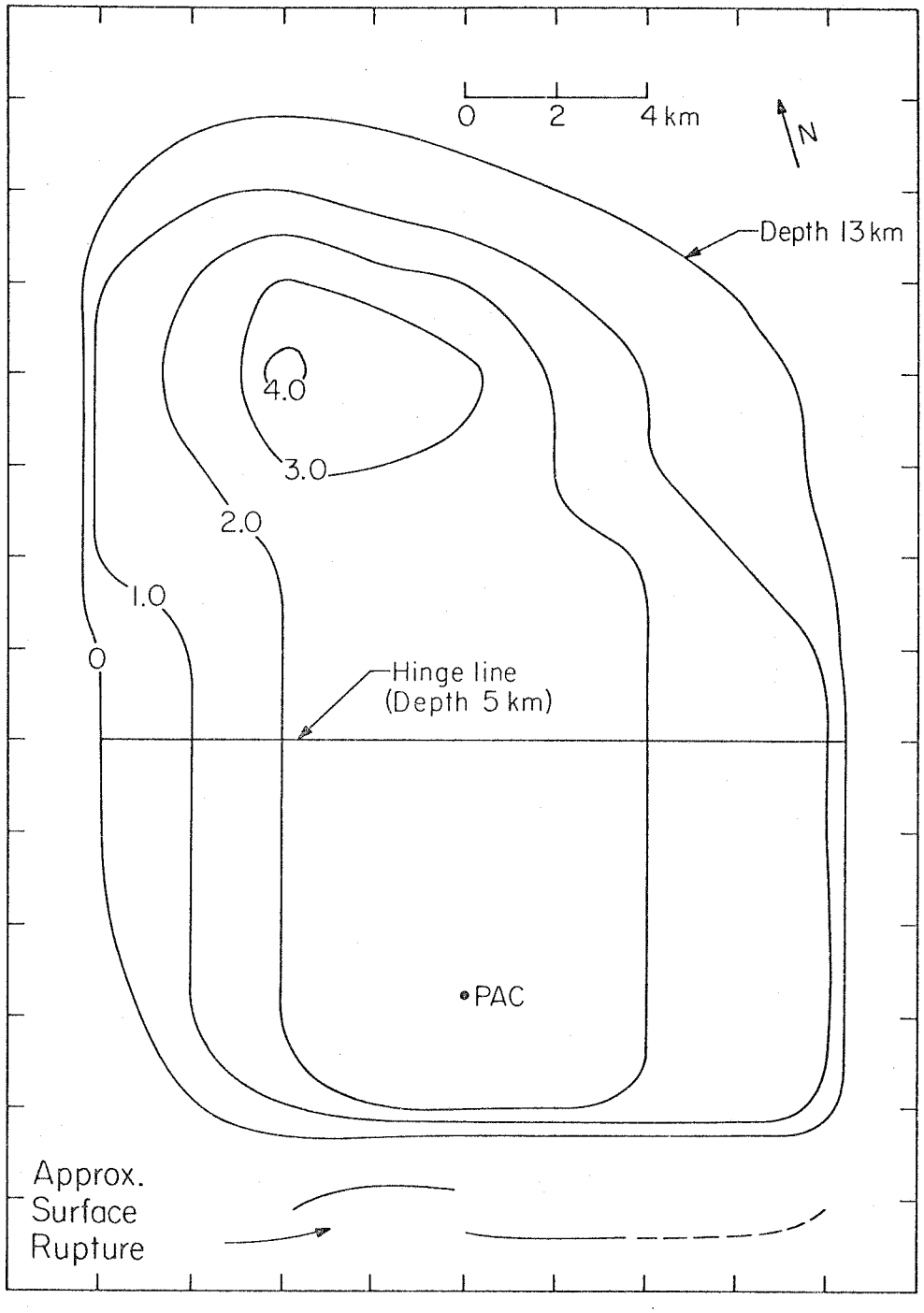

Figure 4.8. Contour map of assumed fault displacements for the model, Norma 140. The rupture velocity is 1.8 km/sec and the hypocenter is near the region of maximum displacement.

Comparisons of synthetic and observed records for the model we designated Norma 140 are shown in Figures 4.9 through 4.12. Two synthetic records are shown for each component. The top trace is the computed ground motion and the middle trace is this synthetic motion with a baseline correction and a high-pass Ormsby filter applied. We used the baseline correction described by Nigam and Jennings (1968) and an 8 second Ormsby filter. This filter is described by Hanks (1975).

The first thing that we notice about Norma 140 is that, although relative amplitudes are approximately correct, the synthetic waveforms are quite dissimilar from the observed. First inspect the synthetics for Pacoima. Notice that the static part of the solution can be very important and also notice that the filtering process can severely alter the shape of the records. The observed record begins with a sharp pulse which is not seen on the synthetics. The polarity and timing of this pulse are that which is expected for a far-field SV wave originating from the hypocentral region. Hanks (1974) has argued that this pulse requires very large localized faulting in the hypocentral region. Norma 160 does not refute this argument since the fault model is smooth and the pulse is absent. The later parts of these synthetics also fit poorly and, for the moment, we will leave this unexplained.

Next study the JPL records. Notice that the observed east record begins with a large pulse which cannot be found in the synthetic record. The comparison of the later parts of the records is more favorable even though the amplitudes of the synthetics are too large. The synthetic records for Lake Hughes compare well with the observed records. Several

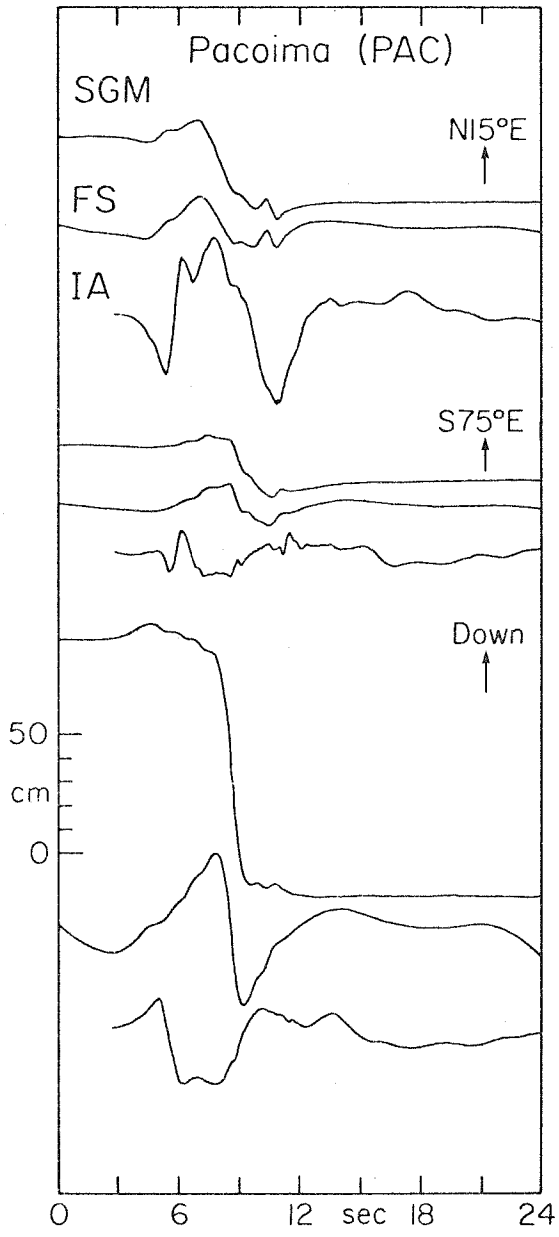

Figure 4.9

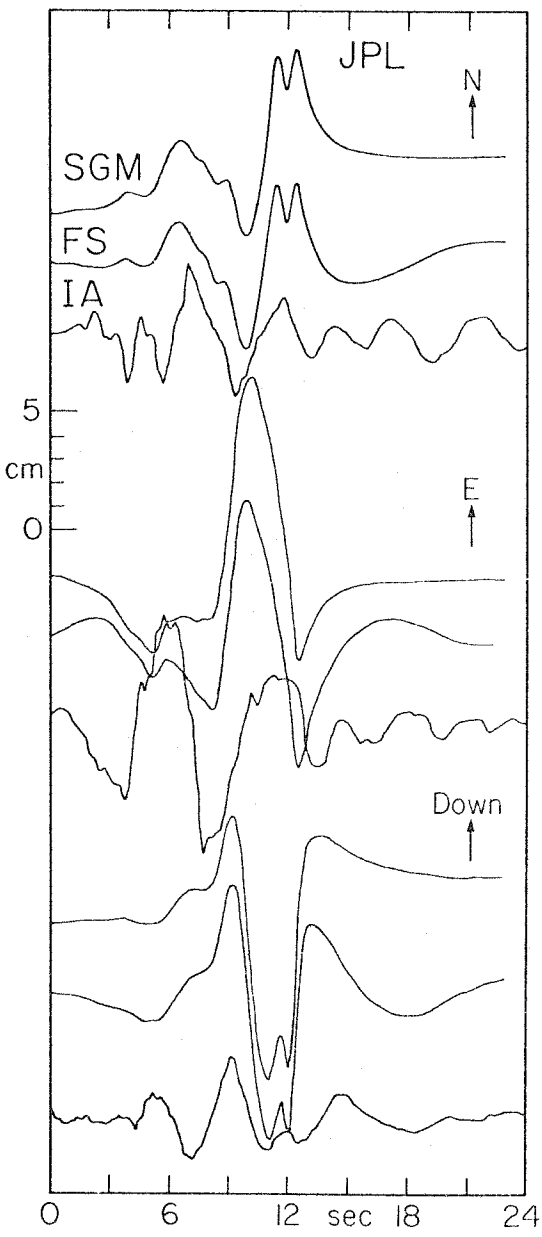

Figure 4.10

Comparison of observed and synthetic records for the model, Norma 140, and the stations, PAC and JPL. The top trace is the synthetic ground motion (SGM); the middle trace is the synthetic ground motion after baseline correction and Ormsby filtering (FS); the bottom trace is the observed displacement which has also been filtered and baseline corrected (IA).

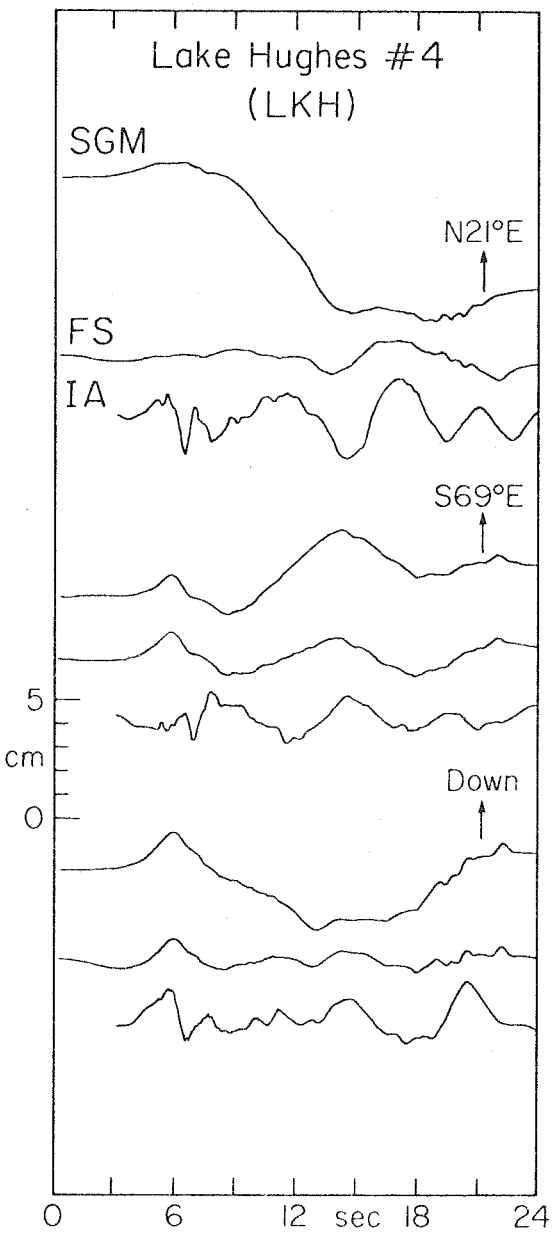

Figure 4.11

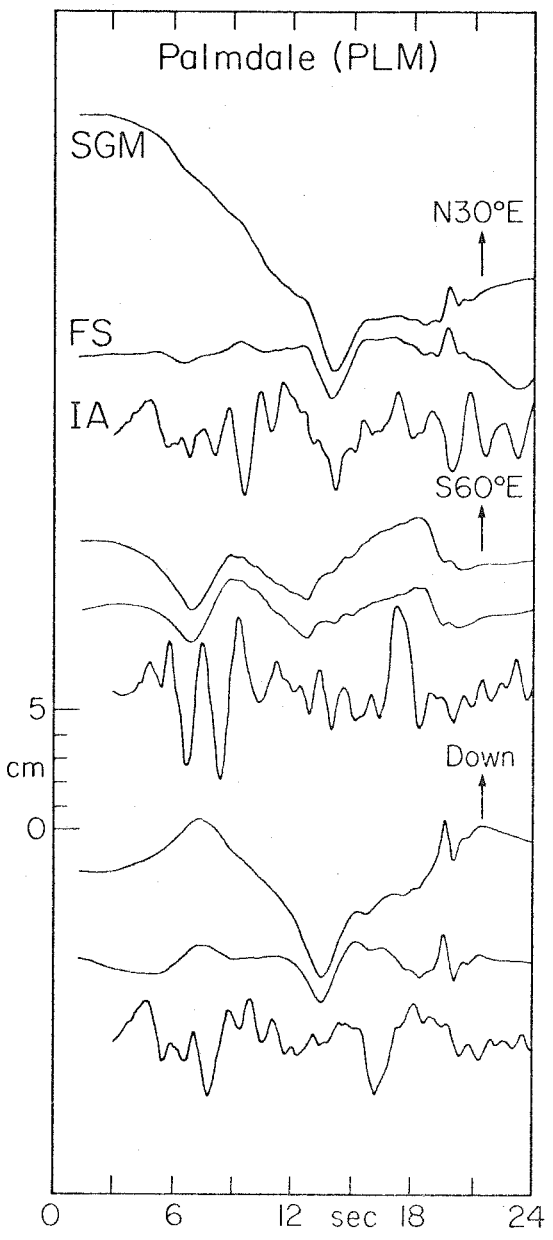

Figure 4.12

Comparison of observed and synthetic records for the model Norma 140, and the stations LKH and PLM. See Figure 4.9 for explanation of SGM, FS and IA.

short-period arrivals which are present in the observed records are absent from the synthetics. Also, the later parts of the observed records contain larger-and shorter-period waves than do the synthetics. Finally, notice that the resemblance between observed and synthetic Palmdale records. The observed records are dominated by a "ringing" at 1 Hz which cannot be found in the synthetics.

In general, Norma 140 is, at best, a marginally successful attempt to explain the observed records. How might we improve this model? Perhaps massive faulting in the hypocentral region will help to make the large first pulses seen at Pacoima and JPL. In Figure 4.13 we show the slip contour map for the model, Norma 170. This model is very similar to Norma 140, except that displacements of up to 12 meters are present in the hypocentral region. Once again the total moment is 1.5×10^{26} ergs with the upper and lower faults contributing equally to this total. The rupture velocity is still 1.8 km/sec.

The comparisons between synthetic and observed records for model Norma 170 are shown in Figures 4.14 through 4.17. A quick glimpse at these figures shows that the hoped for miracle has not yet occurred. The first pulse on the Pacoima and JPL records has grown significantly. Unfortunately, it is still less than half the amplitude of the observed. How might we increase the amplitude of this pulse? We could either further increase the displacements, or we could increase the rupture velocity. Either of these alternatives looks promising until we study the Lake Hughes synthetics. When we increased the first pulse for PAC and JPL, we also increased it for LKH. The trouble is that this synthetic

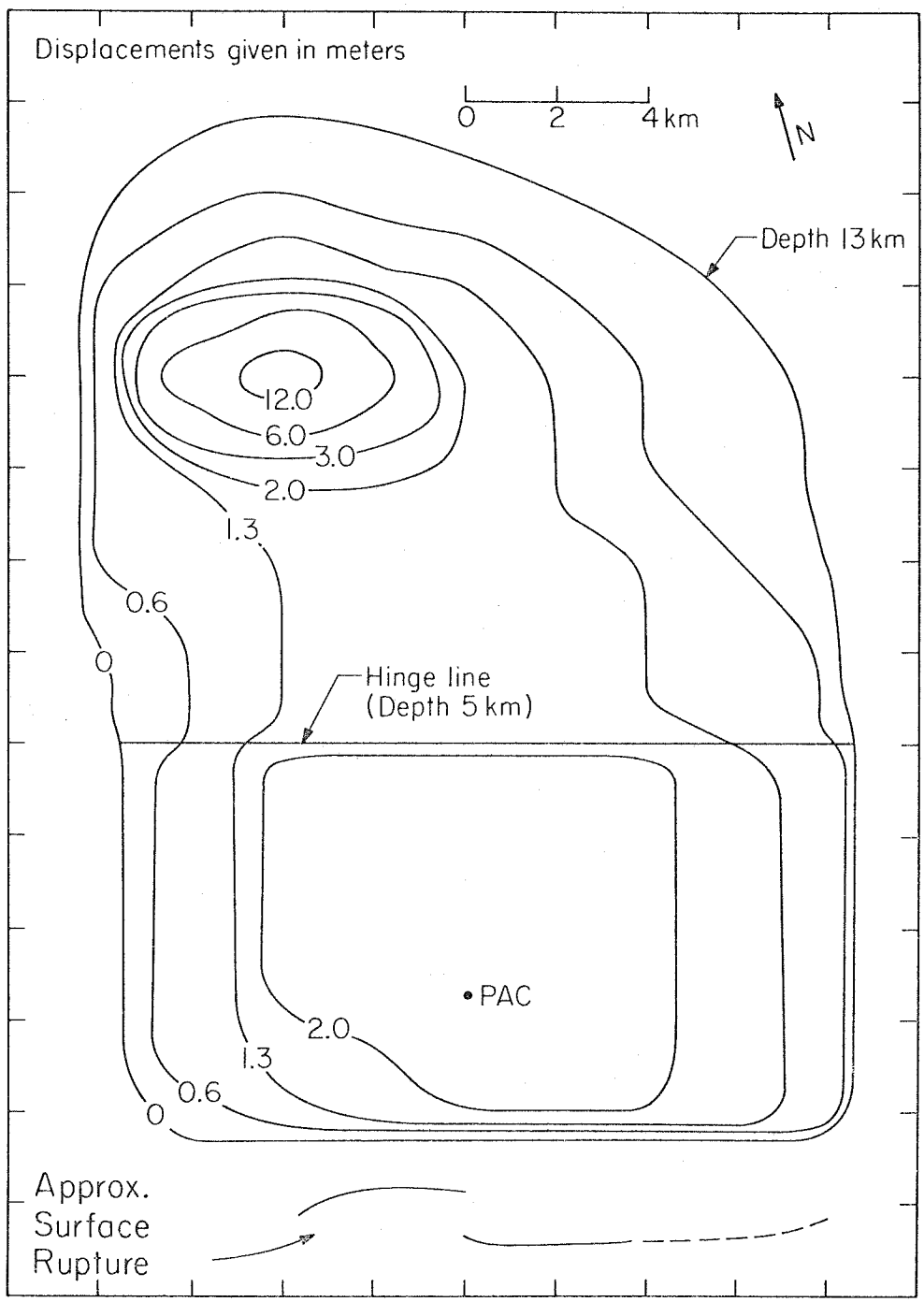

Figure 4.13. Contour map of assumed fault displacements for the model Norma 170. The rupture velocity is 1.8 km/sec and the hypocenter is near the region of maximum displacement.

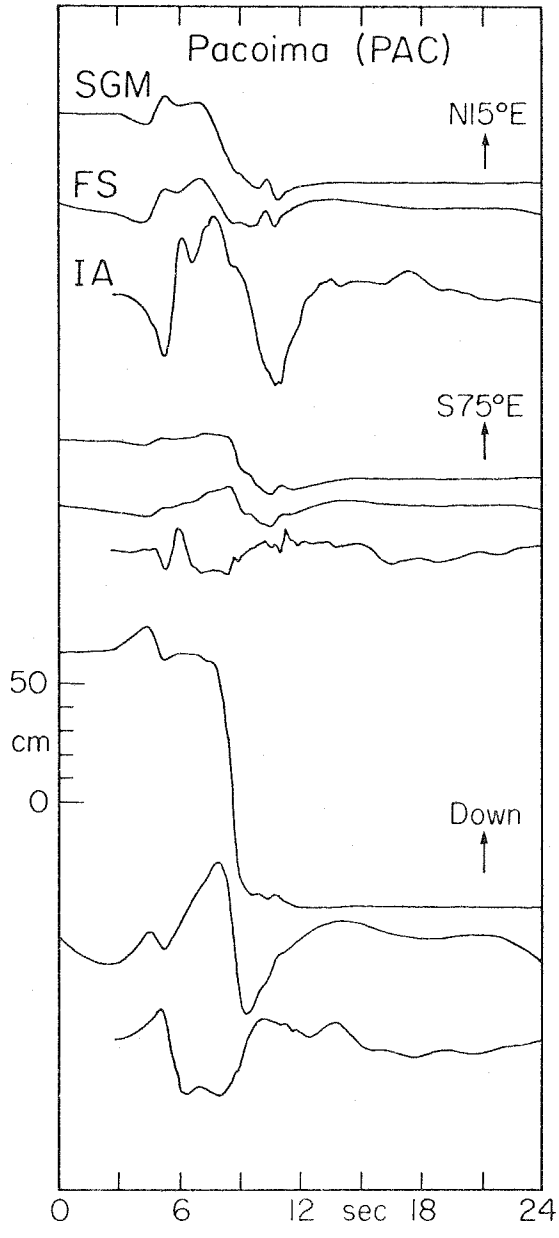

Figure 4.14

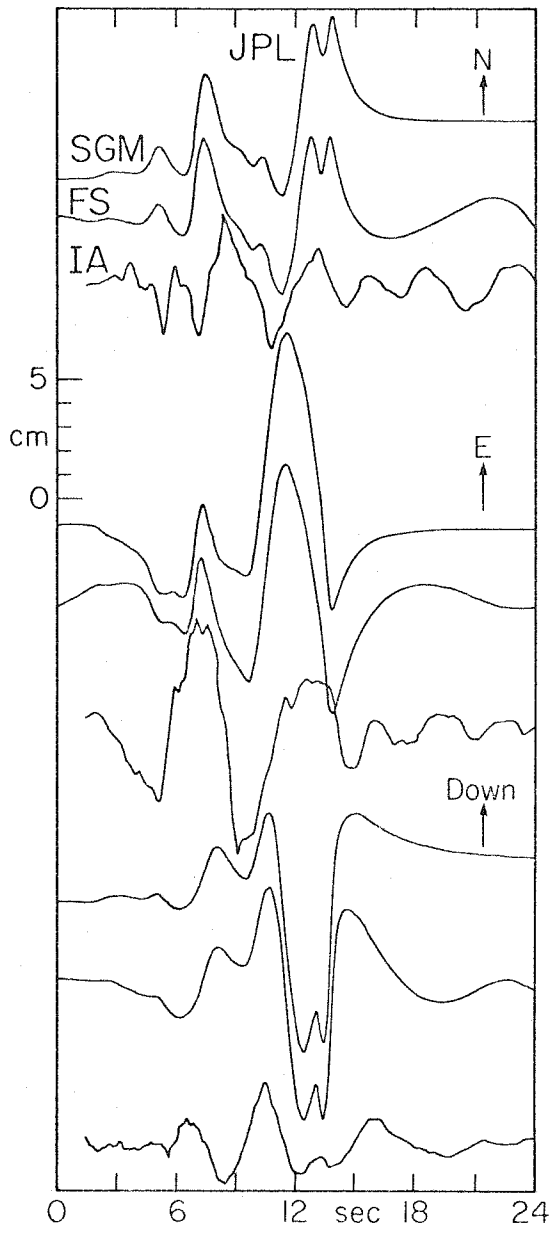

Figure 4.15

Comparison of observed and synthetic records for the model Norma 170, and the stations PAC and JPL. See Figure 4.9 for explanation of SGM, FS and IA.

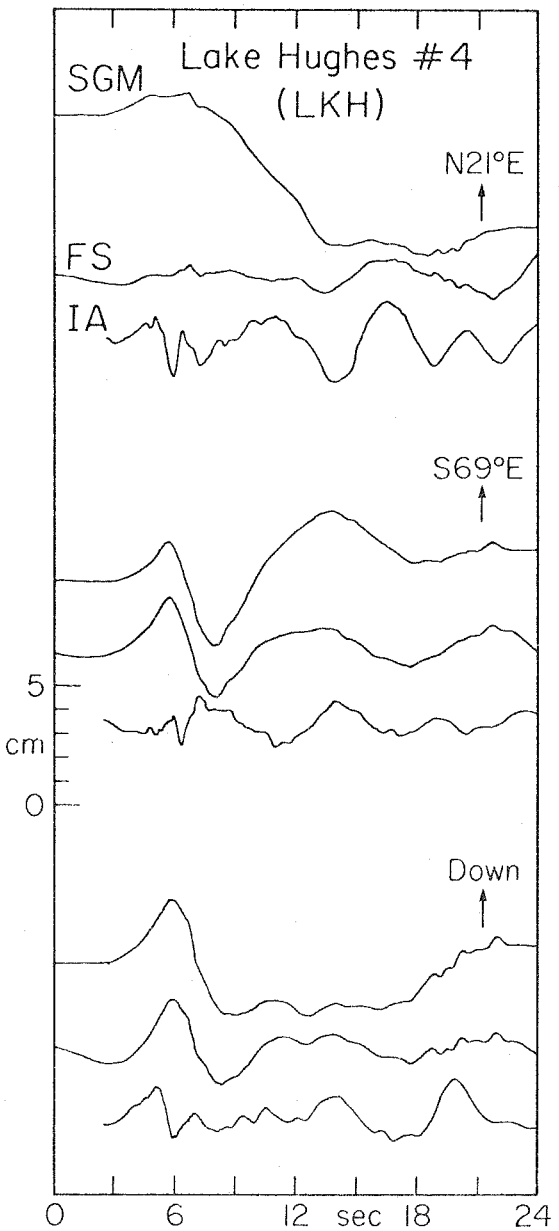

Figure 4.16

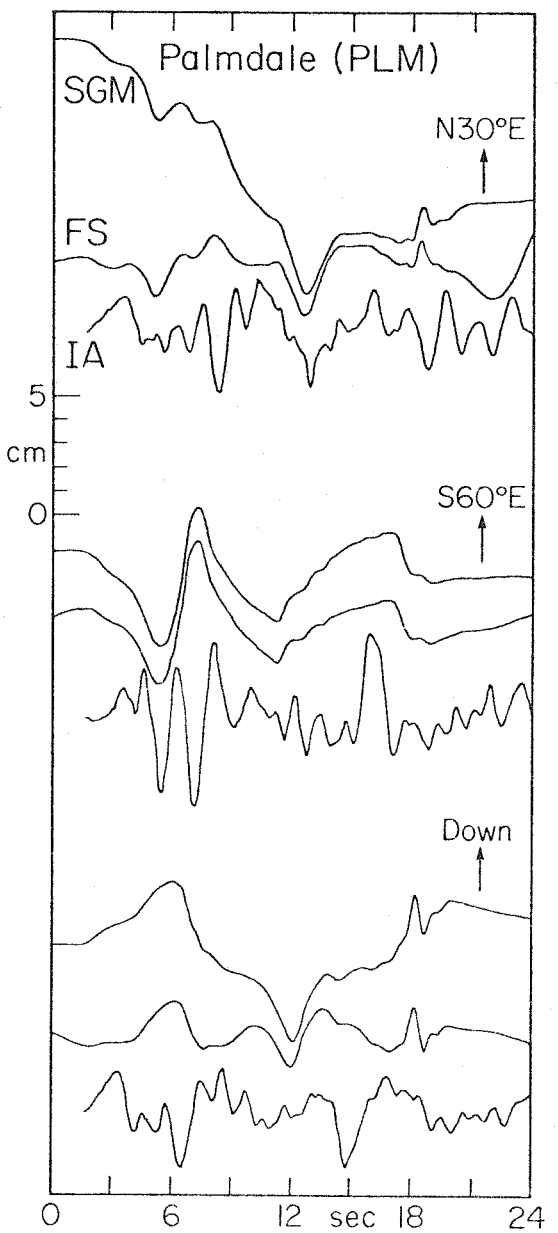

Figure 4.17

Comparison of observed and synthetic records for the model Norma 170, and the stations LKH and PLM. See Figure 4.9 for explanation of SGM, FS and IA.

pulse is now too large at LKH. We are in a dilemma. How can we make the first pulse large at JPL and PAC, and yet still keep it small at LKH and PLM? You have probably already guessed (or read it in the abstract) that directivity is our way out.

Before we get to the details of the lower fault, it is instructive to study the model Norma 170 with greater care. Remember that we have also got to find some way to improve the later part of the synthetics; particularly for the Pacoima records. Figures 4.18 through 4.29 show how the synthetics for Norma 170 were constructed. These figures may seem complicated and tedious, but a careful study of them is very rewarding. Each picture corresponds to one synthetic record. On the left, the fault is subdivided into the five strips designated A through E. The responses of each of these strips are shown and their sums, the synthetics for Norma 170, are shown at the bottom. This allows us to associate arrivals in the synthetics with particular parts of the fault. The middle and right hand columns contain the responses of point dislocations which are convolved with the far-field time functions shown. The durations of these time functions are 0.8 seconds and 3.0 seconds. The locations of these sources are shown to be in the middle of the various strips. The peak amplitudes of these point sources are shown next to each trace. This amplitude, given in cm, corresponds to a point source whose moment is $\pi \times 10^{26}$ ergs.

Notice that there is usually an excellent correspondence between the responses of the fault strips and the point responses which have been convolved with the 3.0 second time functions. Furthermore, it is fairly easy to identify individual arrivals on the short-period point responses,

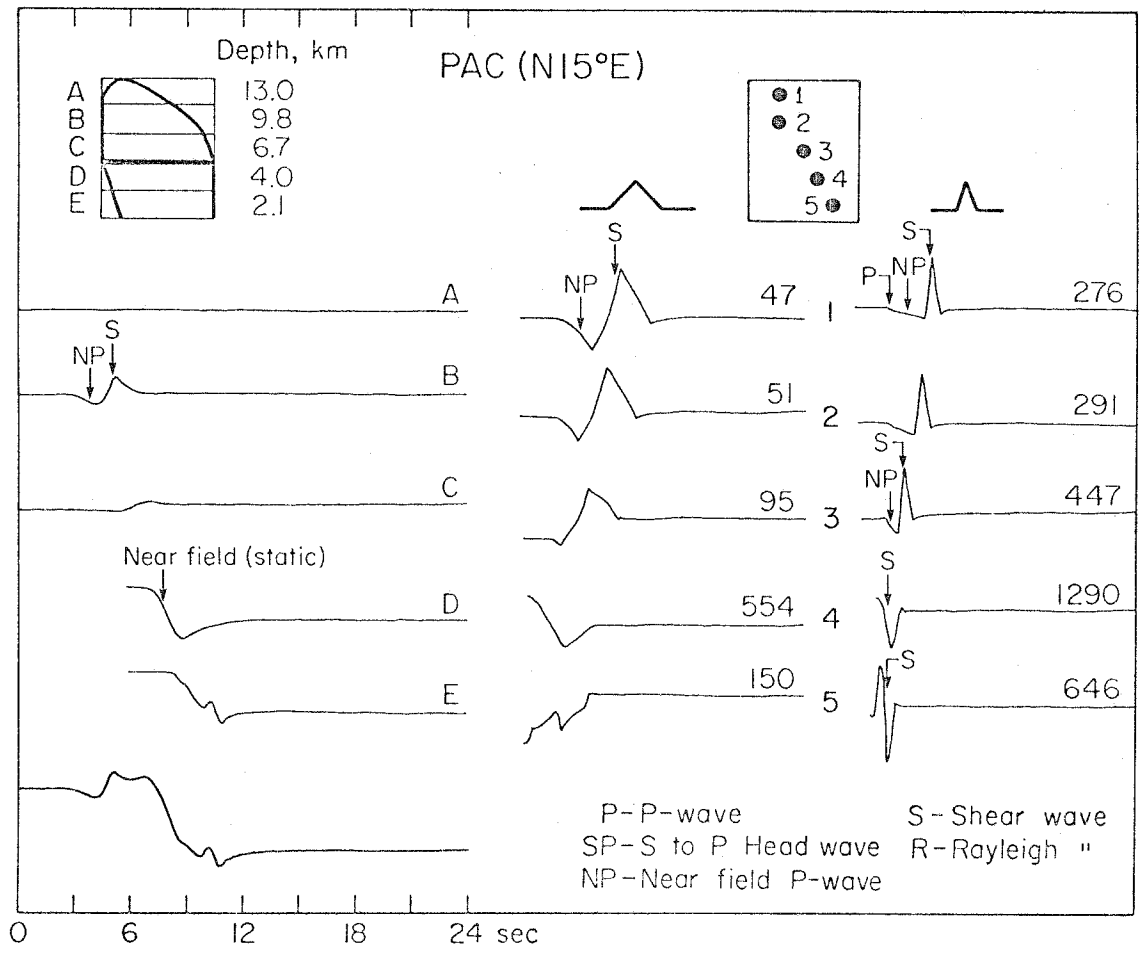

Figure 4.18. Decomposition of the N15°E component of synthetic ground motion for PAC and the model Norma 170. The finite fault is broken into five strips whose individual contributions are shown on the left. Responses of point sources which lie in these strips have been convolved with both 3 sec and 0.8 sec triangular far-field time functions and are displayed in the middle and on the right, respectively. The numbers signify peak displacements in cm for point sources having moments of $\pi \times 10^{26}$ ergs. By studying the point source responses, contributions of individual phases can be recognized in the synthetic motion from the finite fault.

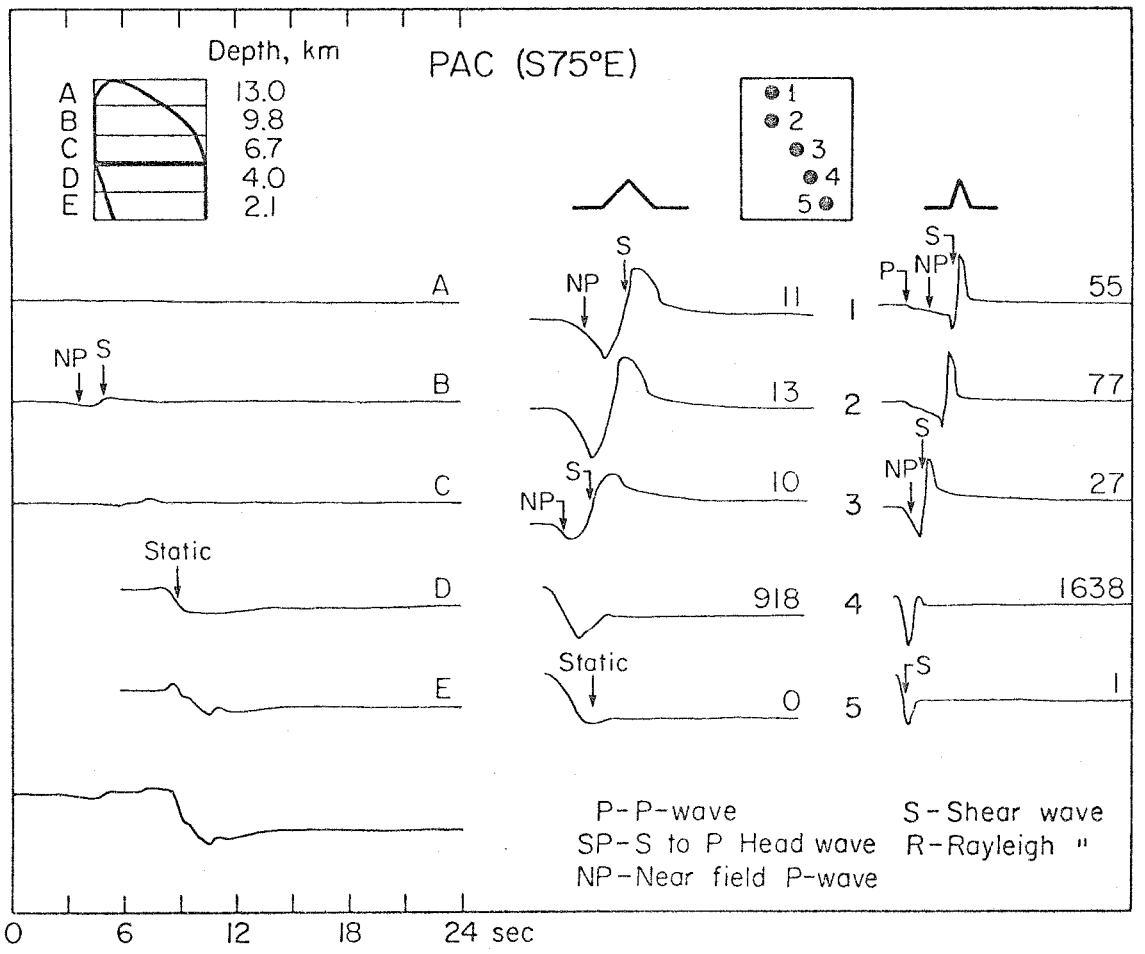

Figure 4.19. Decomposition of the S75°E component of ground motion for PAC and Norma 170. See Figure 4.18 for a more detailed explanation.

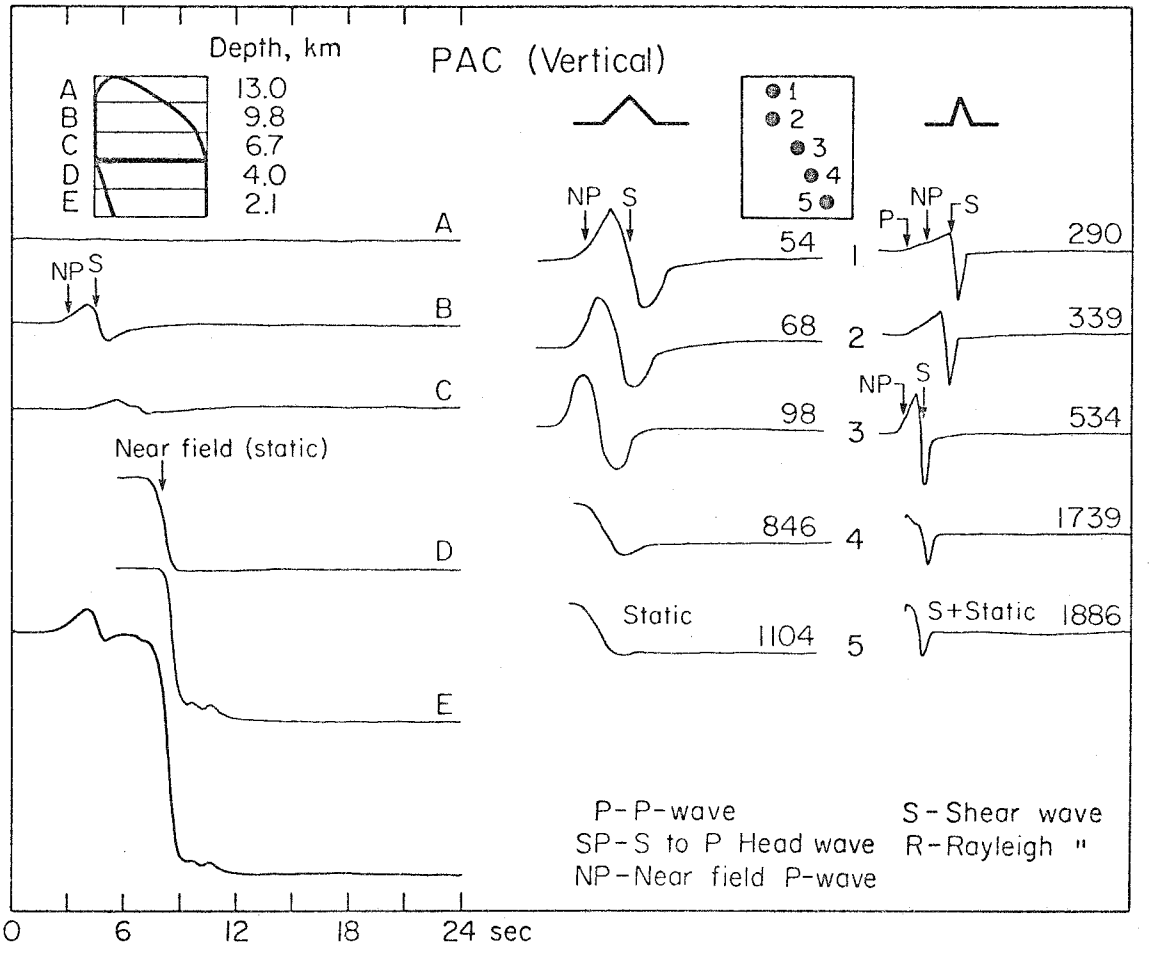

Figure 4.20. Decomposition of the vertical component of ground motion for PAC and Norma 170. See Figure 4.18 for a more detailed explanation.

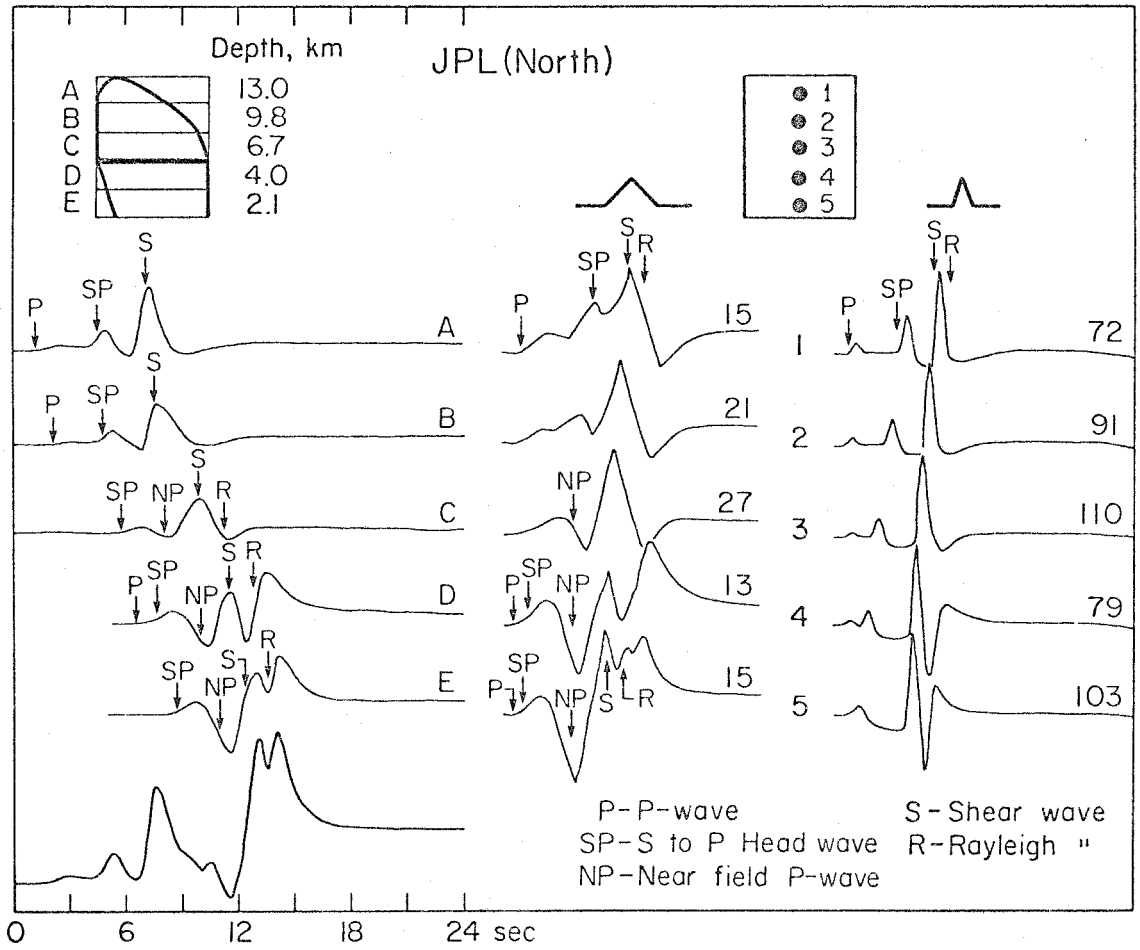

Figure 4.21. Decomposition of the North component of ground motion for JPL and Norma 170. See Figure 4.18 for a more detailed explanation.

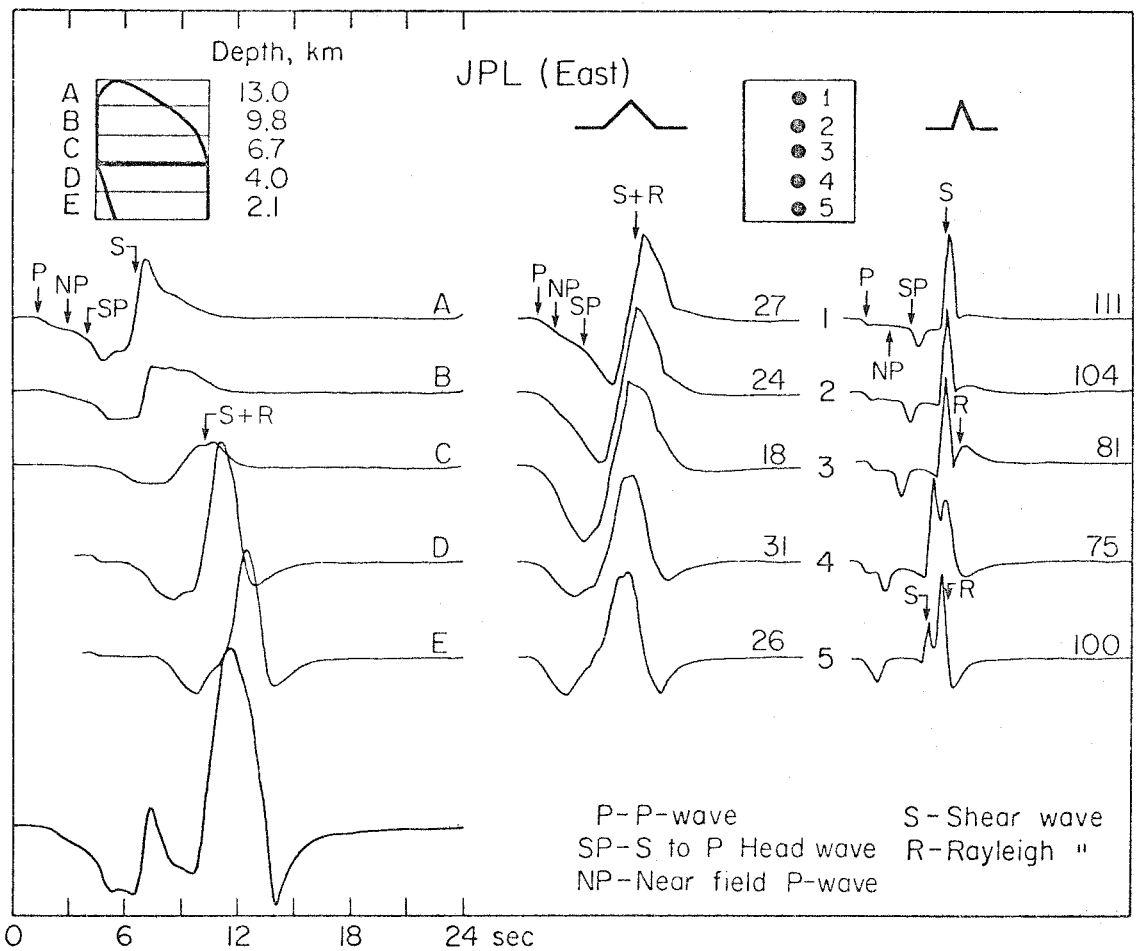

Figure 4.22. Decomposition of the East component of ground motion for JPL and Norma 170. See Figure 4.18 for a more detailed explanation.

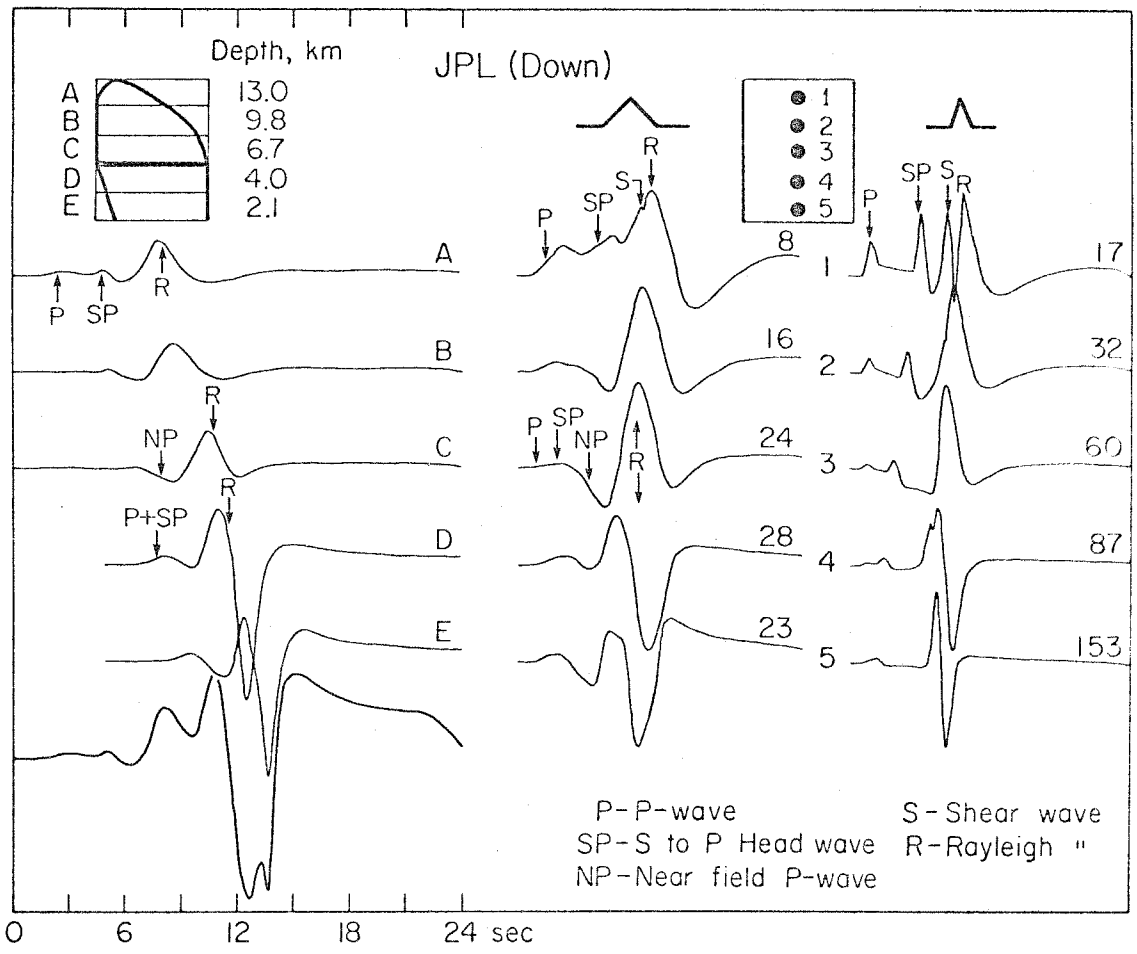

Figure 4.23. Decomposition of the vertical component of ground motion for JPL and Norma 170. See Figure 4.18 for a more detailed explanation.

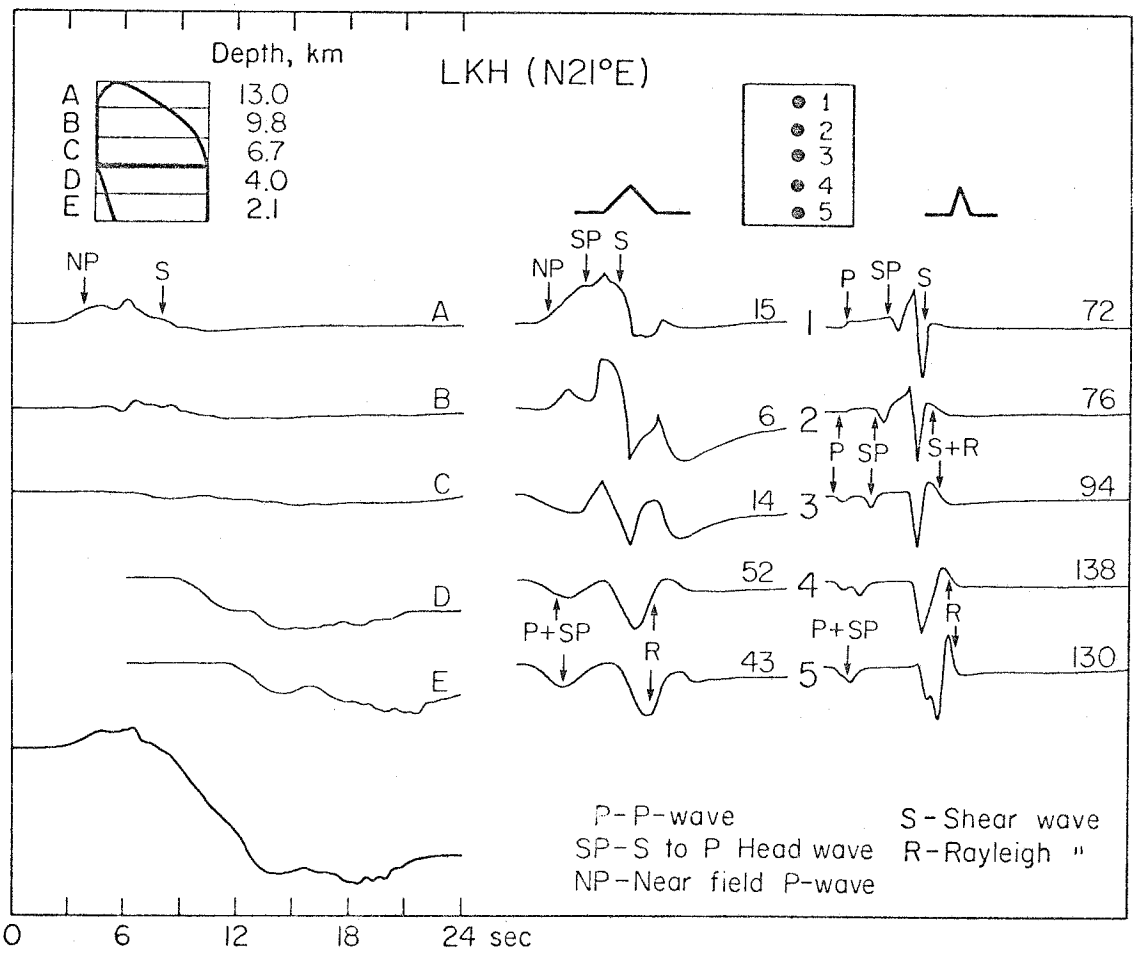

Figure 4.24. Decomposition of the N21°E component of ground motion for LKH and Norma 170. See Figure 4.18 for a more detailed explanation.

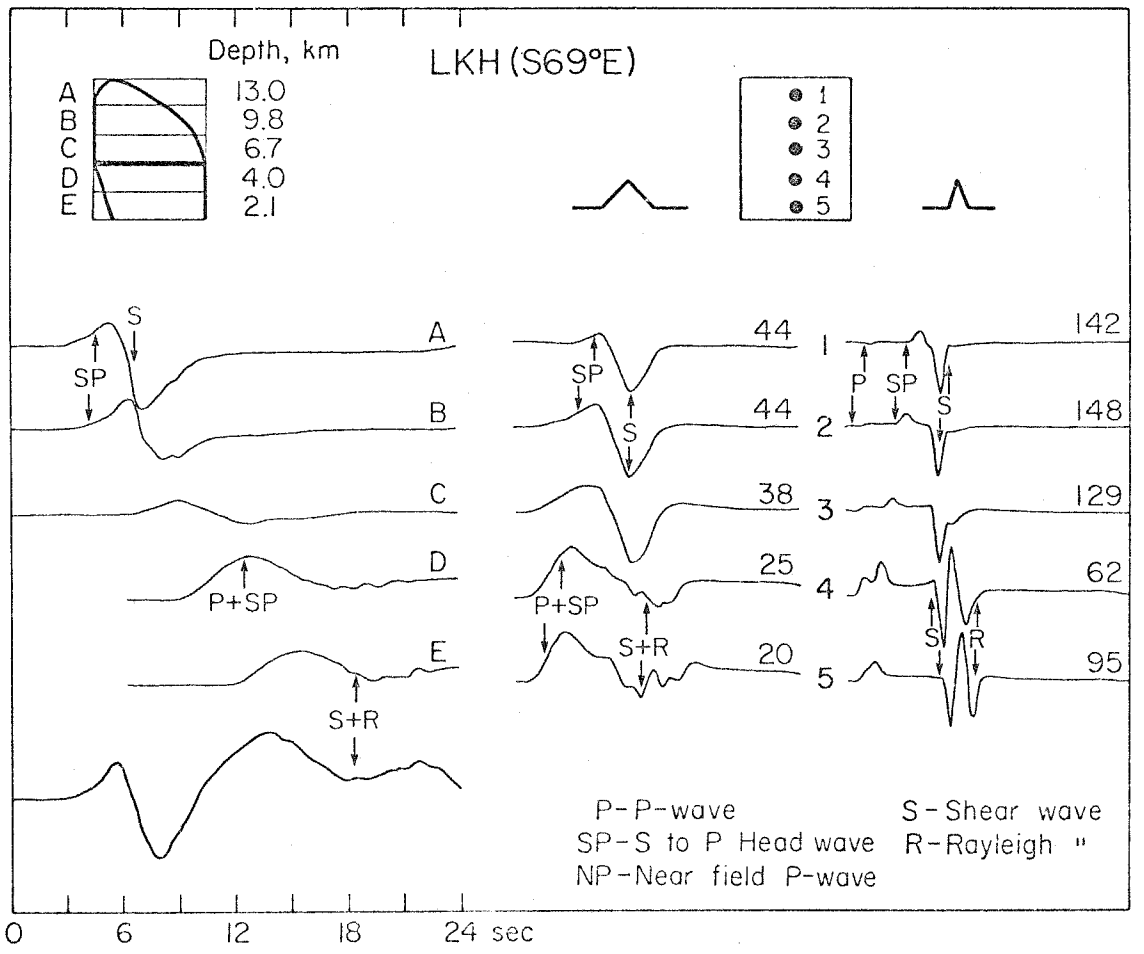

Figure 4.25. Decomposition of the S69°E component of ground motion for LKH and Norma 170. See Figure 4.18 for a more detailed explanation.

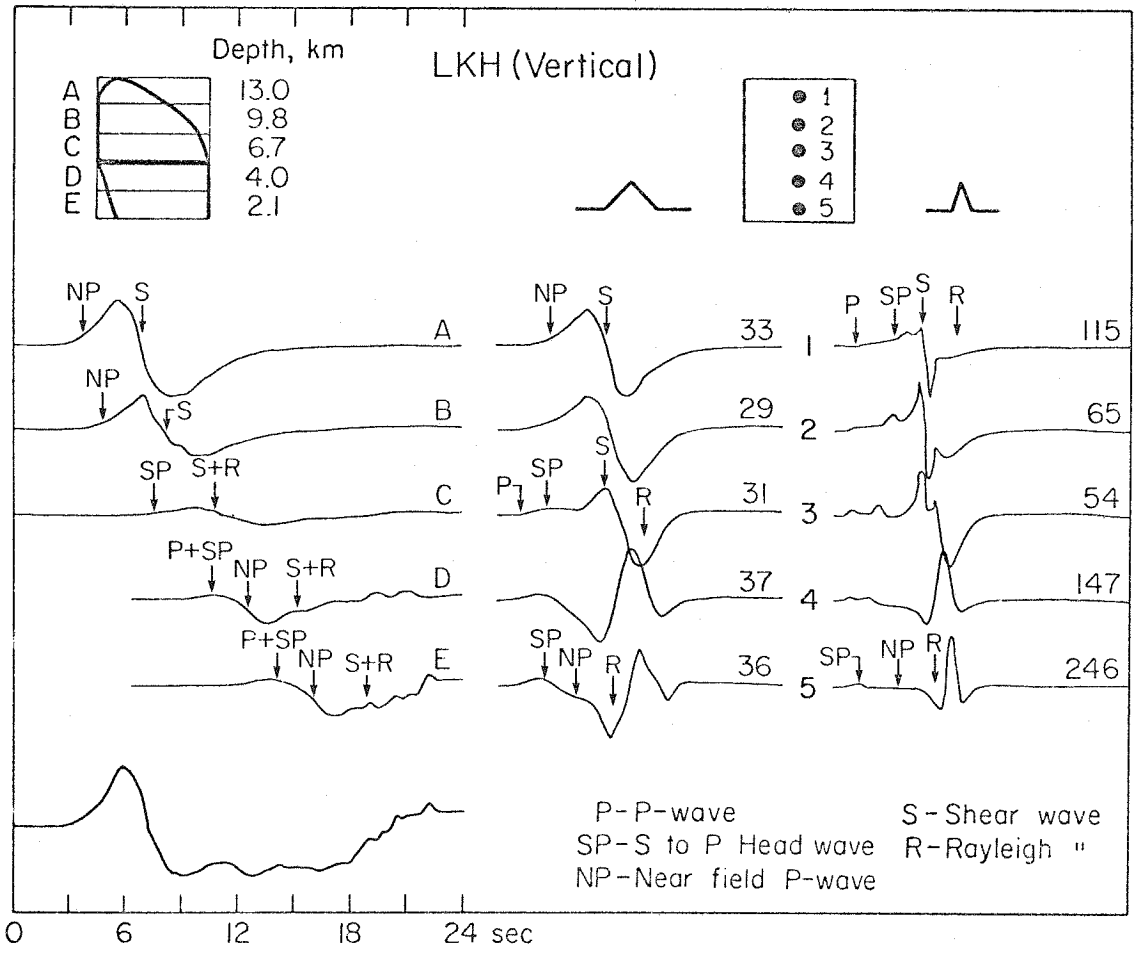

Figure 4.26. Decomposition of the vertical component of ground motion for LKH and Norma 170. See Figure 4.18 for a more detailed explanation.

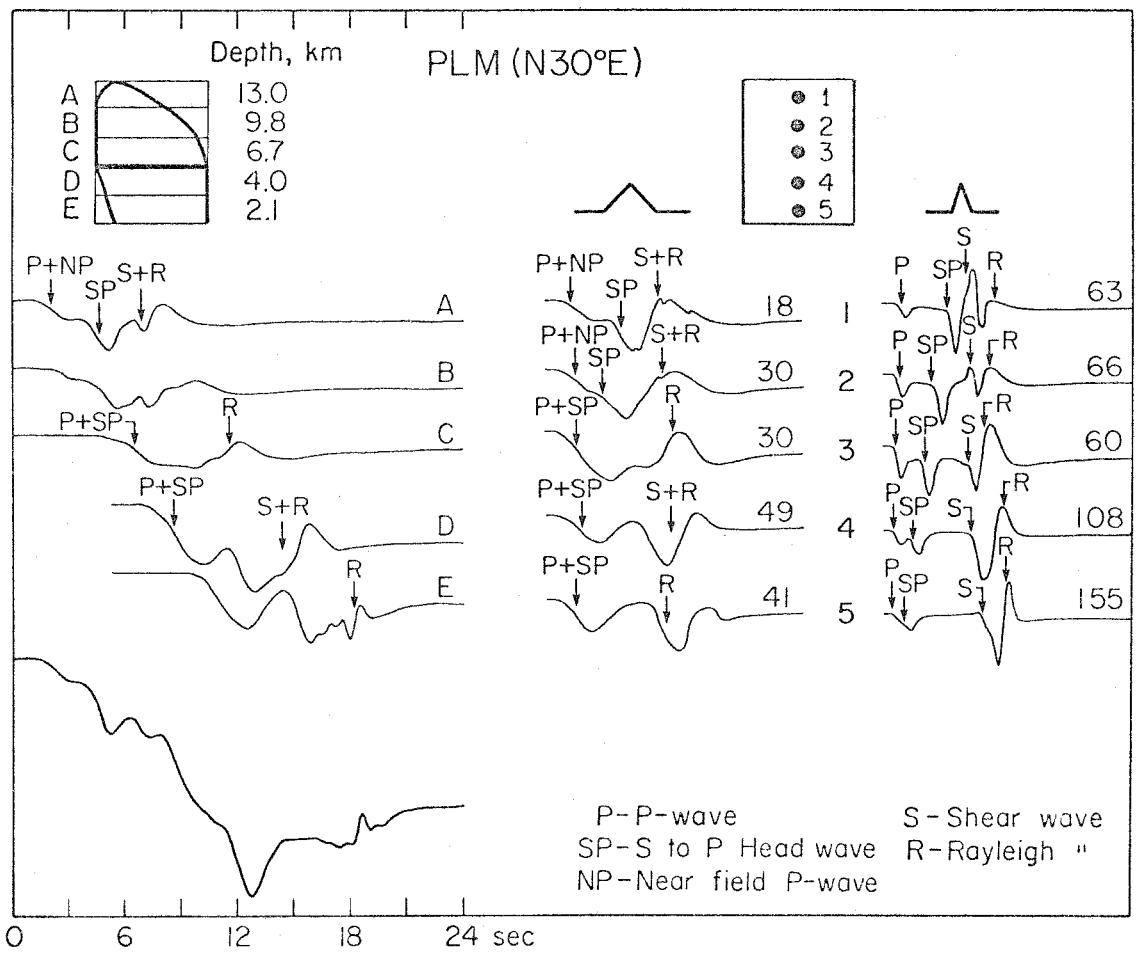

Figure 4.27. Decomposition of the N30°E component of ground motion for PLM and Norma 170. See Figure 4.18 for a more detailed explanation.

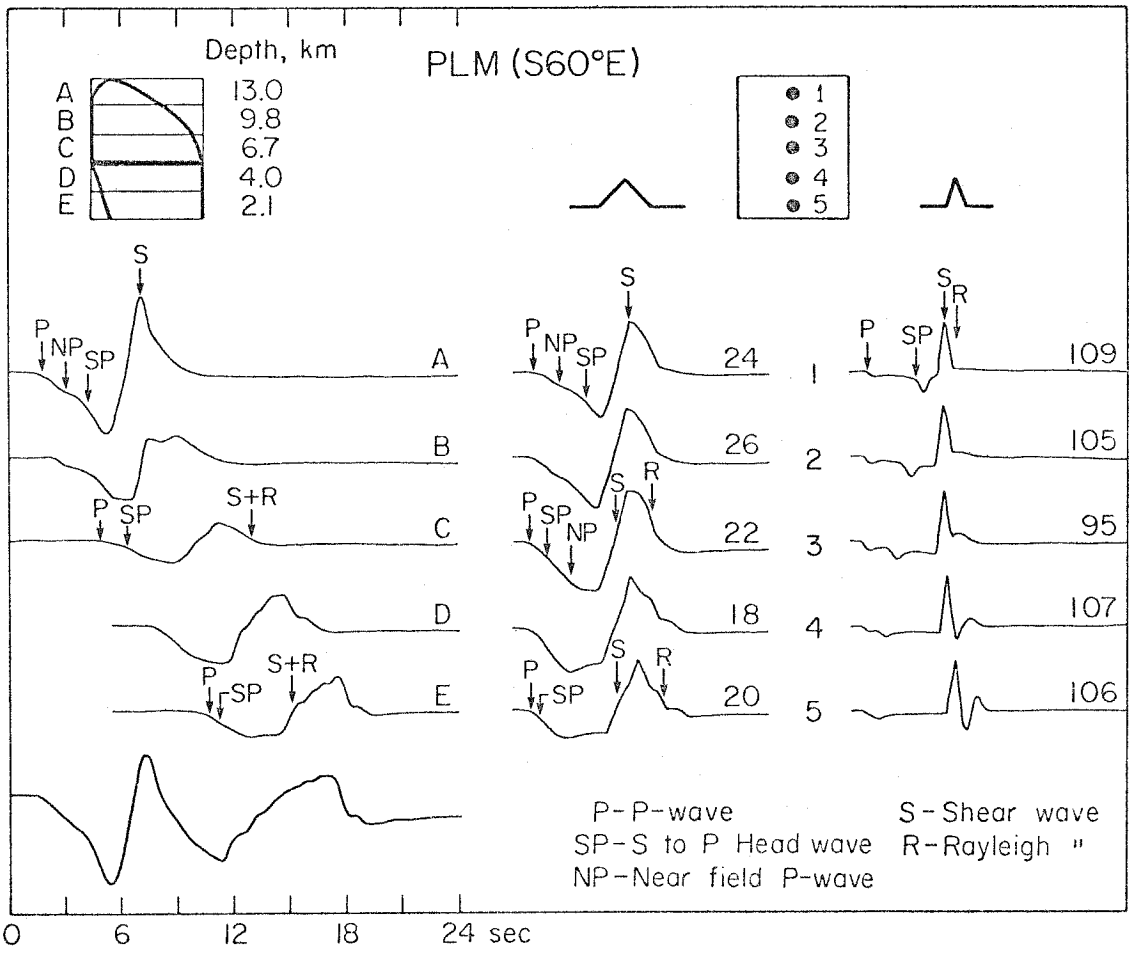

Figure 4.28. Decomposition of the S60°E component of ground motion for PLM and Norma 170. See Figure 4.18 for a more detailed explanation.

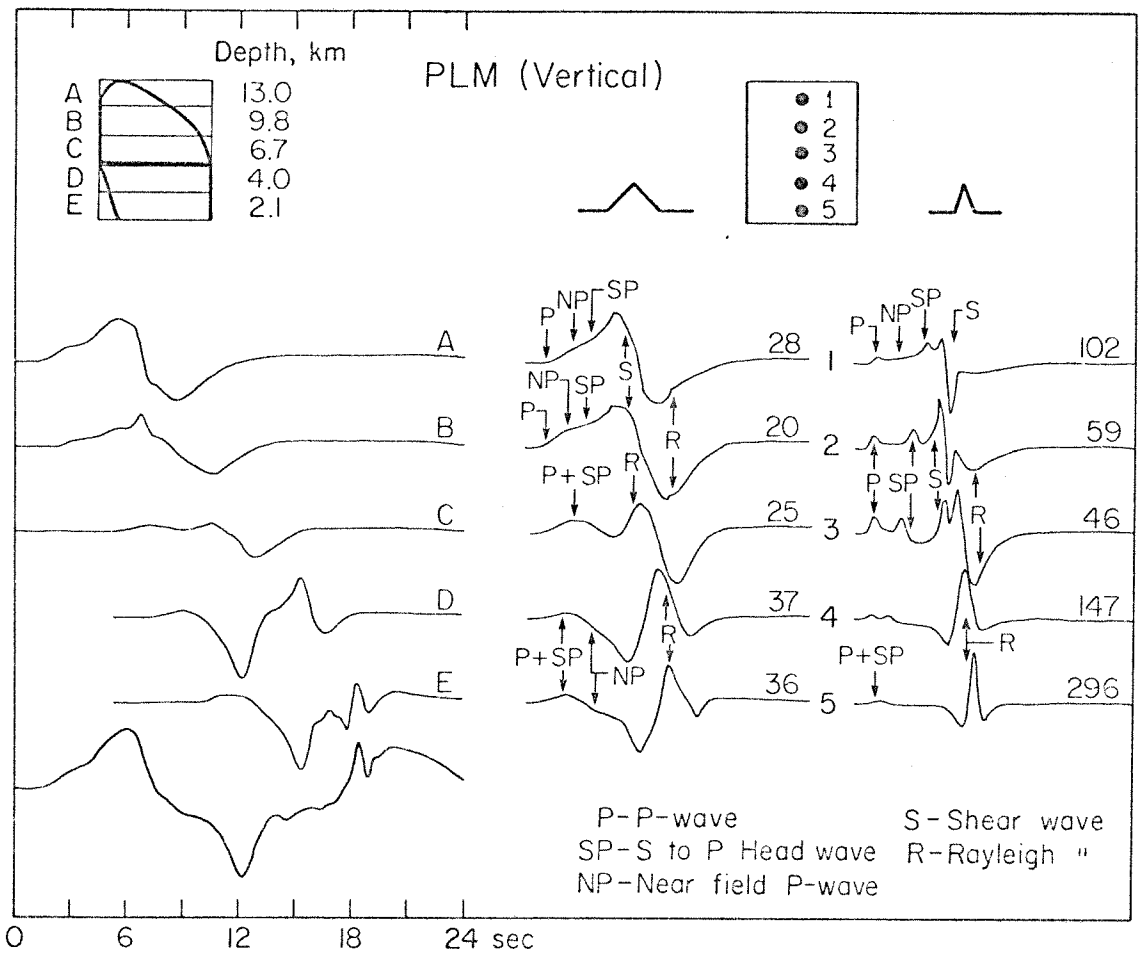

Figure 4.29. Decomposition of the vertical component of ground motion for PLM and Norma 170. See Figure 4.18 for a more detailed explanation.

which in turn allows us to identify arrivals on the long-period responses and on the responses of the fault strips.

Let us begin by studying the response of the lower fault. We have already pointed out that a major problem is the relative amplitudes of the first pulses seen at PAC and LKH. We can see that the first pulse at PAC consists of a near-field P wave which is followed immediately by the far-field shear wave. At LKH, this pulse is formed by the positive interference of the S to P head wave and the near-field P wave. They are directly followed by a post-critical angle shear wave (for a better discussion of the nature of these arrivals, see Chapter 1). Now look at the vertical responses for the deepest point source for the stations PAC and LKH. The ratio of the amplitudes of the vertical components of the PAC and LKH point responses is on the order of 2:1. Now notice that the ratio of the amplitudes of the first vertical pulse that was observed at PAC and LKH was on the order of 20:1! Clearly, there will be trouble explaining this pulse with a deep point source. This observation is crucial to the construction of our later models in which we optimize directivity effects for PAC and LKH.

An interesting consequence of our preceding discussion is that we have discovered a way to easily add high-frequency pulses to northern station records without seriously affecting the synthetics for the southern stations. We can incorporate several short duration events into our model. If these extra events had a moment of only 10^{25} ergs, they could cause visible short duration pulses on the northern stations. Actually the motions observed at LKH are so small and long period, that we suspect that the rupture is fairly coherent.

We will now examine the upper section of the fault in more detail. Since PAC lies only 2.5 km above the fault plane, it is very sensitive to the time history of this upper plane. It is easy to see that the near-field terms, or more specifically, the static parts of the solution, are beginning to dominate over the far-field terms. Particularly large static displacements occur on the vertical component. If we look back to Figure 4.4, then we see that this large vertical offset cannot be seen in the observed records. We can also see that it would be nice if we could produce a similar pulse on the north component of motion. By carefully studying many point responses as well as static solutions for finite faults in a homogeneous half-space (Mansinha and Smylie, 1971), we were able to deduce that as the rupture proceeds towards and just beneath PAC, large static vertical displacements will inevitably occur. Obviously, the way to alleviate the problem of large vertical displacements at PAC is to require that the fault offsets are small for those parts of the fault which are beneath PAC. If the faulting is small beneath PAC, then where does the moment of the upper fault come from? By studying the static solutions, we discover that large displacements to the south would be observed at PAC if there was significant faulting on the very shallowest parts of the fault. Conveniently, a large offset to the south will help explain the north component of motion observed at PAC.

We have studied the inadequacies of Norma 170 and have decided that the following features should have been included: 1) greater directivity on the lower fault to explain the beginning pulses seen

at LKH and PAC; 2) small fault offsets beneath PAC to explain the vertical record at PAC; 3) large fault offsets south of PAC to explain the north component of PAC.

In Figure 4.30 we show a model, Norma 163, which incorporates the features which we have just mentioned. The source parameters for this model are summarized in Table IV.1. The comparisons of observed and synthetic records are shown in Figures 4.31 through 4.34. Clearly Norma 163 fits the records much better than our previous models. This is no accident, since in reality, we tested many other models before arriving at Norma 163. This is not to say that Norma 163 is the best half-space model possible, but it is the best we found before tiring of the game.

There are many details included in Norma 163 and some of these are rather arbitrarily chosen. We will, however, try to justify certain features of this model. Let us begin by examining the lower fault for Norma 163. We have increased the rupture velocity to 2.8 km/sec. There are several reasons for doing this. It substantially increases the amplitude of the shear wave at PAC without increasing the amplitude at LKH; that is, it enhances directivity. It also allows the timing of arrivals from the upper fault at PAC to be compatible with a hypocentral depth of 13 km. Notice that the hypocenter is almost due north of Pacoima and that the faulting seems to be skewed with respect to a line directly down the dip. This has two effects. The first is to produce the beginning pulse seen on the S75°E record of PAC. This pulse disappears when the faulting is aligned directly down the dip. The

Table IV.1

Source Parameters for Norma 163

	Lower Segment	Upper Segment
Depth of hinge (km)	5.0	
Strike	-75°	-75°
Dip	53°	29°
Rake	76°	90°
Rupture velocity (km/sec)	2.8	1.8
Rise time (sec)	0.8	0.8
Moment (x 10^{26} ergs)	0.8	0.6
Hypocentral longitude	118.41°E	118.33°E
Hypocentral latitude	34.44°N	34.42°N
Hypocentral depth (km)	13.	13.

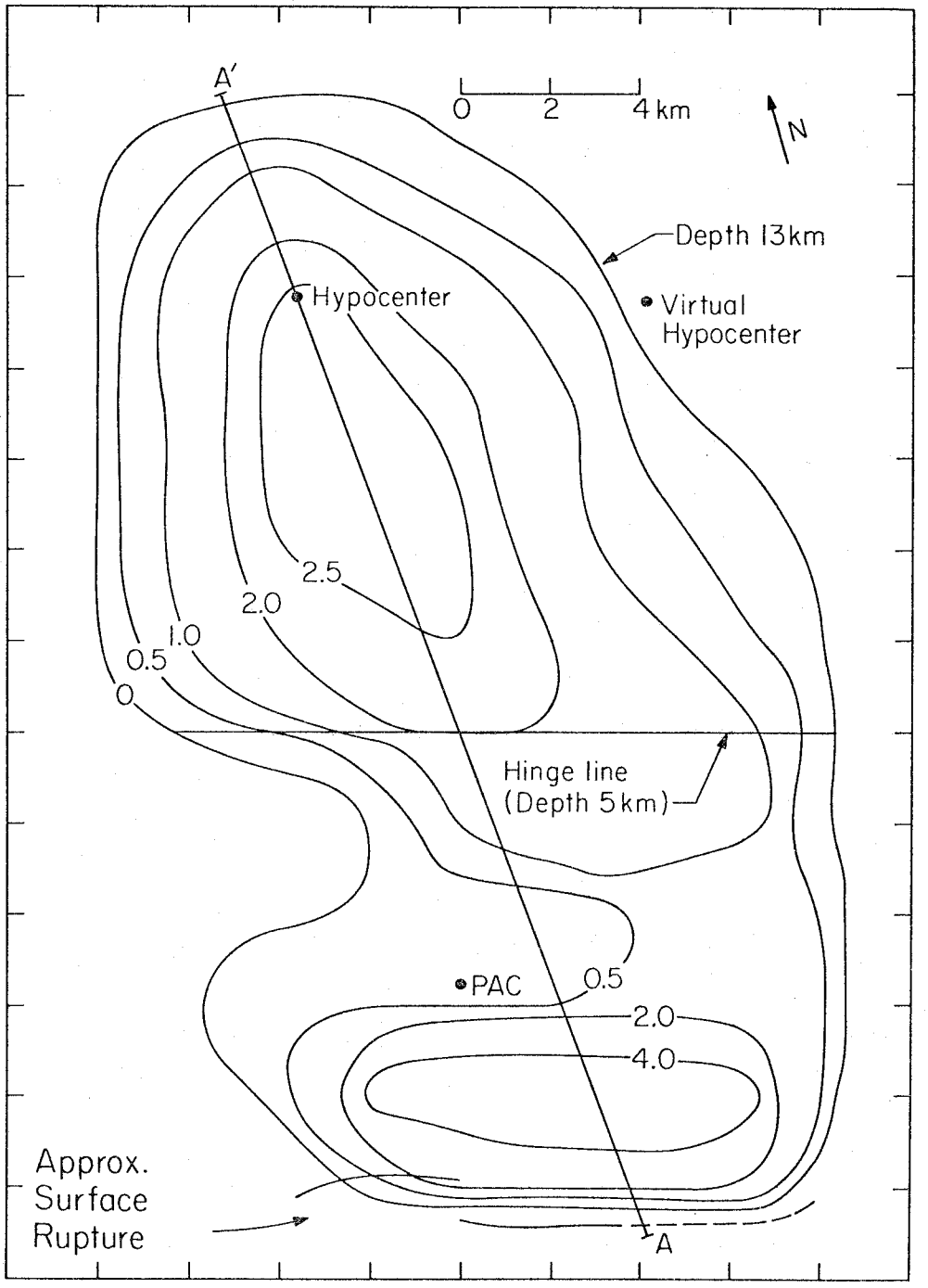

Figure 4.30. Contour map of the assumed fault displacements for the model Norma 163. The details of the rupture process are described in Table IV.1.

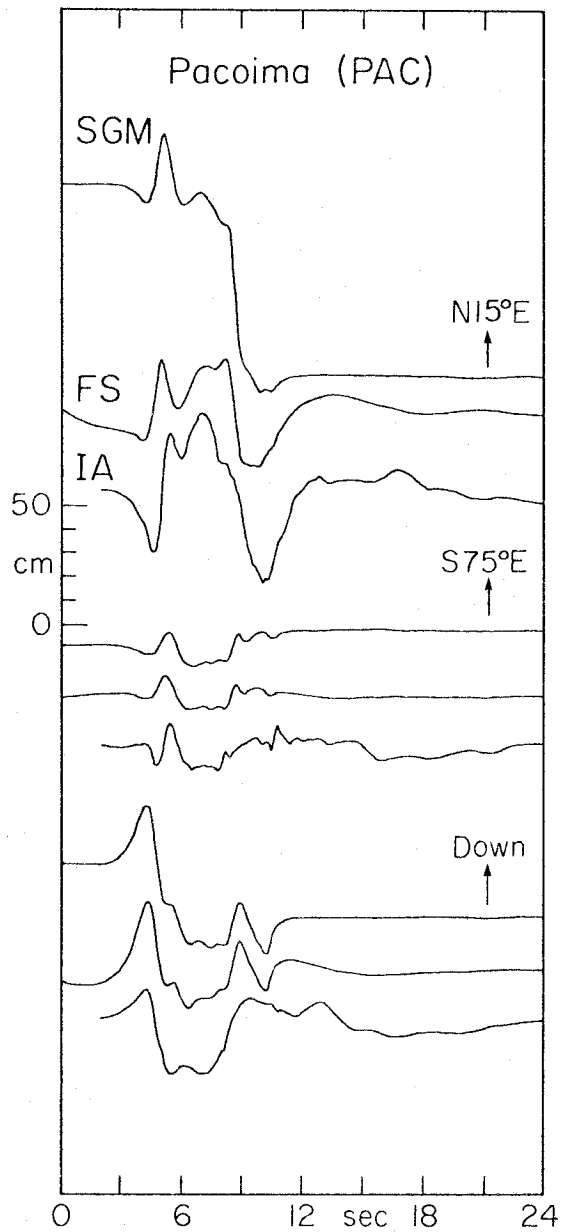

Figure 4.31

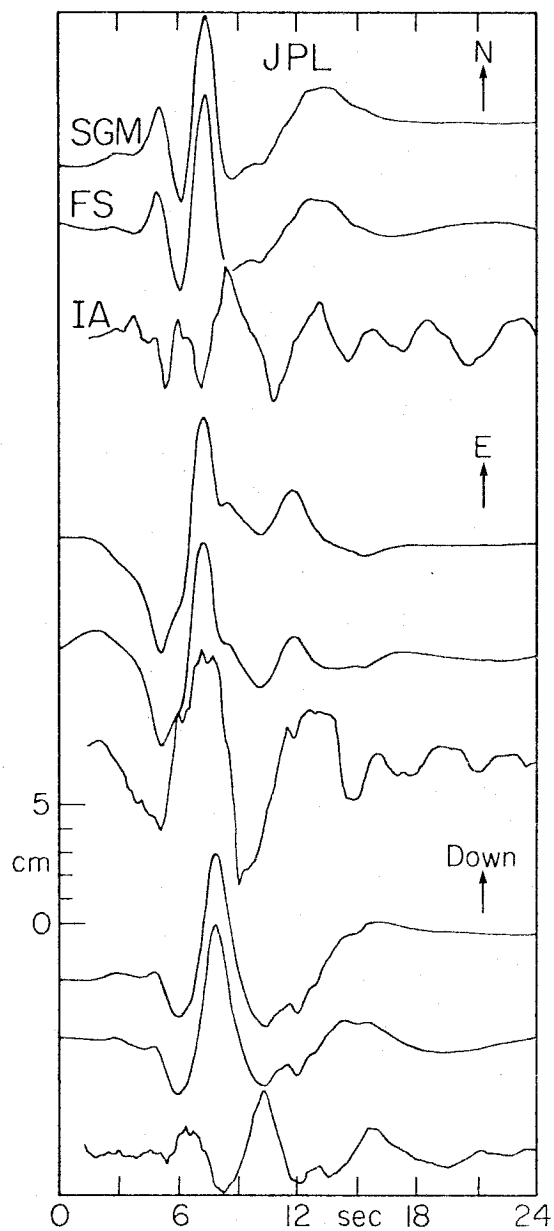

Figure 4.32

Comparison of observed and synthetic records for the model Norma 163, and the stations PAC and JPL. See Figure 4.9 for explanation of SGM, FS and IA.

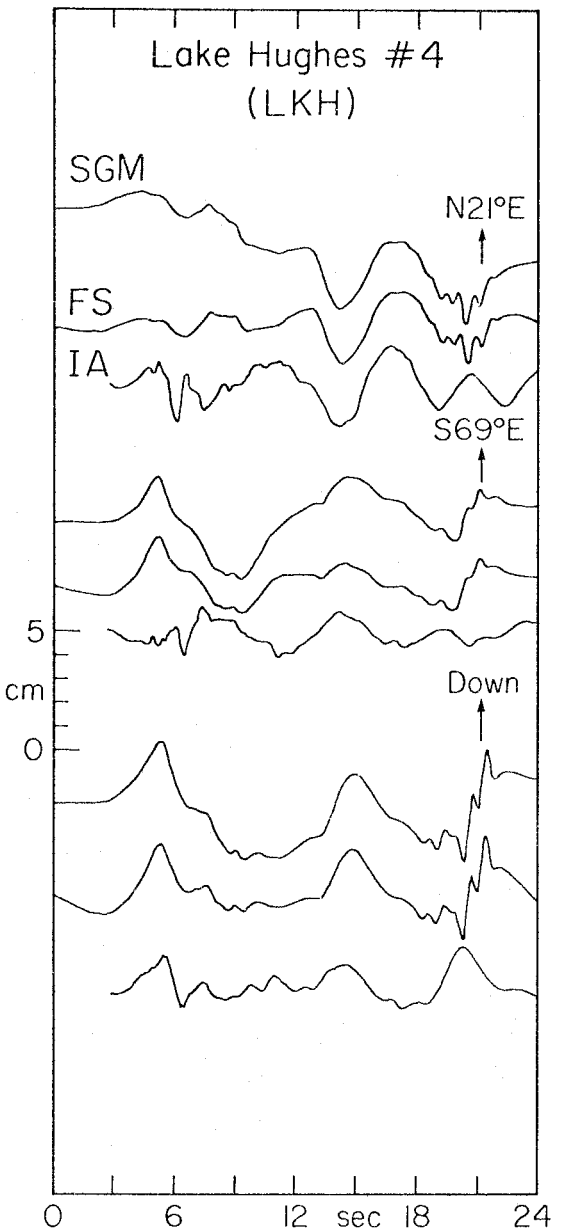

Figure 4.33

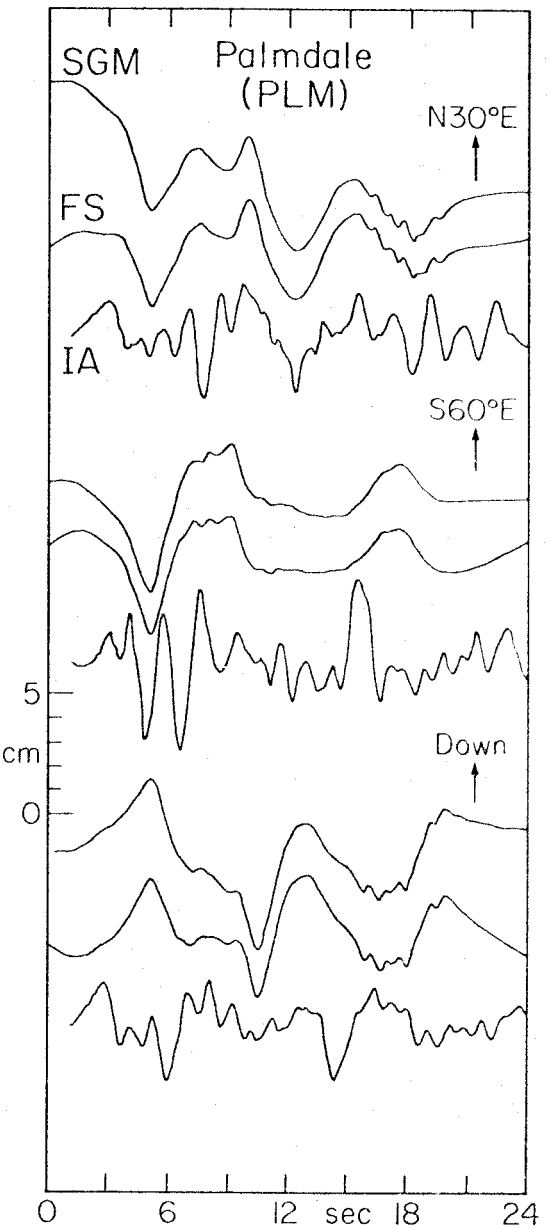

Figure 4.34

Comparison of observed and synthetic records for the model Norma 163, and the stations LKH and PLM. See Figure 4.9 for explanation of SGM, FS and IA.

polarity of this pulse is reversed if the faulting is skewed to the east of the down-dip direction. A second effect is that directivity decreases the amplitude of the first pulse seen at LKH.

The faulting in Norma 163 is predominantly unilateral upwards and this, again, is to optimize directivity effects. We will delay a closer look at this particular problem until a little later. Notice that the 2 meter contour in Figure 4.30 is elongated towards PAC. Again, this increases directivity effects. If the fault width is increased significantly, then the ratio of LKH to PAC amplitudes quickly decays. We are pleasantly surprised to discover that this ratio can help constrain the horizontal dimensions of faulting.

Details used on the upper fault plane are based mostly on an analysis of the PAC records. The hypocenter for the upper fault is equidistant from the hypocenter on the lower fault, but it has been shifted eastward. Thus the direction of rupture propagation changes from a southerly to a south-southwesterly direction at the hinge line. This is a detail which improves the comparison of the synthetic and observed S75°E records. Although it makes the records look better, evidence for this change is hardly definitive. The rupture velocity on the upper fault is reduced to 1.8 km/sec so that the rupture can be continuous across the hinge line and still arrive at the surface with the correct timing. This feature is also not unique. Perhaps the rupture velocity is high and the large event at the top is actually a slightly delayed second shock.

At stations other than PAC, the largest arrival from the upper fault is a Rayleigh wave. Our Rayleigh velocity is the half-space

Rayleigh velocity which is probably significantly higher than the Rayleigh velocity for the real earth which has lower velocities near the surface. We have included a 2 second delay for all arrivals from the upper fault for the three stations, JPL, LKH and PLM. Although this is a rather unsatisfactory way to model slower surficial seismic velocities, it does improve the relative timing of the synthetic JPL records.

Notice that Norma 163 significantly improves the comparison between observed and synthetic records for later portions of the LKH records. This is due to added character of the upper fault. The PLM records do not look much better than they did before, but again, we feel that they are seriously affected by local structure.

Although we used a 0.8 second rise time throughout the fault, there is some justification for a rise time nearer to 2 seconds on the uppermost part of the fault. It appears that the southward displacement at PAC occurs too quickly. This could be alleviated by a longer rise time or perhaps a slower or less coherent rupture process.

In Figures 4.35 through 4.46 we show detailed interpretations of each of the synthetic records for the model, Norma 163. These figures are very similar to the previous set of Figures 4.18 through 4.29. Since the very top of the fault has become so important, we have included a sixth strip which shows the response of the shallowest section of the fault. As before, the middle row of responses shows point source responses which are convolved with a 3 second triangular far-field time function. Peak amplitudes (in cm) are shown for a moment of $\pi \times 10^{26}$ ergs. The right-hand column of responses contains far-field step function responses.

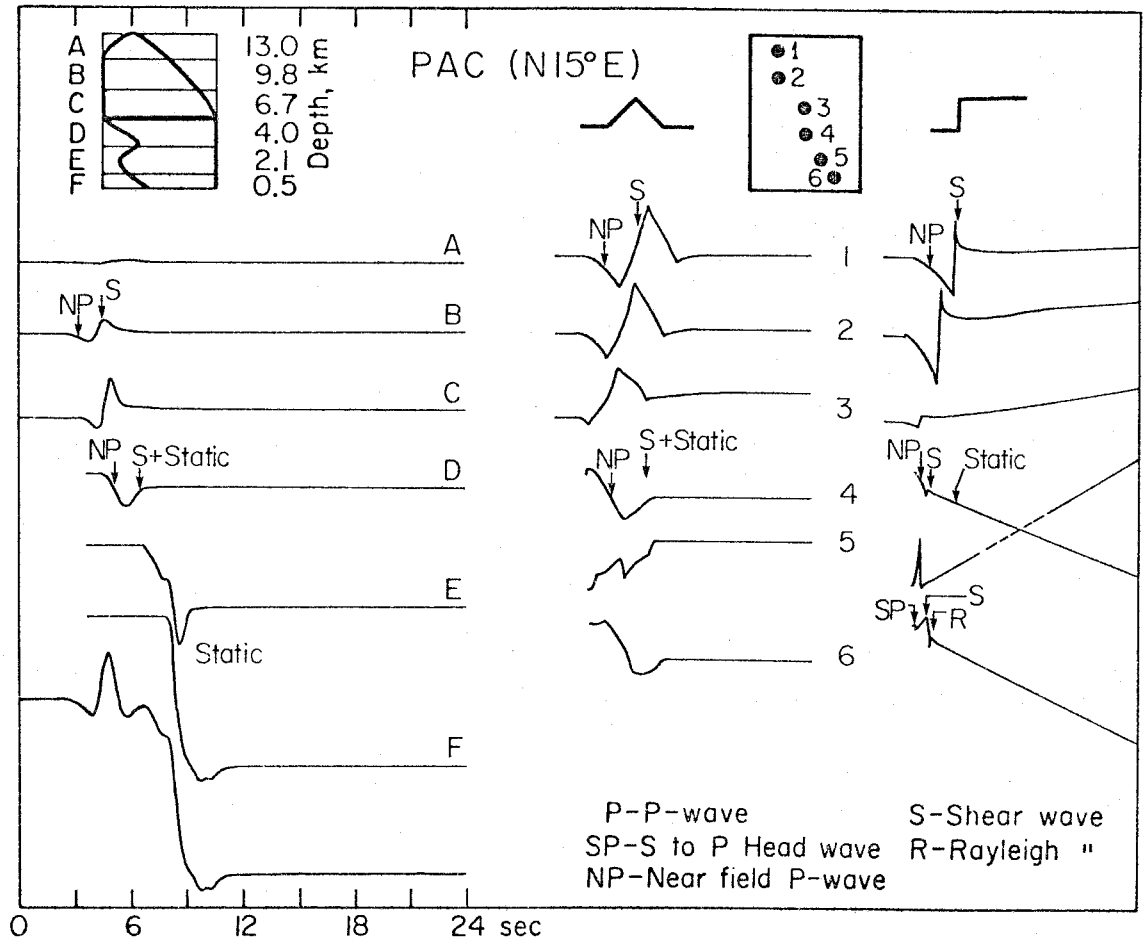

Figure 4.35. Decomposition of the N15°E component of synthetic ground motion for PAC and the model Norma 163. The finite fault is broken into six strips whose individual contributions are shown on the left. Responses of point sources which lie in these strips have been convolved with 3 sec triangular far-field time functions and are displayed in the middle column. A moment of $\pi \times 10^{26}$ ergs was assumed and the corresponding amplitude is shown next to each trace. Far-field step-function responses for the same point sources are shown in the right-hand column.

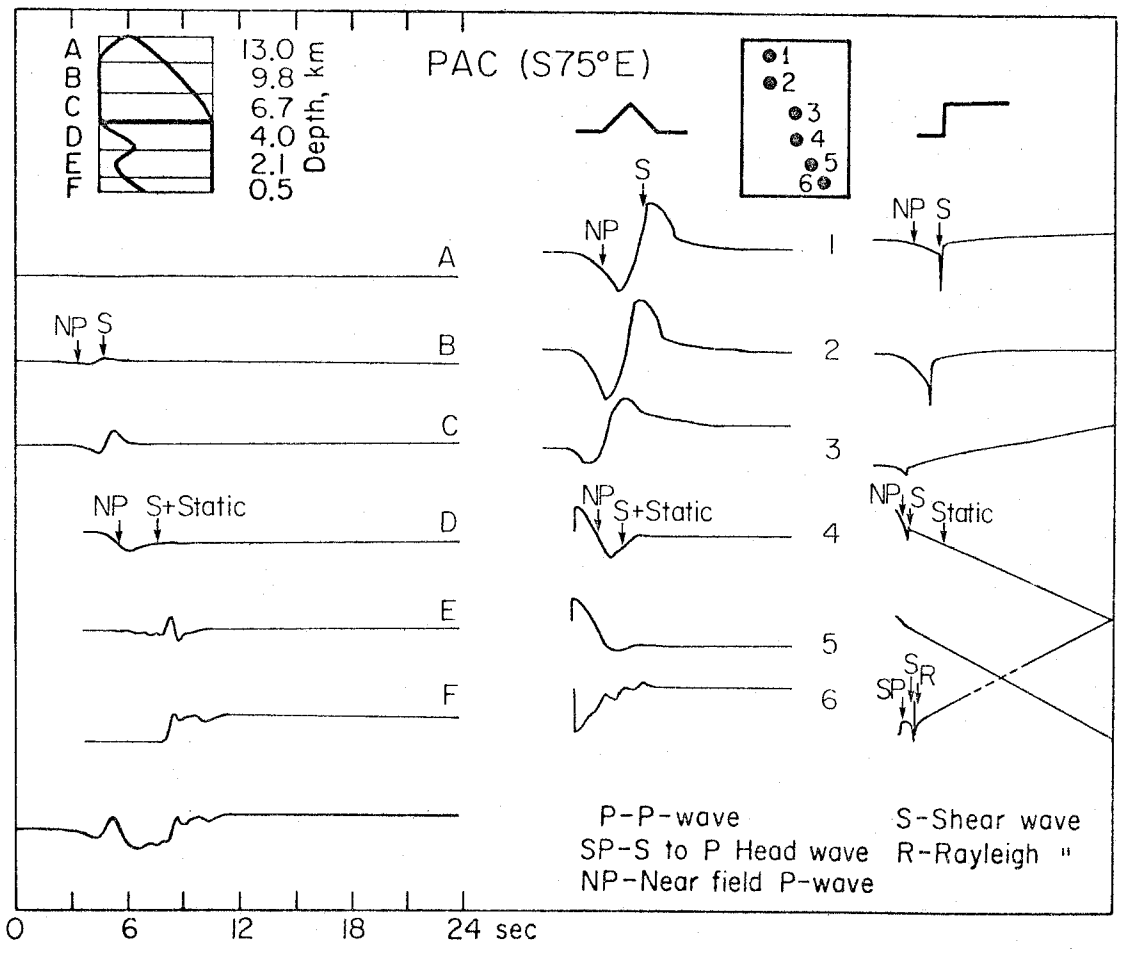

Figure 4.36. Decomposition of the S75°E component of ground motion for PAC and Norma 163. See Figure 4.35 for a more detailed explanation.

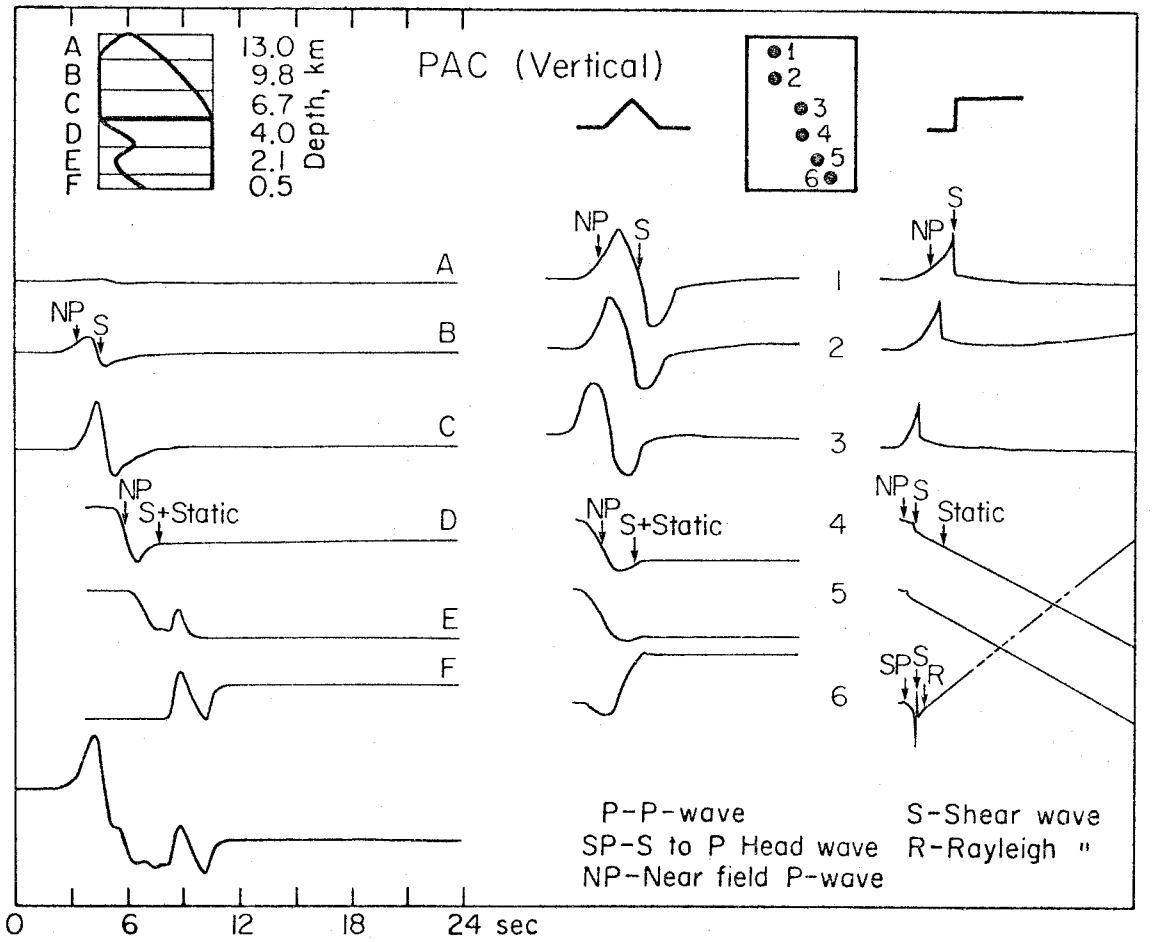

Figure 4.37. Decomposition of the vertical component of ground motion for PAC and Norma 163. See Figure 4.35 for a more detailed explanation.

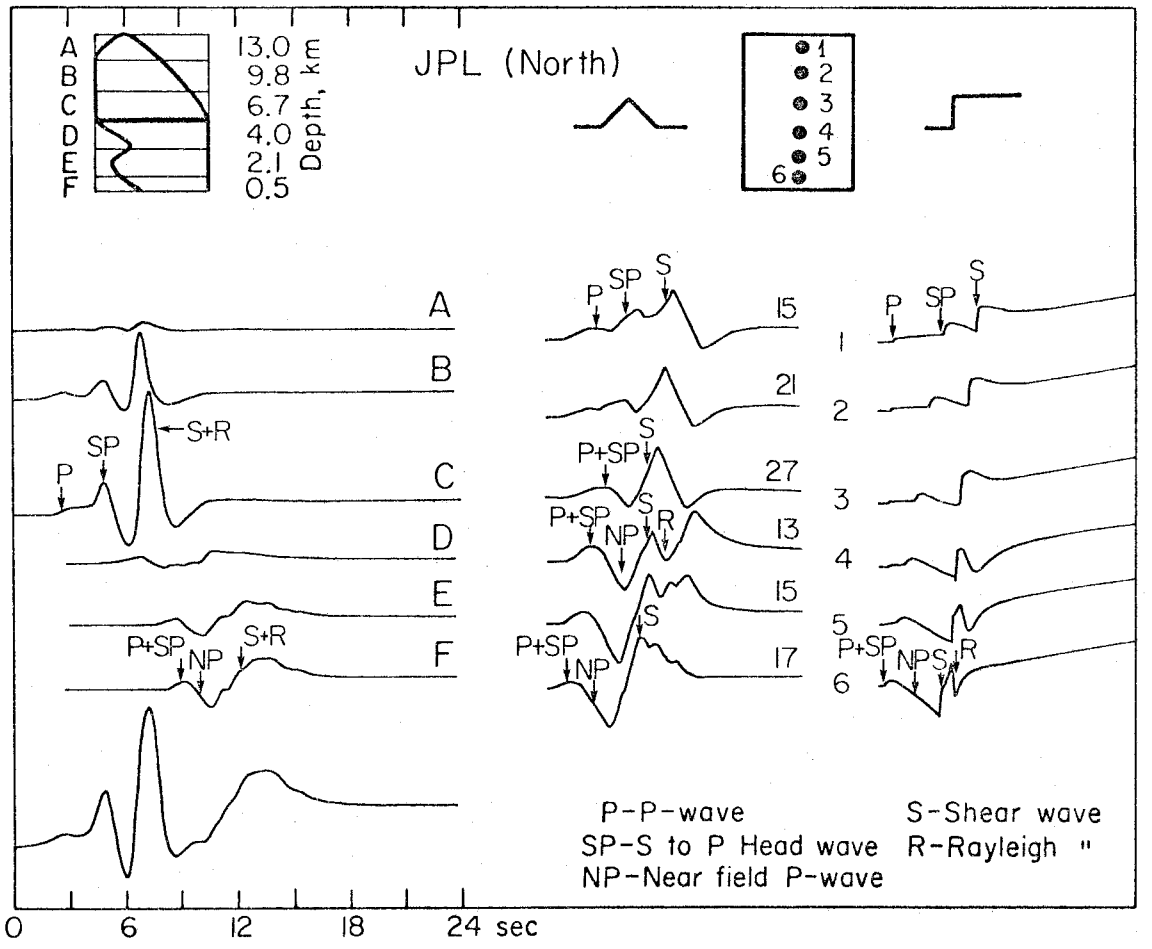

Figure 4.38. Decomposition of the North component of ground motion for JPL and Norma 163. See Figure 4.35 for a more detailed explanation.

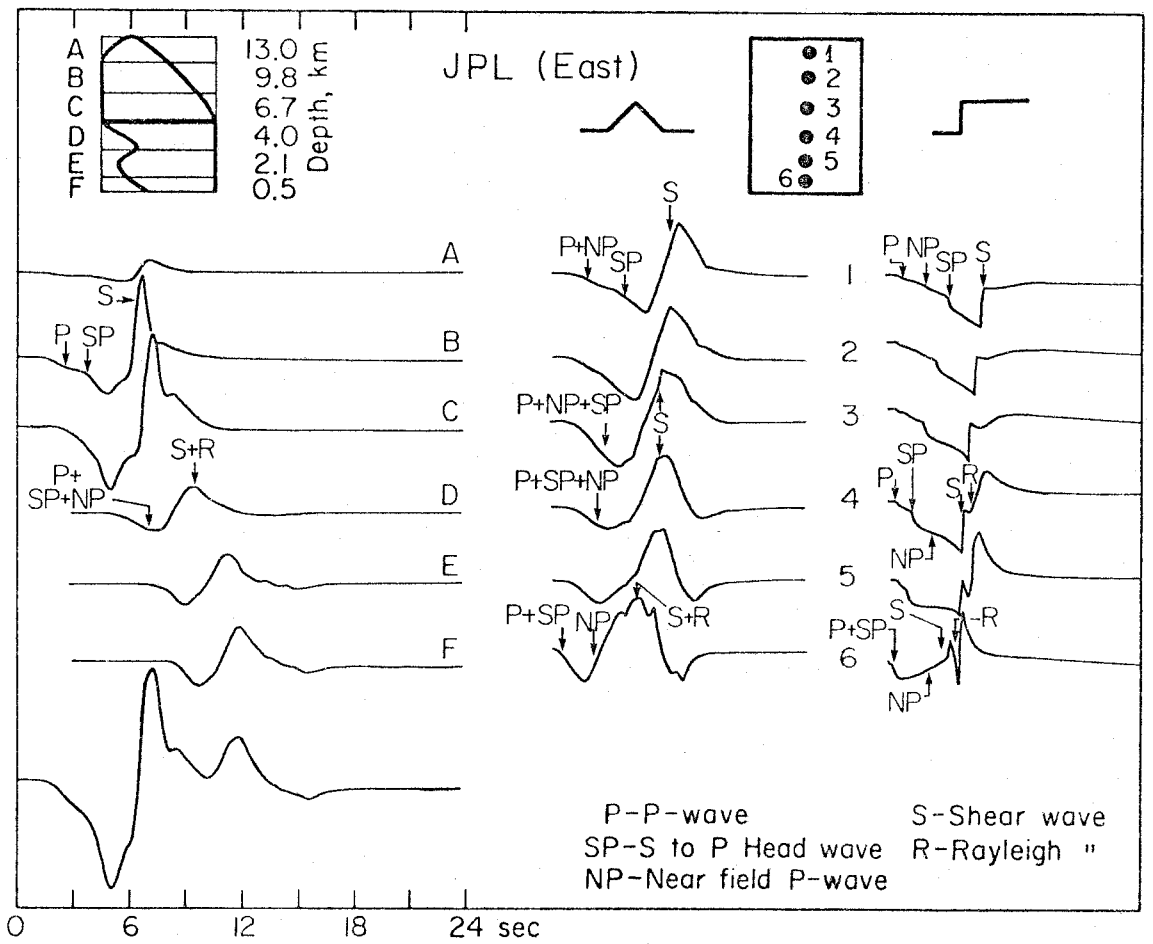

Figure 4.39. Decomposition of the East component of ground motion for JPL and Norma 163. See Figure 4.35 for a more detailed explanation.

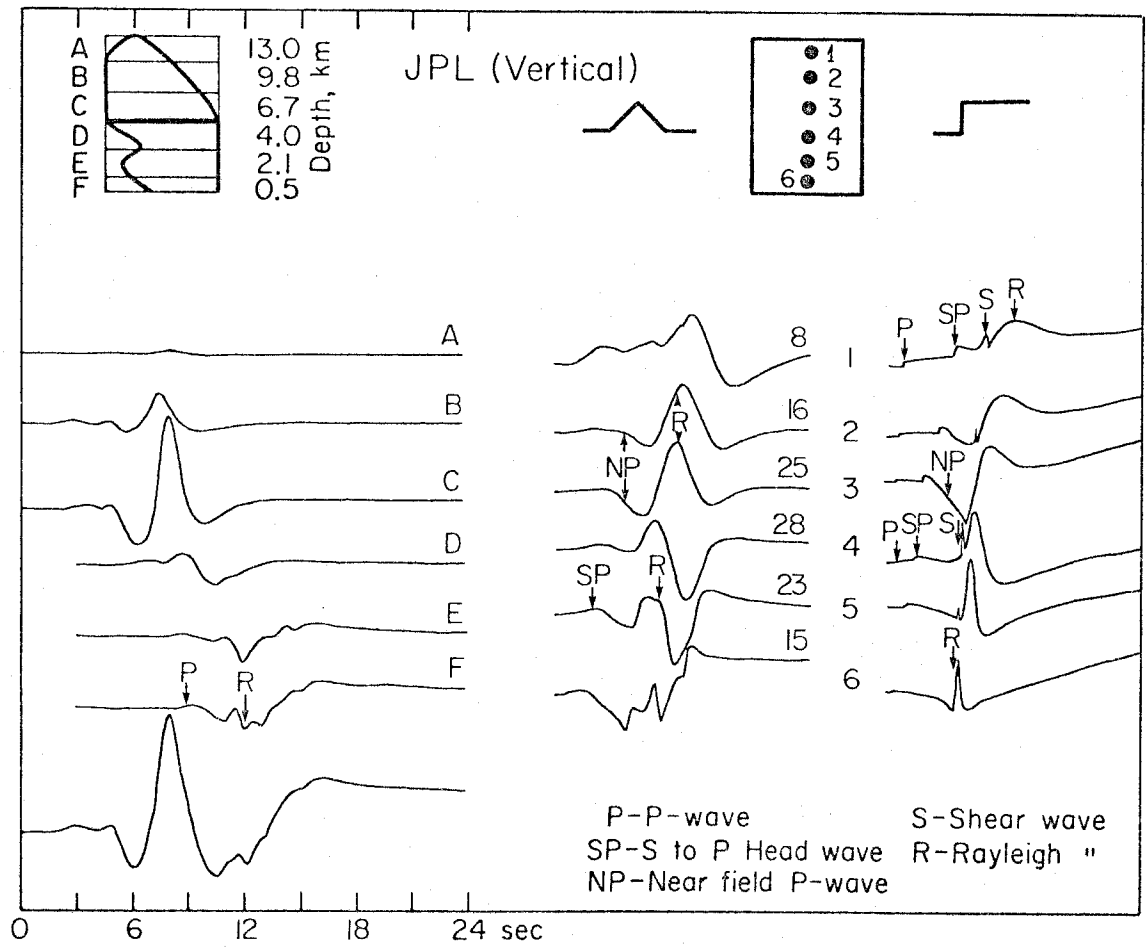

Figure 4.40. Decomposition of the vertical component of ground motion for JPL and Norma 163. See Figure 4.35 for a more detailed explanation.

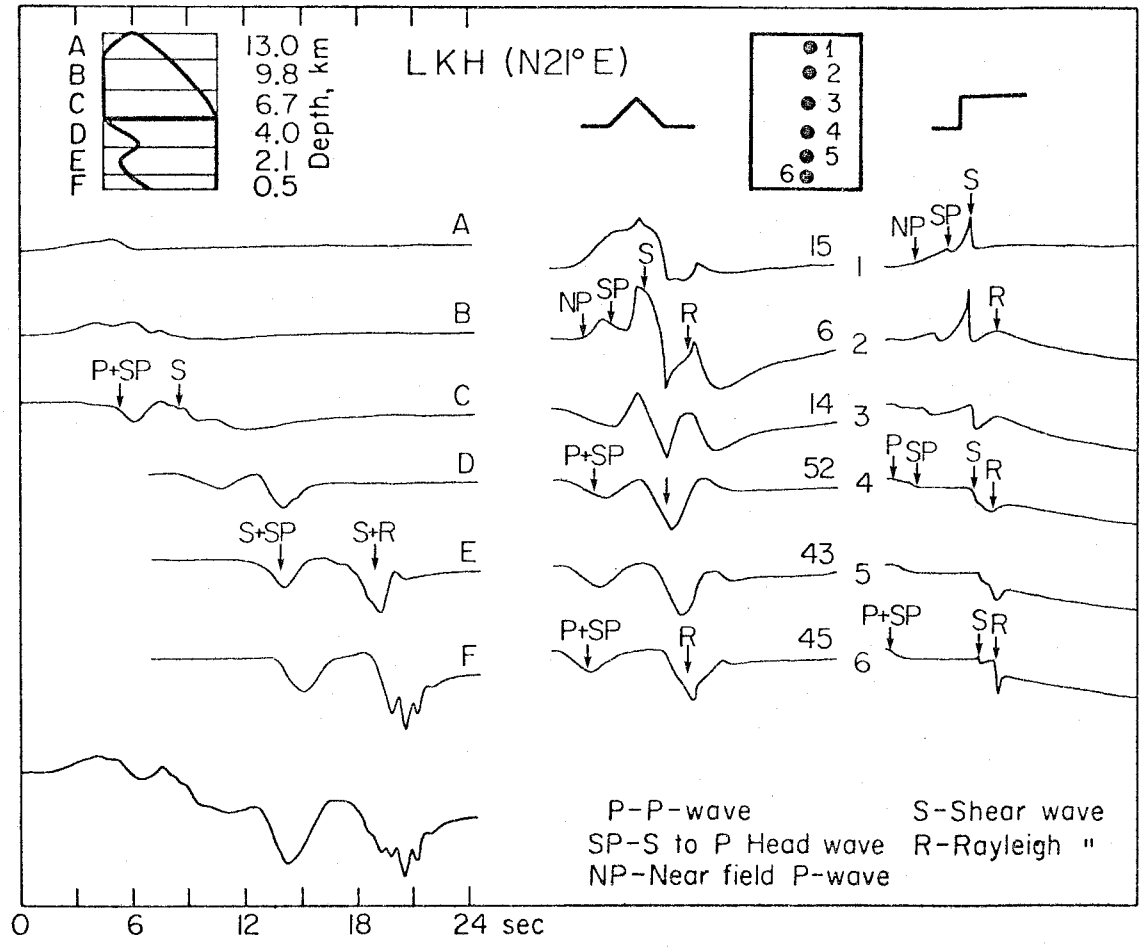

Figure 4.41. Decomposition of the N21°E component of ground motion for LKH and Norma 163. See Figure 4.35 for a more detailed explanation.

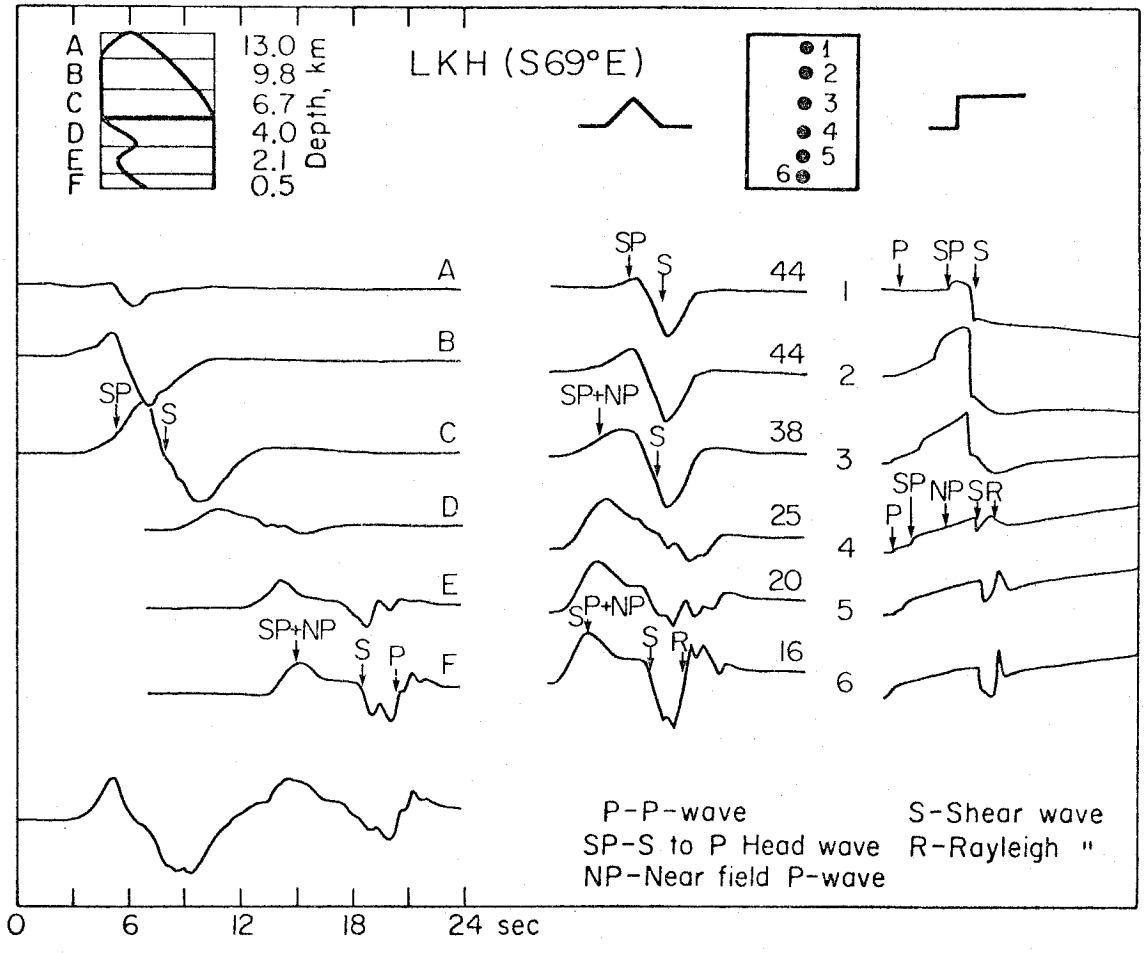

Figure 4.42. Decomposition of the S69°E component of ground motion for LKH and Norma 163. See Figure 4.35 for a more detailed explanation.

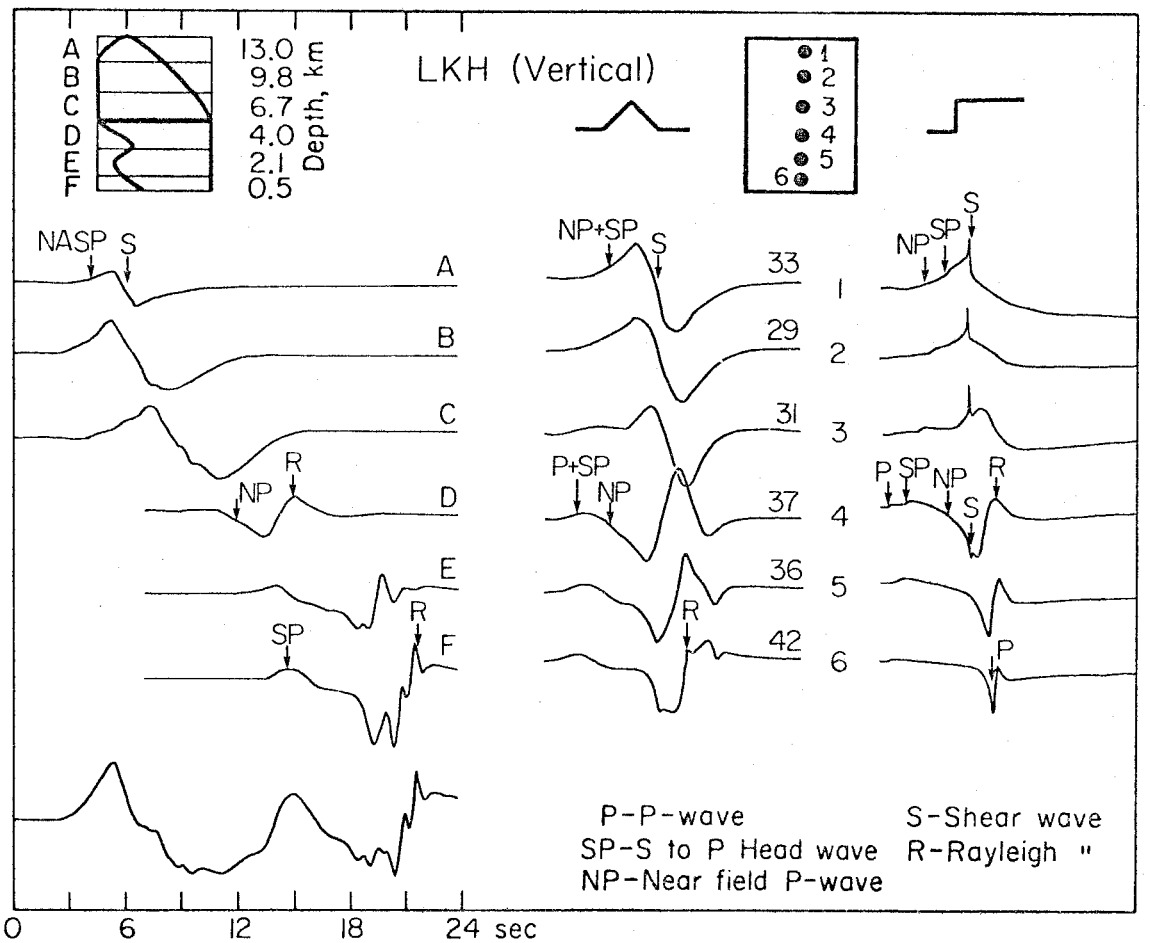

Figure 4.43. Decomposition of the vertical component of ground motion for LKH and Norma 163. See Figure 4.35 for a more detailed explanation.

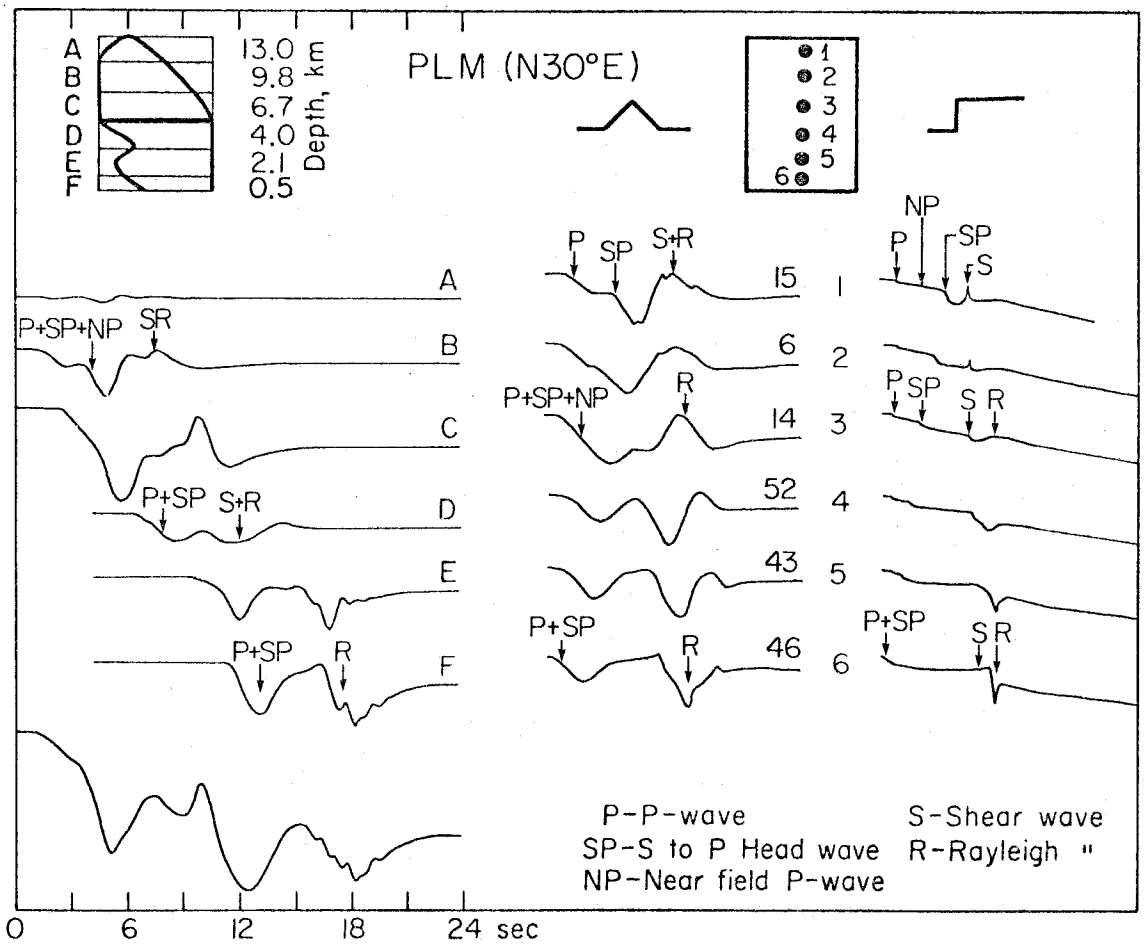

Figure 4.44. Decomposition of the N30°E component of ground motion for PLM and Norma 163. See Figure 4.35 for a more detailed explanation.

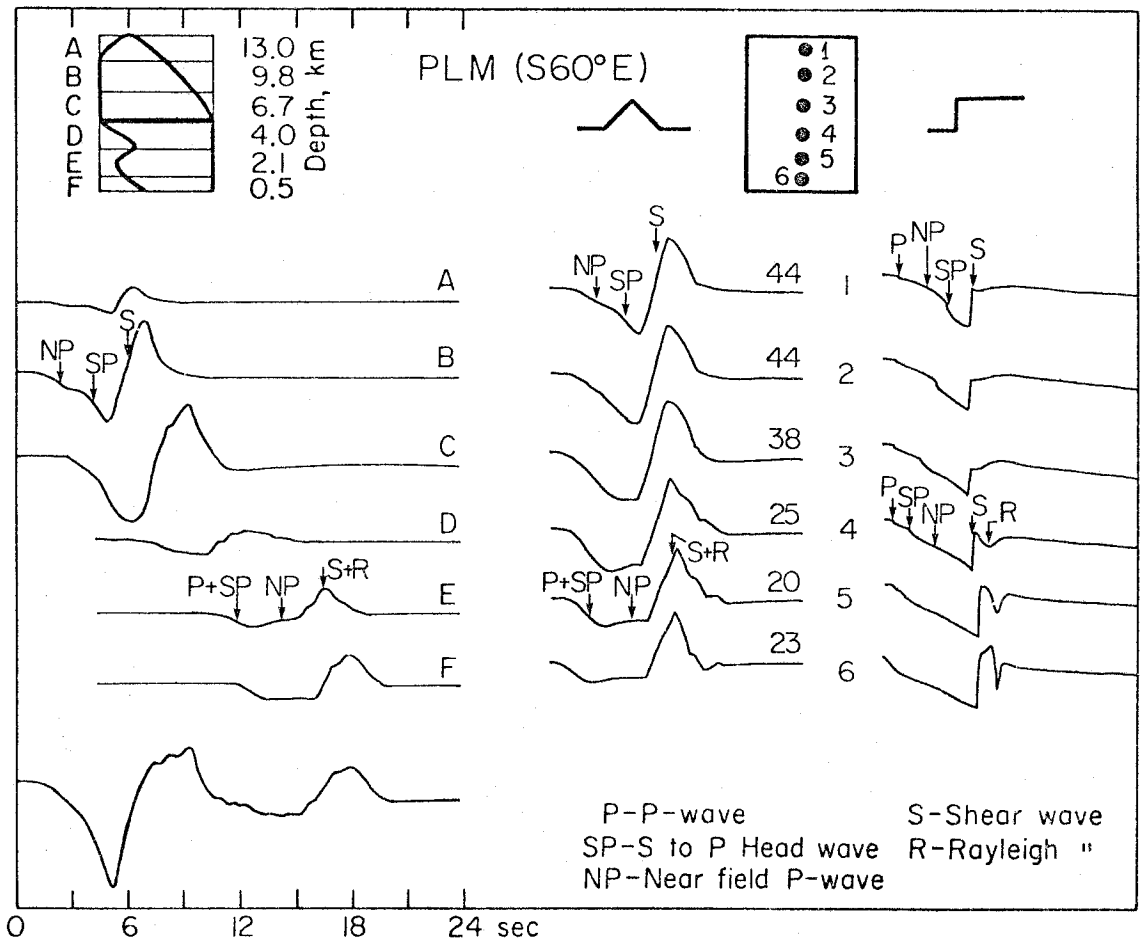

Figure 4.45. Decomposition of the S60°E component of ground motion for PLM and Norma 163. See Figure 4.35 for a more detailed explanation.

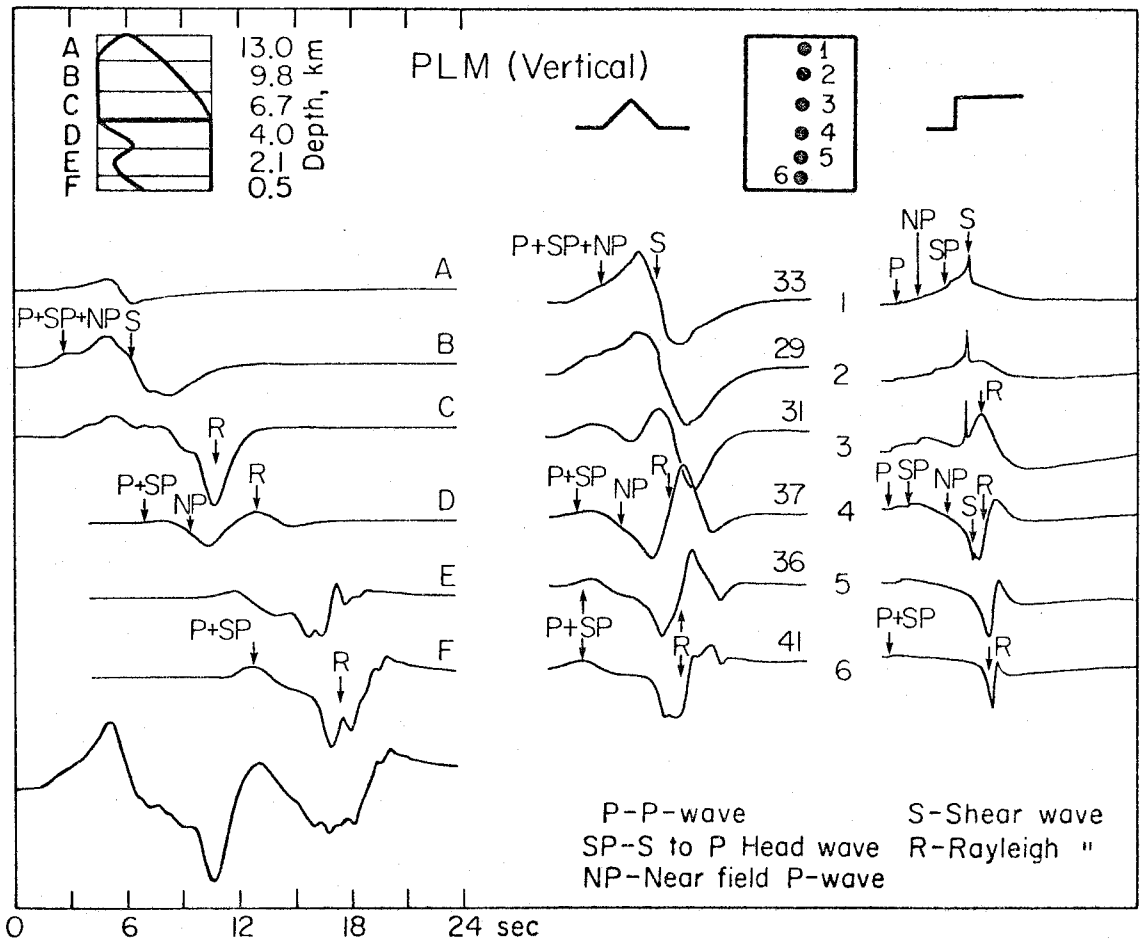

Figure 4.46. Decomposition of the vertical component of ground motion for PLM and Norma 163. See Figure 4.35 for a more detailed explanation.

These are very useful since they allow a positive identification of the various phases present. For the most part, these figures are self-explanatory. There are some features worth noting, though. If one looks back to Figure 4.2, then one can see that the large velocity pulse seen at PAC is the far-field shear wave from the bottom of the fault. This arrival has been greatly enhanced by directivity. Peak accelerations at PAC occurred at about the time that energy is arriving from our strong near-surface faulting. The large displacement pulse seen on the east component of JPL is comprised mainly of the direct S wave. Near-field P waves, S to P headwaves, and Rayleigh waves are particularly important at the northern stations LKH and PLM.

Discussion

Now that we have constructed a model which seems to be compatible with the strong-motion data, we must attempt to evaluate its validity in light of other evidence. Specifically, Alewine's (1974) inversion of static vertical offset data provides us with an excellent test of the upper part of our model. He was able to fit the observed elevation changes with a high degree of accuracy. His model consisted of a three-dimensional fault in a half-space. Fault slip was allowed to vary with depth. Because of the nature of the static inverse problem, Alewine had excellent resolution on the top part of the fault, but the solution for the deeper parts was poorly constrained. Figure 4.47 shows plots of magnitude of fault slip versus distance along the profile A to A' which is shown in Figure 4.30. These plots are for Alewine's inverse

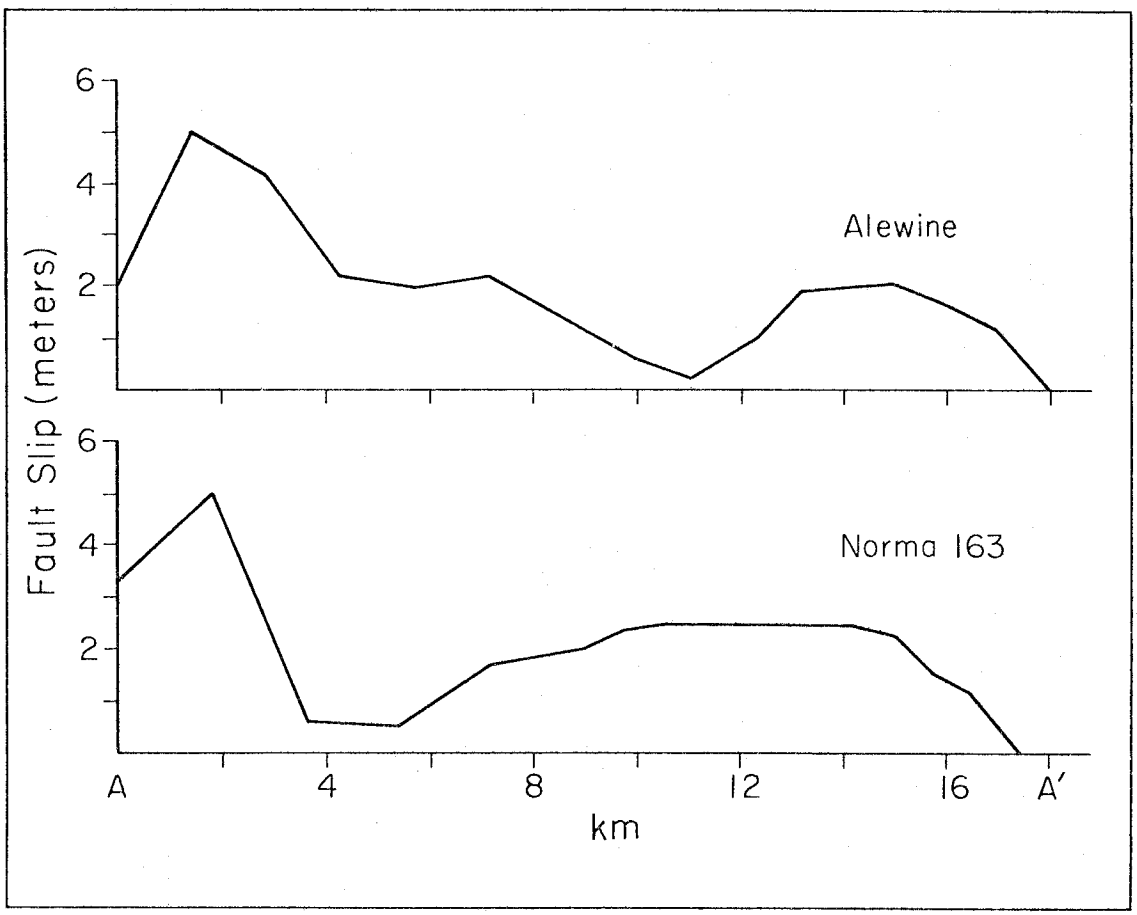

Figure 4.47. Comparison of the fault slip as a function of distance along the line AA' of Figure 4.30. Alewine's (1974) model is from an inversion of static vertical uplift data. Notice that both the static offsets and this study seem to indicate massive faulting very near the free surface.

solution and for our solution, Norma 163. We believe that the most significant feature of this comparison is the 5 meter fault offset which is included in both models for the shallowest part of the fault. Both models also decrease the amount of offset rapidly when proceeding down-dip. Since Alewine's resolution for the deeper part of the fault is poor, it may be fortuitous that our two models produce similar displacements in the hypocentral region. Jungels and Frazier (1973) also studied the static vertical displacement data. They too concluded that large fault offsets were required on the very shallowest part of the fault. Because of the combined strong-motion and static displacement studies, we believe that the evidence for large shallow faulting is very strong.

Very intense shaking was observed in the area just north of the surface ruptures (Nason, 1973; Scott, 1973; Johnsen et al., 1973). This intense shaking occurred just above the section of the fault on which we believe the large offsets occurred. It seems likely that this is less than coincidental. Because of the particular geometry of this upper faulting, it is possible that areas within 1 km north of the surface breaks experienced motions which were significantly different from those recorded at PAC.

The similarities between our model Norma 163 and Langston's (1978) models of teleseismic body waves are difficult to evaluate. We used the same fault geometry and focal mechanism. The relative timing of deep and shallow faulting seems to be roughly comparable. His calculated moment is 0.86×10^{26} ergs and ours is 1.4×10^{26} ergs. Perhaps the largest discrepancy between the models arises when considering directivity effects.

Langston found that the teleseismic short-period direct P arrival was stronger than the pP arrival, even though these waves have roughly similar amplitudes at long periods. His interpretation is that the upward propagating rupture had a velocity of 1.8 km/sec. This low rupture velocity has the effect of depleting the upgoing phase, pP, of short-period energy. Langston also postulates that there is significant downward fault rupture which produces the short-period energy seen in the direct P phase. His modeling indicates that if one-fifth of the moment on the bottom fault were due to downward rupture at a velocity of 3.5 km/sec, then the correct ratio of short-period pP to P amplitudes would result. Here is the problem. We need strong upward directivity to explain PAC. If there is strong upward directivity, then how can we explain the depletion of short-periods in pP? Furthermore, Norma 163 is predominantly unilateral upwards. Can our models accommodate significant downward rupture?

In the model, Norma 171, which is shown in Figure 4.48, we have put roughly one-fifth of our moment for the bottom fault beneath the hypocenter. All parameters are the same as for Norma 163 except that the moment on the bottom fault has grown to 10^{26} ergs. A larger moment was necessary to explain the amplitude of the first pulse seen at PAC. Comparisons between observed and synthetic records are shown for the stations, PAC and LKH, in Figures 4.49 and 4.50. The additional downgoing faulting has virtually no effect on the PAC synthetics. This downgoing faulting has, however, greatly increased the amplitude of the shear wave seen at LKH. The effect of downward faulting is to increase

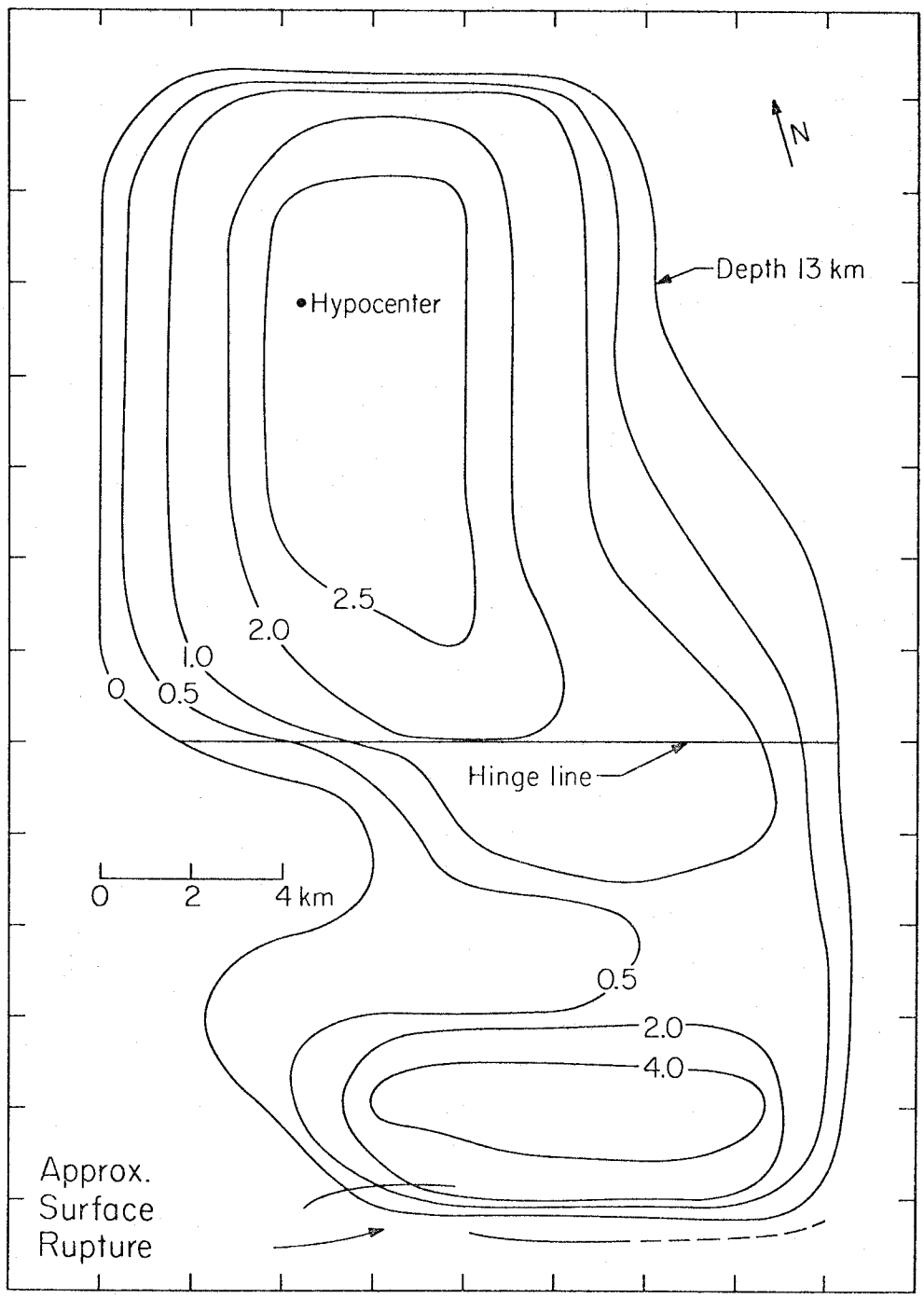

Figure 4.48. Contour map of assumed fault displacements for the model Norma 171. The rupture parameters are given in Table IV.1. The faulting is now bilateral to test the suggested model of Langston (1978).

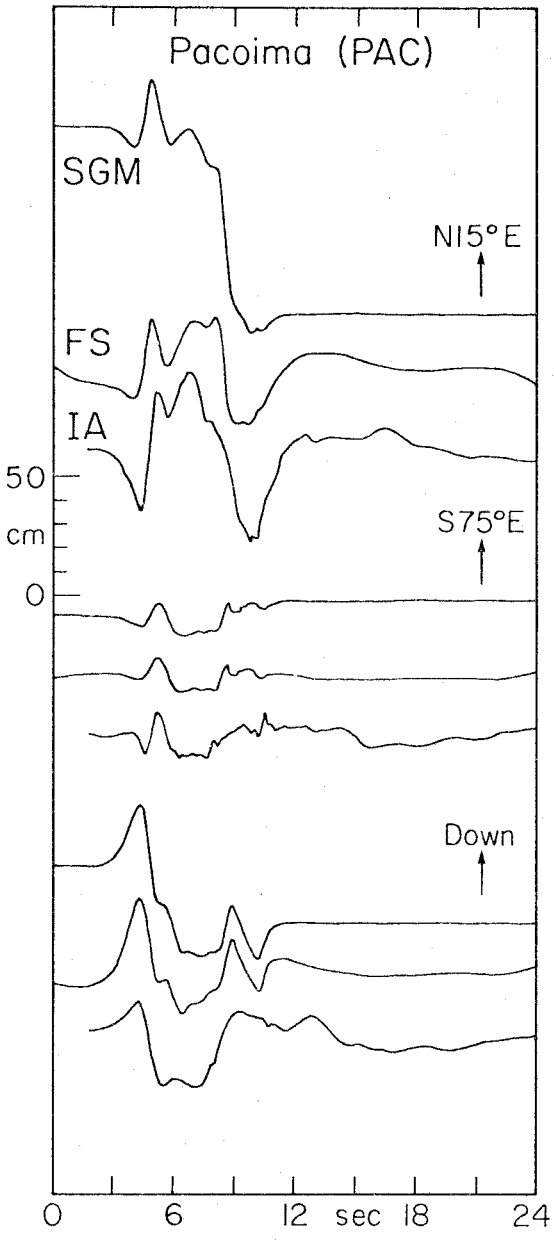

Figure 4.49

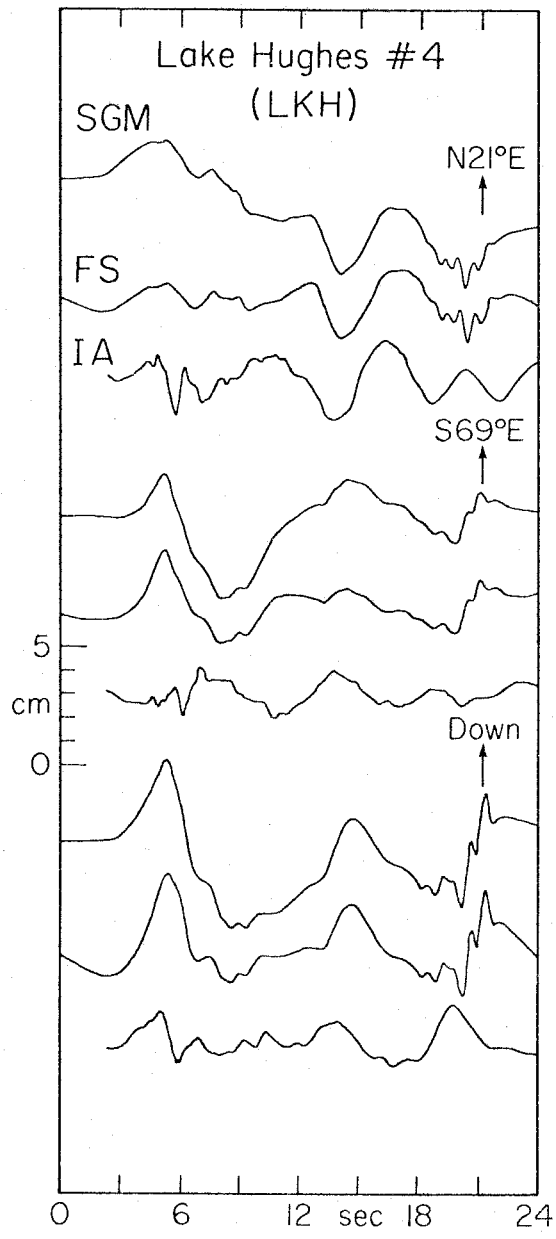

Figure 4.50

Comparison of observed and synthetic records for the model Norma 171, and the stations PAC and LKH. See Figure 4.9 for explanation of SGM, FS and IA.

amplitudes for northern stations. This is an undesirable characteristic. Although we believe that our modeling is not sufficiently accurate to allow us to exclude the possibility of downward faulting, we can conclude that there seems to be no evidence for this downward rupture in the strong motion data. For the present, the explanation of the short-period teleseismic P waveforms remains hidden.

In many respects, our model is very close to Trifunac's (1974) San Fernando model which was obtained by a linear inverse technique. Using a homogeneous whole-space model, Trifunac synthesized displacement records for PAC, JPL, LKH and PLM. Only his PAC synthetics, though, are similar to ours. This should come as no surprise since we have already seen the importance of the free surface for the recordings at JPL, LKH and PLM. Even for PAC, we were uncertain about whether a whole-space model could adequately approximate a half-space model. It is commonly assumed that the whole-space solution need only be doubled in order to approximate the response of a near vertically incident wave on a free surface. As we often do, we allowed our physical intuition to play some tricks on us. We could easily imagine that a wave which dynamically reflects at a free surface could cause twice the motion as that same wave in a whole-space. But what about the static part? Should it also be doubled? Should half-space static displacements be twice as large as whole-space displacements given the same fault offset? Our initial reaction was that the whole-space and half-space answers should not differ by a factor of 2. PAC is so close to the fault that it might as well be on the fault. If we specify a certain dislocation, who cares whether we are on a half-space

or in a whole-space? As you have probably already suspected, you are being baited. In certain instances, the half-space static solution is indeed almost twice the whole-space solution. In the case of the half-space, the upthrown block on which PAC rests experiences almost all of the static offset, whereas the downthrown block is hardly downthrown at all. In the whole-space solution, the upthrown and downthrown blocks move equally. Thus a factor of about 2 is present for this half-space to whole-space comparison for a station directly above a shallow angle thrust. A more complete description of this approximation is given by Boore and Zoback (1974).

The above discussion makes it easier to understand why Trifunac's (1974) and our models are similar. Although the free surface may be important for short-period arrivals from the very shallowest parts of the fault, displacements at PAC are most affected by the quasi-static offset of the upper fault. Trifunac's whole-space model seems to approximate the half-space reasonably well. However, we would urge that each case be examined carefully before deciding the appropriateness of this approximation.

Conclusions

So, where are we? We are probably somewhere in between. We feel that certain gross features of the faulting process can be resolved, but by no means have we fit the records perfectly. Feigning innocence, we have ignored the effects of topography and geologic structure. Furthermore, we probably have not even found the best half-space model. However,

we feel that we can draw some rather important conclusions from our naive study.

Directivity seems to play a major role in the observed motions. Predominantly unilateral faulting originated north of PAC at a depth of 13 km. The rupturing progressed smoothly over a fault with a width of about 6 km and displacements in the hypocentral region were about 2 meters. The rupture velocity was near 2.8 km/sec for the deeper faulting and 1.8 km/sec for the shallow faulting. Fault offsets beneath PAC are very small. Massive faulting with fault offsets of 5 meters occurred within several kilometers of the surface rupture. The large velocity pulse at PAC is a far-field shear wave which is enhanced by directivity. Peak accelerations at PAC are probably associated with the large shallow faulting.

APPENDICES

Introduction to the Appendices

These Appendices are intended to be entirely tutorial. Hopefully they will provide insight into the Cagniard-de Hoop technique as we presently use it. These Appendices are essentially revisions of class notes given by Don Helmberger. Since I am not very familiar with the complete history of the development of these solutions, I can only apologize for inadequately referencing the various parts of these solutions. My only intention is to provide a single source which develops generalized ray theory from reasonably basic concepts.

We will solve only fluid problems since they are scalar problems and therefore they are relatively simple. Since our solid problems can be reduced to scalar potentials, these fluid problems provide the groundwork for solid problems. We will first solve three line source problems. Since the third spatial dimension is quickly dropped in these problems, it is possible to solve them in Cartesian coordinates. These line source problems allow us to demonstrate the basic philosophy of the Cagniard-de Hoop technique without the additional complexity which is introduced by the point source problem. They also allow us to introduce generalized ray theory in a very simple way. Our final problem is that of a point source in a fluid whole-space. This introduces the types of solutions which represent spherical waves in cylindrical coordinates.

Let us give a quick preview of the method. Basically we would like to solve an inhomogeneous scalar wave equation with boundary conditions. The approach is to Laplace transform with respect to time and to then Fourier transform with respect to space. The wave equation

will be reduced to an algebraic equation. In order to find the final solution, we will inverse the transformation procedure. One space transform variable will be inverted by contour integration and the other space variable and the time variable will be inverted simultaneously by using a properly chosen change of variables.

Appendix A

Line Source in an Infinite Fluid

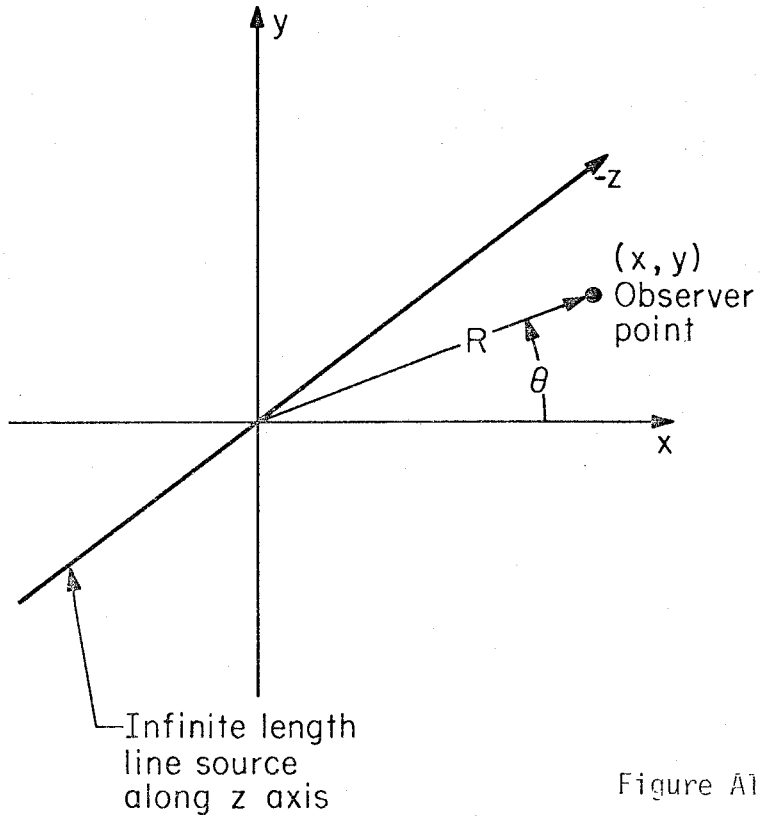

Figure A1

Let x, y and z form the Cartesian coordinate system shown in Figure A1. Suppose there is a disturbance, f(t), along the line x = y = 0. We can then eliminate the z dependence of the solution. Now there exists a scalar potential, $\varsigma(x,y,t)$, such that

$$\underset{\sim}{\nabla}\varsigma(x,y,t) = \underset{\sim}{U}(x,y,t) \equiv \text{displacement vector} \quad . \tag{A.1}$$

Furthermore, ς satisfies the scalar wave equation,

$$\frac{\partial^2 \zeta}{\partial x^2} + \frac{\partial^2 \zeta}{\partial y^2} - \frac{1}{c^2} \frac{\partial^2 \zeta}{\partial t^2} = - \delta(x)\ \delta(y)\ f(t) \quad , \tag{A.2}$$

where $\delta(x)$ is the Dirac-delta function. We will begin by Laplace transforming equation (A.2) with respect to time. Time is transformed to the variable s. Recall the definition of Laplace transform

$$F(s) = \mathcal{LP}(f(t)) = \int_0^\infty f(t)\ e^{-st}\ dt \tag{A.3}$$

and the inverse transform is

$$f(t) = \frac{1}{2\pi i} \int_{\gamma - i\infty}^{\gamma + i\infty} F(s)\ e^{st}\ ds \quad . \tag{A.4}$$

Remember that this is valid only if $f(t < 0) = 0$. Now the Laplace transform has the property that

$$\mathcal{LP}\left\{\frac{d}{dt} f(t)\right\} = s\mathcal{LP}\left\{f(t)\right\} - f(o) \quad . \tag{A.5}$$

If our disturbance, $f(t)$, begins at $t = 0$, then we can transform equation (A.2) to

$$\frac{\partial^2 \bar{\zeta}}{\partial x^2} + \frac{\partial^2 \bar{\zeta}}{\partial y^2} - \frac{s^2}{c^2} \bar{\zeta} = -\delta(x)\ \delta(y)\ F(s) \quad , \tag{A.6}$$

where

$$\bar{\zeta}(x,y,s) = \mathcal{LP}\{\zeta(x,y,t)\} \quad .$$

We will now Fourier transform (A.6) with respect to x. Define

$$\hat{\bar{\zeta}}(\alpha,y,s) \equiv FT\{\bar{\zeta}(x,y,s)\} = \frac{1}{\sqrt{2\pi}} \int_{-\infty}^{\infty} e^{ix\alpha}\, \bar{\zeta}(x,y,s)\, dx \qquad (A.7)$$

and the inverse transformation is

$$\bar{\zeta}(x,y,s) = \frac{1}{\sqrt{2\pi}} \int_{-\infty+i\nu}^{\infty+i\nu} e^{-ix\alpha}\, \hat{\bar{\zeta}}(\alpha,y,s)\, d\alpha \quad . \qquad (A.8)$$

In general, both α and $\hat{\bar{\zeta}}$ are complex. Recall that the Fourier transform has the property that

$$FT\{f'\} = -i\alpha\, FT\{f\} \quad , \qquad (A.9)$$

where the prime denotes differentiation. The Fourier transform of equation (A.6) with respect to x becomes

$$-\alpha^2\, \hat{\bar{\zeta}}(\alpha,y,s) + \frac{\partial^2 \hat{\bar{\zeta}}}{\partial y^2} - \frac{s^2}{c^2}\, \hat{\bar{\zeta}} = -\frac{\delta(y)\, F(s)}{\sqrt{2\pi}} \quad , \qquad (A.10)$$

where we have used the fact that

$$FT(\delta(x)) = \frac{1}{\sqrt{2\pi}} \quad .$$

Finally, we will take the Fourier transform of (A.10) with respect to y, where

$$\hat{\hat{\bar{\zeta}}}(\alpha,\beta,s) \equiv FT\{\hat{\bar{\zeta}}(\alpha,y,s)\} \quad .$$

Equation (A.10) becomes

$$(\beta^2+\alpha^2+\frac{s^2}{c^2})\ \hat{\hat{\hat{\zeta}}}(\alpha,\beta,s) = \frac{F(s)}{2\pi} \quad ,$$

or

$$\hat{\hat{\hat{\zeta}}}(\alpha,\beta,s) = \frac{F(s)}{2\pi(\beta^2+\alpha^2+\frac{s^2}{c^2})} \quad . \tag{A.11}$$

Now if we can take the inverse transforms of (A.11), then the problem will be solved. Using the inverse transformation of $\hat{\hat{\hat{\zeta}}}$ given by equation (A.8), we know that

$$\hat{\hat{\hat{\zeta}}}(\alpha,y,s) = \frac{1}{\sqrt{2\pi}} \int_{-\infty+i\gamma}^{\infty+i\gamma} e^{-iy\beta}\ \hat{\hat{\hat{\zeta}}}(\alpha,\beta,s)\ d\beta$$

$$= \frac{F(s)}{2\pi\sqrt{2\pi}} \int_{-\infty+i\gamma}^{\infty+i\gamma} \frac{e^{-iy\beta}}{(\beta^2+\alpha^2+\frac{s^2}{c^2})}\ d\beta \quad . \tag{A.12}$$

Since the quantity $(\beta^2+\alpha^2+\frac{s^2}{c^2})$ is analytic along Reβ, let $\gamma = 0$. The integral above can be solved by contour integration. There are simple poles when

$$\beta = \pm i(\alpha^2+\frac{s^2}{c^2})^{\frac{1}{2}} \quad . \tag{A.13}$$

Now suppose that

$$\mathrm{Re}[(\alpha^2 + \frac{\delta^2}{c^2})^{\frac{1}{2}}] > 0 \quad , \tag{A.14}$$

then $\beta = -i(\alpha^2 + \frac{\delta^2}{c^2})^{\frac{1}{2}}$ lies in the lower half plane. Consider the contour $C_1 + C_2$ in Figure A2.

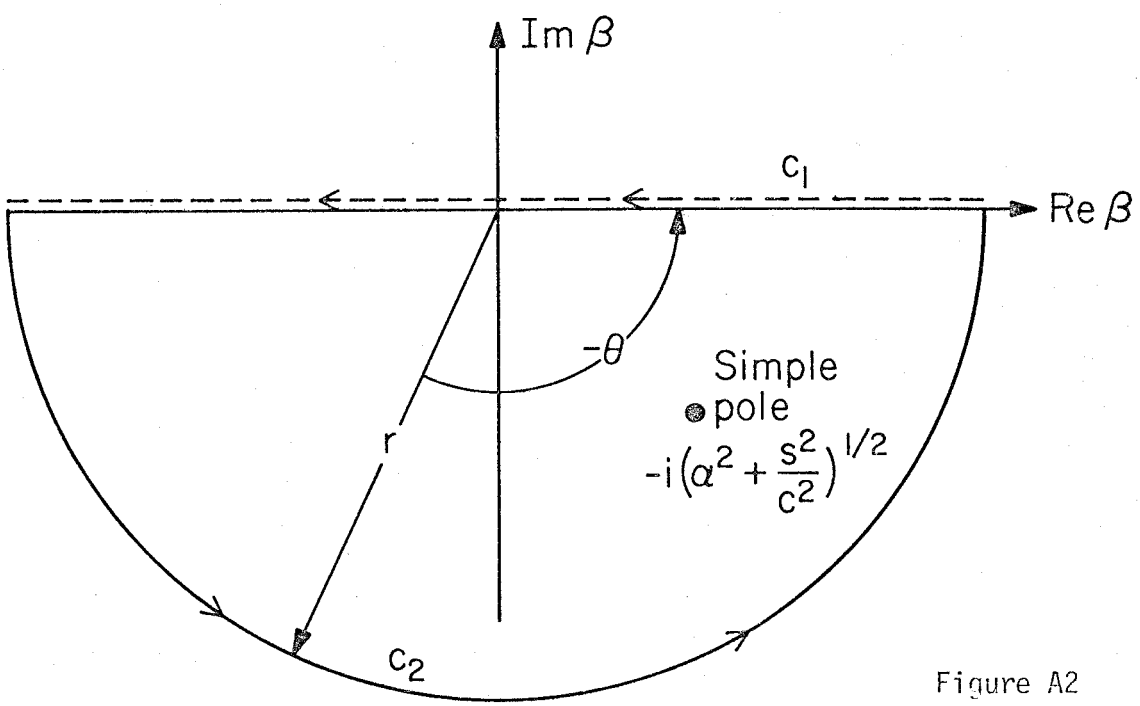

Figure A2

Now by the Residue theorem,

$$\int_{C_1+C_2} G\, d\beta = \int_{C_1} G\, d\beta + \int_{C_2} G\, d\beta = 2\pi i \sum_{j=1}^{n} \mathrm{Res}_j \quad , \tag{A.15}$$

where

$$G \equiv \frac{F(\delta)}{2\pi\sqrt{2\pi}} \frac{e^{-iy\beta}}{(\beta^2 + \alpha^2 + \frac{\delta^2}{c^2})}$$

and where $\sum_{j=1}^{n} \text{Res}_j$ is the sum of the residues of the poles inside $C_1 + C_2$. Notice that the Residue theorem is for integration about the pole in a counter-clockwise sense. The pole is of order 1 and its residue is

$$\underset{\beta=\beta_o}{\text{Res}} = \lim_{\beta \to \beta_o} (\beta - \beta_o) \frac{e^{-iy\beta_o}}{(\beta - \beta_o)(\beta + \beta_o)} ,$$

where

$$\beta_o = -i(\alpha^2 + \frac{\delta^2}{c^2})^{\frac{1}{2}} .$$

Thus

$$\int_{C_1+C_2} G \, d\beta = - \frac{\pi e^{-y(\alpha^2 + \frac{\delta^2}{c^2})^{\frac{1}{2}}}}{(\alpha^2 + \frac{\delta^2}{c^2})^{\frac{1}{2}}} . \qquad (A.16)$$

Now consider the integral $\int_{C_2} G \, d\beta$.

If $y > 0$, then

$$e^{-iy\beta} = e^{iy\text{Re}(\beta)} \, e^{yIm(\beta)} < 1 \quad \text{for} \quad Im(\beta) < 0 .$$

Thus if $y \geq 0$ and $Im(\beta) \leq 0$, then

$$\int_{C_2} \frac{e^{-iy\beta}}{(\beta^2+\alpha^2+\frac{\delta^2}{c^2})}\, d\beta \leq \int_{C_2} \frac{d\beta}{(\beta^2+\alpha^2+\frac{\delta^2}{c^2})} \quad .$$

Now on the contour C_2, $\beta = re^{i\theta}$. Thus

$$\int_{C_2} \frac{e^{-iy\beta}}{(\beta^2+\alpha^2+\frac{\delta^2}{c^2})}\, d\beta \leq \int_{-\pi}^{0} \frac{ir\, e^{i\theta}\, d\theta}{(r^2e^{2i\theta}+\alpha^2+\frac{\delta^2}{c^2})} \quad .$$

The triangle inequality allows us to conclude that

$$|r^2\, e^{2i\theta}+\alpha^2+\frac{\delta^2}{c^2}| \geq r^2 - |\alpha^2+\frac{\delta^2}{c^2}| \quad .$$

Thus

$$\int_{C_2} \frac{e^{-iy\beta}}{(\beta^2+\alpha^2+\frac{\delta^2}{c^2})}\, d\beta \leq \int_{-\pi}^{0} \frac{ir\, e^{i\theta}\, d\theta}{(r^2+\alpha^2+\frac{\delta^2}{c^2})} = \frac{r\pi}{r^2+\alpha^2+\frac{\delta^2}{c^2}}$$

which goes to zero as $r \to \infty$. Thus $\int_{C_2} G\, d\beta = 0$ in equation (A.15). From equations (A.15) and (A.16) we conclude that

$$\int_{-\infty}^{\infty} \frac{e^{-iy\beta}}{(\beta^2+\alpha^2+\frac{\delta^2}{c^2})}\, d\beta = \frac{\pi e^{-y(\alpha^2+\frac{\delta^2}{c^2})^{\frac{1}{2}}}}{(\alpha^2+\frac{\delta^2}{c^2})^{\frac{1}{2}}} \qquad (A.17)$$

for $y \geq 0$ and condition (A.14). Now if $y \leq 0$ and condition (A.14) holds, then we simply integrate over the contour $C_1 + C_2$ which is shown in Figure (A3).

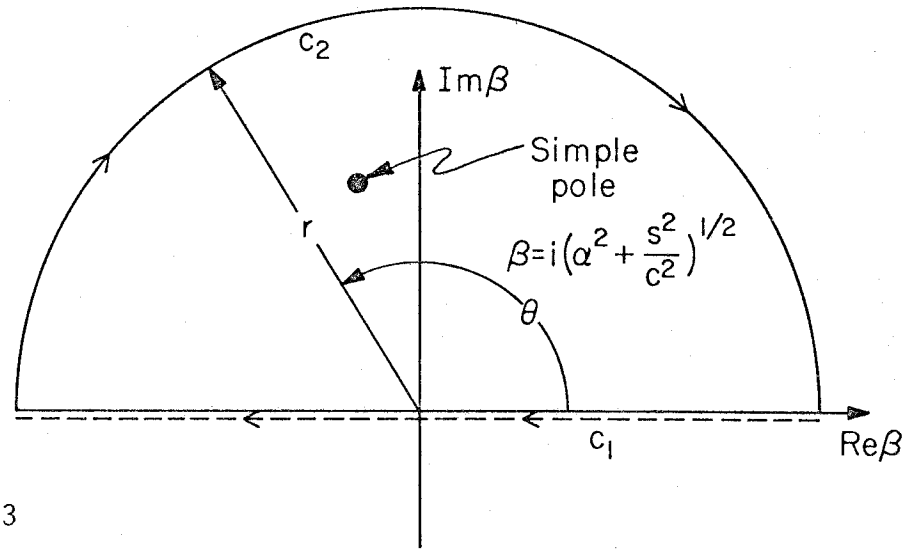

Figure A3

As before, evaluate the residue, but instead at $\beta_o = i(\alpha^2 + \frac{\delta^2}{c^2})^{\frac{1}{2}}$.

$$2\pi i \operatorname*{Res}_{\beta=\beta_o} = \frac{\pi e^{y(\alpha^2 + \frac{\delta^2}{c^2})^{\frac{1}{2}}}}{(\alpha^2 + \frac{\delta^2}{c^2})^{\frac{1}{2}}} \quad .$$

As before, we can show that

$$\lim_{r\to\infty} \int_{C_2} G \, d\beta = 0 \quad .$$

Thus

$$\int_{C_1} G \, d\beta = \int_{-\infty}^{\infty} \frac{e^{-iy\beta}}{(\beta^2 + \alpha^2 + \frac{\delta^2}{c^2})} \, d\beta = \frac{\pi e^{y(\alpha^2 + \frac{\delta^2}{c^2})^{\frac{1}{2}}}}{(\alpha^2 + \frac{\delta^2}{c^2})^{\frac{1}{2}}} \quad , \qquad \text{(A.18)}$$

where $y \leq 0$ and condition (A.14) holds. Thus from equations (A.12), (A.17) and (A.18) we conclude that

$$\hat{\bar{\zeta}}(\alpha,y,\delta) = \frac{F(\delta)}{2\sqrt{2\pi}} \frac{e^{-|y|(\alpha^2+\frac{\delta^2}{c^2})^{\frac{1}{2}}}}{(\alpha^2+\frac{\delta^2}{c^2})^{\frac{1}{2}}} \quad . \tag{A.19}$$

We will next invert the Fourier transform with respect to x. Using equations (A.8) and (A.19) we know that

$$\bar{\zeta}(x,y,\delta) = \frac{F(\delta)}{2\sqrt{2\pi}\sqrt{2\pi}} \int_{-\infty}^{\infty} \frac{e^{-i\alpha x} e^{-|y|(\alpha^2+\frac{\delta^2}{c^2})^{\frac{1}{2}}}}{(\alpha^2+\frac{\delta^2}{c^2})^{\frac{1}{2}}} d\alpha$$

$$= \frac{F(\delta)}{4\pi} \int_{-\infty}^{\infty} \frac{\exp[-ix\alpha - |y|(\alpha^2+\frac{\delta^2}{c^2})^{\frac{1}{2}}]}{(\alpha^2+\frac{\delta^2}{c^2})^{\frac{1}{2}}} d\alpha \quad . \tag{A.20}$$

Up to this point, we have assumed that ζ is a function of the independent variables time and space. Actually, we know that solutions to the wave equation have the characteristic that a pulse travels with the wave velocity. In the time domain, this fact manifests itself through d'Alembert solutions to the wave equation. We are about to make several important transformations which are analogous to transforming to some characteristic coordinate system. We would like to make some change of variables which will allow us to solve equation (A.20) by

inspection. Suppose that we could devise some transformations which will make equation (A.20) look like a Laplace transform. Consider the change of variables,

$$\alpha = -i\delta p \quad . \tag{A.21}$$

Then $d\alpha = -i\delta dp$ and $p(\alpha = \infty+i\nu) = i\alpha + \nu$ and then equation (A.20) becomes

$$\bar{\zeta}(x,y,\delta) = \frac{-i\ F(\delta)}{4\pi} \int_{-i\infty}^{i\infty} \frac{\exp\{-\delta[px + |y|(\frac{1}{c^2} - p^2)^{\frac{1}{2}}]\}dp}{(\frac{1}{c^2} - p^2)^{\frac{1}{2}}} \quad . \tag{A.22}$$

Now Laplace transforms involve integration from zero to infinity and equation (A.22) runs from minus infinity to infinity. The Schwartz reflection principle can help us here. If g(z) is analytic, then the Schwartz reflection principle allows us to assert that if g(z) is real for real z, then $g(\bar{z}) = \overline{g(z)}$; or $\overline{g(\bar{z})} = \overline{\overline{g(z)}} = g(z)$, where the bar denotes complex conjugation. Thus

$$\int_{-i\infty}^{0} \frac{\exp\{-\delta[px + |y|(\frac{1}{c^2} - p^2)^{\frac{1}{2}}]\}dp}{(\frac{1}{c^2} - p^2)^{\frac{1}{2}}}$$

$$= -\int_{0}^{-i\infty} \frac{\exp\{-\delta[px + |y|(\frac{1}{c^2} - p^2)^{\frac{1}{2}}]\}dp}{(\frac{1}{c^2} - p^2)^{\frac{1}{2}}}$$

$$= -\int_{0}^{i\infty} \frac{\exp\{-\delta[px + |y|(\frac{1}{c^2} - p^2)^{\frac{1}{2}}]\}dp}{(\frac{1}{c^2} - p^2)^{\frac{1}{2}}} \quad . \tag{A.23}$$

Thus we can rewrite equation (A.22)

$$\bar{\zeta}(x,y,s) = \frac{iF(s)}{4\pi}\left(\int_0^{i\infty} \exp\{-s[xp + |y|(\frac{1}{c^2} - p^2)^{\frac{1}{2}}]\}\left(\frac{1}{c^2} - p^2\right)^{-\frac{1}{2}} dp \right.$$

$$\left. - \overline{\int_0^{i\infty} \exp\{-s[xp + |y|(\frac{1}{c^2} - p^2)^{\frac{1}{2}}]\}\left(\frac{1}{c^2} - p^2\right)^{-\frac{1}{2}} dp}\right) \quad . \qquad (A.24)$$

Now if $z = \zeta_1 + i\,\zeta_2$, then

$$z - \bar{z} = \zeta_1 + i\,\zeta_2 - \overline{(\zeta_1 + i\,\zeta_2)} = 2i\zeta_2 \quad .$$

Thus equation (A.24) becomes

$$\bar{\zeta}(x,y,s) = \frac{F(s)}{2\pi}\, Im \int_0^{i\infty} \frac{\exp\{-s[xp + |y|(\frac{1}{c^2} - p^2)^{\frac{1}{2}}]\}dp}{(\frac{1}{c^2} - p^2)^{\frac{1}{2}}} \quad . \qquad (A.25)$$

Now how are we to obtain $\zeta(x,y,t)$? We know that

$$\bar{\zeta}(x,y,s) = \int_0^{\infty} \zeta(x,y,t)e^{-st}\, dt \quad . \qquad (A.26)$$

After studying equations (A.25) and (A.26), the value of the next transformation becomes obvious. Let

$$\tau = xp + |y|(\frac{1}{c^2} - p^2)^{\frac{1}{2}} \quad . \qquad (A.27)$$

We can invert equation (A.27) by using the quadratic formula

$$p = \frac{tx}{R^2} \pm i \frac{y}{R^2} \sqrt{t^2 - \frac{R^2}{c^2}} \quad , \tag{A.28}$$

where $R^2 \equiv x^2 + y^2$. We can also calculate dp/dt.

$$dp = \frac{i\eta}{\sqrt{t^2 - \frac{R^2}{c^2}}} dt \quad , \tag{A.29}$$

where we have defined

$$\eta \equiv (\frac{1}{c^2} - p^2)^{\frac{1}{2}}$$

$$= \frac{ty}{R^2} \pm i(t^2 - \frac{R^2}{c^2})^{\frac{1}{2}} \frac{x}{R^2} \quad . \tag{A.30}$$

Now recall the condition (A.14),

$$\mathrm{Re}[(\alpha^2 + \frac{\delta^2}{c^2})]^{\frac{1}{2}} > 0 \quad .$$

Applying the transformation (A.21) to this condition yields,

$$\mathrm{Re}[\delta(p^2 + \frac{1}{c^2})^{\frac{1}{2}}] > 0 \quad . \tag{A.31}$$

If δ is a positive real, then condition (A.14) becomes

$$\mathrm{Re}\ \eta > 0 \ .$$

If condition (A.31) is to hold, then the lower and upper signs in equations (A.28) and (A.30) must be used together. We can now write equation (A.25) in terms of τ .

$$\bar{\zeta}(x,y,s) = \frac{F(s)}{2\pi} Im \int_{\tau(p=0)}^{\tau(p=i\infty)} \frac{e^{-s\tau}}{\eta} \frac{i\eta}{\sqrt{\tau^2 - \frac{R^2}{c^2}}} d\tau$$

$$= \frac{F(s)}{2\pi} Im \int_{\tau(p=0)}^{\tau(p=\infty)} \frac{i\, e^{-s\tau}}{\sqrt{\tau^2 - \frac{R^2}{c^2}}} d\tau \quad . \qquad (A.32)$$

Now equation (A.32) is beginning to look very similar to the definition of the Laplace transform. If τ were real and increasing, then τ would correspond to time. Now the path in the p plane which makes τ real is shown in Figure A4.

$$p = \frac{tx}{R^2} + i\, \frac{y}{R^2} \sqrt{t^2 - \frac{R^2}{c^2}} \quad .$$

Figure A4

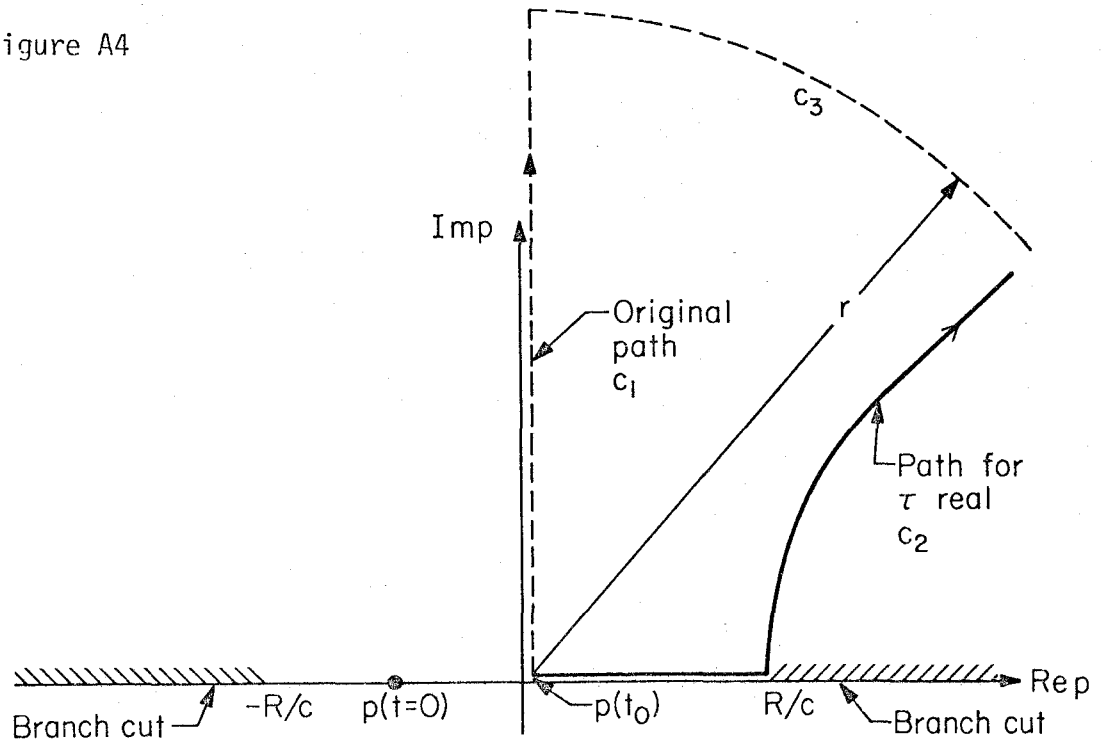

Now it can be shown that the integral along C_3 goes to zero as r becomes infinite. Since our integrand in equation (A.32) is analytic, Cauchy's theorem assures us that the contour C_1 can be replaced by the contour C_2. Now $t_o = t(p=0) = \frac{|y|}{c}$, and thus equation (A.32) becomes

$$\bar{\zeta}(x,y,s) = \frac{F(s)}{2\pi} Im \int_{t_o}^{\infty} \frac{i\, e^{-s\tau}}{\sqrt{\tau^2 - \frac{R^2}{c^2}}}\, d\tau \quad . \tag{A.33}$$

Now the integrand of equation (A.33) becomes complex when $\tau > R/c$. Thus the solution can be written

$$\bar{\zeta}(x,y,s) = \frac{F(s)}{2\pi} \int_{t_o}^{\infty} \frac{H(\tau - \frac{R}{c})\, e^{-s\tau}}{\sqrt{\tau^2 - \frac{R^2}{c^2}}}\, d\tau$$

$$= \frac{F(s)}{2\pi} \int_{o}^{\infty} \frac{H(\tau - \frac{R}{c})\, e^{-s\tau}}{\sqrt{\tau^2 - \frac{R^2}{c^2}}}\, d\tau \quad , \tag{A.34}$$

where H(t) is the heaviside step function. Now we immediately recognize that (A.34) can be rewritten as

$$\bar{\zeta}(x,y,s) = \frac{F(s)}{2\pi}\, \mathcal{LP}\left\{\frac{H(t - \frac{R}{c})}{\sqrt{t^2 - \frac{R^2}{c^2}}}\right\} , \tag{A.35}$$

and thus

$$\zeta(x,y,t) = \frac{f(t)}{2\pi} * \left[\frac{H(t - \frac{R}{c})}{\sqrt{t^2 - \frac{R^2}{c^2}}}\right] \tag{A.36}$$

which is the final solution. Our transformations allowed us to solve two integral equations by inspection. For this problem, though, the victory is somewhat hollow since there are simpler methods for finding the solution. The real value of our method becomes clear in the next section when we include more complicated boundary conditions.

Appendix B

Fluid-Fluid Interface Problem for a Line Source

This problem is closely related to the line source problem which we just solved. The addition of an interface allows us to investigate head waves and critical reflections. Consider the coordinate system shown in Figure B1. The coordinates are such that the x and z axes lie on the interface with y increasing upward.

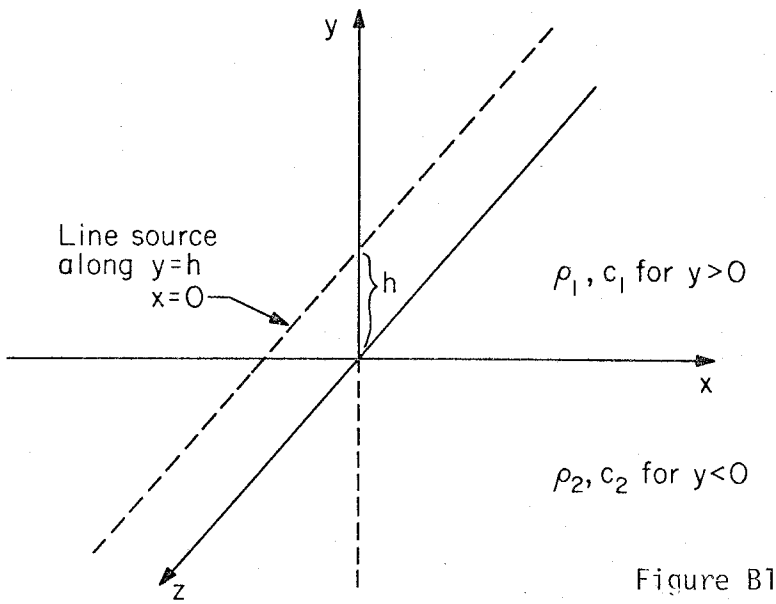

Figure B1

Again, let $\zeta(x,y,t)$ be a displacement potential as in Appendix A. The wave equations for ζ in the upper and lower media are:

$$\frac{\partial^2 \zeta_1}{\partial x^2} + \frac{\partial^2 \zeta_1}{\partial y^2} - \frac{1}{c_1^2}\frac{\partial^2 \zeta_1}{\partial t^2} = -\delta(x)\ \delta(y-h)\ f(t) \qquad (B.1)$$

for $y > 0$, and

$$\frac{\partial^2 \zeta_2}{\partial x^2} + \frac{\partial^2 \zeta_2}{\partial y^2} - \frac{1}{c_2}\frac{\partial^2 \zeta_2}{\partial t^2} = 0 \qquad \text{(B.2)}$$

for $y < 0$.

Now the general solution to equation (B.1) is the sum of the particular solution to equation (B.1) and the homogeneous solution to equation (B.1). The general solution to equation (B.2) is simply the homogeneous solution to equation (B.2). Now in Appendix A, we showed that the particular solution of equation (B.1) can be written in the x and t transformed domain as (see equation (A.19)):

$$p\hat{\bar{\zeta}}_1(\alpha,y,s) = \frac{F(s)}{2\sqrt{2\pi}} \frac{e^{-|y-h|\left(\alpha^2 + \frac{s^2}{c_1^2}\right)^{1/2}}}{\left(\alpha^2 + \frac{s^2}{c_1^2}\right)^{1/2}} \quad , \qquad \text{(B.3)}$$

where again,

$$\hat{\bar{\zeta}}(\alpha,y,s) = FT\{\bar{\zeta}(x,y,s)\} = FT\{\mathcal{L}P[\zeta(x,y,t)]\} \quad .$$

We would now like to find the homogeneous solution for equation (2.1) in the α,y,s space. If you examine Appendix A, you will find that the doubly transformed equation for $\hat{\bar{\zeta}}(\alpha,y,s)$ is given by equation (A.10). Without the forcing term it becomes

$$\frac{\partial^2 {}_h\hat{\bar{\zeta}}_i(\alpha,y,s)}{\partial^2 y^2} = \left(\alpha^2 + \frac{s^2}{c_i^2}\right) {}_h\hat{\bar{\zeta}}_i(\alpha,y,s) \quad ; \qquad i = 1, 2 \ . \qquad \text{(B.4)}$$

The general solution of equation (B.4) is

$$h\hat{\hat{\zeta}}_1(\alpha,y,\delta) = \kappa_1 e^{-y(\alpha^2 + \frac{\delta^2}{c_1^2})^{1/2}} + \kappa_2 e^{y(\alpha^2 + \frac{\delta^2}{c_1^2})^{1/2}} \tag{B.5}$$

where κ_1 and κ_2 are arbitrary functions of α and δ only. Now condition (A.14) must hold if our particular solution is to be valid. Thus we have that

$$\mathrm{Re}(\alpha^2 + \frac{\delta^2}{c_1^2}) > 0 \quad . \tag{B.6}$$

This condition allows us to conclude that

$$\lim_{y\to\infty}\left\{\kappa_2 e^{y(\alpha^2 + \frac{\delta^2}{c_1^2})^{1/2}}\right\} = \infty \quad .$$

Since we have no sources at $y = \infty$, we will assume that $\kappa_2 = 0$. For the sake of convenience, let

$$\kappa_1 \equiv A \frac{F(\delta)}{2\sqrt{2\pi}} \frac{1}{(\alpha^2 + \frac{\delta^2}{c_1^2})^{1/2}}$$

where A is an arbitrary function of α and δ only. The general solution (excluding waves arriving from ∞) for $\hat{\hat{\zeta}}_1$ is the sum of equations (B.3) and (B.5).

$$\hat{\hat{\zeta}}_1(\alpha,y,\delta) = \frac{F(\delta)}{2\sqrt{2\pi}\,(\alpha^2+\frac{\delta^2}{c_1^2})^{\frac{1}{2}}}\left[e^{-|y-h|(\alpha^2+\frac{\delta^2}{c_1^2})^{\frac{1}{2}}} + Ae^{-y(\alpha^2+\frac{\delta^2}{c_1^2})^{\frac{1}{2}}}\right] . \tag{B.7}$$

An argument similar to the one just given allows us to write the solution which converges as $y \to -\infty$ in medium 2.

$$\hat{\hat{\zeta}}_2(\alpha,y,\delta) = \frac{BF(\delta)}{2\sqrt{2\pi}\,(\alpha^2+\frac{\delta^2}{c^2})^{\frac{1}{2}}}\, e^{y(\alpha^2+\frac{\delta^2}{c_2^2})^{\frac{1}{2}}} , \tag{B.8}$$

where B is an arbitrary function of α and δ only. We would now like to find A and B. We do this by examining the conditions on the boundary, $y = 0$. For a fluid-fluid interface, we require that the displacement normal to the boundary is continuous. Also, the pressure must be continuous across the boundary. Normal displacements are continuous across the boundary if

$$\frac{\partial\hat{\hat{\zeta}}_1}{\partial y}(\alpha,0,\delta) = \frac{\partial\hat{\hat{\zeta}}_2}{\partial y}(\alpha,0,\delta) . \tag{B.9}$$

We will now derive the continuity of pressure condition. The pressure in a fluid can be written

$$K\nabla\cdot(\underset{\sim}{\nabla}\zeta(x,y,t)) = P = K\nabla^2\zeta(x,y,t) ,$$

where P ≡ pressure, K ≡ incompressibility, and

$$\nabla^2 = \frac{\partial^2 \zeta}{\partial x^2} + \frac{\partial^2 \zeta}{\partial y^2} \quad .$$

Now recall that the wave equation is

$$\nabla^2 \zeta = \frac{1}{c^2} \frac{\partial^2 \zeta}{\partial t^2}$$

where $c^2 = \frac{K}{\delta}$, and ρ = density. Thus

$$K \nabla^2 \zeta = \rho \frac{\partial^2 \zeta}{\partial t^2} \quad .$$

Thus the continuity of pressure condition can be written

$$\rho_1 \frac{\partial^2 \zeta_1(x,0,t)}{\partial t^2} = \rho_2 \frac{\partial^2 \zeta_2}{\partial t^2}(x,0,t) \quad . \tag{B.10}$$

Taking the Laplace and Fourier transforms of equation (B.10) yields

$$\rho_1 \, \delta^2 \, \hat{\bar{\zeta}}_1(\alpha,0,\delta) = \rho_2 \, \delta^2 \, \hat{\bar{\zeta}}_2(\alpha,0,\delta) \, ,$$

or

$$\rho_1 \, \hat{\bar{\zeta}}_1(\alpha,0,\delta) = \rho_2 \, \hat{\bar{\zeta}}_1(\alpha,0,\delta) \quad . \tag{B.11}$$

Now substituting the general solutions, (B.7) and (B.8), into the boundary conditions, (B.9) and (B.11), yields the two equations

$$\rho_1 \left[e^{-h\left(\alpha^2 + \frac{\delta^2}{c_1^2}\right)^{1/2}} + A \right] = \rho_2 B$$

and

$$\left(\alpha^2 + \frac{\delta^2}{c_1^2}\right)^{1/2} \left[e^{-h\left(\alpha^2 + \frac{\delta^2}{c_1^2}\right)^{1/2}} - A \right] = \left(\alpha^2 + \frac{\delta^2}{c_2^2}\right)^{1/2} B \quad .$$

Now if we define

$$\eta_1 \equiv \left(\frac{\alpha^2}{\rho^2} + \frac{1}{c_1^2}\right)^{1/2} \quad ,$$

$$\eta_2 \equiv \left(\frac{\alpha}{\rho^2} + \frac{1}{c_2^2}\right)^{1/2} \quad ,$$

and

$$\delta = \frac{\rho_2}{\rho_1} \quad ,$$

then the simultaneous solution of the above equations yields

$$A = \left(\frac{\delta\eta_1 - \eta_2}{\delta\eta_1 + \eta_2}\right) e^{-\eta_1 h\delta} \tag{B.12}$$

and

$$B = \left(\frac{2\eta_1}{\delta\eta_1 + \eta_2}\right) e^{-\eta_1 h\delta} \quad . \tag{B.13}$$

By substituting equation (B.12) into (B.7) we find that

$$\hat{\bar{\zeta}}_1(\alpha, y, s) = \frac{F(s)}{2\sqrt{2\pi}\, s\eta_1}\left[e^{-|y-h|\eta_1 s} + \left(\frac{s\eta_1 - \eta_2}{s\eta_1 + \eta_2}\right) e^{-\eta_1(y+h)s}\right] . \quad (B.14)$$

This is the exact solution for $\hat{\bar{\zeta}}$ in the upper medium. The rest of our efforts will be directed towards finding the inverse Fourier and Laplace transforms. We recognize that the first term of equation (B.14) is the solution to the problem of a line source in a whole-space. Essentially, it corresponds to the direct wave. Note that this direct wave part of the solution behaves as if there were no boundary at all. Even if y is small, the direct wave is unaffected by the presence of the boundary. This is true regardless of whether c_1 is greater or less than c_2.

Let us examine the second term in equation (B.14). Define

$$\hat{\bar{\zeta}}_r(\alpha, y, s) = \frac{F(s)}{2\sqrt{2\pi}\, s\eta_1}\left(\frac{s\eta_1 - \eta_2}{s\eta_1 + \eta_2}\right) e^{-\eta_1(y+h)s} . \quad (B.15)$$

The inverse Fourier transform of equation (B.15) is

$$\bar{\zeta}_r(x, y, s) = \frac{F(s)}{2\pi}\int_{-\infty}^{\infty} e^{-i\alpha x - \eta_1(y+h)s}\left(\frac{s\eta_1 - \eta_2}{s\eta_1 + \eta_2}\right)\frac{d\alpha}{\rho\eta_1} . \quad (B.16)$$

Just as in Appendix A, we will solve equation (B.16) by a change of variables. Let

$$\alpha = -is p \quad ; \quad d\alpha = -is\, dp . \quad (B.17)$$

Applying equations (B.17) to equation (B.16) we obtain

$$\bar{\zeta}_r(x,y,s) = \frac{F(s)}{4\pi i} \int_{-i\infty}^{i\infty} e^{-s[px + \eta_1(y+h)]} \left(\frac{s\eta_1 - \eta_2}{s\eta_1 + \eta_2}\right) \frac{dp}{\eta_1} \quad , \tag{B.18}$$

where

$$\eta_i^2 = \frac{1}{c_i^2} + \frac{\alpha^2}{s^2} = \frac{1}{c_i^2} - p^2 \quad . \tag{B.19}$$

As in Appendix A, we will apply the Schwartz reflection principle to equation (B.18) and we obtain

$$\bar{\zeta}_r(x,y,s) = \frac{F(s)}{2\pi} Im \int_{o}^{i\infty} e^{-s[px + \eta_1(y+h)]} \left(\frac{s\eta_1 - \eta_2}{s\eta_1 + \eta_2}\right) \frac{dp}{\eta_1} \quad . \tag{B.20}$$

Just as in Appendix A, we will make a change in variables which will make equation (B.20) look like a Laplace transform equation. We would like to find a path, the Cagniard contour, in the p plane such that if

$$\tau \equiv px + \eta_1(y+h) = px + (y+h)\sqrt{\frac{1}{c_1^2} - p^2} \quad , \tag{B.21}$$

then τ is both real and positive. If it is permissible to deform the path, p runs from o to $i\infty$, to the Cagniard path, then the transformation (B.21) will make equation (B.20) look like a Laplace transform equation. We will first calculate a path, $p(\tau)$, such that τ is real and positive. By inverting equation (B.21) we find that

$$p(\tau) = \frac{\tau x}{R^2} \pm i \frac{(y+h)}{R^2} \sqrt{\tau^2 - \frac{R^2}{c_1^2}} \quad , \tag{B.22}$$

where

$$R \equiv [x^2 + (y+h)^2]^{1/2} \quad .$$

Thus R is the distance that the reflected ray has travelled. We can also solve for $\eta_1(\tau)$.

$$\eta_1(\tau) = \frac{\tau(y+h)}{R^2} \mp i \left(\tau^2 - \frac{R^2}{c_1^2}\right)^{1/2} \frac{x}{R^2} \quad . \tag{B.23}$$

We can also show that

$$\frac{dp}{d\tau} = \frac{i\,\eta_1}{\left(\tau^2 - \frac{R^2}{c_1^2}\right)^{1/2}} \quad . \tag{B.24}$$

Finally,

$$\eta_1^2 = \frac{1}{c_1^2} - p^2 \quad \text{and} \quad \eta_2^2 = \frac{1}{c_2^2} - p^2$$

so

$$\eta_2(\tau) = \left[\eta_1^2(\tau) - \frac{1}{c_1^2} + \frac{1}{c_2^2}\right]^{1/2} \quad . \tag{B.25}$$

The substitution of equations (B.24) and (B.21) into equation (B.20)

yields

$$\bar{\zeta}_r(x,y,s) = \frac{F(s)}{2\pi} Im \int_0^\infty e^{-st} \left(\frac{\delta\eta_1 - \eta_2}{\delta\eta_1 + \eta_2}\right) \frac{i\, H(\tau - t_o)}{(\tau^2 - \frac{R^2}{c_1^2})^{\frac{1}{2}}} d\tau \qquad (B.26)$$

where $t_o = t(p=0) = |y+h|/c_1$.

Now equation (B.22) tells us that $p(\tau)$ becomes complex at $t_r = R/c_1$. Notice that

$$p(t_r) = \frac{t_r x}{R^2} = \frac{x}{Rc_1} \quad .$$

We recognize $p(t_r)$ to be the classical ray parameter for the geometric reflection.

In order to study the integration in more detail, we will need to consider several different cases. First, suppose that $c_1 > c_2$. This is the simplest case since there are no head waves generated. Now $p(t_r) < 1/c_1$ always. Also η_1 and η_2 are real for $t < t_r$ and thus the integrand of equation (B.26) is real for $t < t_r$. The Cagniard path is shown in Figure B2.

The solution when $c_2 < c_1$ is then

$$\bar{\zeta}_r(x,y,s) = \frac{F(s)}{2\pi} Re \int_0^\infty e^{-s\tau} \left(\frac{\delta\eta_1 - \eta_2}{\delta\eta_1 + \eta_2}\right) \frac{H(t - \tau_R)}{(\tau^2 - t_R^2)^{\frac{1}{2}}} d\tau \quad . \qquad (B.27)$$

Figure B2

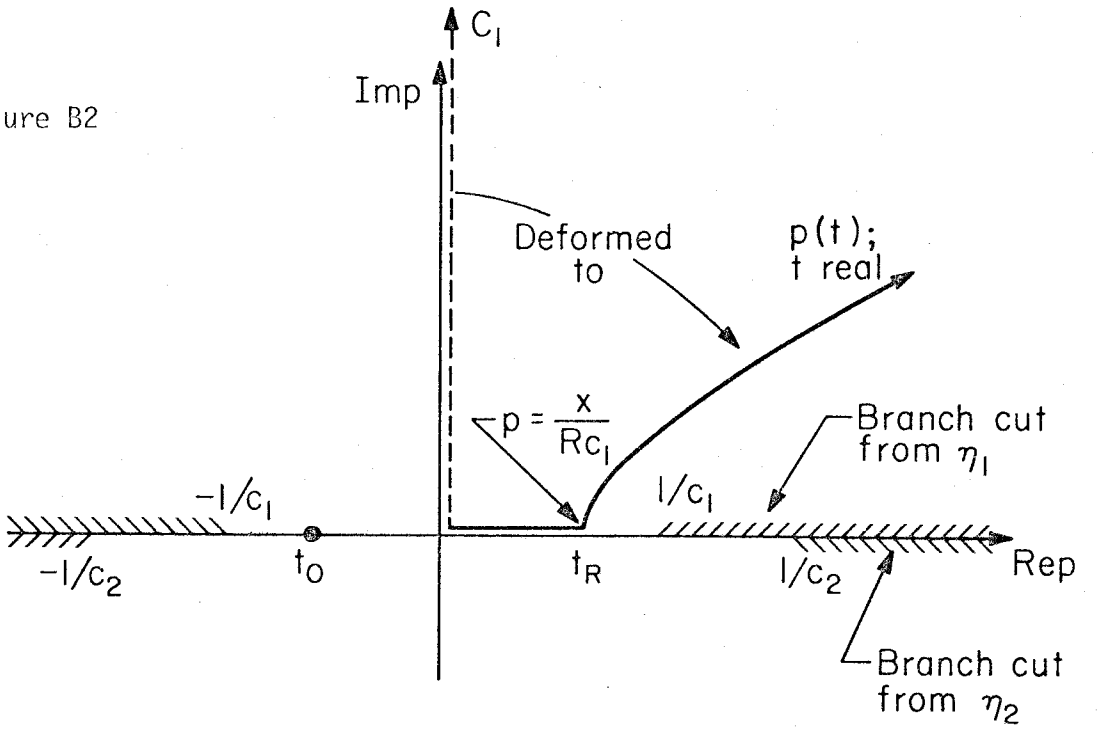

We can immediately recognize the solution to be

$$\bar{\zeta}_r(x,y,t) = \frac{f(t)}{2\pi} * \left[\frac{H(t - t_R)}{(t^2 - t_R^2)^{\frac{1}{2}}} \; R_{12}(t) \right] \tag{B.28}$$

where

$$R_{12}(t) \equiv \left[\frac{\delta\eta_1(t) - \eta_2(t)}{\delta\eta_1(t) + \eta_2(t)} \right] . \tag{B.29}$$

The expression for $R_{12}(t)$ is quite complex. In fact the algebra is so involved that we simply use a computer to numerically calculate this function. R_{12} is a generalized reflection coefficient. Notice that the solution (B.28) is similar to the direct ray solution except for this new complex time dependence which is introduced by $R_{12}(t)$. We can find

an analytic approximation to our solution which will be valid for times near the reflection time. We will call this a first motion approximation. Now recall from equation (B.26) that our solution looks like

$$\bar{\zeta}_r(x,y,s) = \frac{F(s)}{2\pi} Im \int_0^\infty e^{-s\tau} R_{12} \frac{dp}{d\tau} \frac{H(\tau - t_o)}{\eta_1} d\tau \quad , \tag{B.30}$$

where

$$\frac{dp}{d\tau} = \frac{i\,\eta_1}{(\tau^2 - t_r^{\,2})^{\frac{1}{2}}} \quad .$$

First notice that for t near t_r, dp/dt becomes very large since it has a square root singularity. Now also notice that equations (B.23) and (B.25) tell us that η_1 and η_2 are well behaved near t_r. Thus R_{12} is relatively well behaved near t_r. Since $R_{12}(t)$ changes slowly relative to dp/dt, we will consider that $R_{12}(t)$ is constant and equal to $R_{12}(t_r)$. We can immediately write the approximate solution for t near t_r by inspecting equation (B.28).

$$\zeta_r(x,y,t) \overset{\sim}{\sim} \frac{f(t)}{2\pi} * \left\{ \frac{H(t - t_r)}{(t^2 - t_r^{\,2})^{\frac{1}{2}}} R_{12}(t_r) \right\} \tag{B.31}$$

for t near $t_r = R/C_1$.

Except for the constant, $R_{12}(t_r)$, solution (B.31) has the same form as a direct ray which has travelled the reflected distance. We can show that $R_{12}(t_r)$ is the plane wave reflection coefficient for the geometric ray. Now

$$\eta_1(t_r) = \frac{y+h}{Rc_1} = \frac{\cos\theta}{c_1} \quad , \tag{B.32}$$

$$\eta_2(t_r) = \left[\frac{(y+h)^2}{Rc_1^{\,2}} - \frac{1}{c_1^{\,2}} + \frac{1}{c_2^{\,2}}\right]^{1/2}$$

$$= \frac{(c_1^{\,2} R^2 - x^2 c_2^{\,2})}{Rc_1c_2} = \frac{(c_1^{\,2} - c_2^{\,2}\sin^2\theta)^{1/2}}{c_1 c_2} \quad , \tag{B.33}$$

where θ is the incidence angle for the reflected ray. η_1 and η_2 are sometimes called the vertical wave slowness. Just as p could be interpreted as the reciprocal of the horizontal phase velocity, η can be interpreted as the reciprocal of the vertical phase velocity. We can now calculate $R_{12}(t_r)$.

$$R_{12}(t_r) = \left[\frac{\delta\eta_1(t_r) - \eta_2(t_r)}{\delta\eta_1(t_r) + \eta_2(t_r)}\right]$$

$$= \frac{\delta c_2 \cos\theta - (c_1^{\,2} - c_2^{\,2}\sin^2\theta)^{1/2}}{\delta c_2 \cos\theta + (c_1^{\,2} - c_2^{\,2}\sin^2\theta)^{1/2}} \quad . \tag{B.34}$$

Finally, we can write the approximate solution for $c_1 > c_2$ and t near t_r as

$$\zeta_r(x,y,t) \approx \frac{f(t)}{2\pi} * \left\{ \frac{H(t-t_r)}{(t^2 - t_r^{\,2})^{1/2}} \; R_{12}(t_r) \right\}$$

$$= \frac{f(t)}{2\pi} * \left\{ \frac{H(t-t_r)}{(t+t_r)^{1/2}(t-t_r)^{1/2}} \; R_{12}(t_r) \right\}$$

$$\approx \frac{f(t)}{2\pi} * \left\{ \frac{H(t-t_r)}{2t_r(t-t_r)^{1/2}} \; R_{12}(t_r) \right\} \quad . \tag{B.35}$$

We will now consider the case where $c_1 < c_2$. Remember that

$$p(\tau) = \frac{\tau x}{R^2} + i \, \frac{(y+h)}{R^2} \sqrt{\tau^2 - \frac{R^2}{c_1^{\,2}}} \quad .$$

Once again, p becomes complex for $\tau > t_r = R/c_1$. In this case, however, $p(t_r) = x/Rc_1$ can occur after the branch cut $1/c_2$. We will first examine what happens when $p(t_r) = x/Rc_1 < 1/c_2$. The Cagniard contour for this case would appear as shown in Figure B3.

Figure B3

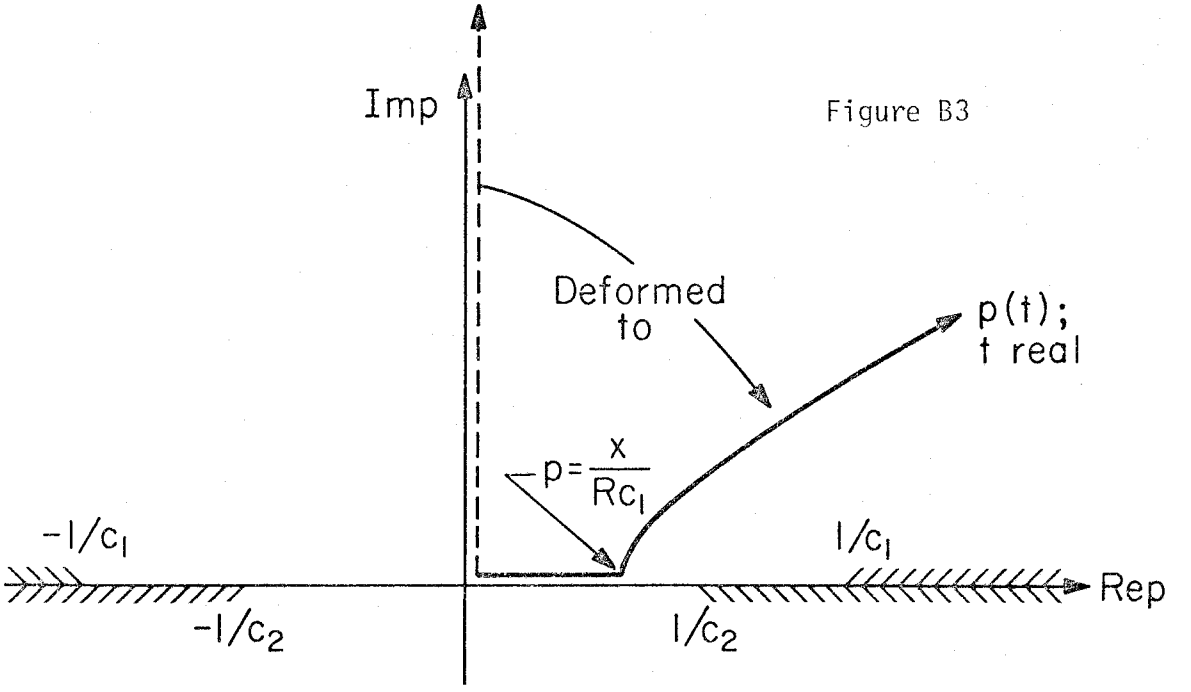

This case turns out to be exactly the same as the case which we just completed. Thus, solution (B.29) applies. Also, the same first motion approximation can be used. Thus the approximation (B.35) applies as long as $x/Rc_1 < 1/c_2$.

Now what if $x > Rc_1/c_2$? We recognize that this is the distance for which a geometric ray would be critically reflected. Recall the definition of η_1 and η_2 .

$$\eta_1 = \sqrt{\frac{1}{c_1^2} - p^2} \quad , \quad \eta_2 = \sqrt{\frac{1}{c_2^2} - p^2} \quad .$$

η_2 becomes imaginary when p becomes larger than $1/c_2$. Thus if $x > Rc_1/c_2$, our contour looks like the one shown in Figure B4.

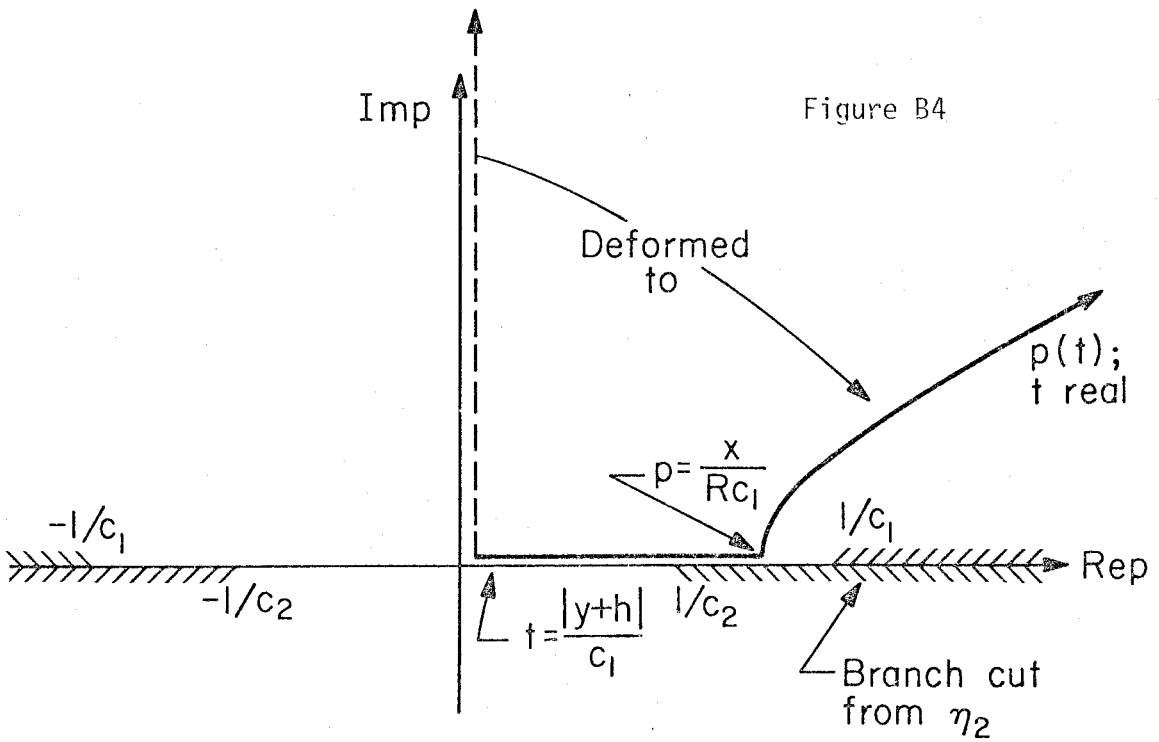

Figure B4

The integral we are to solve is given by equation (B.26)

$$\bar{\zeta}_r(x,y,s) = \frac{F(s)}{2\pi} Im \int_0^\infty e^{-s\tau} \left(\frac{\delta\eta_1 - \eta_2}{\delta\eta_1 + \eta_2}\right) \frac{i\, H(\tau - \frac{|y+h|}{c_1})\, d\tau}{(\tau^2 - t_r^2)} \quad . \qquad (B.36)$$

Since $\eta_2(\tau)$ becomes imaginary for $p > 1/c_2$, we expect a contribution to the integral before p itself becomes complex. This contribution is called the head wave. Notice that the time at which η_2 becomes complex is when $p(t_c) = 1/c_2$, or from equation (B.21),

$$t_c \equiv \frac{x}{c_2} + (y+h) \sqrt{\frac{1}{c_1^2} - \frac{1}{c_2^2}} \quad . \qquad (B.37)$$

This time can be shown to be the travel time for a head wave which is computed using classic geometric ray approaches.

Now define the head wave solution to be $(x,y,t_c < t < t_r)$.

Let

$$\zeta_{head}(x,y,t) = \frac{f(t)}{2\pi} * Im \left\{ \frac{1}{(t_r^2 - t^2)^{1/2}} \cdot \left(\frac{\delta\eta_1 - \eta_2}{\delta\eta_1 + \eta_2}\right) [H(t - t_c) - H(t - t_r)] \right\} . \qquad (B.38)$$

Remember, η_1 and η_2 are functions of time. η_2 is a real mess. Thus it is difficult to fully discuss the nature of ζ_{head} . We can examine the behavior of ζ_{head} near t_c by expanding p(t) near t_c. This will be a first motion approximation again. In our last first motion approximation, dp/dt had a singularity and we therefore considered η_1 and η_2 to be constant. If you examine equation (B.24) you see that dp/dt is nicely

behaved near t_c. Thus we must make a different kind of first motion approximation. Now

$$\eta_2 = -i\eta_2'$$

where

$$\eta_2' = \sqrt{p^2(t) - \frac{1}{c_2^2}} \quad . \tag{B.39}$$

Thus

$$Im\ \left(\frac{\delta\eta_1 - \eta_2}{\delta\eta_1 + \eta_2}\right) = \frac{2\delta\eta_1\eta_2'}{\delta^2\eta_1^2 + \eta_2^{2'}} \quad . \tag{B.40}$$

We can rewrite equation (B.38) as

$$\zeta_{head}(x,y,t) = \frac{f(t)}{\pi} * \left\{ \frac{[H(t - t_c) - H(t - t_r)]}{(t_r^2 - t^2)} \quad \frac{\delta\eta_1\eta_2'}{(\delta^2\eta_1^2 + \eta_2^{2'})} \right\} . \tag{B.41}$$

We will now approximate $\eta_2'(t)$ for t near t_c. Taking the first term in the Taylor expansion for p(t) near t_c, we obtain

$$p(t) \approx p(t_c) + \frac{dp(t_c)}{dt}(t - t_c) \quad .$$

So

$$p^2(t) \approx p^2(t_c) + 2p(t_c) \frac{dp(t_c)}{dt} (t - t_c) + [\frac{dp(t_c)}{dt}]^2 (t - t_c)^2 \quad . \quad (B.42)$$

$(t - t_c)^2$ is negligible for t near t_c and will be dropped. Now

$$\eta_2' = (p^2 - \frac{1}{c_2^2})^{\frac{1}{2}} \quad (B.43)$$

and

$$p(t_c) = \frac{1}{c_2} \quad . \quad (B.44)$$

Combining expressions (B.42), (B.43) and (B.44) we conclude that

$$\eta_2'(t) \approx [2 \frac{dp(t_c)}{dt} \frac{(t - t_c)}{c_2}]^{\frac{1}{2}} \quad .$$

From equation (B.24) we know that

$$\frac{dp(t_c)}{dt} = \frac{\eta_1(t_c)}{(t_r^2 - t_c^2)} \quad . \quad (B.45)$$

Now if t is near t_c, then $\eta_2^2 \ll \eta_1^2$, so

$$\frac{2\delta\eta_1\eta_2'}{\delta\eta_1^2+\eta_2'^2} \approx \frac{2\delta\eta_1\eta_2'}{\delta^2\eta_1^2}$$

$$= \frac{2\eta_2'}{\delta\eta_1} \approx \frac{2(t-t_c)^{1/2}\sqrt{2}\left(\frac{dp(t_c)}{dt}\right)^{1/2}}{\sqrt{C_2}\,\delta\eta_1}$$

$$= \frac{2(t-t_c)^{1/2}\sqrt{2}\ (\eta_1(t_c))^{1/2}}{(t_r^2-t_c^2)^{1/4}\sqrt{C_2}\,\delta\eta_1} \quad . \tag{B.46}$$

Now as $t \to t_c$, $\eta_1(t) \to \eta_1(t_c)$ in a well behaved manner. For our purposes, we can replace $\eta_1(t)$ by $\eta_1(t_c)$. Substituting expression (B.46) into equation (B.41) we obtain

$$\zeta_{head}(x,y,t) \approx \frac{f(t)}{\pi}\frac{\rho_1}{\rho_2} * \left\{ \frac{H(t-t_c)\ \sqrt{2}\ \sqrt{t-t_c}}{\left(\frac{R^2}{c_1^2}-t_c^2\right)^{3/4}\left(\frac{c_2^2}{c_1^2}-1\right)^{1/4}} \right\} \tag{B.47}$$

for t near t_c . Notice that the head wave solution starts off like the time integral of the direct wave solution.

Now let us examine the solution when $c_2 > c_1$ and t is near $t_r = R/c_1 > 1/c_2$. If $t_r < 1/c_2$, we get a noncritical reflection and we have already discussed this case. From equation (B.29) we expect the solution for the reflected wave to look like

$$\zeta_{ref}(x,y,t) = \frac{f(t)}{2\pi} * \left\{ \frac{H(t-t_r)}{(t^2-t_r^2)^{1/2}}\ \mathrm{Re}\left[\frac{\delta\eta_1-\eta_2}{\delta\eta_1+\eta_2}\right] \right\} \quad . \tag{B.48}$$

η_1 and η_2 are both complex for $t > R/c_1$. Once again, we cannot find $\eta_2(t)$ easily; so, we will make another first motion approximation. We will first calculate what the reflection coefficient looks like for $t = t_r = R/c_1$. Now again let

$$\eta_2' \equiv i\,\eta_2 \quad .$$

Then

$$\mathrm{Re}\left[\frac{\delta\eta_1(t_r) - \eta_2(t_r)}{\delta\eta_1(t_r) + \eta_2(t_r)}\right] = \mathrm{Re}\left[\frac{\delta\eta_1(t_r) - i\,\eta_2'(t_r)}{\delta\eta_1(t_r) + i\,\eta_2'(t_r)}\right]$$

$$= \mathrm{Re}\left[\frac{\delta^2\eta_1^{\,2}(t_r) - \eta_2'^{\,2}(t_r) - 2i\,\delta\eta_1(t_r)\,\eta_2'(t_r)}{\delta^2\eta_1^{\,2}(t_r) + \eta_2'^{\,2}(t_r)}\right]$$

$$= \frac{\delta^2\eta_1^{\,2}(t_r) - \eta_2'^{\,2}(t_r)}{\delta^2\eta_1^{\,2}(t_r) + \eta_2'^{\,2}(t_r)} \quad . \tag{B.49}$$

Now

$$\eta_1(t_r) = \frac{\cos\theta}{c_1}$$

and

$$\eta_2'(t_r) = \frac{(c_2^{\,2}\sin^2\theta - c_1^{\,2})^{1/2}}{c_1\,c_2}$$

where θ is the incident angle of the critically reflected geometric ray.

Thus, equation (B.49) becomes

$$\mathrm{Re}\left[\frac{\delta\eta_1(t_r) - \eta_2(t_r)}{\delta\eta_1(t_r) - \eta_2(t_r)}\right] = \frac{c_2^2(\delta^2\cos^2\theta - \sin^2\theta) + c_1^2}{c_2^2(\delta^2\cos^2\theta + \sin^2\theta) - c_1^2} \quad . \tag{B.50}$$

Equation (B.50) seems somewhat disturbing. The amplitude of this reflection coefficient is less than 1 for our post-critical reflection. We expect critically reflected waves to be totally reflected. What is wrong? To find the answer, we must return to the head wave portion of our solution. The exact solution was, from equation (B.41),

$$\zeta_{head}(x,y,t) = \frac{f(t)}{\pi} * \left\{\frac{[H(t-t_c) - H(t-t_r)]\ (\delta\eta_1\eta_2')}{(t_r^2 - t^2)^{1/2}\quad (\delta^2\eta_1^2 + \eta_2'^2)}\right\} \quad . \tag{B.51}$$

Notice that ζ_{head} also has a singularity as $t \to t_r = R/c_1$. Thus to understand a critical reflection, we must also consider the behavior of ζ before the time t_r . We can write down a first motion approximation for the critical reflection by considering contributions from both head wave and reflection terms, with the η_i's computed at t_r .

$$\zeta(x,y,t) \approx \frac{f(t)}{2\pi} * \left\{ \frac{1}{|t_r^2 - t^2|^{\frac{1}{2}}} [H(t_r - t)\ Im\ (\frac{\delta\eta_1 - \eta_2}{\delta\eta_1 + \eta_2}) \right.$$

$$\left. + H(t - t_r)\ Re\ (\frac{\delta\eta_1 - \eta_2}{\delta\eta_1 + \eta_2})] \right\}$$

$$\approx \frac{f(t)}{2\pi} * \left\{ \frac{1}{|t_r - t|^{\frac{1}{2}}(2t_r)} [H(t_r - t)\ Im\ (\frac{\delta\eta_1(t_r) - \eta_2(t_r)}{\delta\eta_1(t_r) + \eta_2(t_r)}) \right.$$

$$\left. + H(t - t_r)\ Re\ (\frac{\delta\eta_1(t_r) - \eta_2(t_r)}{\delta\eta_1(t_r) + \eta_2(t_r)})] \right\} , \qquad (B.52)$$

where t is near t_r. Equation (B.52) consists of the two parts which can be seen in Figure B5. Once again, let

$$R_{12} \equiv \frac{\delta\eta_1 - \eta_2}{\delta\eta_1 + \eta_2} .$$

Figure B5

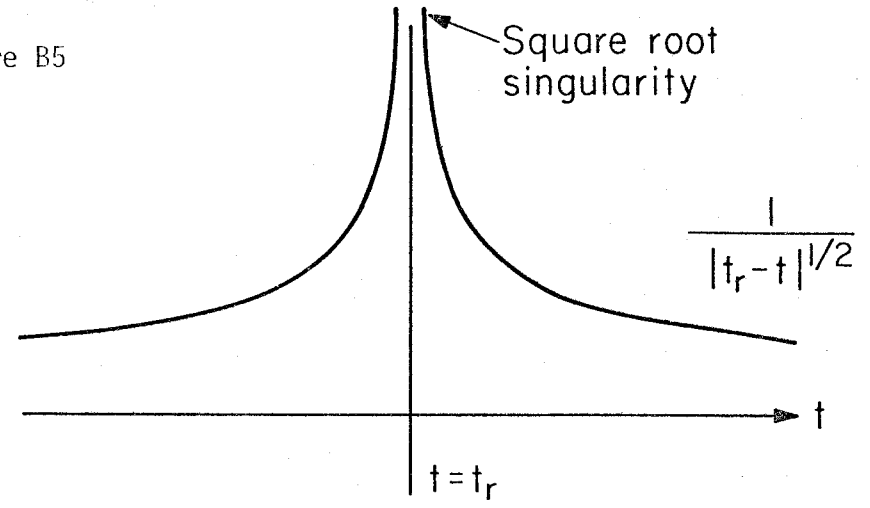

Multiplied by

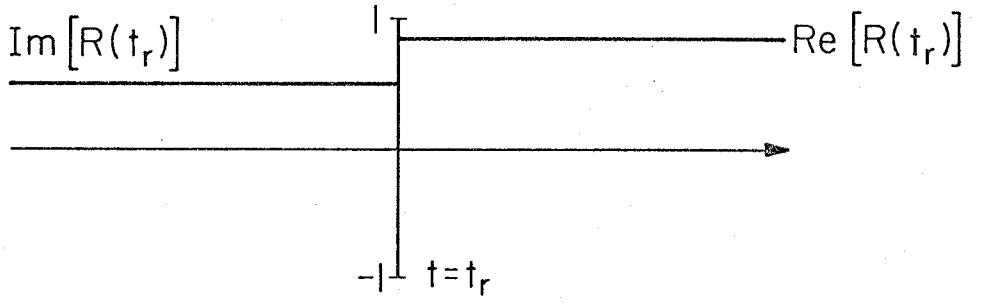

Equals

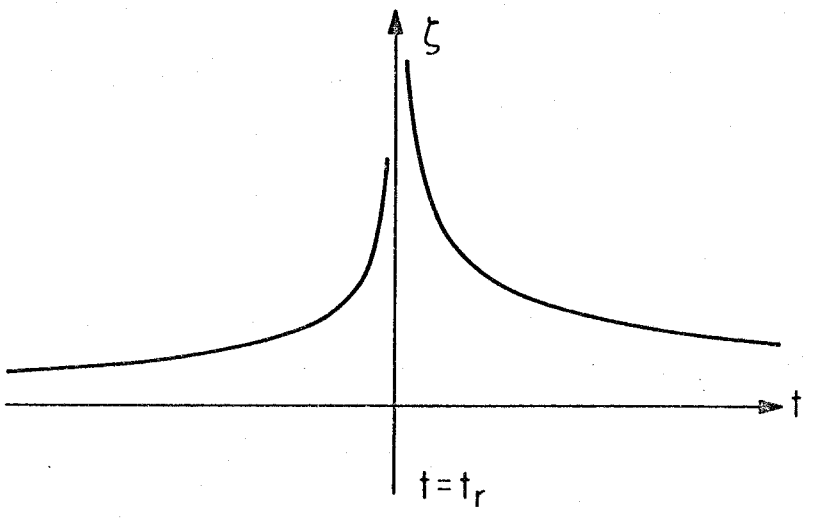

Figure B5

Now $Re(R_{12}(t_r))$ is given by equation (B.50) and $Im(R_{12}(t_r))$ is given by

$$Im(R_{12}(t_r)) = \frac{2\delta\eta_1(t_r) - \eta_2'(t_r)}{\delta^2\eta_1^2(t_r) + \eta_1'^2(t_r)} = \frac{2\delta\ c_2 \cos\theta\ (c_2^2 \sin^2\theta - c_1^2)}{c_2^2(\delta^2\cos^2\theta + \sin^2\theta) - c_1^2} \quad . \tag{B.53}$$

We can also show that $||R_{12}(t_r)|| = 1$ for a critical reflection

$$||R_{12}|| = \left|\left|\frac{\delta\eta_1 - i\eta_2'}{\delta\eta_1 + \eta_2'}\right|\right|$$

$$= \left|\left|\frac{\delta^2\eta_1 - \eta_2'^2 - 2i\eta_1\eta_2'\delta}{\delta^2\eta_1^2 + \eta_2'^2}\right|\right|$$

$$= \left[\frac{\delta^4\eta_1^4 + \eta_1'^4 - 2\delta^2\eta_1^2\eta_2^2 + 4\eta_1^2\eta_2^2\delta^2}{(\delta^2\eta_1^2 + \eta_2'^2)^2}\right]^{1/2}$$

$$= \left[\frac{(\delta^2\eta_1^2 + \eta_2'^2)^2}{(\delta^2\eta_1^2 + \eta_2'^2)^2}\right]^{1/2} = 1 \ .$$

Our complete first motion approximation for a critical reflection is

$$\zeta(x,y,t) \approx \frac{f(t)}{2\pi} * \left\{|t_r - t|^{-1/2}(2t_r)^{1/2}[H(t_r - t)\ Im\ R_{12} + H(t - t_r)\ Re\ R_{12}]\right\} . \tag{B.54}$$

Solution (B.54) is analogous to the phase shift present for critically reflected plane waves. This phase shift is discussed by Ewing, Jardetsky, and Press (1957). Brekhovskikh (1960) also gives a very illuminating discussion of critically reflected beams.

Summary of Waves in the Upper Medium

We can now summarize our solutions for waves in the upper medium. We begin with definitions.

$$r^2 = (y-h)^2 + x^2 \quad .$$

$$R^2 = (y+h)^2 + x^2 \quad .$$

$$t_o = r/C_1 \; ; \quad t_r = R/c_1 \quad .$$

$$\eta_1(t) = \frac{t(y+h)}{R^2} - i\,(t^2 - t_r^{\,2})^{\frac{1}{2}}\,\frac{x}{R^2} \quad .$$

$$\eta_2(t) = (\eta_1(t) - \frac{1}{c_1^{\,2}} + \frac{1}{c_2^{\,2}})^{\frac{1}{2}} \quad .$$

$$R_{12}(t) = \frac{\delta\eta_1 - \eta_2}{\delta\eta_1 + \eta_2} \quad .$$

$$\delta = \frac{\rho_2}{\rho_1} \quad .$$

Now

$$\zeta(x,y,t) = \zeta_{direct} + \zeta_r \quad ,$$

where

$$\zeta_{direct} = \frac{f(t)}{2\pi} * \left[\frac{H(t - \frac{r}{c_1})}{(t^2 - t_o^{\,2})^{\frac{1}{2}}}\right] \quad .$$

$$\zeta_{direct} = \frac{f(t)}{2\pi} * \left[\frac{H(t - \frac{r}{c_1})}{(t^2 - t_o^2)^{\frac{1}{2}}} \right] . \qquad (B.55)$$

The reflected solution has two cases. Case 1: No critical reflection, $x < Rc_1/c_2$

$$\zeta_r(x,y,t) = \frac{f(t)}{2\pi} * \left[\frac{H(t - t_r)}{(t^2 - t_r^2)^{\frac{1}{2}}} \text{ Re } R_{12}(t) \right] .$$

Case 2: Critical reflection, $x > Rc_1/c_2$

$$\zeta_r(x,y,t) = \zeta_{head} + \zeta_{ref} ,$$

where

$$\zeta_{head}(x,y,t) = \frac{f(t)}{2\pi} * \left\{ \frac{[H(t - t_c) - H(t - t_r)]}{(t_r^2 - t^2)^{\frac{1}{2}}} \; Im \; R_{12}(t) \right\} , \qquad (B.56)$$

and where

$$t_c = \frac{x}{c_2} + (y + h) \left(\frac{1}{c_1^2} - \frac{1}{c_2^2} \right)^{\frac{1}{2}} .$$

$$\zeta_{ref} = \frac{f(t)}{2\pi} * \left\{ \frac{H(t - t_r)}{(t^2 - t_r^2)^{\frac{1}{2}}} \text{ Re } R_{12}(t) \right\} . \qquad (B.57)$$

The first motion approximation for the head wave gave

$$\zeta_{head} \approx \frac{f(t)}{\pi} \frac{\rho_1}{\rho_2} * \left\{ \frac{H(t - t_c)\ \sqrt{2}\ \sqrt{t - t_c}}{(t_r^2 - t_c^2)^{3/4} \left(\frac{c_2^2}{c_1^2} - 1\right)^{1/4}} \right\}, \text{ for } t \text{ near } t_c \ . \qquad (B.58)$$

The first motion approximation for any reflected wave yields

$$\zeta_r \approx \frac{f(t)}{2\pi} * \left\{ |t_r - t|^{-1/2} (2t_r)^{-1/2} \left[H(t_r - t)\ Im\ R_{12}(t_r) + H(t - t_r)\ \text{Re}\ R_{12}(t_r) \right] \right\} \ , \text{ for } t \text{ near } t_r \ . \qquad (B.59)$$

Where if $x < Rc_1/c_2$, then

$$\text{Re}\ R_{12}(t_r) = \frac{c_2^2(\delta^2 \cos^2\theta + \sin^2\theta) + c_1^2}{c_2^2(\delta^2 \cos^2\theta + \sin^2\theta) - c_1^2}$$

and

$$Im\ R_{12}(t_r) = 0 \ .$$

If $x > Rc_1/c_2$, then

$$\text{Re}\ R_{12}(t_r) = \frac{\delta c_2 \cos\theta - (c_1^2 - c_2^2 \sin^2\theta)^{1/2}}{\delta c_2 \cos\theta + (c_1^2 - c_2^2 \sin^2\theta)^{1/2}}$$

and

$$Im\ R_{12}(t_r) = \frac{2\delta c_2 \cos\theta\ (c_2^2 \sin^2\theta - c_1^2)^{1/2}}{c_2^2(\delta \cos^2\theta + \sin^2\theta) - c_1^2} \ ,$$

where

$$\cos\theta = \frac{x}{R} \quad \text{and} \quad \sin\theta = \frac{y+h}{R} .$$

Solution for the Transmitted Wave

Let us now look briefly at the nature of the wave which is transmitted into the lower medium. The solution was given in equation (B.8).

$$\hat{\hat{\tau}}_2(\alpha, y, \delta) = \frac{BF(\delta)}{2\sqrt{2\pi}\,(\alpha^2 + \frac{\delta^2}{c_2^2})^{1/2}}\, e^{y(\alpha^2 + \frac{\delta^2}{c_2^2})^{1/2}} , \tag{B.60}$$

where

$$B = \left(\frac{2\eta_1}{\delta\eta_1 + \eta_2}\right) e^{-\eta_1 h\delta}$$

and where

$$\eta_1 = \left(\frac{\alpha^2}{\delta^2} + \frac{1}{c_1^2}\right)^{1/2} \quad , \quad \eta_2 = \left(\frac{\alpha^2}{\delta^2} + \frac{1}{c_2^2}\right)^{1/2}$$

and $y < 0$.

If we take the inverse Fourier transform of equation (B.60) with respect to α, we find that

$$\bar{\zeta}_2(x,y,s) = \frac{F(s)}{2\pi} \int_{-\infty}^{\infty} e^{-ix\alpha + ys\eta_2 - \eta_1 hs} \left(\frac{2\eta_1}{s\eta_1 + \eta_2}\right) \frac{d\alpha}{\rho\eta_1} \quad . \tag{B.61}$$

We now perform a familiar transformation,

$$\alpha = -isp \quad , \qquad d\alpha = -is\,dp \quad .$$

Equation (B.61) becomes

$$\bar{\zeta}_2(x,y,s) = \frac{F(s)}{4\pi} \int_{-i\infty}^{i\infty} e^{-s(xp + y\eta_2 - h\eta_1)} \left(\frac{2\eta_1}{s\eta_1 + \eta_2}\right) \frac{dp}{\eta_1} \quad , \tag{B.62}$$

where

$$\eta_i = \left(\frac{1}{c_i} - p^2\right)^{1/2} \quad .$$

If the Schwarz reflection principle is applied to equation (B.62), then we obtain

$$\zeta_2(x,y,s) = \frac{F(s)}{2\pi}\, Im \int_{0}^{i\infty} e^{-s(xp + y\eta_2 - h\eta_1)} \left(\frac{\eta_1}{s\eta_1 + \eta_2}\right) \frac{dp}{\eta_1} \quad . \tag{B.63}$$

We must now find the contour such that t is real and positive, where

$$t \equiv px + y\,\eta_2 - h\eta_1$$

$$= px + y\sqrt{\frac{1}{c_2^2} - p^2} - h\sqrt{\frac{1}{c_1^2} - p^2} \quad . \tag{B.64}$$

Applying the transformation (B.64) to equation (B.63) we obtain

$$\bar{\zeta}_2(x,y,s) = \frac{F(s)}{2\pi} Im \int_0^{\infty} e^{-st} \left(\frac{\eta_1}{\delta\eta_1 + \eta_2}\right) \frac{\frac{dp}{dt}\, dt}{\eta_1} \quad . \tag{B.65}$$

Now if we can find and deform to the contour given by equation (B.65), then our solution is

$$\zeta_2(x,y,t) = \frac{f(t)}{2\pi} * Im \left\{ \left[\frac{\eta_1(t)}{\delta\eta_1(t) + \eta_2(t)} \right] \frac{dp}{dt} \frac{1}{\eta_1(t)} \right\} \quad . \tag{B.66}$$

Unfortunately, we are not quite finished. We must find the contour, $p(t)$, and we must then calculate $\eta_i(t)$ and dp/dt. This is done by inverting equation (B.64). It does not take long to see that we need to invert a fourth order polynomial. This is hard to do analytically. Normally, we solve for $p(t)$ by using a numerical iteration scheme on the computer.

In general, the Cagniard-De Hoop technique will always force us to invert some n^{th} order polynomial. Usually, this must be done numerically. Actually, we should not be too surprised to see this, since the inversion of n^{th} order polynomials is inherent when computing the travel time of rays which travel an unknown path in a layered space between a source and a receiver. If you doubt this, you might try finding an analytic expression for the following simple problem. What is the travel time for a geometric ray, as a function of x, y, h, c_1 and c_2, for the geometry given in Figure B6?

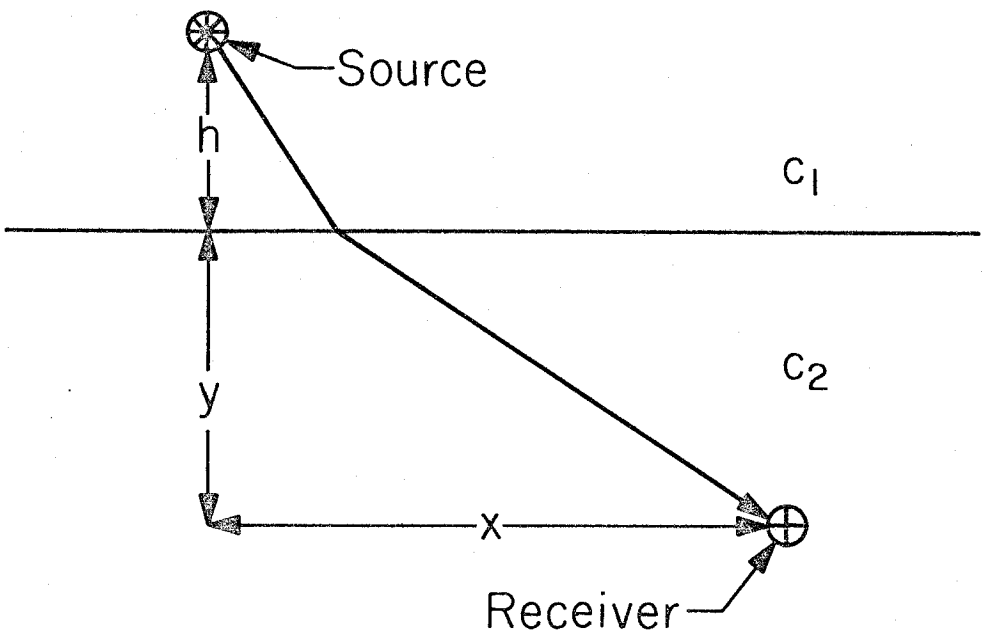

Figure B6

Appendix C

Sandwiched Fluid Layer Problem for a Line Source

In this Appendix, we introduce the notion of a generalized ray expansion as a solution to the layered space problem. Consider the geometry shown in Figure C1.

Figure C1

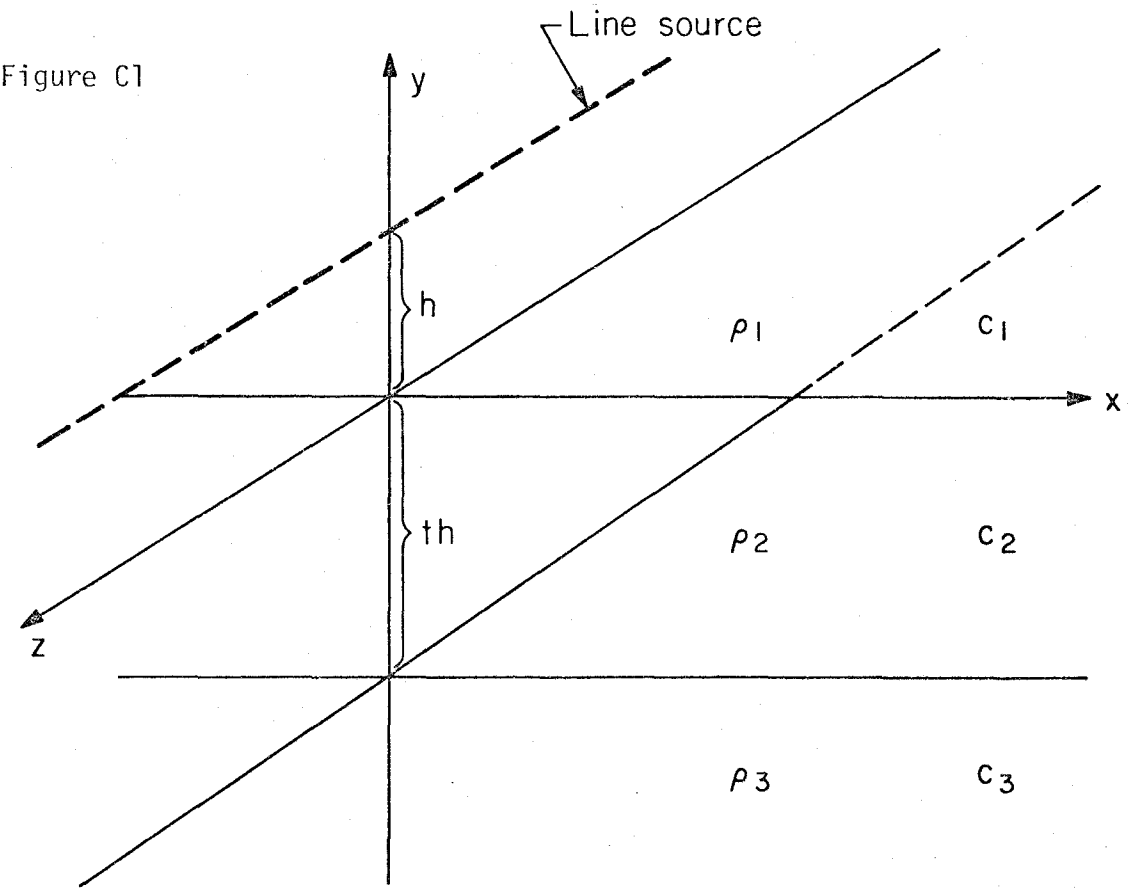

This problem is very similar to the one we just solved. The wave equations are

$$\frac{\partial^2 \zeta_1}{\partial x^2} + \frac{\partial^2 \zeta_1}{\partial y^2} - \frac{1}{c_1^2}\frac{\partial^2 \zeta_1}{\partial t^2} = -\delta(x)\ \delta(y-h)\ f(t)\ ,$$

$$\frac{\partial^2 \zeta_2}{\partial x^2} + \frac{\partial^2 \zeta_2}{\partial y^2} - \frac{1}{c_2^2}\frac{\partial^2 \zeta_2}{\partial t^2} = 0\ ,$$

$$\frac{\partial^2 \zeta_3}{\partial x^2} + \frac{\partial^2 \zeta_3}{\partial y^2} - \frac{1}{c_3^2}\frac{\partial^2 \zeta_3}{\partial t^2} = 0\ . \tag{C.1}$$

Now just as in section 2, we will write down the general solution for the above equations in the space (α, y, δ). We will eliminate solutions which are large at large values of $|y|$. By inspecting equations (B.7) and (B.8) we guess that our general solutions are

$$\hat{\bar{\zeta}}_1(\alpha, y, \delta) = \frac{F(\delta)}{2\sqrt{2\pi}\ \left(\alpha^2 + \frac{\delta^2}{c_1^2}\right)^{1/2}} \left[e^{-|y-h|\left(\alpha^2 + \frac{\delta^2}{c_1^2}\right)^{1/2}} + Ae^{-y\left(\alpha^2 + \frac{\delta^2}{c_1^2}\right)^{1/2}} \right], \tag{C.2}$$

$$\hat{\bar{\zeta}}_2(\alpha, y, \delta) = \frac{F(\delta)}{2\sqrt{2\pi}\ \left(\alpha^2 + \frac{\delta^2}{c_2^2}\right)^{1/2}} \left[Be^{y\left(\alpha^2 + \frac{\delta^2}{c_2^2}\right)^{1/2}} + Ce^{-y\left(\alpha^2 + \frac{\delta^2}{c_2^2}\right)^{1/2}} \right], \tag{C.3}$$

and

$$\bar{\zeta}_3(\alpha, y, \delta) = \frac{F(\delta)}{2\sqrt{2\pi}\ \left(\alpha^2 + \frac{\delta^2}{c_3^2}\right)^{1/2}} \left[De^{y\left(\alpha^2 + \frac{\delta^2}{c_3^2}\right)^{1/2}} \right]. \tag{C.4}$$

We now apply the boundary conditions at the two interfaces. This has been discussed in Appendix B. We will first require continuity of pressure across the boundaries.

$$\rho_1 \hat{\bar{\zeta}}_1(\alpha,0,s) = \rho_2 \hat{\bar{\zeta}}_2(\alpha,0,s) \quad ,$$

$$\rho_2 \hat{\bar{\zeta}}_2(\alpha,-th,s) = \rho_3 \hat{\bar{\zeta}}_3(\alpha,-th,s) \quad . \tag{C.5}$$

We now require the continuity of displacements across the boundaries.

$$\frac{\partial \hat{\bar{\zeta}}_1(\alpha,0,s)}{\partial y} = \frac{\partial \hat{\bar{\zeta}}_2(\alpha,0,s)}{\partial y} \quad ,$$

$$\frac{\partial \hat{\bar{\zeta}}_2(\alpha,-th,s)}{\partial y} = \frac{\partial \hat{\bar{\zeta}}_3(\alpha,-th,s)}{\partial y} \quad . \tag{C.6}$$

If we apply the boundary conditions to the general solutions in equations (C.2) through (C.4), then we obtain

$$\rho_1(e^{-hs\eta_1} + A) = (B + C)\,\rho_2 \quad , \tag{C.7}$$

$$\rho_2(e^{-ths\eta_2} + Ce^{ths\eta_2}) = \rho_3\, De^{-ths\eta_3} \quad , \tag{C.8}$$

$$s\,\eta_1(e^{-hs\eta_1} - A) = \eta_2(B - C) \quad , \tag{C.9}$$

$$s\,\eta_2(Be^{-ths\eta_2} - Ce^{ths\eta_2}) = s\,\eta_3\, De^{-ths\eta_2} \quad , \tag{C.10}$$

where

$$\eta_i = \left(\frac{\alpha^2}{\delta^2} + \frac{1}{c_i^2}\right)^{1/2} \quad .$$

We need to simultaneously solve the linear equations, (C.7) through (C.10), for A, B, C and D. After some painful algebra, one can show that

$$A = \left[\frac{R_{12} + R_{23}\, e^{-2th\delta\eta_2}}{1 + R_{12}\, R_{23}\, e^{-2th\delta\eta_2}}\right] e^{-\delta\eta_1 h} \quad , \tag{C.11}$$

where

$$R_{12} = \frac{\rho_2\eta_1 - \rho_1\eta_2}{\rho_2\eta_1 + \rho_1\eta_2} \quad , \tag{C.12}$$

and

$$R_{23} = \frac{\rho_3\eta_2 - \rho_2\eta_3}{\rho_3\eta_2 + \rho_2\eta_3} \quad . \tag{C.13}$$

Notice that if $th \to 0$, then

$$A \to \left(\frac{\rho_3\eta_1 - \rho_1\eta_3}{\rho_3\eta_1 + \rho_1\eta_3}\right) e^{-\delta\eta_1 h}$$

which is the simple interface result. Also if $th \to \infty$, then

$$A \to R_{12}\, e^{-\delta\eta_1 h}$$

which is the result from Appendix B.

Now as it turns out, the form of equation (C.11) will not allow us to apply our Cagniard-de Hoop technique. We would like exponentials involving s to be in the numerator. This can be accomplished by expanding the coefficient, A, in terms of a binomial series. Recall the binomial series

$$\frac{1}{1+x} = \sum_{n=0}^{\infty} (-1)^n x^n \qquad \text{where } x < 1 .$$

If we let $x = R_{12} R_{23} e^{-2th s\eta_2}$, then equation (C.11) can be written

$$A = R(p,s)\, e^{-s\eta_1 h} , \tag{C.14}$$

where

$$R(p,s) \equiv (R_{12} + R_{23} e^{-2th s\eta_2}) \sum_{n=0}^{\infty} (-1)^n R_{12}^{\,n} R_{23}^{\,n} e^{-2nth s\eta_2} , \tag{C.15}$$

or

$$R(p,s) = \sum_{n=0}^{\infty} (-1)^n R_{12}^{n+1} R_{23}^{n} e^{-2th s\eta_2 n}$$

$$+ \sum_{n=0}^{\infty} (-1)^n R_{12}^{n} R_{23}^{n+1} e^{-2th s\eta_2 (n+1)}$$

$$= \sum_{n=0}^{\infty} (-1)^n R_{12}^{n+1} R_{23}^{n} e^{-2th s\eta_2 n}$$

$$+ \sum_{n=1}^{\infty} (-1)^{n-1} R_{12}^{n-1} R_{23}^{n} e^{-2th s\eta_2 n}$$

$$= R_{12} + \sum_{n=1}^{\infty} [(-1)^n R_{12}^{n+1} + (-1)^{n-1} R_{12}^{n-1}] R_{23}^{n} e^{-2th s\eta_2 n}$$

$$= R_{12} + \sum_{n=1}^{\infty} (-1)^{n+1} R_{23}^{n} R_{12}^{n-1} (1 - R_{12}^{2}) e^{-2th s\eta_2 n} \quad . \qquad (C.16)$$

By substituting the coefficient, A, back into our solution in the upper medium, equation (C.2), we find that $\hat{\bar{\zeta}}_1(\alpha,y,s)$ can be written

$$\hat{\bar{\zeta}}_1 = \hat{\bar{\phi}}_{direct} + \hat{\bar{\phi}}_o (R_{12}) + \sum_{n=1}^{\infty} \hat{\bar{\phi}}_n \quad , \qquad (C.17)$$

where

$$\hat{\bar{\phi}}_{direct} = \frac{F(s)}{2\sqrt{2\pi}\,\eta_1 s} e^{-|y-h|\eta_1 s} , \tag{C.18}$$

$$\hat{\bar{\phi}}_o(R_{12}) = \frac{F(s)}{2\sqrt{2\pi}\,\eta_1 s} R_{12}\, e^{-(y+h)\eta_1 s} , \tag{C.19}$$

and

$$\hat{\bar{\phi}}_n(\alpha, y, s) = \frac{F(s)}{2\sqrt{2\pi}} e^{-s\eta_1(y+h)} (-1)^{n+1} R_{23}^{\,n} R_{12}^{\,n-1} (1 - R_{12}^{\,2}) e^{-2ths\eta_2} . \tag{C.20}$$

From Appendices A and B we immediately recognize $\hat{\bar{\zeta}}_{direct}$ and $\hat{\bar{\zeta}}_o$ to be the solution for the whole-space problem and the reflected solution for the interface problem, respectively. We already know how to find the inverse transforms for these parts of the solution. Our chore is to now take the inverse transforms of $\hat{\bar{\zeta}}_n(\alpha, y, s)$. As usual, we will first take the inverse Fourier transform with respect to α .

$$\bar{\phi}_n(x, y, s) = \frac{1}{\sqrt{2\pi}} \int_{-\infty}^{\infty} e^{-ix\alpha}\, \hat{\bar{\phi}}_n(\alpha, y, s)\, d\alpha \quad . \tag{C.21}$$

Now we make the familiar variable change

$$\alpha = is p \qquad ; \qquad d\alpha = -is\, dp \quad .$$

Equation (C.21) becomes

$$\bar{\phi}_n(x,y,s) = \frac{1}{\sqrt{2\pi}} \int_{-i\infty}^{i\infty} e^{-spx}\, \hat{\bar{\phi}}_n(-isp,y,s)\, \frac{d\alpha}{dp}\, dp \quad , \tag{C.22}$$

where

$$\bar{\phi}_n(-isp,y,s) = \frac{F(s)}{2\sqrt{2\pi}\, s\eta_1}\, f_n(p)\, e^{-sg_n(p)} \quad , \tag{C.23}$$

and where

$$f_n(p) = R_{23}^{\,n}\, R_{12}^{\,n-1}\, (1 - R_{12}^{\,2})(-1)^{n+1} \quad ,$$

$$g_n(p) = \eta_1(y+h) + 2\text{th } n\, \eta_2 \quad , \tag{C.24}$$

$$\eta_i(p) = \left(\frac{1}{c_i^2} - p^2\right)^{1/2} \quad ,$$

and

$$R_{ij} = \frac{\rho_j\eta_i - \rho_i\eta_j}{\rho_j\eta_i + \rho_i\eta_j} \quad .$$

We now apply the Schwartz reflection principle to equation (C.22) and obtain

$$\bar{\phi}_n(x,y,s) = \frac{F(s)}{2\pi}\, Im \int_0^{i\infty} e^{-s[px+g_n(p)]}\, f_n(p)\, \frac{dp}{\eta_1} \quad . \tag{C.25}$$

Applying the Cagniard-de Hoop method, one finds that the path in the p plane, where

$$\tau = px + g_n(p) \tag{C.26}$$

and τ is real and positive. A deformation of the contour, such as the one shown in Figure C2 is then made.

Figure C2

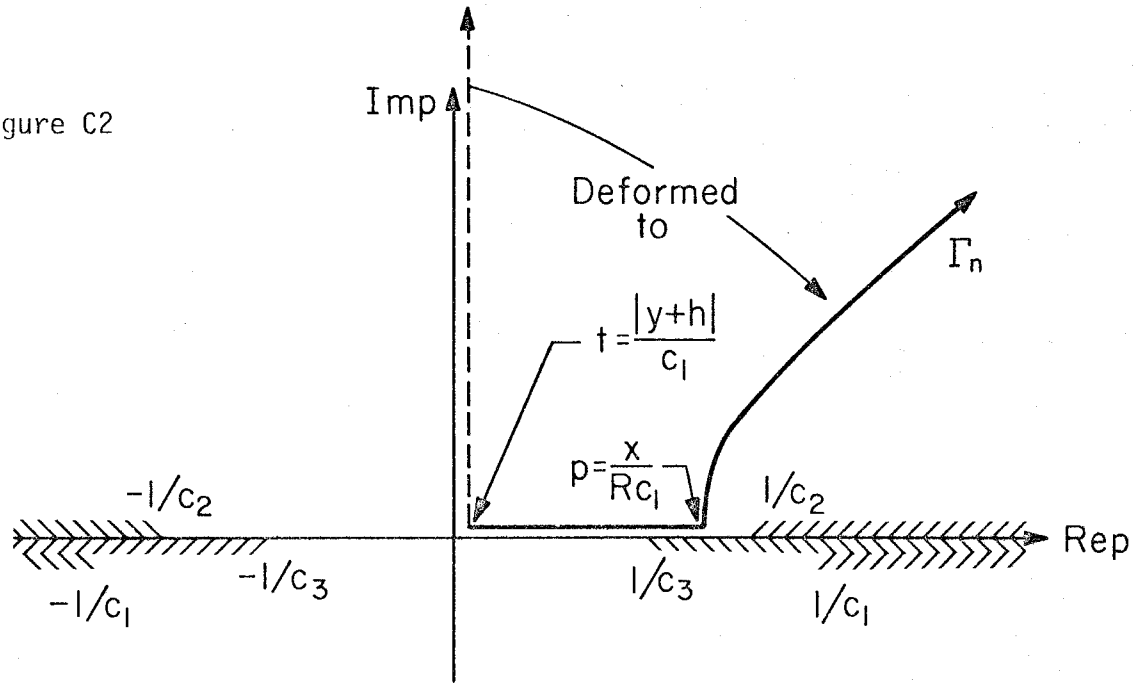

Equation (C.25) becomes

$$\bar{\phi}_n(x,y,s) = \frac{F(s)}{2\pi} Im \int_0^\infty H\left(\frac{|y+h|}{c_1} - \tau\right) f_n[p(\tau)] e^{-s[p(\tau)x+g_n(p(\tau))]} \frac{dp}{d\tau} \frac{d\tau}{\eta_1} . \tag{C.27}$$

The solution can then be written

$$\phi_n(x,y,t) = \frac{f(t)}{2\pi} * Im \left\{ f_n[p(t)] \frac{dp(t)}{dt} \frac{1}{\eta_1(t)} \right\}_{\Gamma_n} , \tag{C.28}$$

where $p(t)$ is defined by Γ_n . In general, we cannot analytically invert equation (C.26) to find $p(t)$. Thus Γ_n is found numerically.

Each ϕ_n can be given a simple physical interpretation. As an example, let n = 1. Then

$$t = px + \eta_1(y+h) + 2\eta_2 \, th \quad ,$$

and

$$f_1(p) = R_{23}(1 - R_{12}^2) \quad .$$

First notice that R_{23} contains η_3 which becomes imaginary at $p = 1/c_3$. This may occur before the point $p = x/Rc_1$, and thus there is the possibility of a head wave due to R_{23}. Next notice that

$$(1 - R_{12}^2) = 1 - \left(\frac{\rho_2\eta_1 - \rho_1\eta_2}{\rho_2\eta_1 + \rho_1\eta_2}\right)^2$$

$$= \left(\frac{2\eta_1}{\delta\eta_1 + \eta_2}\right)\left(\frac{2\eta_2\delta}{\delta\eta_1 + \eta_2}\right)$$

$$= T_{12}(p)\, T_{21}(p) \quad .$$

Thus

$$f_1(p) = T_{12}(p)\, R_{23}(p)\, T_{21}(p) \quad .$$

If you look back to equation (B.13), you will recognize that $T_{21}(p)$ is the transmission coefficient for a wave travelling from region 1 into region 2, and T_{21} is the transmission coefficient for a wave travelling

from region 2 into region 1. Thus the geometrical ray interpretation of ϕ_1 is shown in Figure C3.

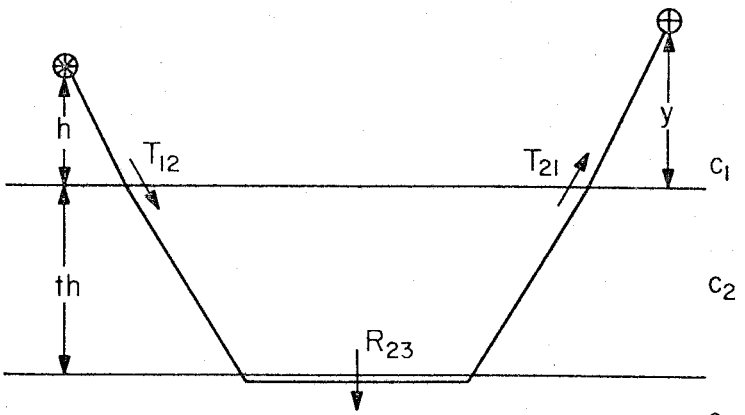

Figure C3

Now consider n = 2. Then

$$t = px + (y+h)\,\eta_1 + 4th\,\eta_2$$

and

$$f_2 = R_{23}^{\,2}\,R_{12}\,(1 - R_{12}^{\,2})(-1)$$

$$= T_{12}\,R_{23}\,R_{12}\,R_{23}\,T_{21} \quad ,$$

where we used the identity, $R_{21} = -R_{12}$. One can immediately see that ϕ_2 corresponds to the ray interpretation shown in Figure C4.

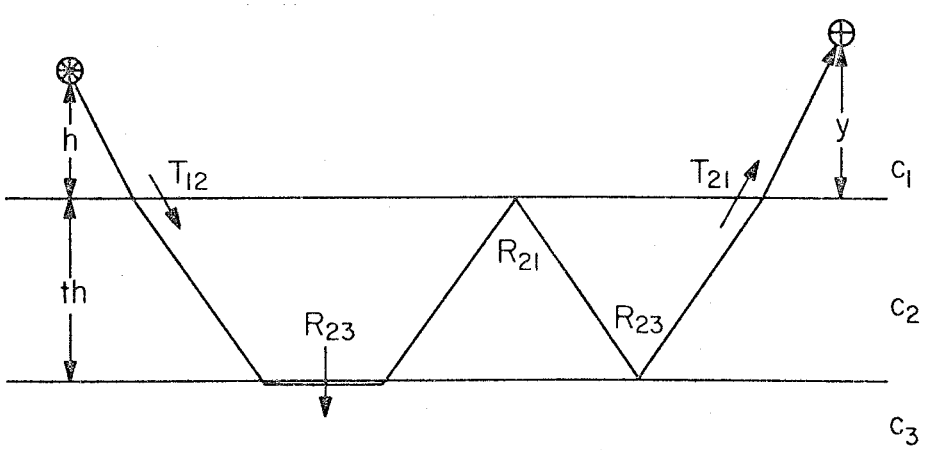

Figure C4

Similar ray interpretations can be made of each ϕ_n .

The objective of this Appendix is to provide motivation for a method for determining the response of a source embedded in a layered space. The method is called the method of generalized reflection and transmission coefficients. Simply consider any solution to be the sum over all possible generalized ray paths which connect the source and receiver. As a further example, we can easily construct the solution for waves transmitted through the sandwiched layer. We could go back and solve equations (C.8) through (C.10), but this is an algebraic headache. For more complex structures, it becomes a nightmare. We can easily guess the answer, however.

$$\zeta_3 = \sum_{n=1}^{\infty} {}_3\phi_n \quad ,$$

where

$${}_3\phi_n = f(t) * Im \left[{}_3f_n(p(t)) \frac{dp(t)}{dt} \frac{1}{\eta_1(p(t))} \right]_{{}_3\Gamma_n} \quad ,$$

where

$${}_3f_1 = T_{12} T_{23}$$

and ${}_c\Gamma_1$ is the contour which makes

$$t = -\eta_1 h + \eta_2 Th + \eta_3(y + Th) + px$$

positive and real. The ray interpretation is given in Figure C5.

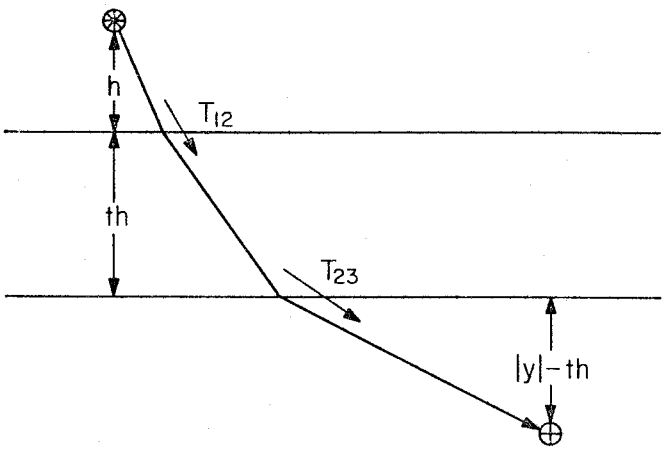

Figure C5

If n = 2, then we would choose the ray shown in Figure C6.

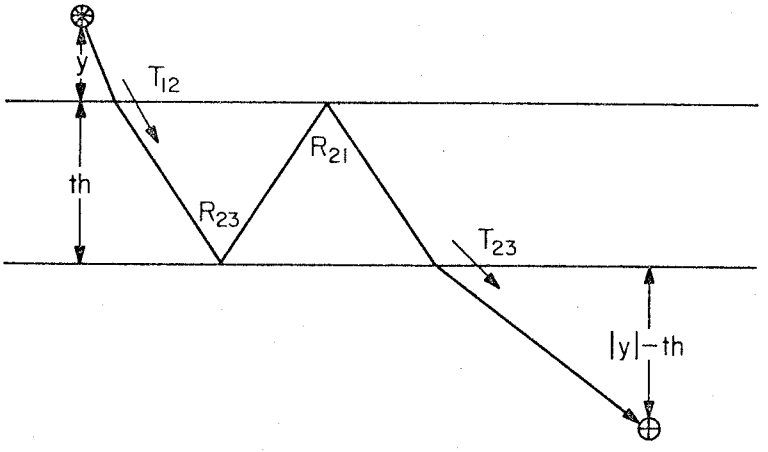

Figure C6

Now

$$c f_2 = T_{21} R_{23} R_{21} T_{32}$$

and the contour ${}_3\Gamma_2$ is the contour that keeps

$$t = \eta_1 h + 3\eta_2 \overline{T} h + \eta_3 (y + h) + px$$

positive and real. As n becomes larger, the rays simply have more bounces.

Appendix D

Point Source in an Infinite Medium

In the previous Appendices, we have worked the inherently two-dimensional problem of a line source. Because we eliminated motions parallel to the line source, Cartesian coordinates formed a convenient two-dimensional coordinate system. Unfortunately, line source problems are rather rare in nature. The solutions to point source problems turn out to be more useful to us. We did not present the line source problems without reason, however. Most of what we learned from line sources is easily transferred to the point source problem. Unfortunately, the point source problem does not reduce to two-dimensions in Cartesian coordinates. Assume that our solution is given in terms of some scalar potential, ζ, which has the properties that

$$\underset{\sim}{\nabla}\zeta = \underset{\sim}{\mu} \equiv \text{displacement vector} \tag{D.1}$$

and that ζ satisfies the wave equation,

$$\nabla^2\zeta - \frac{1}{c^2}\frac{\partial^2\zeta}{\partial t} = -\delta(x)\,\delta(y)\,\delta(z)\,f(t) \quad . \tag{D.2}$$

In Cartesian coordinates,

$$\nabla^2\zeta = \frac{\partial^2\zeta}{\partial x^2} + \frac{\partial^2\zeta}{\partial y^2} + \frac{\partial^2\zeta}{\partial z^2}$$

and the problem explicitly contains three spatial dimensions. We would

like to simplify this problem by changing coordinate systems. For a point source in an infinite medium, it would be easiest to solve this problem in spherical coordinates. We would be faced with a trivial one-dimensional wave equation. However, spherical coordinates are inappropriate for problems which involve boundary conditions on plane layers. Since it is our ultimate goal to solve layered space problems, we instead choose to solve this problem in cylindrical coordinates. We will write ζ as some function of r, θ and z. Our boundary conditions will then be specified along some planes of constant z. Consider the coordinate system in Figure D1.

Figure D1

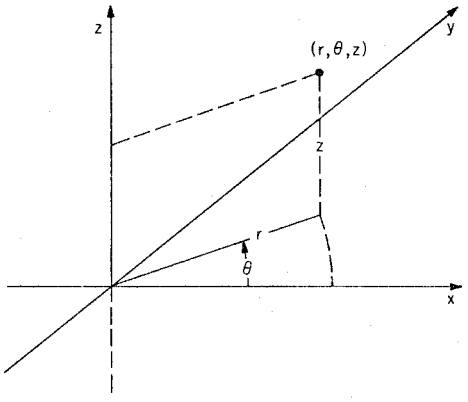

Now in cylindrical coordinates,

$$\nabla^2\zeta = \frac{1}{r}\frac{\partial}{\partial r}\left(r\frac{\partial\zeta}{\partial r}\right) + \frac{1}{r^2}\left(\frac{\partial^2\zeta}{\partial\theta^2}\right) + \frac{\partial^2\zeta}{\partial z^2} \quad . \tag{D.3}$$

If we consider the solution to be symmetric with respect to θ, then the wave equation can be written

$$\frac{\partial^2\zeta}{\partial r^2} + \frac{1}{r}\frac{\partial\zeta}{\partial r} + \frac{\partial^2\zeta}{\partial z^2} - \frac{1}{c^2}\frac{\partial^2\zeta}{\partial t^2} = -\delta(r)\ \delta(z)\ f(t) \tag{D.4}$$

and now in cylindrical coordinates

$$\underset{\sim}{u} = \underset{\sim}{\nabla}\zeta(r,\theta,z) = \underset{\sim}{e}_r \frac{\partial \zeta}{\partial r} + \underset{\sim}{e}_\theta \frac{1}{r}\frac{\partial \zeta}{\partial \theta} + \underset{\sim}{e}_z \frac{\partial \zeta}{\partial z} \quad . \tag{D.5}$$

We will find the solution to equation (D.4) by first finding the homogeneous solution to equation (D.4) and then we will construct the particular solution from the homogeneous solution. The homogeneous form of the wave equation (D.4) is

$$\frac{\partial^2 \zeta}{\partial r^2} + \frac{1}{r}\frac{\partial \zeta}{\partial r} + \frac{\partial^2 \zeta}{\partial z^2} = \frac{1}{c^2}\frac{\partial^2 \zeta}{\partial t^2} \quad . \tag{D.6}$$

We now take the Laplace transform of equation (D.6) with respect to time and find that

$$\frac{\partial^2 \bar{\zeta}}{\partial r^2} + \frac{1}{r}\frac{\partial \bar{\zeta}}{\partial r} + \frac{\partial^2 \bar{\zeta}}{\partial z^2} = \frac{s^2}{c^2}\bar{\zeta}(r,z,s) \quad , \tag{D.7}$$

where

$$\bar{\zeta}(r,z,s) = \int_0^\infty \zeta(r,z,t)e^{-st}\,dt \quad , \tag{D.8}$$

and

$$\mathcal{LP}\left\{\frac{\partial^2 \zeta}{\partial t^2}\right\} = s^2 \mathcal{LP}\{\zeta\} \quad .$$

We will solve equation (D.7) by a separation of variables. Assume that

$$\tilde{\zeta}(r,z,\delta) = R(r)\, Z(z)\, F(\delta) \quad . \tag{D.9}$$

Substituting equation (D.9) into (D.7) we obtain

$$\frac{\partial^2(RZF)}{\partial r^2} + \frac{1}{r}\frac{\partial}{\partial r}(RZF) + \frac{\partial^2}{\partial z^2}(RZF) = \frac{\delta^2}{c^2} RZF \quad ,$$

or

$$\frac{R''}{R} + \frac{1}{r}\frac{R'}{R} + \frac{Z''}{Z} - \frac{\delta^2}{c^2} = 0 \quad . \tag{D.10}$$

Then

$$\frac{R''}{R} + \frac{1}{r}\frac{R'}{R} = -k^2 = \frac{-Z''}{Z} + \frac{\delta^2}{c^2}$$

and equation (D.10) reduces to the two differential equations

$$\frac{R''}{R} + \frac{1}{r}\frac{R'}{R} = -k^2 \tag{D.11}$$

and

$$\frac{Z''}{Z} = \frac{\delta^2}{c^2} + k^2 \equiv \nu^2 \quad , \tag{D.12}$$

where k is some arbitrary constant. We immediately recognize the solutions of equations (D.11) and (D.12) to be $R(r) = J_0(kr)$ and $Z(z) = e^{\pm \nu z}$, respectively. Thus a solution of equation (D.7) is of the form

$$\bar{\zeta}(r,z,s) = e^{\pm\nu z}\, J_0(kr)\, F(s) \quad . \tag{D.13}$$

Because equation (D.13) is a solution to the wave equation, and because the wave equation is linear, we can immediately construct a more general solution.

$$\bar{\zeta}(r,z,s) = F(s)\int_0^\infty J_0(kr)\,[A(k)e^{-\nu z} + B(k)e^{\nu z}]dk \quad . \tag{D.14}$$

We will keep only those solutions which converge as $|z| \to \infty$. Thus we will pick those solutions which can be written

$$\bar{\zeta}(r,z,s) = F(s)\int_0^\infty A(k)e^{-\nu|z|}\, J_0(kr)\, dk \quad . \tag{D.15}$$

We now need to find A(k), such that equation (D.15) meets the condition that $\zeta(r,z,t) \to \delta(r)\,\delta(z)\,f(t)$ as $r \to 0$ and $z \to 0$. In order to find A(k), we will cheat. We will take the known solution to our problem in spherical coordinates and we will then transform this solution to cylindrical coordinates. We know that in spherical coordinates our solution can be written

$$\zeta(R,t) = \frac{1}{R}\, f(t - \frac{R}{c}) \quad . \tag{D.16}$$

If we take the Laplace transform of equation (D.16), then we find that

$$\bar{\zeta}(R,s) = \frac{1}{R}\int_0^\infty e^{-st}\, f(t - \frac{R}{c})\, dt \quad ,$$

or

$$\bar{\zeta}(R,s) = \frac{1}{R} e^{-(s/c)R} F(s) \ , \tag{D.17}$$

where we have used the shift rule. The question now is: Can we find a way to match solution (D.17) to our general solution (D.15)? To answer this, we will employ a transformation which was originated by Lamb (1904). This transformation makes it possible to express any spherical symmetric source function in terms of cylindrical coordinates. We will give this transformation, which is often called the Sommerfeld integral, in terms of a lemma.

lemma: Sommerfeld Integral

$$\frac{e^{-(s/c)R}}{R} = \int_0^\infty J_0(kr) e^{-\nu|z|} \frac{k}{\nu} dk \ , \tag{D.18}$$

where $R^2 = r^2 + z^2$ and $\nu^2 = (k^2 + \frac{s^2}{c^2})$. We can derive equation (D.18) in the following manner. We have already shown that equations (D.15) and (D.16) are solutions to the wave equation. Furthermore, equation (D.15) is a particular solution to the class of solutions defined by equation (D.16). We would like to find A(k) such that

$$\frac{e^{-(s/c)R}}{R} = \int_0^\infty A(k) e^{-\nu|z|} J_0(kr) \, dk \ . \tag{D.19}$$

Now A is a function of k only, and thus we can determine k by fixing either z or r and then solving equation (D.19). For example, when

$z = 0$, $R = r$ and equation (D.19) becomes

$$\frac{e^{-(\delta/c)r}}{r} = \int_0^\infty A(k)\, J_0(kr)\, dk \quad . \tag{D.20}$$

Now suppose $A(k) = k\, g(k)$, then by Whittaker and Watson (1950, p. 385)

$$\frac{e^{-(\delta/c)r}}{r} = \int_0^\infty k\, g(k)\, J_0(kr)\, dk \quad , \tag{D.21}$$

where

$$g(k) = \int_0^\infty \frac{x\, e^{-(\delta/c)x}}{x}\, J_0(kx)\, dx = \int_0^\infty e^{-(\delta/c)x}\, J_0(kx)\, dx \quad . \tag{D.22}$$

By Dwight (1947, formula 875.1), we know that

$$\int_0^\infty e^{-(\delta/c)x}\, J_0(kx) = \left(\frac{\delta^2}{c^2} + k^2\right)^{-\frac{1}{2}} \quad . \tag{D.23}$$

Thus, from equations (D.22) and (D.23) we conclude that

$$g(k) = \left(\frac{\delta^2}{c^2} + k^2\right)^{-\frac{1}{2}} = \frac{1}{\nu} \tag{D.24}$$

and thus

$$A(k) = \frac{k}{\nu}$$

and

$$\frac{e^{-(s/c)R}}{R} = \int_0^\infty J_0(kr)e^{-\nu|z|}\,\frac{k}{\nu}\,dk \quad . \tag{D.25}$$

Equation (D.25) is the formula we were trying to derive. We could also have derived equation (D.25) by choosing $r = 0$, and then by showing that

$$\frac{e^{-(s/c)z}}{z} = \int_0^\infty A(k)e^{-\nu|z|}\,dk = \int_0^\infty \frac{k}{\nu}\,e^{-\nu|z|}\,dk \quad .$$

Although we have now derived the Sommerfeld integral, equation (D.18), we have not provided much physical motivation for it. This integral is of fundamental importance to the solution of spherical wave problems. I suggest that the reader carefully study its meaning. Unfortunately, I know of no intuitive arguments which would have allowed us to guess the form of this important transformation.

We now have constructed a solution to the point source problem in cylindrical coordinates. That solution is simply

$$\bar{\zeta}(r,z,s) = F(s)\int_0^\infty J_0(kr)\,\frac{e^{-\nu|z|}}{\nu}\,k\,dk \quad . \tag{D.26}$$

We would like to develop techniques for evaluating integrals of the form which is present in equation (D.26). Just as in the line source problem, we would eventually like to transform equation (D.26) to one which allows

us to do the inverse Laplace transform by inspection. We will begin by making the transformation

$$k = -is p \quad ; \quad dk = -is\,dp \quad . \tag{D.27}$$

Then

$$\nu \equiv (k^2 + \frac{s^2}{c^2})^{1/2} = (\frac{1}{c^2} - p^2)^{1/2} \equiv s\,\eta \tag{D.28}$$

and

$$J_o(kr) = J_o(-ispr) = \frac{i}{\pi} K_o(spr) - \frac{i}{\pi} K_o(-spr) \quad , \tag{D.29}$$

where K_o is a modified Bessel function. Actually the derivation of equation (D.29) is not trivial. A short digression will allow us to derive this relationship. We begin with several formulae from Abramowitz and Stegun (1972).

$$H_\mu^{(1)}(z) = J_\mu(z) + iY_\mu(z) \tag{D.30}$$

and

$$H_\mu^{(2)}(z) = J_\mu(z) - iY_\mu(z) \quad ,$$

where $H_\mu^{(1)}$ and $H_\mu^{(2)}$ are Hankel functions of the first and second kind of order μ. Y_μ is a Bessel function of the second kind of order μ.

Combining equations (D.30) we obtain

$$J_\mu(z) = \frac{H_\mu^{(1)}(z) + H_\mu^{(2)}(z)}{2} \quad . \tag{D.31}$$

From Abramowitz and Stegun (1972) we also know that

$$K_\mu(z) = \frac{1}{2}\pi i e^{\frac{1}{2}\mu\pi i} H_\mu^{(1)}(iz)$$

and

$$K_\mu(z) = -\frac{1}{2}\pi i e^{-\frac{1}{2}\mu\pi i} H_\mu^{(2)}(-iz) \quad .$$

Thus

$$K_\mu(-z) = -\frac{1}{2}\pi i e^{-\frac{1}{2}\mu\pi i} H_\mu^{(2)}(iz) \quad .$$

For our present purposes, $\mu = 0$, and thus

$$H_o^{(1)}(iz) = -\frac{2i}{\pi} K_o(z)$$

and

$$H_o^{(2)}(iz) = \frac{2i}{\pi} K_o(-z) \quad . \tag{D.32}$$

If we combine equations (D.31) and (D.32), we find that

$$J_0(iz) = -\frac{i}{\pi} K_0(z) + \frac{i}{\pi} K_0(-z) \quad . \tag{D.33}$$

We also know that

$$J_0(-iz) = J_0(iz)$$

and thus equation (D.33) becomes

$$J_0(-iz) = \frac{i}{\pi} K_0(z) - \frac{i}{\pi} K_0(-z) \tag{D.34}$$

which is the desired relationship.

Now from equations (D.26) through (D.29) we conclude that

$$\bar{\zeta}(r,z,s) = \frac{-iF(s)s}{\pi} \int_0^\infty K_0(spr)\, e^{-s\eta|z|}\, \frac{p}{\eta}\, dp$$

$$+ \frac{iF(s)}{\pi} s \int_0^{i\infty} K_0(spr)\, e^{-s\eta|z|}\, \frac{p}{\eta}\, dp$$

$$= \frac{-iF(s)}{\pi} s \int_{-i\infty}^{i\infty} K_0(spr)\, e^{-s\eta|z|}\, \frac{p}{\eta}\, dp \quad . \tag{D.35}$$

We can now use the Schwartz reflection principle to rewrite equation (D.35) as

$$\bar{\zeta}(r,z,s) = \frac{2sF(s)}{\pi}\, Im \int_0^{i\infty} \frac{p}{\eta} K_0(spr)\, e^{-s\eta|z|}\, dp \quad . \tag{D.36}$$

Now if K_0 were not a function of s, then we could perform our transformation

to the variable, t, and we could then identify (D.36) as a Laplace transform equation. Since K_o is a function of s, the exact solution of this integral is difficult to find. Before we discuss the exact solution, we will find an approximate solution which requires no special integration techniques. For spr large, we can use the asymptotic approximation,

$$K_o(spr) \approx \sqrt{\frac{\pi}{2spr}}\, e^{-spr} \left[1 - \frac{1}{8spr} + \cdots\right] \quad . \tag{D.37}$$

Combining equations (D.36) and (D.37) we find that

$$\bar{\zeta}(r,z,s) \approx \frac{sF(s)}{\sqrt{\pi r s}} \left[\sqrt{2}\, Im \int_o^{i\infty} \frac{\sqrt{p}}{\eta}\, e^{-s(pr+\eta|z|)}\, dp \right.$$

$$\left. + \frac{1}{s4\pi\sqrt{2}}\, Im \int_o^{i\infty} \frac{1}{\sqrt{p}\,\eta}\, e^{-s(pr+\eta|z|)}\, dp + \cdots \right] \quad . \tag{D.38}$$

We now make our usual transformation

$$\tau = pr + \eta|z| \quad , \tag{D.39}$$

where

$$\eta = \left(\frac{1}{c^2} - p^2\right)^{1/2} \quad .$$

If we invert (D.39), then we find that

$$p = \frac{r}{R^2}\tau + i(\tau^2 - \frac{R^2}{c^2})^{\frac{1}{2}} \frac{|z|}{R^2} \qquad \text{(D.40)}$$

and

$$\eta = \frac{|z|}{R^2}\tau - i(\tau^2 - \frac{R^2}{c^2})^{\frac{1}{2}} \frac{r}{R^2} \qquad \text{(D.41)}$$

$\tau > R/c$

and

$$p = \frac{r}{R^2}\tau - (\frac{R^2}{c^2} - \tau^2)^{\frac{1}{2}} \frac{|z|}{R^2} \qquad \text{(D.42)}$$

and

$$\eta = \frac{|z|}{R^2}\tau + (\frac{R^2}{c^2} - \tau^2)^{\frac{1}{2}} \frac{r}{R^2} \qquad \text{(D.43)}$$

$\tau < R/c$

Taking the derivative of equation (D.40) we obtain

$$\frac{dp}{d\tau} = \frac{r}{R^2} + i(\tau - \frac{R^2}{c^2})^{-\frac{1}{2}} \tau \frac{|z|}{R^2} = \frac{i\eta}{(\tau^2 - \frac{R^2}{c^2})^{\frac{1}{2}}} \qquad \text{(D.44)}$$

Notice that by choosing the positive root in equation (D.40) we have managed to keep Re $\eta > 0$. This keeps the Cagniard contour in the upper half of the p plane. We would like the variable, τ, to be positive and real along our integration. Thus we would like to deform our path of integration from $p = 0$ to $p = i\infty$, to a new path Γ, along which τ is positive and real. Such a path is shown in Figure D2.

Figure D2

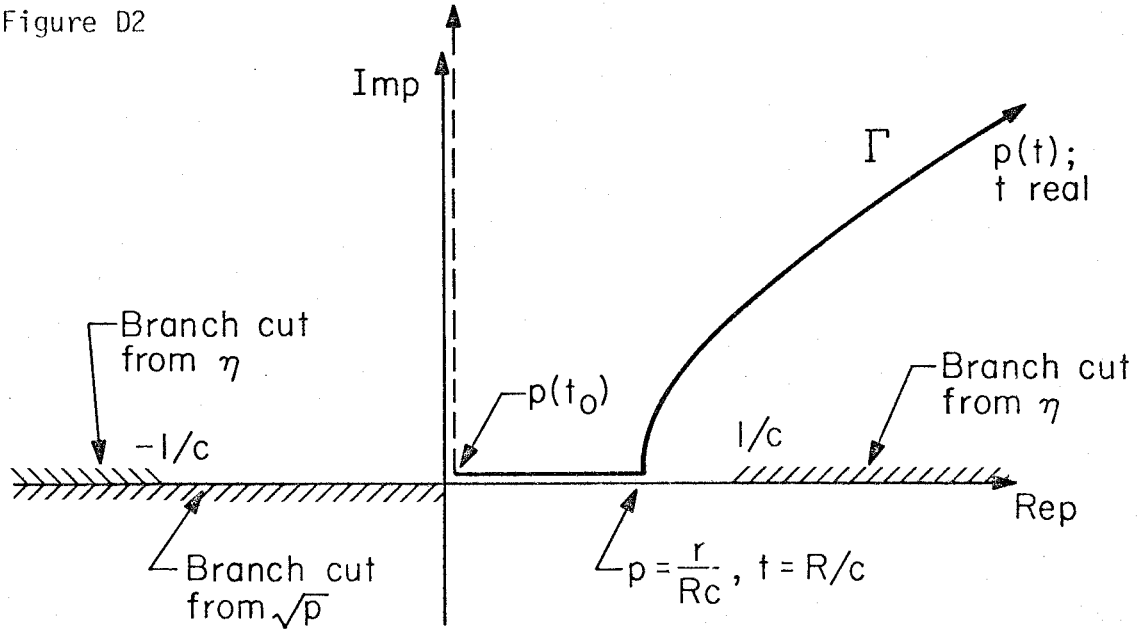

If we keep only the first term of the asymptotic expansion, then the change of variables will allow us to rewrite equation (D.30) as

$$\bar{\zeta}(r,z,s) \approx \frac{\sqrt{2}\, s}{\sqrt{\pi r s}} F(s)\ Im \int_{t_o}^{i\infty} \frac{\sqrt{p}}{\eta}\ e^{-s\tau}\ \frac{i\,\eta}{(\tau^2 - \frac{R^2}{c^2})^{1/2}}\ d\tau$$

$$= \frac{\sqrt{2}\, s}{\sqrt{\pi r s}} F(s) \left\{ Im \int_{t_o}^{R/c} e^{-s\tau}\ \frac{\sqrt{p}}{(\frac{R^2}{c^2} - \tau^2)^{1/2}}\ d\tau \right.$$

$$\left. + Im \int_{R/c}^{\infty} e^{-s\tau}\ \frac{i\,\sqrt{p}}{(\tau^2 - \frac{R^2}{c^2})}\ d\tau \right\} . \qquad (D.45)$$

The integrand of the first term is real and thus its imaginary part is zero. Thus

$$\bar{\zeta}(r,z,s) \approx \frac{\sqrt{2}\, s}{\sqrt{\pi r s}} F(s)\ \mathrm{Re} \int_0^\infty H(\tau - \tfrac{R}{c})\ \frac{\sqrt{p}}{(\tau^2 - \frac{R^2}{c^2})^{1/2}}\ e^{-s\tau}\ d\tau \quad . \tag{D.46}$$

We immediately recognize that

$$\zeta(r,z,t) \approx \sqrt{\frac{2}{\pi r}}\ \mathcal{L}P^{-1}\left\{\frac{1}{\sqrt{s}}\right\} * \mathcal{L}P^{-1}\left\{sF(s)\right\} * \left[\frac{H(t-\frac{R}{c})\ \mathrm{Re}\ \sqrt{p}}{(t^2 - \frac{R^2}{c^2})^{1/2}}\right]$$

$$= \sqrt{\frac{2}{r}}\,\frac{1}{\pi}\,\frac{H(t)}{\sqrt{t}} * f'(t) * \frac{H(t-\frac{R}{c})\ \mathrm{Re}\ \sqrt{p}}{(t^2 - \frac{R^2}{c^2})^{1/2}} \quad . \tag{D.47}$$

Notice that this solution is very similar to the line source solution. A convolution with the $\sqrt{t}$ is the only difference. We can simplify equation (D.47) even further by making a first motion approximation for times near R/c . If $t \approx R/c$, then

$$(t^2 - \frac{R^2}{c^2})^{1/2} = (t - \tfrac{R}{c})^{1/2}\ (t + \tfrac{R}{c})^{1/2} \approx (t - \tfrac{R}{c})^{1/2}\ (\tfrac{2R}{c})^{1/2} \quad .$$

Equation (D.47) becomes

$$\zeta(r,z,t) \approx \sqrt{\frac{2}{r}}\,\frac{1}{\pi}\,\frac{H(t)}{\sqrt{t}} * f'(t) * \frac{H(t-\frac{R}{c})\ \mathrm{Re}\ \sqrt{p}}{\sqrt{2\,\frac{R}{c}}\ (t - \frac{R}{c})^{1/2}} \quad . \tag{D.48}$$

Now recall that

$$p = \frac{r}{R^2}\, t + i\left(t^2 - \frac{R^2}{c^2}\right)^{1/2} \frac{|z|}{R^2}$$

and thus for $t \gtrsim R/c$,

$$p(t) \gtrsim \frac{r}{Rc} \quad \text{and} \quad \sqrt{p} \gtrsim \sqrt{\frac{r}{Rc}} \quad .$$

Thus

$$\zeta(r,z,t) \gtrsim \sqrt{\frac{2}{r}\,\frac{c}{2R}\,\frac{r}{cR}}\; \frac{f'(t)}{\pi} * \frac{H(t)}{\sqrt{t}} * \frac{H(t-\frac{R}{c})}{(t-\frac{R}{c})^{1/2}}$$

$$= \frac{f'(t)}{R\pi} * \frac{H(t)}{\sqrt{t}} * \frac{H(t-\frac{R}{c})}{(t-\frac{R}{c})^{1/2}} \quad .$$

Now

$$f(t-\frac{R}{c}) * H(t) = H(t-\frac{R}{c}) * f(t)$$

and thus

$$\zeta(r,z,t) \gtrsim \frac{f'(t-\frac{R}{c})}{R\pi} * \frac{H(t)}{\sqrt{t}} * \frac{H(t)}{\sqrt{t}}$$

$$= \frac{f'(t-\frac{R}{c})}{R\pi} * \pi H(t)$$

$$= \frac{f(t-\frac{R}{c})}{R} \quad . \qquad \text{(D.49)}$$

Despite all of the approximations, we recognize this to be the exact solution. All this means, though, is that this is a simple problem.

Now if you were especially observant, then our contour deformation in Figure D2 might have made you nervous. K_0 has a square root singularity as $\lambda pr \to 0$. Fortunately there is no residue associated with this singularity and our contour deformation was valid. In the point dislocation problem, there is some trouble caused by the existence of simple poles at the origin. This is discussed briefly in Chapter 1. Also, be aware that the asymptotic approximation is not strictly convergent. Even if we took many terms in the approximation, we could not adequately represent the Bessel function when $\lambda pr \to 0$. By the way, $\lambda \to 0$ as the wavelength of interest becomes large, $p \to 0$ for vertically incident waves and $r \to 0$ as the epicentral distance becomes small. It is easy to see that there will be times when we need to compute the exact solution.

Exact Solution

Let us return to the exact solution which is given by equation (D.36),

$$\bar{\xi}(r,z,\lambda) = \frac{2\,F(\lambda)}{\pi}\, Im \int_0^{i\infty} \frac{p}{\eta}\, K_0(\lambda pr) e^{-\lambda \eta |z|}\, dp \quad , \tag{D.50}$$

Taking the inverse Laplace transform of equation (D.50) and assuming that we can exchange the order of integration (that is, bring the inverse transform operation inside of the integral), we obtain

$$\zeta(r,z,t) = \mathcal{L}P^{-1}\left\{\frac{2s}{\pi} F(s)\right\} * \mathcal{L}P^{-1}\left\{Im\int_0^{i\infty} \frac{p}{\eta} K_o(spr)e^{-s\eta|z|}\, dp\right\}$$

$$= \frac{2}{\pi} f'(t) * Im\int_0^{i\infty} \frac{p}{\eta}\, \mathcal{L}P^{-1}\left\{K_o(spr)e^{-s\eta|z|}\right\} dp \quad . \qquad (D.51)$$

Now from page 278 of Erdelyi (1954) we know that

$$\mathcal{L}P^{-1}\left\{e^{zs} K_o(zs)\right\} = (t^2 + 2zt)^{-\frac{1}{2}} \qquad (D.52)$$

for $|\arg z| < \pi$. We also know that

$$\mathcal{L}P^{-1}\left\{e^{-sa}\, \bar{g}(s)\right\} = g(t-a)\, H(t-a) \quad , \qquad (D.53)$$

provided that a is real. Now then,

$$\mathcal{L}P^{-1}\left\{K_o(spr)e^{-s\eta|z|}\right\} = \mathcal{L}P^{-1}\left\{e^{spr} K_o(spr)e^{-s(\eta|z|+pr)}\right\}$$

$$= \mathcal{L}P^{-1}\left\{e^{spr} K_o(spr)e^{-s\tau}\right\} \quad , \qquad (D.54)$$

where

$$\tau \equiv pr + \eta|z| \quad . \qquad (D.55)$$

If we deform the contour of the integral in equation (D.51) to another

contour which assures that τ is real, then we can find the inverse Laplace transform by applying equations (D.52) and (D.53). We immediately recognize that this new contour is the same one which we showed in Figure D2. Once this deformation is complete, we can then solve the inverse Laplace transform.

$$\mathcal{L}p^{-1}\left\{K_o(\delta pr)e^{-\eta|z|}\right\} = \mathcal{L}p^{-1}\left\{e^{\delta pr}\,K_o(\delta pr)e^{-\delta\tau}\right\}$$

$$= \frac{H(t-\tau)}{(t-\tau)^{\frac{1}{2}}\,(t-\tau+2pr)^{\frac{1}{2}}} \quad . \tag{D.56}$$

Our solution then becomes

$$\zeta(r,z,t) = \frac{2}{\pi}\,f'(t) * Im\int_{\Gamma}\frac{p}{\eta}\,\frac{H(t-\tau)\,dp}{(t-\tau)^{\frac{1}{2}}\,(t-\tau+2pr)^{\frac{1}{2}}} \quad , \tag{D.57}$$

where Γ is defined by

$$p(t) = \frac{r}{R^2}\,t + i\left(t^2 - \frac{R^2}{c^2}\right)^{\frac{1}{2}}\frac{|z|}{R^2} \quad . \tag{D.58}$$

Recall that

$$dp = \frac{i\,\eta\,d\tau}{\left(\tau^2 - \frac{R^2}{c^2}\right)^{\frac{1}{2}}} \quad .$$

Thus our solution can be written

$$\zeta(r,z,t) = \frac{2}{\pi} f'(t) * Im \int_{t_o}^{\infty} \frac{ip(\tau)H(t-\tau)\, d\tau}{(\tau^2 - \frac{R^2}{c^2})^{\frac{1}{2}} (t-\tau)^{\frac{1}{2}} (t-\tau+2p(\tau)r)^{\frac{1}{2}}} \quad . \quad (D.59)$$

After some close scrutiny, we realize that this reduces to

$$\zeta(r,z,t) = \frac{2}{\pi} f'(t) * Re \int_{R/c}^{t} \frac{p(\tau)\, d\tau}{(\tau^2 - \frac{R^2}{c^2})^{\frac{1}{2}} (t-\tau)^{\frac{1}{2}} (t-\tau+2p(\tau)r)^{\frac{1}{2}}} \quad . \quad (D.60)$$

This is a very messy integral, and frankly I do not know how to analytically show its solution. We already know what the answer is, so we can easily write the value of the integral. However, finding an analytic method for determining this particular integral is not important to us. We already know the solution to this problem. Later, though, we will have to solve similar, but more complicated, integrals. Notice that the integrand has square root singularities at $\tau = R/c$ and $\tau = t$. Although they are mathematically integrable, these singularities present certain problems for numerical integration schemes. We can make this integral easier to numerically calculate, simply by changing variables. If we define a change of variables

$$\theta = \sin^{-1} \left(\frac{t-\tau}{t-\frac{R}{c}} \right)^{\frac{1}{2}} \quad , \quad (D.61)$$

then equation (D.60) becomes

$$\zeta(r,z,t) = \frac{4}{\pi} f'(t) * Re \int_{0}^{\pi/2} F(\theta)\, d\theta \quad , \quad (D.62)$$

where

$$F(\theta) = \frac{p(\tau(\theta))}{(\tau(\theta) + \frac{R}{c})^{\frac{1}{2}} \; (t(\theta) - \tau(\theta) + 2p(\tau(\theta))r)^{\frac{1}{2}}} \quad . \tag{D.63}$$

Equation (D.62) can now be numerically integrated.

Bibliography

Abramowitz, M. and I. A. Stegun (1972). Handbook of Mathematical Functions, 8th ed., Dover Publications, Inc., New York.

Aki, K. (1968). Seismic displacements near a fault, J. Geophys. Res. 73, 5359-5376.

Alewine, R. W., III (1974). Application of Linear Inversion Theory toward the Estimation of Seismic Source Parameters, Ph.D. Thesis, California Institute of Technology, Pasadena, California, 303 p.

Allen, C. R. and J. M. Nordquist (1972). Foreshock, main shock and larger aftershocks of the Borrego Mountain earthquake. U.S. Geol. Survey Prof. Paper 787, 16-23.

Allen, C. R., M. Wyss, J. N. Brune, A. Grantz and R. E. Wallace (1972). Displacements on the Imperial, Superstition Hills and San Andreas faults triggered by the Borrego Mountain earthquake, U.S. Geol. Survey Prof. Paper 787, 87-104.

Allen, C. R., T. C. Hanks, J. H. Whitcomb (1973). San Fernando earthquake: Seismological studies and their implications, in San Fernando California, Earthquake of February 9, 1971, Vol. I, Geological and Geophysical Studies, U.S. Government Printing Office, Washington, D.C.

Anderson, J. (1974). A dislocation model for the Parkfield earthquake, Bull. Seism. Soc. Am. 64, 671-686.

Anderson, J. G. and P. G. Richards (1975). Comparison of strong ground motion from several dislocation models, Geophys. J. R. Abstr. Soc. 42, 347-373.

Biehler, S. (1964). Geophysical Study of the Salton Trough of Southern California, Ph.D. Thesis, California Institute of Technology, Pasadena, California.

Biehler, S., R. L. Kovach and C. R. Allen (1964). Geophysical framework of the northern end of the Gulf of California structural province, in Marine Geology of the Gulf of California, T. Van Andel and G. Shor, (eds.), Am. Assoc. Petrol. Geologists Mem. 3, 126-296.

Boore, D. M. and M. D. Zoback (1974). Near-field motions from kinematic models of propagating faults, Bull. Seism. Soc. Am. 64, 321-342.

Brekhovskikh, L. M. (1960) (translation by D. Lieberman). Waves in Layered Media, Applied Mathematics and Mechanics, Vol. 6, Academic Press, New York, London.

Burdick, L. J. and G. R. Mellman (1976). Inversion of the body waves from the Borrego Mountain earthquake to the source mechanism, Bull. Seism. Soc. Am., in press.

Burford, R. O. (1972). Continued slip on the Coyote Creek fault after the Borrego Mountain earthquake, U.S. Geol. Survey Prof. Paper 787, 105-111.

Cagniard, L. (1939). Rêflexion et rêfraction des on des sêismiques progressives, Gauthier-Villars, Paris.

Clark, M.M. (1972). Surface ruptures along the Coyote Creek fault, U.S. Geol. Survey Prof. Paper 787, 55-86.

de Hoop, A. T. (1958). Representation theorems for the displacement in an elastic solid and their application to elastodynamic diffraction theory, Thesis, Techrische Hogeschool, Delft.

de Hoop, A. T. (1960). A modification of Cagniard's method for solving seismic pulse problems, Appl. Sci. Res. Section B, 8, 349-356.

Dwight, H. B. (1957). Tables of Integrals and Other Mathematical Data, 3rd rev. ed., Macmillan Co., New York.

Erdelyi, A. (1954). Tables of Integral Transforms, Vol. I, McGraw-Hill, Inc., New York.

Ewing, M. W., W. S. Jardetsky, and F. Press (1957). Elastic Waves in Layered Media, McGraw-Hill Book Co., New York, Toronto, London.

Hadley, D. and H. Kanamori (1978). Recent seismicity in the San Fernando region and tectonics in the west-central transverse ranges, California, Bull. Seism. Soc. Am., in press.

Hamilton, R. M. (1970). Time-term analysis of explosion data from the vicinity of the Borrego Mountain, California, earthquake of 9 April 1968, Bull. Seism. Soc. Am., 60, 367-381.

Hanks, T. C. (1974). The faulting mechanism of the San Fernando earthquake, J. Geophys. Res., 79, 1215-1228.

Hanks, T. C. (1975). Strong ground motion of the San Fernando California earthquake: Ground displacements, Bull. Seism. Soc. Am. 65, 193-225.

Hanks, T. C., J. A. Hileman and W. Thatcher (1975). Seismic moments of the larger earthquakes of the Southern California region, Geol. Soc. American Bull., 86, 1131-1139.

Harkrider, D. G. (1964). Surface waves in multilayered elastic media I. Rayleigh and Love waves from buried sources in a multilayered elastic half-space, Bull. Seism. Soc. Am. 54, 627-679.

Harkrider, D. G. (1976). Potentials and displacements for two theoretical seismic sources, Geophys. J. R. Abstr. Soc. 47, 97-133.

Harkrider, D. G. and D. V. Helmberger (1977). A note on non-equivalent quadrupole source cylindrical shear potentials which give equal displacements, Bull. Seism. Soc. Am., in press.

Hartzell, S. H., G. A. Frazier and J. N. Brune (1978). Earthquake modeling in a homogeneous half-space. Bull. Seism. Soc. Am. 68, 301-316.

Haskell, N. A. (1964). Total energy and energy spectral density of elastic wave radiation from propagating faults, Bull. Seism. Soc. Am., 54, 1811-1831.

Heaton, T. H. and D. V. Helmberger (1978). Predictability of strong ground motion in the Imperial Valley: Modeling the M 4.9, November 4, 1976 Brawley earthquake, Bull. Seism. Soc. Am., 68, 31-48.

Helmberger, D. V. (1968). The crust-mantle transition in the Bering Sea, Bull. Seism. Soc. Am., 58, 179-214.

Helmberger, D. V. (1974). Generalized ray theory for shear dislocations, Bull. Seism. Soc. Am. 64, 45-64.

Helmberger, D. V. and S. D. Malone (1975). Modeling local earthquakes as shear dislocations in a layered half-space, J. Geophys. Res. 80, 4881-4888.

Helmberger, D. V. and L. R. Johnson (1977). Source parameters of moderate size earthquakes and the importance of receiver crustal structure in interpreting observations of local earthquakes, Bull. Seism. Soc. Am. 64, 301-313.

Helmberger, D. V. and D. G. Harkrider (1978). Modeling earthquakes with generalized ray theory.

Hudson, D. E., A. G. Brady, M. D. Trifunac and A. Vijayaraghavan (1971). Strong-motion earthquake accelerograms, corrected accelerograms and integrated velocity and displacement curves, Vol. II, Part A, Earthquake Eng. Res. Lab., EERL 86-88, California Institute of Technology, Pasadena, California.

Johnsen, K. E. and C. M. Duke (1973). Damage distribution in the Sylmar Valley area, in San Fernando, California, Earthquake of February 9, 1971, Vol. I, Part B, Effects on Building Structures, U.S. Government Printing Office, Washington, D.C.

Johnson, C. E. and D. M. Hadley (1976). Tectonic implications of the Brawley earthquake swarm, Imperial Valley, California, January 1975, Bull. Seism. Soc. Am. 66, 1133-1144.

Johnson, L. R. and T. V. McEvilly (1974). Near-field observations and source parameters of Central California earthquakes, Bull. Seism. Soc. Am. 64, 1855-1886.

Jungels, P. H. and G. A. Frazier (1973). Finite element analysis of the residual displacements for an earthquake rupture: Source parameters for the San Fernando earthquake, J. Geophys. Res. 78, 5062-5083.

Kawasaki, I. (1975). On the dynamical process of the Parkfield earthquake of June 28, 1966, J. Phys. Earth 23, 127-144.

Lamb, H. (1904). On the propagation of tremors over the surface of an elastic solid, Phil. Trans. Roy. Soc. London, Series A 203, 1-42.

Langston, C. A. and D. V. Helmberger (1975). A procedure for modeling shallow dislocation sources, Geophys. J. R. Abstr. Soc. 42, 117-130.

Langston, C. A. (1978). The February 9, 1971 San Fernando earthquake: A study of source finiteness in teleseismic body waves, Bull. Seism. Soc. Am. 68, 1-29.

Mansinha, L. and D. E. Smylie (1971). The displacement fields of inclined faults, Bull. Seism. Soc. Am. 61, 1433-1440.

Nason, R. (1973). Increased seismic shaking above a thrust fault, in San Fernando, California, earthquake of February 9, 1971, Vol. I, Part A, Geological and Geophysical Studies, U.S. Government Printing Office, Washington, D.C.

Nigam, N. C. and P. C. Jennings (1968). Digital Calculation of Response Spectra from Strong-Motion Earthquake Records, Report from the Earthquake Engineering Research Laboratory, California Institute of Technology, Pasadena, California, 65 p.

Pekeris, C. L., Z. Alterman, F. Abramovici and H. Jarosh (1965). Propagation of a compressional pulse in a layered solid, Rev. Geophys. 3, 25-47.

Savage, J. C. (1966). Radiation from a realistic model of faulting, Bull. Seism. Soc. Am. 56, 2, 577-592.

Scott, N. H. (1973). Felt area and intensity of San Fernando earthquake, in San Fernando, California, Earthquake of February 9, 1971, Vol. I, Part A, Geological and Geophysical Studies, U.S. Government Printing Office, Washington, D.C.

Sharp, R. V. (1976). Surface faulting in Imperial Valley during the earthquake swarm of January-February, 1975, Bull. Seism. Soc. Am. 66, 1145-1154.

Sommerfeld (1949). Optics, Academic Press, Inc., New York, 383 p.

Spencer, T. W. (1960). The method of generalized reflection and transmission coefficients, Geophysics 25, 625-641.

Strick, E. (1959). Propagation of elastic wave motion from an impulsive source along a fluid-solid interface, Parts II and III, Phil. Trans. Roy. Soc. London, Series A, 251, 465-523.

Swanger, H. J. and D. M. Boore (1978). Simulation of strong motion displacements using surface wave modal superposition, Bull. Seism. Soc. Am., in press.

Trifunac, M. D. (1971). Zero base-line correction of strong motion accelerograms, Bull. Seism. Soc. Am. 61, 1201-1211.

Trifunac, M. D., F. E. Udwadia and A. G. Brady (1973a). Analysis of errors in digitized strong-motion accelerograms, Bull. Seism. Soc. Am. 63, 157-187.

Trifunac, M. D., A. G. Brady and D. E. Hudson (1973b). Strong-motion earthquake accelerograms, Vol. II C, G, J, corrected accelerograms and integrated ground velocity and displacement curves, EERL 73-75, Earthquake Eng. Res. Lab., California Institute of Technology, Pasadena, California.

Trifunac, M. D. (1974). A three dimensional dislocation model for the San Fernando, California, earthquake of February 9, 1971, Bull. Seism. Soc. Am. 64, 149-172.

Trifunac, M. D. and F. E. Udwadia (1974). Parkfield, California earthquake of June 27, 1966: A three dimensional moving dislocation, Bull. Seism. Soc. Am. 64, 511-533.

Tucker, B. E. and J. N. Brune (1973). S-wave spectra and source parameters for aftershocks of the San Fernando earthquake of February 9, 1971, in Geological Geophysical Studies, Vol. 3, San Fernando Earthquake of February 9, 1971, NOAA, U.S. Department of Commerce, Washington, D.C.

U.S. Coast and Geodetic Survey, Seismological Field Study, and California Institute of Technology, Earthquake Engineering Research Laboratory (1968). Strong-motion instrument data on the Borrego Mountain earthquake of 9 April 1968: San Francisco, California, 119 p.

Vered, M. and A. Ben-Menahem (1974). Application of synthetic seismograms to the study of the low-magnitude earthquakes and crustal structure in the northern Red Sea region, Bull. Seism. Soc. Am. 64, 1221-1237.

Whittaker, E. T. and G. N. Watson (1969). A Course of Modern Analysis, Cambridge University Press.

Wiggins, R. A. and D. V. Helmberger (1974). Synthetic seismogram computation by expansion in generalized rays, Geophys. J. R. Abstr. Soc. 37, 73-90.

Wiggins, R. and G. Frazier (1977). The Parkfield earthquake of 1966 - A study of the dislocation parameters based on a complete modeling of elastic wave propagation. EOS, Vol. 58, no. 12.